Experiments with Degenerate Bose and Fermi Gases

by

Subhadeep Gupta

Submitted to the Department of Physics
in partial fulfillment of the requirements for the degree of

Doctor of Philosophy

at the

MASSACHUSETTS INSTITUTE OF TECHNOLOGY

August 2003

Author . . . .
Department of Physics
August 29, 2003

Certified by . . . .
David E. Pritchard
Cecil and Ida Green Professor of Physics
Thesis Supervisor

Certified by . . . .
Wolfgang Ketterle
John D. MacArthur Professor of Physics
Thesis Supervisor

Accepted by . . . .
Thomas J. Greytak
Professor of Physics, Associate Department Head for Education

Experiments with Degenerate Bose and Fermi Gases

by

Subhadeep Gupta

Submitted to the Department of Physics
on August 29, 2003, in partial fulfillment of the
requirements for the degree of
Doctor of Philosophy

Abstract

Two sets of studies are described in this thesis. In the first set, an atom interferometry technique was developed for the measurement of the fine structure constant using a Bose-Einstein Condensate. In the second set, degenerate Fermi gases were prepared and their properties explored in a regime of strong interactions.

We have developed an atom interferometer which is capable of measuring with high precision the "photon recoil frequency" (ω_{rec}). ω_{rec} corresponds to the kinetic energy of an atom recoiling due to absorption of a photon. ω_{rec} can be used to determine the quantity h/m_{atom} and the fine structure constant, α. A preliminary measurement using a ^{23}Na Bose-Einstein Condensate yielded ω_{rec} with a precision of 7×10^{-6} which deviated by 2×10^{-4} from the currently accepted value. Plausible upgrades to the apparatus should produce a precision of 10^{-9} which would bring within reach a measurement of h/m_{atom} and α in the 10^{-9} range. Such accuracy would be of considerable scientific and metrological import.

A quantum degenerate gas of ^{6}Li fermions was produced by sympathetic cooling with ^{23}Na bosons in a two-species atom trapping apparatus. The cooling strategy was optimized to enable production of fermions with atom numbers up to 7×10^7 at half the Fermi temperature (T_F), or temperatures down to $0.05\,T_F \sim 100\,\mathrm{nK}$ with 3×10^7 atoms. We can also produce degenerate Bose-Fermi mixtures with several million atoms in each species.

We studied the behavior of mixtures of fermi gases in regimes of strong interactions near "Feshbach" resonances. A study of system stability enabled the experimental observation of two such Feshbach resonances.

We carried out a theoretical study to interpret the observation (by many experimental groups) of hydrodynamic behavior of fermi gases during expansion out of an atom trap in a strongly-interacting regime. The study concluded that this behavior was not a qualitative signature of fermionic superfluidity and could arise from classical collisions.

Finally, radio-frequency (RF) spectroscopy was used to probe interaction in ^{6}Li. We demonstrated the absence of mean field "clock" shifts of RF transitions in a two-(spin)state fermion system. Using a three-state system, we measured the interaction strength between different spin states. The measurements near Feshbach resonances indicate a saturation of the interaction strength at a large negative value. This result is of relevance in the continuing quest for fermionic superfluidity in atomic gases.

Thesis Supervisor: David E. Pritchard
Title: Cecil and Ida Green Professor of Physics

Thesis Supervisor: Wolfgang Ketterle
Title: John D. MacArthur Professor of Physics

To Ma, Baba,

and my brother Rajdeep.

Acknowledgments

There are many individuals I wish to thank for making this work possible. This official forum for acknowledgements stands only as a small token of the gratitude I feel towards them all.

I was attracted to atomic physics and MIT by Dave Pritchard. I owe him a huge thank you for providing me with the opportunity to be a part of the atomic physics family on the second floor(s) of Building 26 (and 36). His enthusiasm and love for all aspects of physics has always been inspiring to me. Dave's hands-off attitude has allowed me to develop as a physicist at my own pace. He has also provided a good ratio of encouragement and criticism which kept me excited and challenged over the last several years.

I have been extremely fortunate to have had Wolfgang Ketterle as a co-advisor. Wolfgang's skill at simultaneously grasping the nuts and bolts as well as the big picture of a research endeavor has always been a key element for his group's success. Even with the increased burden of multiple research groups, he continues to perform this feat every day. Just about every conversation I have had with him left me feeling excited and fired up about the task at hand as well as how it related to the overall goal we were aiming for. It has been a privilege and a pleasure to work with him and learn from him.

I want to single out and thank the people I have worked most closely with over the last few years. Their efforts formed key elements in all the work presented in this thesis.

Zoran Hadzibabic has been much more than a colleague and a friend to me over the last two-three years. Zoran and I were on the same time track at MIT and defended our PhDs within a day of each other. Zoran's infectious friendliness, his passion for science and his obsession with understanding have been instrumental in making my life at MIT joyful and productive. We spent many memorable nights wrestling the machine, fuelled by The Minutemen and by the never-stale references to The Big Lebowski. In addition, Zoran's deep understanding of physics provided a fantastic resource to bounce ideas back and forth several times a day.

Claudiu has set high "Stan"-dards of technical excellence in the lab from the very beginning. If someone wants to know the correct way to build some experimental component, he can provide. His attention to details as well as aesthetics while building seminal pieces of the machine have made the lab more reliable as well as easier on the eye!

Martin Zwierlein's amazing scientific capabilities are enhanced by his irrepressible enthusiasm towards everything in lab (and elsewhere). I have thoroughly enjoyed working with him and learning from him during various projects. In him, I also found a partner for the frequent good(?) pun.

Another amazing scientist and the newest addition to the Lithium team, Christian Schunck, has become an efficient and dependable lab companion in a very short time. I have enjoyed good times with him from drilling holes in plexiglass to figuring out the best way to pack a lunch buffet take-out box. The Lithium lab now remains in the solid hands

of Claudiu, Martin and Christian. I have learned from all of you and will miss working with you.

I thank post-doc Kai Dieckmann for all his efforts towards ensuring the success of the atom interferometer project. His prior experience at building a BEC machine was also brought to bear on the building of the double-species sodium-lithium apparatus.

I now turn to thanking the people I learned from during my initial stages at MIT.

I first joined Dave Pritchard's beam atom interferometer group and learned about AMO research from David Kokorowski, Tony Roberts, Rich Rubenstein, Al-Amin Dhirani and Ed Smith. In particular, David introduced me to various facets of laboratory life including a love-hate relationship with dye lasers.

As Dave Pritchard's interests changed towards ultracold-atom interferometry, I became a "cross-over" student in the Ketterle/Pritchard BEC collaboration. I learned about ultracold atom research from Dan Stamper-Kurn, Shin Inouye, Ananth Chikkatur and Axel Görlitz. Shin was the person I worked most closely with during my early period in the BEC I group.

Shin's superb scientific skills and calm presence provided a terrific example to learn from. In addition, I have to thank him for providing copious quantities of cookies during late night runs as well as tasty Miso soup on more social occasions. I also had the good fortune of collaborating closely with Tilman Pfau, Robert Löw and Till Rosenband. Each an extraordinary individual, they provided physical insights, hard work and technical innovations which pushed the research forward. I also learned a great deal from interactions with the BEC II group: Chandra Raman, Roberto Onofrio, Dallin Durfee, Chris Kuklewicz, and Michael Köhl.

During the middle part of my graduate career, a major goal of the sodium BEC I experiment was the building of BEC III - the "science chamber" machine. I have fond memories of working with Todd Gustavson, Ananth Chikkatur, Aaron Leanhardt and Axel Görlitz, during this phase. The expertise and work ethics which the post-docs Todd and Axel brought into the group sped everything up in the lab and also provided models to aspire towards. Ananth and I not only collaborated on building pieces of the new apparatus, but also went through the first-year problem sets together, and then shared an apartment for three years. Our friendship has spanned DJ Shadow-inspired earth-compensation coil winding to spiked-chai-enhanced drumming.

From the early days of winding a Zeeman slower ("it'll only take a few hours"), Aaron Leanhardt has remained a trusted collaborator and friend. His wide ranging physics skills have been an invaluable asset to the whole group. Aaron has also been a staunch partner-in-crime to Jamil Abo-Shaeer - together, they have organized a steady stream of memorable gatherings which tied the whole group together in a very festive manner. Jamil's cheerful spirit and resounding hallway high-5's have become an integral part of the group. I will also fondly remember a fun-filled conference trip to Kissimmee, Florida with Jamil, Aaron, Zoran, Gretchen Campbell, Micah Boyd, and Jit Kee Chin. The high-spirits shared will

not easily slide from memory.

Huge thank you's to various people in the AMO community for helpful advice, miscellaneous favors, loan of equipment, computer expertise and uplifting conversations at various times: Mike Bradley, Alex Cronin, Joel deVries, Yong-Il Shin, Cort Johnson, David Kielpinski, Jana Lehner, Lia Matos, Dan Miller, Takashi Mukaiyama, Tom Pasquini, Simon Rainville, Michelle Saba, Andre Schirotzek, Dominik Schneble, Julia Steinberger, Jeff Steinhauer, Erik Streed, James Thompson, Yoshio Torii, Kendra Vant, Mukund Vengalatorre, Johnny Vogels, and Kaiwen Xu. It has been great to get to know all of you.

Thanks to Dr. James Anglin for explaining subtleties of hydrodynamics to me as well as his continual interest in our work. I also thank Prof. Winn Smith with whom I had the pleasure to collaborate on several papers. Thanks also to Prof. Daniel Kleppner who was my academic advisor during my time at MIT and also served on my thesis committee.

Carol Costa's presence in the CUA hallway has been calming and her pleasant and efficient dissemination of information has always served to quickly simplify bureaucratic procedures at MIT. The entire RLE support staff deserve thanks for providing a shady administrative umbrella - in particular I will point out Maxine Samuels, Gerry Power and Al McGurl who have helped a lot at critical times.

Life at MIT has to be balanced with life outside MIT. For this I have to thank several friends around town. In particular, Zeenat Potia has been a frequent source of good cheer and good food. Kinger Mallik's chilling nature, skills at Scrabble, and (shared) love for anything Austin Powers, formed the basis of several entertaining evenings. Thanks to Pradeep "The Champ" Sarin for his generosity with home built electronics as well as the frequent use of his car for driving practice. Pradeep was also my apartment-mate for several years as was Augustine Urbas. I enjoyed many post 3 a.m. dinners with Pradeep and Augustine at (the now sadly extinct) Deli-Haus. Several late-night experimental runs found a tasteful conclusion in Virtua Fighter battles with Augustine. Thanks also to Sanjoy and Doel Ghosh, Nick Gould and Adrian Quackenbush for the occasional food and wine.

I especially thank Munira Khalil for always being there for me and supporting me. Her companionship is a constant source of joy and strength. I hope that her grad school life was as much enriched by me as mine was by her.

Finally, I would like to thank my family. My parents Bhaskar and Ruby Gupta have consistently provided encouragement and support during my studies. Their love and blessings continue to energize me as I move on in the world. My brother Rajdeep has inspired me from childhood and was a key factor in my decision to study abroad. Thanks to you all.

Contents

List of Figures

Chapter 1

Introduction

Over the last century, the scientist's understanding of the world has undergone a profound change. The gradual realization of the underlying discreteness of nature has shaped a "quantum" picture of the world. In this picture, Nature is divided into very small but discrete units called quantum states. The behavior of particles which cannot be described without assuming this underlying disreteness is called quantum behavior. Typically, such behavior is exhibited at very small *microscopic* scales of length, energy, etc. However, experimental advances can sometimes lead to spectacular *macroscopic* quantum phenomena. One such incredible advance occurred in 1960 with the invention of the optical laser [13, 14]. A laser is created when particles of light, *photons*, occupy a single quantum state. Since all the photons are in the same state, they share the same energy, polarization, direction of propagation and so on. This is the reason for the spectacular difference between laser light and ordinary light for example from a light bulb.

With the turn of the century, a new paradigm of macroscopic quantum phenomena is rapidly establishing itself. Particles of matter, *atoms*, can also occupy a single quantum state. This marks a phase transition into a new state of matter - the Bose-Einstein Condensate (BEC). This phase transition was observed in dilute alkali metal vapors in 1995 [15, 16, 17]. Since then, gaseous BECs have been in the limelight of science.

As with lasers, BECs can be applied towards spectroscopy and metrology[1]. The weak interactions in dilute gas BECs make it an ideal testing ground for basic quantum theories. This was not possible for the previous realization in ^{4}He[18]. In addition, gaseous atomic systems are equipped with a whole range of experimental "knobs" which allow studies in a wide regime of temperatures, densities, interaction strengths, internal state composition, and so on.

The early achievements of BEC in ^{87}Rb[15], ^{7}Li[16], and ^{23}Na[17], have been followed by the creation of BECs in other dilute atomic gases: ^{1}H[19], ^{85}Rb[20], metastable ^{4}He[21, 22], ^{41}K[23], ^{133}Cs[24], and ^{174}Yb[25]. This list is constantly growing.

1.1 Degenerate Atomic Gases

There are only two types of particles in nature. Identical particles which can occupy the same quantum state (such as photons and ^{23}Na atoms) are called bosons. The other type of particles are called fermions. Two identical femions cannot occupy the same quantum state.

Pronounced quantum behavior of atomic gases can occur when the number of available quantum states approaches the number of identical particles in the system. Such conditions induce behavior which begins to depart dramatically from the classical characteristics of room temperature gases. BEC is an example of such behavior. Let's estimate the conditions for this to happen.

The Heisenberg Uncertainty principle of quantum mechanics relates the size Δx and momentum Δp of a quantum state:

$$\Delta x \Delta p = \hbar.$$

Using the kinetic energy relation (for a particle of mass m at temperature T):

$$\frac{(\Delta p)^2}{2m} = k_B T$$

then gives the de-Broglie wavelength

$$\Delta x \approx \lambda_{\mathrm{dB}} = \frac{h}{\sqrt{2mk_B T}}.$$

λ_{dB} describes the spatial extent of the quantum state at temperature T. For a gas of particles of mass m at temperature T, quantum behavior will ensue if the density n of the gas is large enough to cause overlap between the different quantum states. This requirement produces the condition:

$$n\lambda_{\mathrm{dB}}^3 \gtrsim 1 \quad \Rightarrow \quad nT^{-\frac{3}{2}} \gtrsim (\frac{2mk_B}{\hbar^2})^{3/2}. \tag{1.1}$$

Under these conditions, quantum phenomena can be expected to occur. Very often, the phrase "quantum degenerate" is applied to a gas under these conditions.

At room temperature ($\sim 300\,\mathrm{K}$), Eqn. 1.1 gives a degeneracy density for ^{23}Na atoms of $n \sim 10^{27}\,\mathrm{cm}^{-3}$. At these densities, the system is no longer a gas at room temperature. The phase transition to liquid and then solid will mar the approach to degeneracy. Several technical advances have been required to keep the particles in a gaseous state while lowering their temperature in order to reach degeneracy. In current experiments on alkali metal vapors, degeneracy is reached at a temperature of $\lesssim 1\,\mu\mathrm{K}$ (a billion times colder than air). Eqn. 1.1 then implies a density of $\sim 10^{14}\,\mathrm{cm}^{-3}$. This requirement makes the gas dilute and allows for simplified theoretical treatments.

13

1.2 Different Quantum Matters

Bosons and fermions, behave differently near degeneracy. This is formally understood from the difference in their quantum statistics which relates equilibrium state occupation probabilities with thermodynamic quantities.

Bosonic degeneracy involves the formation of the Bose-Einstein Condensation - macroscopic occupation of a single quantum state. Fermionic degeneracy involves single occupation of "nearest neighbor" quantum states. This tight packing creates a Fermi Sea of particles. A minimum size is thus maintained giving rise to the so-called Fermi pressure. Additional particles cannot penetrate into the Fermi Sea, giving rise to a "Pauli blocking" behavior.

The first observation of Fermi degeneracy in 1999 was in ^{40}K[26] by the group of D. Jin at the University of Colorado. Since then five other groups have made similar observations in ^{6}Li[27, 28, 29, 3] as well as in ^{40}K[30].

Several groups are now actively trying to observe another kind of quantum behavior which arises when degenerate fermions attract each other and form particle-pairs with long range correlations. This state is known as the Bardeen-Copper-Schreiffer (BCS) superfluid[31]. For reasons similar to those mentioned in the case of BEC, in spite of previous realizations in ^{3}He and superconductors, gaseous fermionic superfluids should provide a whole new range of tests and explorations.

This thesis reports on studies using both degenerate bosons and degenerate fermions with particular emphasis on experiments towards creating the BCS superfluid.

1.3 Outline of this thesis

The work reported in this thesis can be divided into two parts. The first part was performed under the supervision of Dave Pritchard and involves an application of BECs to high precision measurements. We developed a BEC atom interferometer using optical standing waves that is capable of precisely measuring ω_{rec}, the recoil frequency (energy) of an atom due to absorption of a photon. ω_{rec} in turn can be used to determine h/m_{atom} and α, the fine structure constant. This work is described in Chapter 2. Our publication of a "first-generation" measurement of ω_{rec} in sodium is included as Appendix A.

The second part of the thesis was performed under the supervision of Wolfgang Ketterle and involves the development of a new quantum system which holds promise for producing a BCS superfluid of paired gaseous atoms. Chapter 3 describes some theoretical aspects necessary for a motivation and understanding of the experiments while Chapter 4 describes the apparatus used for the work. The remaining chapters discuss our experimental and theoretical results.

Chapter 5 describes our studies of stability in strongly interacting fermion systems which resulted in the first observation of Feshbach resonances in ^{6}Li. Chapter 6 describes a theo-

retical study of the role of Pauli blocking of collisions during the expansion of an interacting Fermi gas. Our results are relevant for understanding the observations (in many laboratories) of hydrodynamic behavior during expansion of a strongly-interacting Fermi gas. Chapter 7 describes studies of fermionic interactions by observations of resonance shifts of radio-frequency transitions in ultracold gases. The relevant publications are included as Appendices B,C, D, and E.

Chapter 2

Atom Interferometry for h/m and α

We have demonstrated a new atom interferometer configuration capable of measuring the "photon recoil frequency" to high accuracy. The photon recoil frequency is the frequency corresponding to the kinetic energy of an atom recoiling due to absorption of a photon. This frequency is an important ingredient for a high accuracy measurement of α, the fine structure constant. Our publication describing the first generation measurement using Bose-Einstein Condensates is included in Appendix A:

- *S. Gupta, K. Dieckmann, Z. Hadzibabic, and D.E. Pritchard, "Contrast Interferometry using Bose-Einstein Condensates to measure h/m and α" Phys. Rev. Lett, **89**, 140401 (2002) [1]. Included in Appendix A.*

A key aspect of our atom interferometer is the use of optical standing waves as diffraction gratings. Methods of atom manipulation using optical standing waves are described in Section 2.2. This section is taken from our review paper:

- *S. Gupta, A.E. Leanhardt, A.D. Cronin and D.E. Pritchard, "Coherent manipulation of atoms with standing light waves." Special Issue of Compte rendus de l'académie des sciences, Série IV - Physique Astrophysique **2**, 479 (2001) [2].*

Matter-wave duality is one of the fascinating features of quantum mechanics. This duality can also be disturbing since it departs so directly from everyday experience. Matter-wave duality lies at the heart of the relatively new fields of atom optics and Bose-Einstein condensates (BECs). The combination of these two fields should then be even more fascinating. In addition, the traditional experiments with atom interferometers: testing of fundamental principles, studies of atomic properties, applications as inertial sensors, and measurements of fundamental constants [32] can benefit from the brightness (intensity and small momentum spread) of BEC sources. Finally, the coherence properties of condensates may allow BEC based atom interferometers to approach the Heisenberg detection limit [33]. This corresponds to a measurement precision which scales like $1/N$ for N atoms and not like $1/\sqrt{N}$ as for independent measurements on N atoms.

As techniques of atom manipulation and those for creating condensates have developed, the last few years have seen the birth of BEC atom-optics. Free falling condensates have been coherently manipulated with standing waves of light creating "free-falling" atom interferometers [34, 35, 1]. "Trapped" BEC atom interferometers have also been created using optical potentials [36]. This chapter deals with our efforts towards developing a free-falling atom interferometer for measuring the photon recoil frequency.

Section 2.1 contains a discussion of the requirements for making an atom interferometer. I then introduce the tools of standing wave diffraction gratings that can be used to construct a BEC atom interferometer in Section 2.2. Section 2.3 discusses a simple Mach-Zehnder interferometer geometry and its realization with a BEC. In Section 2.5, I present our scheme to measure the recoil frequency and the "first-generation" results. Finally, in Section 2.6.1 I discuss prospects for scaling up our interferometer for scientifically significant measurements.

2.1   Atom Interferometers

Interference is an underlying principle of quantum mechanics embedded in the superposition principle. An interferometer is a device designed to exploit this principle to measure some useful physical quantity.

The working of an atom interferometer can be broken into 3 simple steps: (1) starting from a single atom source, coherently create multiple states[1] (sometimes called "paths"), (2) let these multiple states evolve over some time during which the interaction to be measured occurs, and (3) recombine the states and then detect the (interference pattern of) atoms. Measurements are then sensitive to the different evolution characteristics of the different states/paths. Various interferometer "architectures" or "geometries" based on atom beams as well as laser-cooled atomic sources have been summarized elsewhere [32].

A basic requirement of atom interferometers is then state manipulation, in order to accomplish steps (1) and (3). The usefulness of the interferometer is dependent on what happens during step (2). For example, one can place diffraction gratings ($\sim 200\,\mathrm{nm}$) in the path of a supersonic sodium atomic beam ($\sim 1000\,\mathrm{m/s}$). This results in a splitting into different transverse momentum states travelling at a small angle from each other. These follow physically different paths which can be bent with additional gratings and recombined at an atom detector. An electric field placed in a way that affects the different paths differently will affect the phase of the final atom signal. This can then be used to measure the electric polarizability of an atom [37].

Although different atomic *internal* states can be used to make an interferometer[38], the use of different *external* momentum states turns out to be advantageous[39]. Most of the work towards making a meaningful measurement usually comes from trying to isolate

---

[1]Here "coherently" means that the different states have a definite phase relationship with each other

the system into feeling only the interaction of interest (in the above example, the electric field) and nothing else. The use of a single internal state can reduce many perturbations to "common mode" so that they do not shift the relative atom phases. Perturbations from light shifts and magnetic fields can be suppressed in this way[39, 1]. Optical standing waves can be used to manipulate momentum states of atoms in a very controlled manner to create arbitrary interferometer geometries.

2.2 Manipulation of Atoms with Standing Waves of Light

When an atom scatters a photon, it recoils due to the momentum exchanged with it. Thus photons can change the momentum of atoms. The recoil from spontaneous scattering processes is the key element of laser cooling[40].

The photon absorbed by an atom from a laser beam can be *spontaneously* emitted (scattered), making the atom recoil in a random direction. If the atom is exposed to two laser beams, the photon absorbed from one beam can scatter in a coherent *stimulated* manner into the other beam. If the stimulated process is faster than the spontaneous process, the atom recoils in the direction given by the difference in wavevectors of the two laser beams. This condition can be achieved with sufficient detuning of the laser beams from the electronic resonance. The two beams of course form a standing wave, and an equivalent description of this process can be given in terms of atom diffraction off the resulting standing wave. For momentum state manipulation, counter-propagating laser beams are usually used, which constrains the atom to change its momentum in multiples of $2\hbar k$, where k is the wavevector associated with a single photon.

Two standard processes used in the manipulation of external states of neutral atoms using optical standing waves are the Bragg and the Kapitza-Dirac processes. These are used in the construction of our atom interferometer. The rest of this section is taken from [2] and describes these processes in some detail.

2.2.1 Bragg Scattering, Ref. 2

Although it can be difficult to realize the physical conditions that assure its occurrence, Bragg scattering is the simplest example of coherent momentum transfer to atoms by light. Consider a standing wave light grating formed by two counter-propagating plane waves (travelling parallel to the z-axis) of equal amplitude, E_0, wavevector, k, frequency, ω, polarization vector, $\hat{e}$, and temporal envelope function, $f(t)$:

$$\vec{E}(z,t) = E_0 f(t) \sin(kz - \omega t)\hat{e} + E_0 f(t) \sin(kz + \omega t)\hat{e}, \qquad (2.1)$$

$$= 2E_0 f(t) \sin(kz) \cos(\omega t)\hat{e}. \qquad (2.2)$$
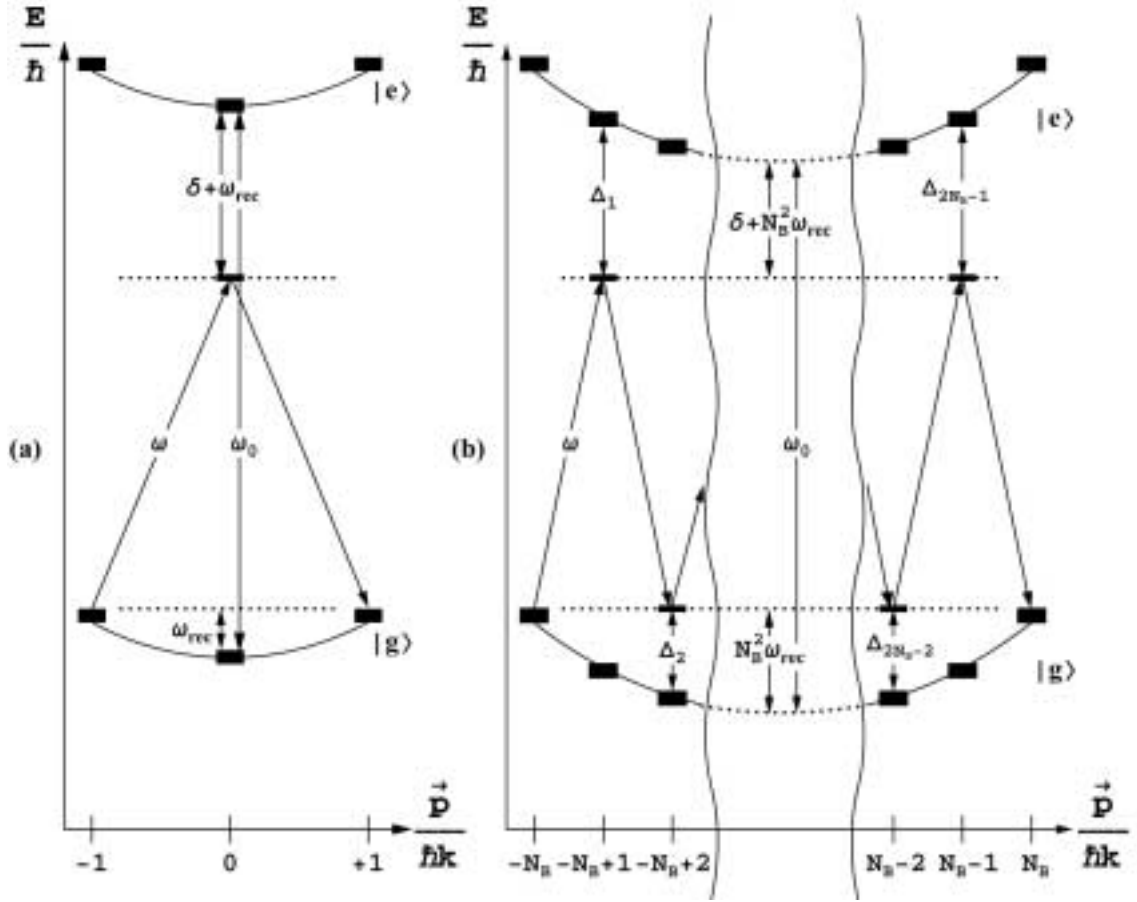
Figure 2-1: (a) First and (b) N_B^{th} order Bragg transition diagram. The atomic kinetic energy lies on the parabola $N^2 \hbar \omega_{\text{rec}}$, $N = 0, \pm 1, \pm 2, \ldots$ where the associated atomic momentum is given by $N \hbar k$.

We would like to work with momentum states as our basis, thus it is easiest to consider the description of the electric field driving the transitions in terms of two counter-propagating travelling waves of definite momentum (Equation 2.1), as opposed to the single standing wave they jointly form (Equation 2.2).

Momentum is transferred by paired stimulated absorption and emission processes, resulting in a transfer of photons between the travelling waves. An N_B^{th} order diffraction process transfers N_B photons from one travelling wave to the counter-propagating travelling wave and changes the atomic momentum by $2N_B\hbar k$. Furthermore, atomic population is transferred only between $|g, -N_B\hbar k\rangle$ and $|g, +N_B\hbar k\rangle$, where $|g(e), \pm N\hbar k\rangle$ denotes a two-level atom in its ground (excited) state with momentum $\pm N\hbar k$ parallel to the standing wave axis. The excited state remains nominally unpopulated so long as the temporal envelope function, $f(t)$, does not have strong frequency components near the laser detuning, $\delta = \omega - \omega_0$, where ω_0 is the unperturbed frequency of the atomic transition. Furthermore, for a given initial state $(|g, -N_B\hbar k\rangle)$ the uniqueness of the final state $(|g, +N_B\hbar k\rangle)$ comes about because of the fundamental assumption that makes Bragg scattering so simple to describe; the uncertainty in the photon energy driving the transitions is small compared to the energy separation between neighboring momentum states. A quantitative discussion of the validity of this assumption will be given later.

We now calculate the probability, $P_1^B(\tau)$, of the first order ($N_B = 1$) Bragg process taking an atom from $|g, -\hbar k\rangle$ to $|g, +\hbar k\rangle$ when the atoms interact with a constant light intensity for a time τ (i.e. in Equations 2.1 and 2.2 $f(t)$ is a square wave of unit amplitude and duration τ). The transition is depicted in Figure 2-1(a). In the electric dipole approximation, the interaction Hamiltonian is $\mathcal{H}_{int}(t) = -\vec{\mu} \cdot \vec{E}(t)$. By momentum conservation, only the plane wave travelling in the $\pm\hat{z}$ direction couples the $|e, 0\rangle \leftrightarrow |g, \mp 1\rangle$ transitions. By using this argument, we are effectively viewing the electric field as a quantum mechanical operator. Expanding the sinusoidal variation of the electric field in terms of complex exponentials and treating the spatially dependent complex exponential terms as quantum mechanical momentum translation operators $(e^{\pm ik\hat{z}}|g(e), n\hbar k\rangle = |g(e), (n \pm 1)\hbar k\rangle)$ yields the interaction Hamiltonian [41, 42, 43]:

$$\mathcal{H}_{int}(t) = -\imath e^{-\imath\omega t}\frac{\hbar\omega_R}{2}(|e, 0\rangle\langle g, -1| - |e, 0\rangle\langle g, +1|) + h.c., \tag{2.3}$$

where the depicted terms are responsible for absorption and the hermitian conjugate (h.c.) terms give rise to stimulated emission. The light-atom interaction is parameterized by the single-photon Rabi frequency,

$$\omega_R = \frac{\mu E_0}{\hbar}, \tag{2.4}$$

where $\mu = \langle e|e\vec{r}|g\rangle \cdot \hat{e}$ is the electric dipole matrix element connecting the ground ($|g\rangle$) and excited ($|e\rangle$) states of the atom. Without loss of generality, we will take μ and hence ω_R to be positive, real-valued quantities. In formulating H_{int}, we have neglected any frequency

components associated with the sudden switch on of the fields and the finite duration of the light-atom interaction. The total Hamiltonian, $\mathcal{H}(t) = \mathcal{H}_0(t) + \mathcal{H}_{int}(t)$, follows simply by including the electronic and kinetic energy terms,

$$\mathcal{H}_0(t) = \hbar\omega_0 |e,0\rangle\langle e,0| + \hbar\omega_{\mathrm{rec}}(|g,-1\rangle\langle g,-1| + |g,+1\rangle\langle g,+1|), \tag{2.5}$$

where the single-photon recoil energy, E_{rec}, of an atom of mass m is given by:

$$E_{\mathrm{rec}} = \hbar\omega_{\mathrm{rec}} = \frac{\hbar^2 k^2}{2m}. \tag{2.6}$$

Making the *ansatz* for the solution wavefuntion as,

$$|\Psi(t)\rangle = c_{-1}(t)e^{-\imath\omega_{\mathrm{rec}}t}|g,-1\rangle + c_0(t)e^{-\imath\omega_0 t}|e,0\rangle + c_{+1}(t)e^{-\imath\omega_{\mathrm{rec}}t}|g,+1\rangle, \tag{2.7}$$

and substituting into the Schrödinger equation yields the three coupled first order differential equations:

$$\dot{c}_{\pm 1}(t) = \mp\frac{\omega_R}{2}e^{\imath\Delta t}c_0(t), \tag{2.8}$$

$$\dot{c}_0(t) = \frac{\omega_R}{2}e^{-\imath\Delta t}(c_{+1}(t) - c_{-1}(t)), \tag{2.9}$$

where $\Delta = \delta + \omega_{\mathrm{rec}}$. Differentiating Equation 2.8 and substituting Equation 2.9 into the result yields the two coupled second order differential equations:

$$\ddot{c}_{\pm 1}(t) - \imath\Delta\dot{c}_{\pm 1}(t) + \frac{\omega_R^2}{4}(c_{\pm 1}(t) - c_{\mp 1}(t)) = 0. \tag{2.10}$$

With the initial conditions,

$$c_{-1}(0) = 1, \tag{2.11}$$

$$c_0(0) = 0 \implies \dot{c}_{\pm 1}(0) = 0, \tag{2.12}$$

$$c_{+1}(0) = 0, \tag{2.13}$$

and the assumption $\Delta^2 \gg \omega_R^2$, the solutions to Equation 2.10 read:

$$c_{-1}(t) = e^{-\imath\frac{\omega_R^{(2)}}{2}t}\cos(\frac{\omega_R^{(2)}}{2}t), \tag{2.14}$$

$$c_{+1}(t) = \imath e^{-\imath\frac{\omega_R^{(2)}}{2}t}\sin(\frac{\omega_R^{(2)}}{2}t), \tag{2.15}$$

where the two-photon Rabi frequency is:

$$\omega_R^{(2)} = \frac{\omega_R^2}{2\Delta} \rightarrow \frac{\omega_R^2}{2\delta}, \quad |\delta| \gg \omega_{\mathrm{rec}}, \tag{2.16}$$

with both transitions driven at equal single-photon Rabi frequencies, ω_R.

Substituting the solution of Equation 2.14 or 2.15 into Equation 2.8 yields an expression for the excited state amplitude:

$$c_0(t) = -i\frac{\omega_R}{2\Delta}e^{-i\Delta t}e^{-i\omega_R^{(2)}t}.$$ (2.17)

This will be important in calculating the rate of spontaneous emission events later.

The solutions for $c_{-1}(t)$ and $c_{+1}(t)$ oscillate with the interaction duration, τ, yielding the result for the $|g, -\hbar k\rangle \to |g, +\hbar k\rangle$ transition probability:

$$P_1^B(\tau) = |c_{+1}(\tau)|^2 = \sin^2\left(\frac{\omega_R^{(2)}}{2}\tau\right).$$ (2.18)

Thus, the system oscillates between the two momentum states $|g, -\hbar k\rangle$ and $|g, +\hbar k\rangle$ in a manner analogous to the Rabi oscillation of atomic population between two resonantly coupled states. This solution with oscillatory probabilities for the two Bragg coupled states is known as the Pendellösung and has been observed for atoms [44], neutrons [45], and x-rays [46].

Viewing Bragg scattering as a two-photon transition from the initial ground state to the final ground state with opposite momentum illuminates the close connection with a Raman transition between two internal substates of the ground state manifold, each with its own external momentum state. The formalism describing the Raman transition is basically the same as that presented here, except the two transitions can be driven at different single-photon Rabi frequencies, ω_{R1} and ω_{R2}, so that the generic two-photon Rabi frequency is given by $\omega_R^{(2)} = \omega_{R1}\omega_{R2}/2\Delta$, where Δ is the detuning from the intermediate state.

An N_B^{th} order Bragg process (similar to a $2N_B$-photon Raman process) is a coherent succession of N_B two-photon transitions with $2N_B - 1$ intermediate states of the form $|e, (-N_B + 1)\hbar k\rangle$, $|g, (-N_B + 2)\hbar k\rangle, \ldots, |g, (N_B - 2)\hbar k\rangle$, $|e, (N_B - 1)\hbar k\rangle$. Such a process is characterized by a $2N_B$-photon Rabi frequency given by [47]:

$$\omega_R^{(2N_B)} = \frac{[\omega_R]^{2N_B}}{2^{2N_B-1}\Delta_1\Delta_2\cdots\Delta_{2N_B-1}},$$ (2.19)

where Δ_n is the detuning from the nth intermediate state. Figure 2-1(b) shows what this process would look like for an N_B^{th} order Bragg transition where the intermediate state detunings are given by:

$$\Delta_n = \begin{cases} \delta + (2N_B n - n^2)\omega_{\text{rec}} & : \quad n \ odd \\ (2N_B n - n^2)\omega_{\text{rec}} & : \quad n \ even \end{cases}.$$ (2.20)

Substituting these detunings into Equation 2.19 yields the N_B^{th} order Bragg transition $2N_B$-

photon Rabi frequency, $\omega_R^{(2N_B)}$ [47]:

$$\omega_R^{(2N_B)} = \frac{[\omega_R]^{2N_B}}{2^{4N_B-3}[(N_B-1)!]^2\delta^{N_B}\omega_{\mathrm{rec}}^{N_B-1}}, \tag{2.21}$$

where we have assumed $|\delta| \gg N_B^2\omega_{\mathrm{rec}}$.

To ensure that the system truly undergoes Bragg scattering, and validate the assumption that only states of equal kinetic energy and opposite momentum are coupled, the overall exposure time, τ, of the atoms to the fields must be limited both from below and above.

The lower bound on τ is necessary to resolve the final momentum state ($|g, N_B\hbar k\rangle$) from neighboring momentum states ($|g, (N_B \pm 2)\hbar k\rangle$) two photon recoil momenta away. This bound also prohibits resonant transitions from the initial momentum state ($|g, -N_B\hbar k\rangle$) to its neighboring momentum states ($|g, (-N_B \pm 2)\hbar k\rangle$) two photon recoil momenta away. For first order Bragg scattering processes ($N_B = 1$) the initial and final state are only separated by two photon recoil momenta, thus the nearest lying momentum states that may be mistakenly populated are $|g, \pm 3\hbar k\rangle$. Avoiding population transfer into these states requires $\tau \gg \pi/4\omega_{\mathrm{rec}}$. For all higher order ($N_B > 1$) Bragg scattering processes, the nearest momentum states are $|g, \pm(N_B - 2)\hbar k\rangle$, which limits the interaction time to:

$$\tau \gg \frac{\pi}{2(N_B-1)\omega_{\mathrm{rec}}}, \tag{2.22}$$

which for $N_B \gg 1$ reduces to:

$$\tau \gg \frac{\pi}{2N_B\omega_{\mathrm{rec}}}. \tag{2.23}$$

The upper bound on the interaction duration is necessary to avoid spontaneous emission. The interaction duration must be short enough so that the expected number, N_s, of spontaneous emission events per atom during the time τ is negligible. N_s is simply given by the product of the excited state fraction (Equation 2.17) and the probability of spontaneous decay given that the atom is in the excited state:

$$N_s = |c_0(t)|^2\Gamma\tau = \frac{\omega_R^2}{4\Delta^2}\Gamma\tau, \tag{2.24}$$

where Γ is the natural decay rate of the excited state. Avoiding spontaneous emission ($N_s \ll 1$) while still having a significant probability for transitions ($\omega_R^{(2N_B)}\tau \simeq \pi$), is a practical requirement to maintain coherence. For a first-order Bragg process, this requires $\Delta \gg \Gamma$.

Bragg scattering of atoms from a standing light wave was first observed at MIT in 1988 [44]. A supersonic atomic beam was diffracted from a standing wave of near-resonant laser light. The angle between the atomic beam (of thermal wavelength λ_{dB}) and the light

grating (of periodicity $\lambda_L/2$) was tuned to the appropriate Bragg angle, θ_B, where:

$$\lambda_{dB} = \lambda_L \sin(\theta_B), \tag{2.25}$$

and population transfer corresponding to both first and second order Bragg scattering was observed. The experiment required a sub-recoil transverse momentum spread of the atomic beam in order to resolve the different momentum states in the far field and limit the final state to only one diffracted order. The Pendellösung was observed as an oscillation in population transfer as a function of standing wave intensity, $I \propto \omega_R^{(2)}$, for a fixed interaction time, τ.

Atomic beam diffraction from an optical standing wave is a continuous-wave (CW) experiment in which the selectivity needed for the Bragg process is imposed by good angular resolution of the particle beam and a high degree of parallelism between the light crystal planes. This ensures that of the various final Bragg orders allowed by momentum conservation, only one conserves energy (energy conservation is exact in a CW experiment). For atoms scattering from a light crystal, parallelism of the crystal planes requires highly parallel photon momentum that implies a minimum width of the standing wave (the diffraction limit for the collimated photons). The transit time, τ, of the atoms across this width then exceeds the lower bound given in Equation 2.22.

The excellent collimation required of the atomic beam to ensure resolution of the Bragg scattered atoms reduces the intensity of the source by many orders of magnitude. A Bose-Einstein Condensate (BEC) is an attractive alternative source of atoms because its momentum spread is typically an order of magnitude below a single-photon recoil momentum. To Bragg diffract atoms initially in a stationary BEC, it is easier to move the light crystal than to accelerate the condensate. This is done by simply frequency shifting one of the travelling waves so that the resultant standing wave formed by its interference with the unshifted travelling wave moves with the proper velocity ($N_B\hbar k/m$) relative to the stationary atoms to impart the necessary momentum. The Bragg scattered atoms will then have momentum $2N_B\hbar k$ in the laboratory frame. The resonance condition thus becomes a condition on relative detuning, δ_{N_B}, between the two laser beams forming the diffraction grating. For N_B^{th} order Bragg diffraction, the relative detuning is given by:

$$\delta_{N_B} = \frac{2N_B\hbar k^2}{m} = 4N_B\omega_{\text{rec}}. \tag{2.26}$$

The first demonstration of Bragg scattering in a BEC was at NIST in 1999 [48]. They used Bragg scattering mainly as a tool to manipulate the momentum of the BEC, observing up to sixth order processes. At MIT the interaction time was lengthened (to ≈ 100 times the lower bound of Equation 2.22 for first order Bragg scattering), creating a new type of spectroscopy called Bragg Spectroscopy. This was used to observe the momentum distribution of a BEC in a magnetic trap [49].

2.2.2 Kapitza-Dirac Scattering, Ref. 2

In 1933, Kapitza and Dirac predicted that an electron beam incident onto a properly oriented standing light wave would undergo stimulated Compton scattering and be reflected [50]. Since then, scattering that can be properly described by neglecting particle motion over the duration of the interaction (the Raman-Nath approximation) has become known as Kapitza-Dirac scattering. Atoms may also undergo such scattering from a standing light wave.

To restrict the atomic motion during the interaction time to distances small compared to the characteristic dimensions of the interaction potential requires short interaction times. Mathematically, this regime can be treated by neglecting the atomic kinetic energy term in the Hamiltonian (the Raman-Nath approximation). This is equivalent to the eikonal(thin-lens) approximation for scattering(optics). For a standing wave interaction, this approximation is well satisfied if the atomic motion during the interaction time is small compared to the wavelength of the illuminating radiation. As a result, Kapitza-Dirac scattering is limited (relative to Bragg scattering) to short interaction times, τ, generally much smaller than the inverse recoil frequency ($\tau \ll 1/\omega_{\rm rec}$). To observe appreciable population transfer at such short times, large intensities are needed. Since Kapitza-Dirac scattering is a coherent process, the interaction time must also be short enough to make spontaneous emission negligible. Thus the constraint $N_s \ll 1$ (Equation 2.24) holds in this regime as well, where N_s is the expected number of spontaneous emission events per atom during the time τ.

The standing wave interaction may be treated by considering the standing wave (AC Stark shift) potential resulting from the applied fields given in Equations 2.1 and 2.2:

$$U(z,t) = \frac{\hbar \omega_R^2}{\delta} f^2(t) \sin^2(kz), \tag{2.27}$$

where we have assumed $\delta^2 \gg \Gamma^2/4$.

The quickest route to the momentum distribution of the diffracted atoms in the Kapitza-Dirac regime is to use the eikonal approximation for treating the scattering of the incident atomic waves after passing through the AC Stark shift potential of the standing wave. Given the initial atomic wavefunction, $|\Psi_0\rangle$, the atomic wavefunction imediately after the interaction is given by:

$$\begin{aligned}
|\Psi\rangle &= |\Psi_0\rangle e^{-\frac{i}{\hbar} \int dt' U(z,t')}, &(2.28)\\
&= |\Psi_0\rangle e^{-i\frac{\omega_R^2}{2\delta}\tau} e^{i\frac{\omega_R^2}{2\delta}\tau \cos(2kz)}, &(2.29)
\end{aligned}$$

where $\tau = \int dt' f^2(t')$ and the integral is over the interaction duration. With the use of the identity for Bessel functions of the first kind, $e^{i\alpha \cos(\beta)} = \sum_{n=-\infty}^{\infty} i^n J_n(\alpha) e^{in\beta}$, the atomic

wavefunction can be written as:

$$|\Psi\rangle = |\Psi_0\rangle e^{-i\frac{\omega_R^2}{2\delta}\tau} \sum_{n=-\infty}^{\infty} i^n J_n\left(\frac{\omega_R^2}{2\delta}\tau\right) e^{i2nkz}, \tag{2.30}$$

$$= e^{-i\frac{\omega_R^2}{2\delta}\tau} \sum_{n=-\infty}^{\infty} i^n J_n\left(\frac{\omega_R^2}{2\delta}\tau\right) |g, 2n\hbar k\rangle, \tag{2.31}$$

where the position space representation of the momentum states has been used ($|g, p\rangle = \mathcal{N}e^{i\frac{p}{\hbar}z}$, with $\mathcal{N}$ an arbitrary normalization factor) and we have taken $|\Psi_0\rangle = |g, 0\rangle$.

It is now clear that states with $2N\hbar k$ of momentum are populated with probability [51, 52]:

$$P_N = J_N^2(\theta), \ N = 0, \pm 1, \pm 2, \ldots, \tag{2.32}$$

where

$$\theta = \frac{\omega_R^2}{2\delta}\tau = \omega_R^{(2)}\tau \tag{2.33}$$

is the pulse area. This leads to a transverse rms momentum of the diffracted atoms that is linearly proportional to the pulse area [51]:

$$p_{rms} = \sum_{n=-\infty}^{\infty} (n\hbar k)^2 P_n = 2^{1/2}\theta\hbar k. \tag{2.34}$$

Kapitza-Dirac diffraction of atoms was first observed at MIT in 1986 [51]. Diffraction of a well-collimated (sub-recoil) supersonic atomic beam was observed after passage through the tightly focused waist of a near-resonant standing wave. Significant diffraction into momentum states $|g, \pm 10\hbar k\rangle$ was observed [51]. Even higher diffracted orders should be observable in the future using laser beams directed at small Bose-Einstein Condensates for somewhat longer times.

2.3 A simple atom interferometer - the Mach-Zehnder configuration

Steps (1) and (3) of creating an atom interferometer (Section 2.1) can be performed by either Bragg or Kapitza-Dirac processes. If the momentum states used to construct the interferometer physically separate between steps (1) and (3), an intermediate process to ensure their spatial overlap during recombination is necessary. This is often the case with interferometers based on optical gratings, since the photon recoil momentum $\omega_{\rm rec}$ can be quite large. In such situations, an intermediate "reversal" diffraction grating can be applied which reverses the relative momentum of the interferometer arms. The interferometer would then consist of three diffraction grating. In this section, a simple 3-grating atom interferometer based on the Bragg process is discussed.

First consider the first order Bragg process applied on a BEC (Eqn. 2.18, and Eqn. 2.26 with $N_B = 1$). A $\pi/2-$pulse ($\omega_R^{(2)}\tau = \frac{\pi}{2}$) splits the atom 50-50 into the two momentum states (a 50-50 beamsplitter). A $\pi-$pulse ($\omega_R^{(2)}\tau = \pi$) puts the entire atom into the other momentum-state (a mirror[2]). As we will see shortly, such beamsplitters and mirrors can be used to construct interferometers for atoms.

A simple interferometer geometry known as the Mach-Zehnder interferometer is shown in Fig.2-2. This was the configuration of choice in MIT's first atom interferometer which was constructed using material gratings to deflect thermal beams [53]. This configuration has also been used to demonstrate a BEC atom interferometer [34]. Understanding this simple geometry elucidates several aspects of atom interferometry, so let's go through it.
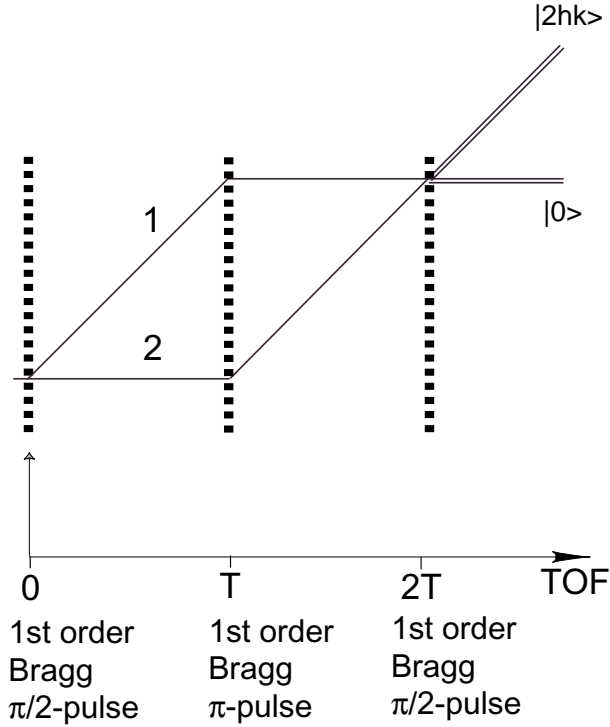
Figure 2-2: Schematic of a Mach-Zehnder interferometer. Paths 1 and 2 are in states $|0\,\hbar k\rangle$ and $|2\,\hbar k\rangle$ for equal lengths of time T. This makes this interferometer insensitive to the photon recoil.

Beginning with atoms at rest , the first $\pi/2-$pulse creates an even superposition of momentum states $|0\,\hbar k\rangle$ (at rest, path 2) and $|2\,\hbar k\rangle$ (in motion, path 1). The two paths have a relative velocity of 2 photon recoils (6 cm/s for sodium). After time T, they are

---

[2]The analogy between a Bragg $\pi-$pulse and a mirror is not entirely correct because of their action on a *distribution* of momenta. In the reference frame of a real mirror, all incoming atoms will reverse their momentum $\hbar k_{\mathrm{atom}} \rightarrow -\hbar k_{\mathrm{atom}}$. This means different incoming momentum states receive different momentum kicks. For standing wave diffraction, all incoming atoms receive the *same* momentum kick $= 2\hbar k_{\mathrm{photon}}$.

"reflected" by the Bragg $\pi-$pulse and the momenta are swapped. The third pulse projects the phase of the atomic interference pattern onto the fractional population of the two momentum states.

I now derive the interferometer signal, trying to emphasize the relevant physics. I first present a derivation following the treatment of light pulse interferometers by Steve Chu et. al. [54]. Gravity is neglected in this derivation, making this a 1-D problem, with the only direction defined by direction of the optical standing wave (vertical in Fig. 2-2). Immediately before the first pulse is applied, the atoms are at rest:

$$|\Psi\rangle = |0\rangle$$

Let the 3 diffraction gratings have spatial phases ϕ_1, ϕ_2, ϕ_3 relative to any fixed position, with positive being upwards in this 1-D problem (Fig. 2-2). These phases can be manipulated by the RF synthesizers controlling the AOMs but may also vary randomly due to vibrations of the apparatus. The first $\pi/2$-pulse rotates the statevector in Hilbert space into an even superposition of the two states given by [54]:

$$|\Psi\rangle = \frac{1}{\sqrt{2}}\left(|0\rangle - \mathrm{i}e^{i\phi_1}|2\hbar k\rangle\right)$$

Path 2 acquires the energy phase $-Et/\hbar$ relative to path 1 during the time T. The wavefunction immediately before the second pulse:

$$|\Psi\rangle = \frac{1}{\sqrt{2}}\left(|0\rangle - \mathrm{i}e^{i(\phi_1-4\omega_{\mathrm{rec}}T)}|2\hbar k\rangle\right)$$

The action of the π-pulse is another coherent rotation:

$$|\Psi\rangle = \frac{1}{\sqrt{2}}\left(-e^{i(\phi_1-\phi_2-4\omega_{\mathrm{rec}}T)}|0\rangle - \mathrm{i}e^{i\phi_2}|2\hbar k\rangle\right)$$

Evolution for another time T produces the following wavefunction immediately before the third pulse:

$$|\Psi\rangle = \frac{1}{\sqrt{2}}\left(-e^{i(\phi_1-\phi_2-4\omega_{\mathrm{rec}}T)}|0\rangle - \mathrm{i}e^{i(\phi_2-4\omega_{\mathrm{rec}}T)}|2\hbar k\rangle\right)$$

The third pulse produces the final wavefunction:

$$
\begin{aligned}
|\Psi\rangle &= \frac{1}{2}\left(-e^{i(\phi_1-\phi_2-4\omega_{\mathrm{rec}}T)} - e^{i(\phi_2-\phi_3-4\omega_{\mathrm{rec}}T)}\right)|0\rangle \\
&+ \frac{1}{2}\left(\mathrm{i}e^{i(\phi_1-\phi_2+\phi_3-4\omega_{\mathrm{rec}}T)} - \mathrm{i}e^{i(\phi_2-4\omega_{\mathrm{rec}}T)}\right)|2\hbar k\rangle
\end{aligned}
\tag{2.35}
$$

The probabilities for being in the two states (which can be called the output ports of

the atom interferometer) is just the amplitude squared of the respective components:

$$P_0 = |\frac{1}{2}\left(e^{i(\phi_1-\phi_2-4\omega_{\text{rec}}T)} + e^{i(\phi_2-\phi_3-4\omega_{\text{rec}}T)}\right)|^2 = \frac{1}{2}\left(1 + \cos(\phi_1 + \phi_3 - 2\phi_2)\right)$$

$$P_{2\hbar k} = |\frac{1}{2}\left(e^{i(\phi_1-\phi_2+\phi_3-4\omega_{\text{rec}}T)} - e^{i(\phi_2-4\omega_{\text{rec}}T)}\right)|^2 = \frac{1}{2}\left(1 - \cos(\phi_1 + \phi_3 - 2\phi_2)\right)(2.36)$$

The phase of the interferometer, $\phi_1 + \phi_3 - 2\phi_2$, is a result of the interference of the two paths with this phase difference at time $2T$. Let's represent the phase picked up by path i as Φ_i. After pulse 1,

$$\Phi_1 = \phi_1, \qquad \Phi_2 = 0.$$

After time T free evolution,

$$\Phi_1 = \phi_1 - 4\omega_{\text{rec}}T, \qquad \Phi_2 = 0.$$

After the second pulse,

$$\Phi_1 = \phi_1 - 4\omega_{\text{rec}}T - \phi_2, \qquad \Phi_2 = \phi_2.$$

After time $2T$,

$$\Phi_1 = \phi_1 - 4\omega_{\text{rec}}T - \phi_2, \qquad \Phi_2 = \phi_2 - 4\omega_{\text{rec}}T.$$

After the third pulse, there are actually 4 paths. At the $|0\,\hbar k\rangle$ port:

$$\Phi_1 = \phi_1 - 4\omega_{\text{rec}}T - \phi_2, \qquad \Phi_2 = \phi_2 - 4\omega_{\text{rec}}T - \phi_3.$$

At the $|2\,\hbar k\rangle$ port:

$$\Phi_1 = \phi_1 - 4\omega_{\text{rec}}T - \phi_2 + \phi_3, \qquad \Phi_2 = \phi_2 - 4\omega_{\text{rec}}T.$$

Thus, $\Phi_1 - \Phi_2 = \phi_1 + \phi_3 - 2\phi_2$, as expected. Now, any interaction placed differentially on one of the arms would be picked up by $\Phi_1 - \Phi_2$ and show up in the interferometer signal. Thus a Mach-Zehnder interferometer can be used to for example measure rotational phases, gravitational phases, electric polarizability, or index of refraction of gases [32].

2.4   Atom Optics with Bose-Einstein Condensates

In this section, we will see how the ideas of the previous sections can be experimentally realized with a BEC source.

2.4.1 Standing Wave Diffraction of sodium Bose-Einstein Condensates

To make and control the optical diffraction gratings, one needs control over the intensity, timing and relative detuning of the two laser beams comprising the standing wave. All these features are provided by acousto-optic modulators (AOMs)[3] driven by standard RF electronics. Phase control is another feature which can easily be incorporated and has proven to be useful in the diagnosis of our atom interferometer. The switching time for AOMs is ~ 100 ns.
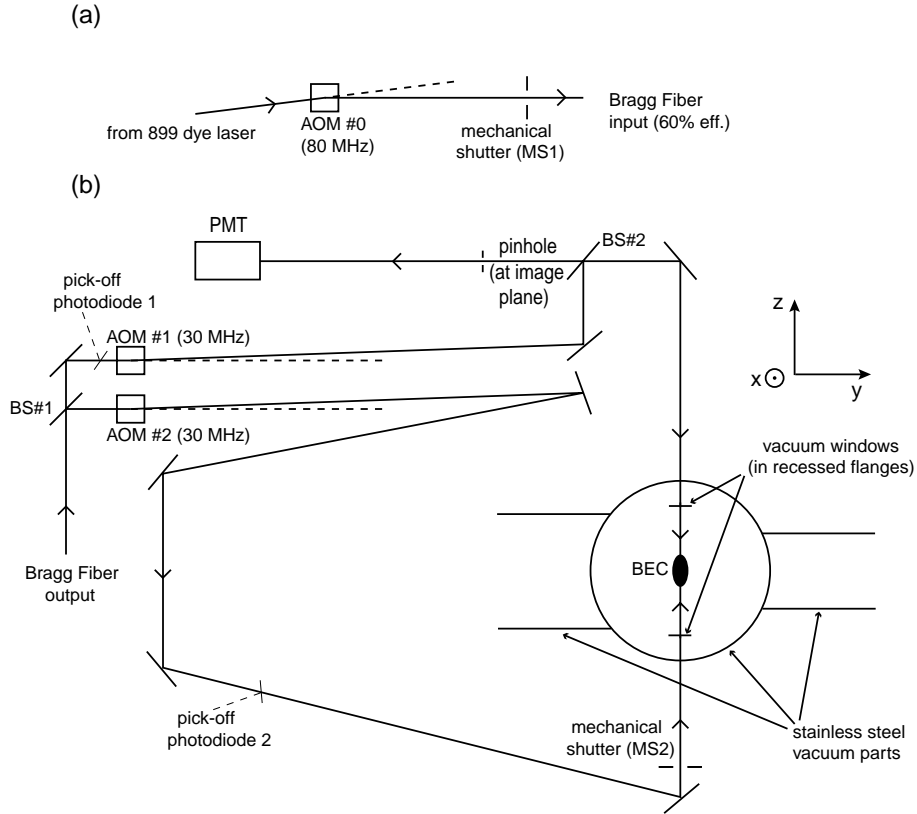
Figure 2-3: Top view of apparatus for the BEC contrast interferometer. (a) shows the beam derived from the sodium dye laser and coupled into the Bragg fiber. (b) shows the setup next to the vacuum chamber. The standing waves were horizontal and along the long axis (z-axis) of the condensate in the trap. The reflected beam was separated from the ingoing beam by beamsplitter BS#2, sent through a $100\,\mu$m pinhole at an intermediate image plane of the atoms and then imaged once more onto the photomultiplier tube (PMT). The standing waves are applied along the z-axis while atoms are imaged along the x-axis.

The details of the apparatus to produce sodium BECs in the $|1, -1\rangle$ state can be found

---

[3]these are commercial devices in which an RF drive ($\sim 100\,$MHz-$\sim 1\,$GHz) applied to a crystal (usually Tellurium Dioxide) sets up a phonon wave. A laser beam travelling through a well aligned crystal can be Bragg diffracted off the phonon grating, resulting in a diffracted beam which is shifted both in frequency and in direction (usually only first order diffraction is used). Note that AOMs also depend on Bragg diffraction!

in earlier theses [9, 10]. For the experiments described in this chapter, we used light tuned close to the $F = 2 \rightarrow F' = 3$ transition to create the diffraction gratings (fig.2-3). This is $\sim 1.8\,\text{GHz}$ (approximately the hyperfine splitting) red-detuned from the D2 line $(^3S_{1/2} \rightarrow{}^3 P_{3/2})$ for the $F = 1$ atoms in the BEC. We used an $80\,\text{MHz}$ AOM (AOM#0) as a switch for this light. The light was then sent though an optical fiber to clean up the mode and transported to the experiment. The output of the fiber was split in two and sent through independent $30\,\text{MHz}$ AOMs (AOM#1 and AOM#2). These were controlled with Stanford Research Systems SRS DS-345 synthesizers. The two light beams were then aligned counter-propagating and horizontal through the vacuum windows of the apparatus (z-axis in fig.2-3).
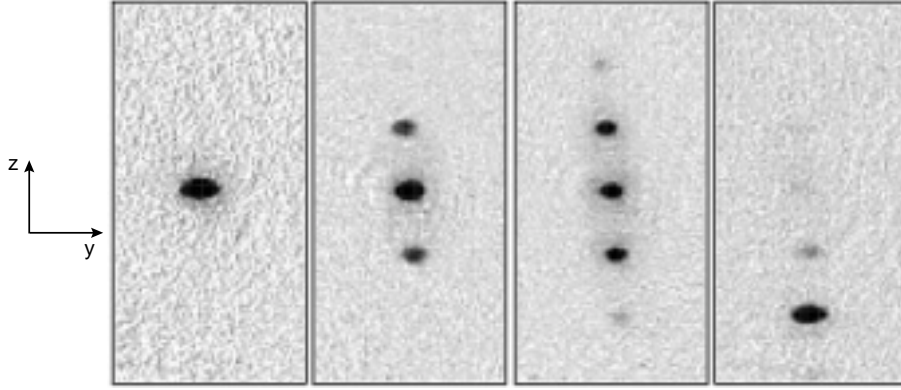
Figure 2-4: Resonant absorption images of BECs diffracted by pulsed standing waves. The images were taken with a resonant laser beam which propagated through the vacuum chamber along the (vertical) x-axis (see Fig. 2-3). Pulses were applied a few ms after release of the BEC from the magnetic trap. The standing waves were aligned in the z-direction (see Fig. 2-3). Total time-of-flight was $20\,\text{ms}$. (a) No pulse was applied. The position of the BEC in the image corresponds to the state $|0\,\hbar k\rangle$. (b) A $600\,\text{ns}$ Kapitza-Dirac pulse was applied which split the BEC into 3 momentum states $|0\,\hbar k\rangle$, $|2\,\hbar k\rangle$, and $|-2\,\hbar k\rangle$. (c) A $1\,\mu\text{s}$ Kapitza-Dirac pulse with similar intensity. The second orders $|4\,\hbar k\rangle$ and $|-4\,\hbar k\rangle$ can now be seen. (d) A $10\,\mu\text{s}$ Bragg pulse with $200\,\text{kHz}$ detuning was applied and caused a near-perfect transfer into the state $|-4\,\hbar k\rangle$.

Let's estimate some numbers necessary for the implementation of Bragg and Kapitza-Dirac pulses on a stationary BEC. First we introduce the usual definition of the saturation intensity:

$$\frac{\Gamma^2}{2} \frac{I}{I_{\text{sat}}} = \omega_R^2, \tag{2.37}$$

For sodium, the saturation intensity $I_{\text{sat}} = 6\,\text{mW/cm}^2$, the natural linewidth $\Gamma = 2\pi \times 10\,\text{MHz}$ and the recoil frequency $\omega_{\text{rec}} = 2\pi \times 25\,\text{kHz}$. This gives, $1/\omega_{\text{rec}} \sim 6\mu\text{s}$, giving us the timescale separating Bragg and Kapitza-Dirac processes. Assume $2\,\text{mm}$ diameter beams at $1.8\,\text{GHz}$ red-detuning. Using Eqns.2.16, 2.37, and 2.18, the power needed for

a $10\,\mu s$ long, first order Bragg $\pi/2-$pulse is $\sim 0.4\,\mathrm{mW}$ in each beam of a standing wave with relative detuning $100\,\mathrm{kHz}$. Using Eqn. 2.21, the power needed for a $10\,\mu s$ second order Bragg $\pi-$pulse is $\sim 1.7\,\mathrm{mW}$, with $200\,\mathrm{kHz}$ relative detuning. A $\sim 3.3\,\mathrm{mW}$ $1\,\mu s$ pulse with 0 relative detuning will operate in the Kapitza-Dirac regime and populate both states $|\pm 2\hbar k\rangle$ with 25% of the original condensate (Eqn. 2.32).

The diagnosis of momentum states in atom trapping experiments is traditionally done by turning of the atom trap suddenly and observing the ballistic expansion of atoms. Long time-of-flight (TOF) converts the momentum information into spatial information which can then be directly detected using standard absorption imaging techniques. The sub-recoil momentum spread of BEC's implies the complete separation of momentum states/diffraction orders separated by $2\hbar k$.

Fig.2-4 shows time-of-flight images of BECs split into different momentum states by optical standing wave pulses. The standing wave pulses were applied after releasing the BEC from the trap in order to reduce the density and associated mean-field effects. Combinations of such gratings can be used to create atom interferometers.

2.4.2 BEC Mach-Zehnder interferometer

The extension of atom diffraction to an atom interferometer follows directly with the application of multiple diffraction pulses in succession.

A frequency difference of $\delta_1 = 2\pi \times 100\,\mathrm{kHz}$ (Eqn. 2.20) between AOMs 1 and 2 fulfilled the requirements for a first order Bragg process. Using 2 phase locked SRS DS-345 synthesizers to control the 2 AOMs, we were able to control the relative phase of the RF supplied to the AOMs from the front panel of the instruments. This in turn controlled the phase of the optical standing wave (ϕ_i). Varying the relative phase of the second grating, we obtained the interferometer signal shown in Fig. 2-5. The contrast or visibility is defined as (max-min)/(max+min) of an interference signal. The contrast in Fig. 2-5 is $\gtrsim 90\%$, a result of the extreme sub-recoil nature of the atom source. A large momentum distribution would cause the Bragg resonance condition (Eqn. 2.26) to be different for different initial momenta. This would mean that the $\pi/2$-pulse and π-pulse condition could not be fulfilled simultaneously for all the atoms and lead to a reduced contrast. This makes the use of a BEC with its narrow momentum spread particularly useful for atom interferometry with standing light waves.

The Mach-Zehnder interferometer just described is an example of a "phase" interferometer, where the signal is sensitive to the phase of the atomic interference pattern. The phase is of course sensitive to mirror vibrations (via the ϕ_i's) and interferometers constructed on this principle in general require considerable vibration isolation to achieve high accuracy measurements [55]. As I will show, a signal sensitive to the *contrast* of the atomic interference pattern might not have this problem. The following section discusses a contrast interferometer scheme for measuring the photon recoil frequency. The scheme has
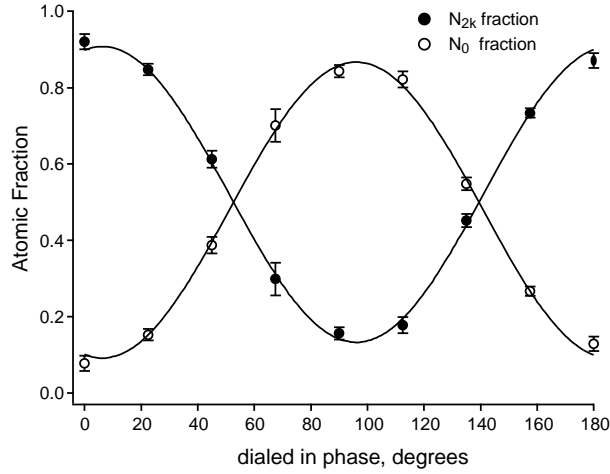
Figure 2-5: Signal from the BEC Mach-Zehnder Bragg interferometer of Fig. 2-2. The 1st-order condition was met by applying a frequency detuning 100 kHz between AOM#1 and AOM#2. The time between pulses is 50 μs for this example. The pulse time τ was 10 μs for each pulse. Pulse 2 was twice as intense as pulses 1 and 3.

additional advantages (beyond vibrational immunity) which make it a viable high accuracy measurement scheme.

2.5 First Generation Recoil Measurement

The techniques for condensate manipulation with standing waves can be applied to measuring the fine structure constant.

2.5.1 Motivation for measuring α

α, the fine structure constant, is a fundamental quantity of physics. It lies at the very heart of quantum electrodynamics (QED), since it plays an important role whenever the electromagnetic interaction is involved. This makes α essentially ubiquitous. Measurements of α are therefore relevant for various subfields of physics. In turn, a whole range of independent physical measurement methods have been developed with several competing values below the ppm (part-per-million) level [56]. Fig. 2-6 shows some of these.

Our experiment is relevant to the atomic physics route to measure α, based on the relation [57]:

$$\alpha^2 = \left(\frac{e^2}{\hbar c} \right)^2 = \frac{2R_\infty}{c} \frac{h}{m_e} = \frac{2R_\infty}{c} \frac{M}{M_e} \frac{h}{m} \; . \tag{2.38}$$

Here e is the electron charge, c is the speed of light, R_∞ is the Rydberg constant, $M_e(m_e)$ is the electron mass in atomic (S.I.) units and $M(m)$ is the mass of some test particle in atomic (S.I.) units. For a particular choice of test particle (atom), interferometry can provide $\omega_{\rm rec}$,

which is related to h/m by the relation:

$$\omega_{\mathrm{rec}} = \frac{1}{2}\frac{\hbar}{m}k^2 \tag{2.39}$$

All the other quantities are either already known to sub-ppb (part-per-billion) accuracy or are accurately accessible for alkalis (see [1] for details). An atom interferometer developed in Steve Chu's group at Stanford has measured ω_{rec} in cesium to $15\,\mathrm{ppb}$ accuracy [58].
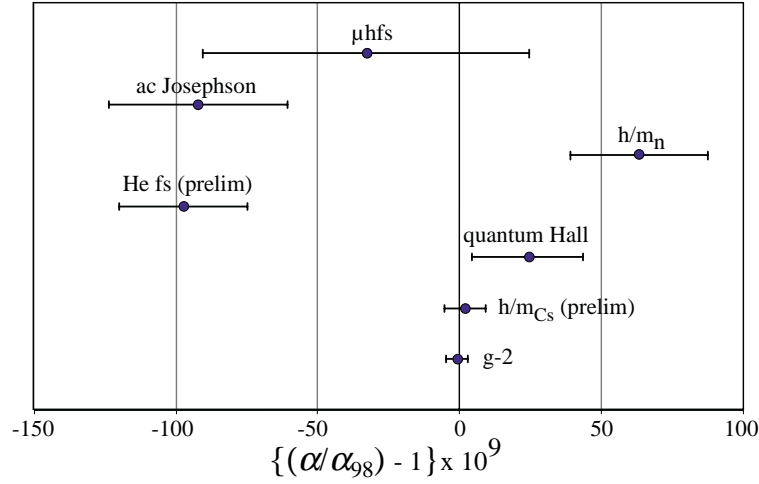
Figure 2-6: Best measurements of α shown as ppb deviation from the 1998 CODATA value [59].

2.5.2   Scheme of Contrast Interferometer

First consider the phase interferometer of Fig. 2-7(a). It is a 2-path scheme, just like the Mach-Zehnder, but has an important difference in how the 2 paths are recombined. Instead of a first order Bragg $\pi-$pulse, a second order one is applied. In the Mach-Zehnder, both paths are in the $|0\,\hbar k\rangle$ and $|2\,\hbar k\rangle$ states for the same length of time T, though not simultaneously. This means that the phase difference between the 2 paths at $2T$ is not sensitive to the photon recoil frequency ω_{rec} (Eqn. 2.36). In contrast, path 1 in the interferometer of Fig. 2-7(a) is in the state $|2\,\hbar k\rangle$ for time T and state $|-2\,\hbar k\rangle$ for time T, whereas path 2 is always in the state $|0\,\hbar k\rangle$. Around $t=2\,T$, a moving matter wave grating, with spatial periodicity $\lambda/2$ (wavevector $2k = \frac{2\pi}{\lambda/2}$), is formed due to the overlap and interference of the two paths. The phase of this grating at $2T$ is determined by the relative phase $\Phi_1 - \Phi_2 = 8\,\omega_{\mathrm{rec}}\,T$, accumulated between paths 1 and 2 due to the difference in their kinetic energies. A measurement of this phase for different values of T will then determine ω_{rec}.

Using the reasoning presented earlier, after the first pulse,

$$\Phi_1 = \phi_1, \qquad \Phi_2 = 0.$$

After time T free evolution,

$$\Phi_1 = \phi_1 - 4\omega_{\text{rec}}T, \qquad \Phi_2 = 0.$$

After the second pulse,

$$\Phi_1 = \phi_1 - 4\omega_{\text{rec}}T - 2\phi_2, \qquad \Phi_2 = 0$$

(second order Bragg pulse gives $-2\phi_2$). After time $2T$,

$$\Phi_1 = \phi_1 - 8\omega_{\text{rec}}T - 2\phi_2, \qquad \Phi_2 = 0.$$

At time $2T$, the phase difference between the two paths contains the recoil frequency. This is the element we want to exploit for our measurement. We note at this point that if Nth order and $2N$th order Bragg processes had been used in the interferometer of Fig. 2-7(a),

$$\Phi_1 - \Phi_2 = \phi_1 - 2\phi_2 - 8N^2\omega_{\text{rec}}T, \tag{2.40}$$

giving us a *quadratic* sensitivity to the number of photon recoils applied.
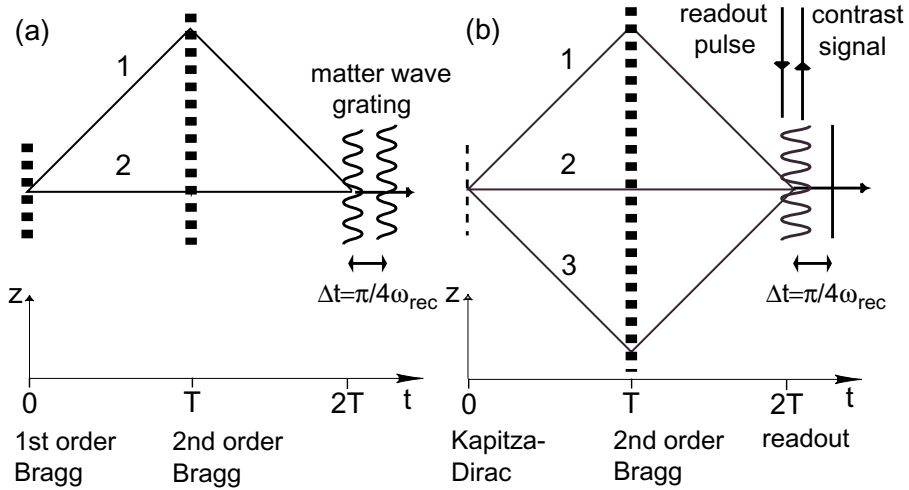
Figure 2-7: Space-Time representation of the contrast interferometer. (a) shows a simple 2-path interferometer sensitive to the photon recoil phase. The $2k$ matter wave grating is shown at $2T$ and at $2T + \pi/4\,\omega_{\text{rec}}$. The extension to the 3-path geometry is shown in (b). The overall $2k$ grating has large contrast at $2T$ and zero contrast at $2T + \pi/4\,\omega_{\text{rec}}$.

The extension of the phase interferometer into a contrast interferometer is shown in Fig. 2-7(b). Three momentum states (paths 1, 2 and 3) are generated by replacing the first Bragg pulse with a short Kapitza-Dirac pulse. At $t = 2T$, there are now two matter wave gratings with period $\lambda/2$, one from paths 1 and 2 and one from paths 2 and 3. These move

35

in opposite directions at a relative speed $4\hbar k/m$. If the maxima of the two gratings line up to produce large contrast at time t, the maxima of one will line up with the minima of the other at $t + \pi/4\,\omega_{\mathrm{rec}}$, to produce zero contrast. This results in an oscillatory growth and decay of the contrast of the overall pattern with time. The recoil induced phase can be determined from this temporally oscillating contrast.

Extending the two path analysis to three paths, we find at time $2T$,

$$\Phi_1 = \phi_1 - 2\phi_2 - 8\omega_{\mathrm{rec}}T, \qquad \Phi_2 = 0, \quad \text{and} \quad \Phi_3 = -\phi_1 + 2\phi_2 - 8\omega_{\mathrm{rec}}T.$$

Let a_i be the amplitudes of the three paths determined by the splitting in pulse 1. The wavefunction at time $2T$ is then

$$|\Psi\rangle = a_1 e^{i\Phi_1}|2\hbar k\rangle + a_2 e^{i\Phi_1}|0\rangle + a_3 e^{i\Phi_1}|-2\hbar k\rangle.$$

This is a 1-D problem, so lets use $|2\,\hbar k\rangle = e^{i2kz}$, etc. The atomic interference due to the three paths at time $2T$.

$$\begin{aligned}
\langle\Psi^\star|\Psi\rangle &= \left(a_1 e^{-i\Phi_1}e^{-i2kz} + a_2^\star e^{-i\Phi_1} + a_1^\star e^{i\Phi_1}e^{i2kz}\right) \times \left(a_1 e^{i\Phi_1}e^{i2kz} + a_2 e^{i\Phi_1} + a_1 e^{i\Phi_1}e^{-i2kz}\right) \\
&= 2a_1^2 + a_2^2 + 2a_1 a_2\left(\cos(2kz + \Phi_2 - \Phi_1) + \cos(2kz + \Phi_3 - \Phi_2)\right) + 2a_1^2\cos(4kz + \Phi_3 - \Phi_1) \\
&= 2a_1^2 + a_2^2 + 2a_1 a_2\cos\left(\Phi_2 - \frac{\Phi_1 + \Phi_3}{2}\right)\cos(2kz + \Phi_3 - \Phi_1) + 2a_1^2\cos(4kz + \Phi_3 - \Phi_1)
\end{aligned}$$

The contrast of the $2kz$ matter wave grating is proportional to $\cos\left(\Phi_2 - \frac{\Phi_1 + \Phi_3}{2}\right)$. At time $2T$, we can probe this matter wave grating by reflecting a probe beam off it. The process is equivalent to Bragg scattering of an optical travelling wave off a matter wave grating. The intensity of the reflected light is then proportional to the square of the density modulation (strength of the matter wave grating). Thus the reflected signal is proportional to:

$$\cos^2\left(\Phi_2 - \frac{\Phi_1 + \Phi_3}{2}\right) = \cos^2(8\omega_{\mathrm{rec}}T). \tag{2.41}$$

Note that Eqn. 2.41 has a phase which evolves with ω_{rec}, the recoil frequency and does not contain any of the ϕ_i's. This makes it insensitive to vibrations (i.e, phase shifts) of the pulses. Allowing for phase offsets due to diffraction phase shifts, light shifts and other effects, the reflected signal becomes $\cos^2(4\omega_{\mathrm{rec}}T + \phi'_{\mathrm{off}})$. At an arbitrary time t, the reflected signal can then be written as

$$S(T,t) = C(T,t)\sin^2(8\omega_{\mathrm{rec}}T + 4\omega_{\mathrm{rec}}(t - 2T) + \phi_{\mathrm{off}}). \tag{2.42}$$

where $C(T,t)$ is an envelope function which goes to zero for t much different from $2T$. The extent of C in the variable $t - 2T$ is the coherence time of the matter wave grating. It is caused by the momentum spread of the atom source, and can be quite large for a BEC.

The diffraction phase shift contributing to ϕ_{off} has been modelled for this interferometer in the group of J. Vigué in France [60]. They find a value $\pi/6$ for our geometry. Note that this phase offset has no direct consequence since we only want to determine the *slope* of the measured phase vs T, as I discuss in the next subsection.

2.5.3 Advantages of the contrast interferometer

The phase interferometer of Fig. 2-7(a) captures the essential spirit of our measurement. Pulse 1 starts the clock and creates a component of the wavefunction on path 1 which accumulates phase at a multiple of the recoil frequency. Path 2 serves as the zero phase reference. Since optical wavelengths have considerable recoil momentum, pulse 2 is used to reverse the momentum of path 1, without disturbing its phase evolution. At time $2T$, the 2 paths are back together. The phase of their interference is then a direct measure of ω_{rec} if the time T is known.

Lets see how an error in the phase measurement is related to the uncertainty in the recoil frequency determined. We expect a linear relationship between phase and time:

$$\Phi = 8\omega_{\text{rec}}N^2T + \phi_{\text{off}}$$

where ϕ_{off} is the sum of all possible offset phases. The relative errors are then given by:

$$\frac{\Delta\Phi}{\Phi} = \frac{8N^2(\omega_{\text{rec}}\Delta T + T\Delta\omega_{\text{rec}}) + \Delta\phi_{\text{off}}}{8\omega_{\text{rec}}N^2T + \phi_{\text{off}}}.$$

We will be measuring large phases, so $8\omega_{\text{rec}}N^2T \gg \phi_{\text{off}}$:

$$\frac{\Delta\Phi}{\Phi} \approx \frac{(\omega_{\text{rec}}\Delta T + T\Delta\omega_{\text{rec}})}{\omega_{\text{rec}}T}.$$

The relative error in the phase will be much larger than that in T. Thus:

$$\frac{\Delta\Phi}{\Phi} \approx \frac{\Delta\omega_{\text{rec}}}{\omega_{\text{rec}}}, \tag{2.43}$$

the relative error in the recoil frequency is simply the relative error in the phase[4]. To improve the precision of the experiment, we should try to reduce the error in the measurement of the recoil phase and try to increase the largest recoil phase we can measure.

This phase vs time measurement is very similar in concept to the way mass measurements are performed in Dave Pritchard's Penning trap experiments at MIT [62]. Extending the scheme into a contrast interferometer suppresses several "common mode" noise sources, improving both the precision and accuracy of the measurement.

---

[4]Even if $\frac{\Delta T}{T}$ is comparable to $\frac{\Delta\Phi}{\Phi}$, the linear relationship between phase and time allows Eqn. 2.43 to still hold [61].

Using Eqn. 2.43, one can make an estimate of what to expect from the recoil measurement. For 10^5 atoms contributing to the reflected signal detected at the shot noise level, the phase error $\Delta\Phi$ is $\sim 2/\sqrt{10^5} \sim 6.3$ mrad (the factor of 2 comes from using the $\cos^2$ function). To set the scale, take $N = 1$ and $T = 1$ ms. Then Φ is $8 \times 1^2 \times 2\pi \times 25$ kHz$\times 1$ ms$\sim 1.3 \times 10^3$ and $\frac{\Delta\Phi}{\Phi} \sim 5 \times 10^{-6}$. Scaling this value with $T = 50$ ms and $N = 10$, one would estimate $\frac{\Delta\Phi}{\Phi} \sim 1 \times 10^{-9}$ i.e, 1 ppb! This is the result for a single shot! Averaging over many shots would beat this value down even further. Allowing the very conservative 60 s per shot (dominated by the formation time of the BEC), one would still obtain $< 10^{-10}$ with less than 2 hours of data. This simple calculation demonstrates the inherent power of the method. I will return to this point in the final section of this chapter.

The precision is a measure of the sensitivity of the device to the effect of interest. The device can also be sensitive to other systematic perturbations which if not properly taken into account may make the final measurement *inaccurate*. Almost all high accuracy measurements are limited not by precision but by accuracy. Even if a small accuracy is quoted, there could still be some perturbation that the experimenter has not thought of yet! For a quantity as important as α, it is thus important to make different types of measurements to see how they compare against each other. This is well exemplified in Fig. 2-6.

I now summarize the properties of this scheme which make it a viable choice for the photon recoil measurement:

- The use of a single internal state reduces systematics from AC Stark shifts. This has been a major source of systematic in the Stanford experiment, which relies on Raman transitions between different internal states [55].

- The contrast scheme is insensitive to mirror vibrations between pulses. This is immediately obvious from the form of Eqn. 2.41. The vibration phase picked up by path 1 is opposite in sign to that picked up by path 3. Path 2 is not diffracted at all and so does not pick up vibrational phase. Thus $\Phi_2 - \frac{\Phi_1 + \Phi_3}{2} = 0$ for the vibrational contribution. Vibrations during a diffraction pulse are equivalent to a phase modulation. This may make the grating depart from the Bragg condition. However, the typical pulse durations of $10\,\mu$s are much shorter than the typical timescales of vibrations in the laboratory ($\lesssim 1$ kHz). T, the interferometer evolution time, should be scaleable to hundreds of ms. The Stanford scheme uses a fairly elaborate vibration isolation system to fight this problem for a phase interferometer [55]. Our contrast interferometer should not require such an elaborate system.

- The recoil phase is proportional to kinetic energy. This makes the interferometer quadratically sensitive to the number of recoils. This is useful for scaling up the interferometer towards high precision. For comparison, the Stanford scheme is linearly sensitive to the number of recoils.

- The symmetry of the 3-path geometry suppresses effects from stray magnetic bias fields and gradients. This scheme is sensitive only to $\partial^2 B/\partial z^2$, the magnetic field curvature[5]. The time dependence of ambient magnetic fields enters the phases Φ_i through the time integrals over the energies. Thus time-dependent stray bias and gradients are also suppressed.

- Immunity to accelerations, including those from gravity. This follows from the same reasoning as the vibrational immunity. Insensitivity to gravity forgives to a large extent any accidental vertical component to the beam alignment.

- The use of Bragg processes allows for arbitrarily high diffraction orders to be generated (limited by heating due to spontaneous scattering). This issue will be dealt with in more detail in the Outlook section.

- The contrast readout allows for a high S/N, since the entire photon signal comes out of a small solid angle (diffraction-limited by the size of the BEC) and the corresponding background is thus reduced by this small fraction $\div 4\pi$.

2.5.4 Contrast Interferometer Signal
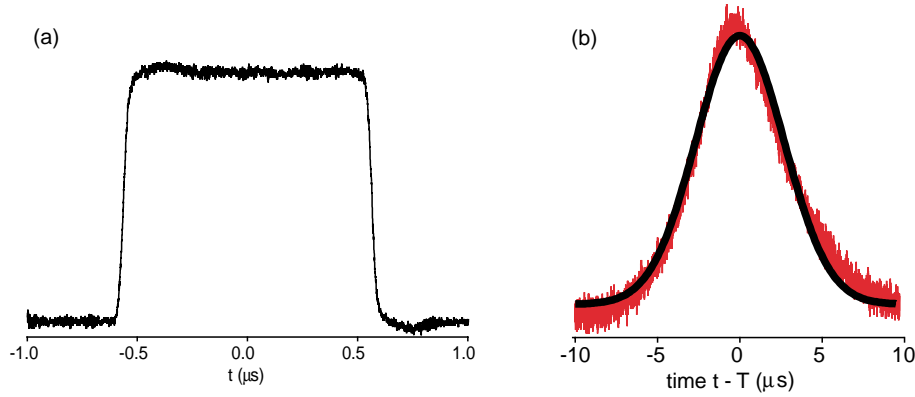
Figure 2-8: Pulse 1 and pulse 2 of the interferometer sequence. (a) Pulse 1 is $\sim 1\,\mu$s long, square. (b) Pulse 2 is near-Gaussian shaped. The best fit Gaussian with $1/e$ full width of $7.6\,\mu$s is also shown. The vertical scale for (a) and (b) are different and arbitrary.

The "first-generation" experiment was performed on the "old" sodium BEC machine, with horizontal laser beams. We wanted to demonstrate that the scheme worked and obtain the best measurement of $\omega_{\rm rec}$ without major changes to the BEC machine. Learning from this initial phase could then be incorporated into plans for a high-accuracy measurement using a vertical fountain geometry (Section 2.6).

---

[5] All odd spatial derivatives are suppressed by the symmetry. If someone up comes with a way to cancel the sensitivity to curvature, then we would only be sensitive to $\partial^4 B/\partial z^4$.

The first generation experiment demonstrated the concept of the scheme and produced a value for ω_{rec} in sodium to 7 ppm precision and 200 ppm accuracy. This is several orders of magnitude away from a competitive value. However the demonstration of the useful features of the scheme bodes well for future high accuracy work.

Each interferometer shot measured $\Phi(T)$, the phase of $S(T, 2T)$ in Eqn. 2.42 for a given T. The shot consisted of making a BEC in the magnetic trap, releasing it for a variable TOF, followed by the 3 pulse sequence forming the contrast interferometer and then readout by Bragg back-scattering. We also monitored the atom number by imaging the atoms after a long time-of-flight (Fig. 2-10). The standard technique for $|F = 1, m_F = -1\rangle$ BEC production was followed[63, 9]. We loosened the trap at the end of evaporation to final trapping frequencies of about 50 Hz radially and 20 Hz axially. Almost pure BECs (negligible thermal component) of a few million atoms were then released suddenly and allowed to expand for ~ 15 ms before the application of the interferometer pulses. Loosening the trap effectively "decompresses" the atoms thereby reducing the density. Both the decompression and initial TOF stages were important to lower the atomic density (to $\sim 10^{13}\,\mathrm{cm}^{-3}$), thereby reducing superradiance [64] and mean-field effects. The initial decompression also lowered the momentum spread and allowed for more efficient Bragg diffraction (2nd pulse).
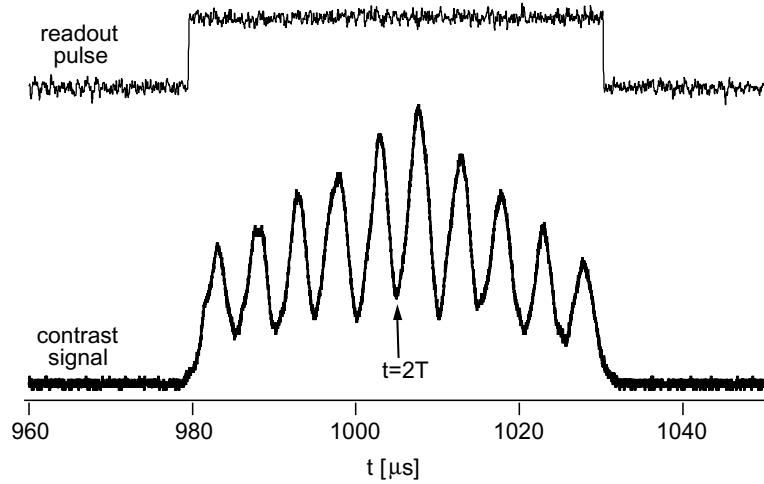
Figure 2-9: Typical single shot signal from the contrast interferometer. $T = 502.5\,\mu$s, for this example. Ten oscillations with $\approx 60\,\%$ contrast and $\approx 30\,\mu$s width are observed during the $50\,\mu$s readout. A low-pass filter at 300 kHz (12dB per octave) was applied to the signal.

To form the interferometer of Fig. 2-7(b), we phase-locked two SRS DS-345 synthesizers and applied the same frequency to both AOM#1 and AOM#2 for all pulses. Examples of pulses 1 and 2 are shown in Fig. 2-8. We used laser beams with 1.8 mm waist. For pulse 1, the Kapitza-Dirac symmetric splitting pulse, we obtained $\sim 25\%$ of the condensate

pulse 1 and 2 only   pulse 1, 2 and
strong pulse 3
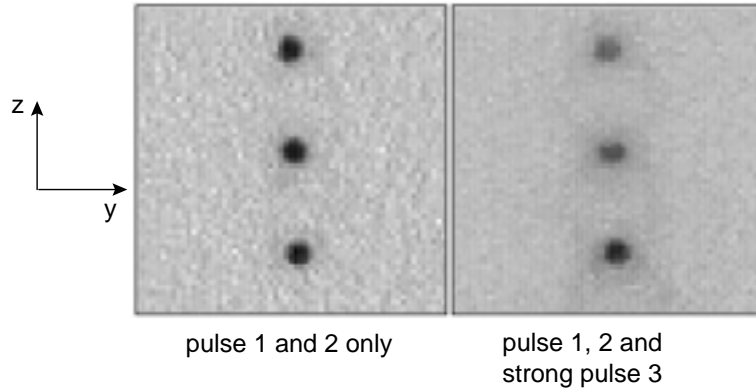
Figure 2-10: Atom signal from the contrast interferometer. When only pulses 1 and 2 were applied, the TOF atom signal was symmetric about the 0 momentum state. When a strong readout pulse was applied, clear asymmetry is observed between the $|2\hbar k\rangle$ (upper) and $|-2\hbar k\rangle$ (lower) states, in keeping with the direction of reflection of the readout pulse (Fig. 2-3). These pictures are from the first night that we observed the interferometer signal and provide clear evidence that we had reflection from a matter wave grating. For actual data collection we reduced the intensity of the readout pulse, and measured the backscattered light.

in each of paths 1 and 3 (Eqn.2.32). For the second-order Bragg grating (pulse 2), we used a near-Gaussian light pulse (to suppress other unwanted orders of diffraction) and obtained a diffraction efficiency greater than 90%. The timing control computer used in all our BEC experiments has a resolution of $10\,\mu$s and is therefore inadequate to control these pulses. We used Wavetek 50 MHz pulse generators, Model 801 to trigger the Bragg AOMs. For the readout pulse, we simply switched off AOM#2 and back-reflected the light from AOM#1 onto a photomultiplier tube (PMT, Fig. 2-3). A typical signal from the contrast interferometer is shown in Fig. 2-9.

There was some effort to obtain this "typical" signal. Since the probing beam and the reflected beam counter-propagated and essentially overlapped each other, we used a non-polarizing beam splitter cube (BS#2) to separate them (figure 2-3). However, this also meant that the probe beam reflected off BS#2 and other optics (including the vacuum windows) could get into the PMT. Angling the beam relative to the optics by a small amount (few degrees) was enough to get rid of most of the reflections by physical blocks. The light due to the leakage RF driving AOM#2 was blocked with a mechanical shutter. A pinhole ($100\,\mu$m) was placed at an image plane of the atoms to allow only the light from the condensate to go through towards the PMT. This pinhole was in turn imaged onto the PMT, to further improve the signal-to noise.

Fig. 2-10 shows the atom signal corresponding to the contrast interferometer. For a strong readout pulse, an obvious asymmetry was observed between $|2\hbar k\rangle$ and $|-2\hbar k\rangle$. This was our first sign (even before we obtained a PMT signal) that the contrast scheme

was working. Such a strong readout quickly destroys the matter wave grating. We lowered the readout pulse and measured perturbatively to obtain the recoil frequency.

2.5.5 Measurement of the Recoil Frequency

We fit the reflected signal with a gaussian-weighted sinusoid and obtained the recoil phase $\Phi(T)$. The results of five iterations of the signal at different time points T are shown in Fig. 2-11. We chose two ranges of times T for our measurements. The short time $T \sim 0.5\,\text{ms}$, was restricted by the closing time of a mechanical shutter ($\sim 300\,\mu\text{s}$) which blocked the leakage from AOM#2 (MS2 in Fig 2-3). The long time $T \sim 3\,\text{ms}$ was limited by the atoms falling out of the ($\sim 2\,\text{mm}$ diameter) horizontal beam due to gravity.
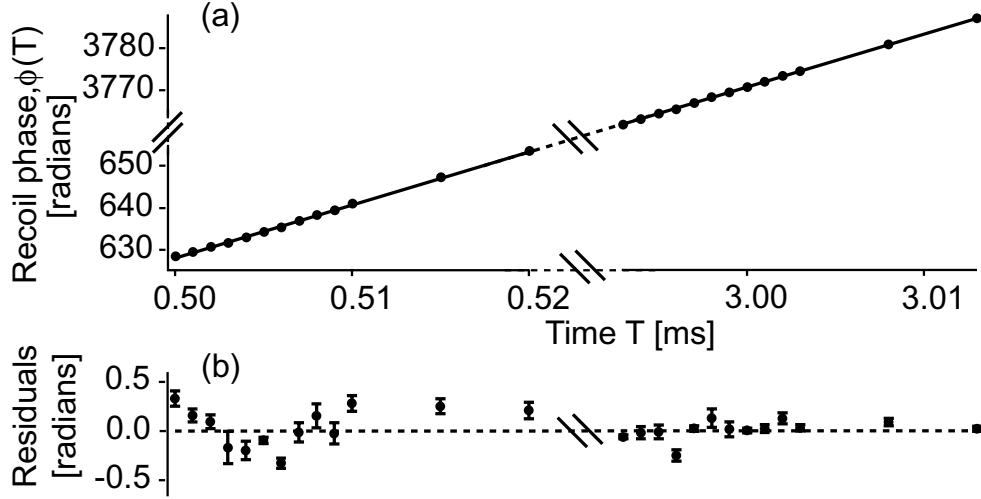
Figure 2-11: Measurement of ω_{rec} in sodium. Two sets of recoil phase scans, around $T = 0.5\,\text{ms}$ and $T = 3\,\text{ms}$, are shown in (a). Each point is the average of five measurements. The slope of the linear fit gave ω_{rec} to 7 ppm. The error bars ($\approx 0.05 - 0.1\,\text{rads}$) are shown with the fit residuals in (b). The total time for this measurement was $\sim 2\,\text{hours}$.

Our measurement for sodium from these data is $\omega_{\text{rec}} = 2\pi \times 24.9973\,\text{kHz}(1 \pm 6.7 \times 10^{-6})$. The precision was limited by $\sim 200\,\text{mrad}$ shot-to-shot variations of the fitted value of Φ. Our measured value is 2×10^{-4} lower than the sub-ppm value calculated using the published measurements of α_{g-2} [65, 66], R_∞ [67, 68], M_{Na} [62], M_e [69], and λ_{Na}[70] in Eqs. 2.38 and 2.39.

The shot-to-shot deviation of 200 mrad far exceeds the expectation from the shot noise limit for $\sim 10^5$ atoms ($\sim 6.3\,\text{mrad}$, Section 2.5.3) which is approximately the atom number contributing to our signal. It is possible that this is due to fluctuating differential mean field shifts in the different interferometer arms arising from fluctuations in atom number. This is discussed in Section 2.6.2. Another possibility is the different diffraction phase shifts from fluctuations in light intensity as suggested by [60].

2.5.6 Insensitivity to Vibrations
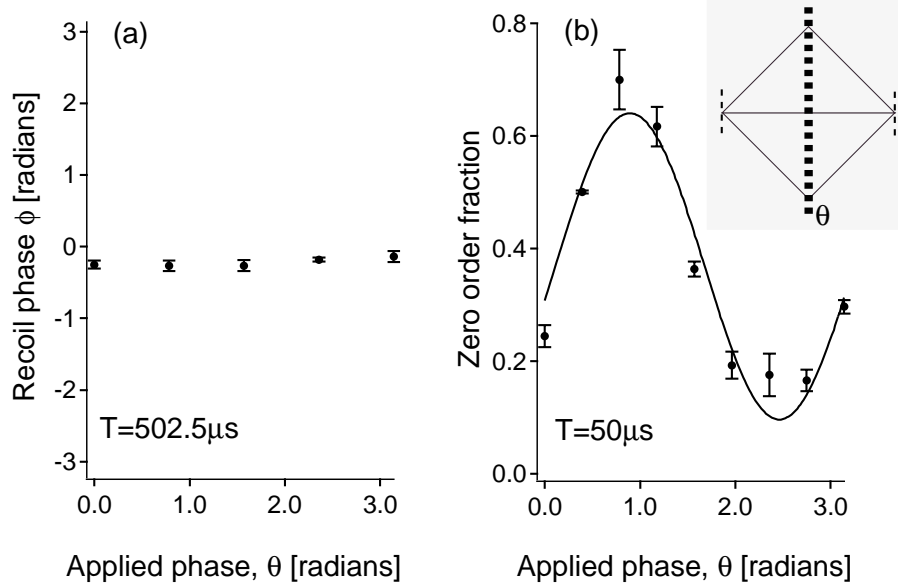
Figure 2-12: Vibration insensitivity of the contrast interferometer. (a) shows the measured recoil phase at $T = 502.5\,\mu s$ from the contrast interferometer as a function of the applied phase θ. The recoil phase is constant and demonstrates our insensitivity to phase noise from the gratings. (b) shows the fractional population of the $|0\,\hbar k\rangle$ state from the phase-sensitive interferometer (inset) for a similar scan of θ at $T = 50\,\mu s$. Also shown is the best-fit sinusoid of the expected period.

To demonstrate the insensitivity of the measurement to phase noise of the light due to mirror vibrations, we intentionally varied the phase θ of the second grating relative to the first one. The contrast signal was not visibly affected by such phase variations (Fig. 2-12(a)). We compared this to a phase-sensitive readout method (Fig. 2-12(b), inset). This was realized by replacing the readout pulse with a third pulsed $1\,\mu s$ light grating in the Kapitza-Dirac regime, phase-locked to the first two pulses. This projected the phase of the $2k$ pattern at $t = 2T$ onto the fractional populations of the states $|0\,\hbar k\rangle$, $|2\,\hbar k\rangle$, and $|-2\,\hbar k\rangle$ which leave this interferometer. The populations were measured by time-of-flight absorption imaging. The $|0\,\hbar k\rangle$ fraction is shown for the same variation of θ, in Fig. 2-12(b). The oscillation demonstrates the phase sensitivity of any position-sensitive readout.

Both the Mach-Zehnder interferometer signal (Fig. 2-5) and the phase interferometer signal (Fig. 2-12(b)) became much more noisy and essentially random for $T \geq 3\,ms$. This is probably due to the mechanical vibrations of the apparatus. The contrast interferometer on the other hand retains a steady signal as can be judged from the small error bars of Figure 2-11 at the large times.

2.5.7 N^2 scaling
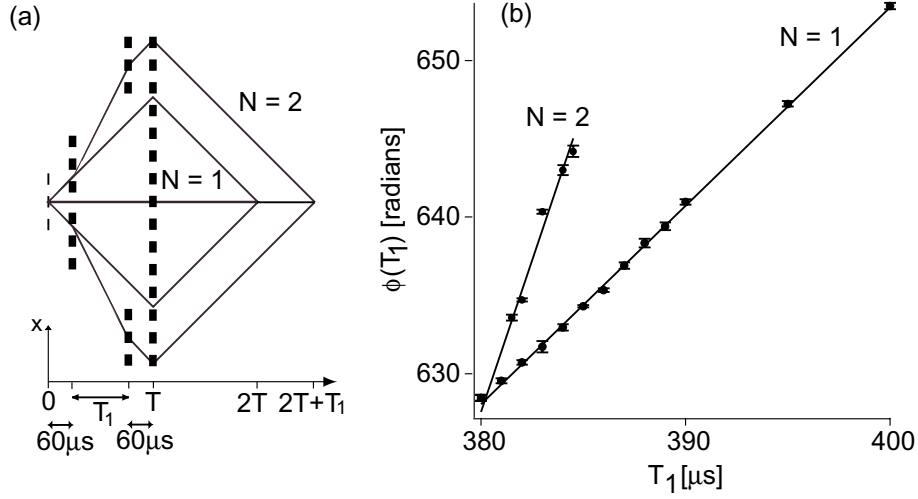
Figure 2-13: Demonstration of the quadratic scaling of the recoil phase with additional photon recoils. (a) shows the $N = 1$ (inner) and $N = 2$ (outer) interferometers used. (b) shows the recoil phase at the recombination time under variation of T_1.

The quadratic scaling with number of recoils N was demonstrated using the interferometer geometry shown in Fig. 2-13(a). For an intermediate time T_1, paths 1 and 3 were transferred into states $|4\,\hbar k\rangle$ and $|-4\,\hbar k\rangle$ respectively. The two paths were simultaneously addressed by driving AOMs 1 and 2 with two frequencies (using an RF mixer), centered at 29 MHz (near the AOM central frequency) but separated by 300 kHz. The pulses were square and 10 μs long and adjusted in intensity to match the 1st order Bragg π-condition. Paths 1 and 3 were then resonant with only the frequencies (one from each beam) satisfying the Bragg condition.

During the period T_1, paths 1 and 3 accumulate phase $2^2 = 4$ times faster in the $N = 2$ scheme than in the $N = 1$ scheme. Additional time T_1 is required for the three paths to overlap in the $N = 2$ scheme. For this geometry, the $N = 2$ recoil phase should therefore evolve three times faster as a function of T_1 than the $N = 1$ recoil phase. The corresponding data sets are shown in Fig. 2-13(b). The linear fits give a slope ratio of 3.06 ± 0.1, demonstrating the quadratic scaling.

2.6 Outlook

The first-generation recoil measurement demonstrates the validity of the contrast interferometer scheme. Having accomplished this, we can move on to planning a future high-accuracy measurement. The purpose of this section is to outline our preliminary ideas in this direction. Subsection 2.6.1 describes conceptually how a vertical geometry with an in-

creased number of diffraction pulses can scale up the current precision by a few orders of magnitude. Subsection 2.6.2 provides some estimates of the BEC mean field contribution to both precision and accuracy.

2.6.1   Scaling up the Contrast Interferometer - improving the precision

As argued earlier (Section 2.5.3), scaling up the precision of the contrast interferometer involves increasing the interferometer time T, increasing the number of recoils N and reducing the shot-to-shot measurement error $\Delta\Phi$. The limitations on T are mainly from gravity and finite beam size. This can be remedied by setting up a vertical geometry where the atoms fall down the beams and not out of the beams. For a given vertical extent, even longer times can be achieved by launching the atoms upwards before starting the interferometer pulse sequence, as shown in Figure 2-14. The parameters of $T = 50\,\mathrm{ms}$ and $N = 10$ chosen for the figure should allow ppb precision for detection at the shot noise limit (Section 2.5.3). One drawback of the vertical geometry is that Doppler corrections to the relative frequencies of the Bragg gratings are needed to compensate for the changing velocities of the dropping atoms. However, this is a small overhead if such an elaborate setup is indeed constructed.
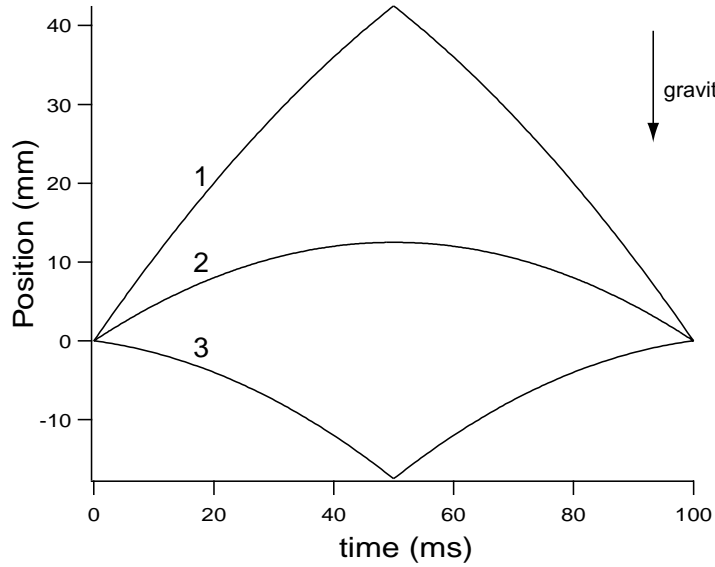
Figure 2-14: Scaling up the contrast interferometer - vertical fountain configuration. The 3 path scheme in a vertical geometry allows long evolution times and multiple pulses without the problem of the atoms "falling" out of the beams. The case of a fountain launch with velocity $0.5\,\mathrm{m/s}$, Bragg π-pulse acceleration up to $N = 10$ recoils and $T = 50\,\mathrm{ms}$, is shown. This setup should approach the ppb-precision and is only $6\,\mathrm{cm}$ in vertical extent.

Fountain geometries can provide free fall times of a few hundred milliseconds[71]. Additional Bragg acceleration π-pulses to increase the interferometer order N can then be

applied.

2.6.2   The Mean Field Contribution

The first-generation experiment has yielded a result for $\omega_{\mathrm{rec,Na}}$ accurate to 2×10^{-4}. We have not performed experimental studies of systematic effects in the interferometer. However, we believe the mean field to be the main contribution to the deviation of our measurement from the accepted value. Here we provide some estimates of the contributions from the mean field due to atom-atom interactions in a BEC.

As shown in Eqn. 2.41, the phase of the reflected signal at time $2T$ is $\Phi_2 - \frac{\Phi_1 + \Phi_3}{2}$, where Φ_i is the phase accumulated by path i. Any mechanism which can shift the relative phases of the three paths such that $\Phi_2 - \frac{\Phi_1 + \Phi_3}{2}$ is affected, is a possible source of a systematic error. Atom-atom interactions (mean field) can introduce errors into the measurement in this manner.

Strong atom-atom interactions in dense sodium BECs can easily produce mean field energies as large as $2\pi \times 5 \, \mathrm{kHz}$ [72]. Since $\omega_{\mathrm{rec,Na}} \sim 2\pi \times 25 \, \mathrm{kHz}$, energy shifts due to mean field interactions can be an important systematic in our interferometer. A gas of ultracold bosons at density n and interacting with s-wave scattering length a, has a mean field energy of[73][6]:

$$E_{\mathrm{mf}} = \frac{4\pi\hbar^2}{m} n a \qquad (2.44)$$

For $^{23}\mathrm{Na}$ in the $|F = 1, m_F = -1\rangle$ state, $a = 2.8 \, \mathrm{nm}$. This means that a density of $n = 3.4 \times 10^{14} \, \mathrm{cm}^{-3}$ produces $E_{\mathrm{mf}} = 2\pi \times 5 \, \mathrm{kHz}$. If different arms of the interferometer have different densities, then $\Phi_{\mathrm{meas}} = \Phi_2 - \frac{\Phi_1 + \Phi_3}{2}$ may be affected. If we have control over the interferometer pulses to allow a maximum fractional arm imbalance of x, the systematic contribution will be:

$$\frac{\Delta\Phi}{\Phi_{\mathrm{meas}}} = \frac{E_{\mathrm{mf}} 2T x}{8 \omega_{\mathrm{rec}} N^2 T} \qquad (2.45)$$

In our first-generation measurement, we used a peak density of $n \sim 10^{13} \, \mathrm{cm}^{-3}$. For an arm imbalance of $\sim 25\%$, this would contribute at a relative level of $\sim 4 \times 10^{-4}$, twice the obtained error. Further, if the mean field is larger in path 2 than the sum of the mean field in paths 1 and 3, the interferometer will measure a lower value for ω_{rec}, since the difference in total energy between an extreme path (1 or 3) and path 2 is then smaller that $4\omega_{\mathrm{rec}}$. This is consistent with our measurement being less than the currently accepted value.

We also note that atom number fluctuations will change the density shot-to-shot and give rise to variations of the measured recoil phase. Few percent variations in arm imbalance could then explain our observed shot-to-shot variations of $\Delta\Phi \sim 200 \, \mathrm{mrad}$ (Section 2.5.4).

The way to reduce the mean field contribution is to control the interferometer imbalance and reduce the atomic density. Further, even though this systematic scales with the inter-

---

[6] a discussion of basic scattering processes can be found in Chapter 3

ferometer time T, it is insensitive to the number of recoils N. Using $x = 0.05$ and $N = 20$ in Eqn. 2.45, we get the requirement of $n \lesssim 10^{11} \, \mathrm{cm}^{-3}$ in order to be at the ppb-level. Such low densities have recently been achieved in sodium BECs[74].

Another method to suppress the mean field contribution would be to alter the scattering length a to negligible values by means of a magnetic field Feshbach resonance (Section 3.3). This may be possible to do with the recently achieved cesium BEC because of the availability of such resonances at low magnetic field [24].

Chapter 3

Interacting Fermi Gases

From the late 70's to the early 90's, the prospect of creating a dilute gas superfluid from atomic vapor was a holy grail in the field of ultracold atoms. The realization of such a superfluid - the Bose-Einstein Condensate in 1995 opened the doors for a rich variety of exploration, both experimentally and theoretically. The previous chapter on atom interferometry with BEC's represents one such avenue of research.

Fermionic superfluidity is the next holy grail which has emerged in the field of ultracold atoms. At very low temperatures, interacting fermions can undergo a pairing transition resulting in a BCS type superfluid. The quest for this is now well underway with fermions being routinely produced in the quantum degenerate state in 6 laboratories around the world. This degeneracy is an essential ingredient towards superfluid pairing. Our group at MIT is one of these six to produce Fermi degenerate gases. The next step is to induce interactions between fermions. Several groups, including ours, have made steady progress in this endeavor over the last couple of years. The rest of this thesis deals with our efforts at inducing and studying strong interactions in ultracold fermions.

In this chapter, I discuss theoretical concepts which play a key role in understanding the current state of the field of interacting fermions. Although this chapter nominally deals with theory, I try to make the connection with the relevant experimental aspects in various parts of the presentation. The discussion is divided into five groups:

(1) In Section 3.1, I introduce the non-interacting Fermi gas and its static properties in a harmonic trap. Strength of interactions can be gauged by the (observed) deviations of the gas from this ideal behavior.

(2) In Section 3.2, different types of collision processes are introduced with particular attention given to s-wave collisions, the dominant interaction mechanism in ultracold gases.

(3) In Section 3.3, I introduce the concept of a Feshbach resonance. This is our main experimental tool to tune interaction strengths between fermions.

(4) In Section 3.4, I discuss the ground state hyperfine structure of ^{6}Li, the fermionic atom that we use for experiments. Using the ideas from the previous sections, I outline the reasons why certain choices of internal states are more suited for studying interactions.

(5) The final part of this chapter, Section 3.5, discusses the predicted transition of interacting fermions to a superfluid state.

3.1 Non-interacting Fermi Gases

An intermediate goal towards BCS is the production of degenerate Fermi gases. We can produce a spin-polarized ^{6}Li Fermi gas in a harmonic trap at ultra high degeneracy. Since s-wave interactions are forbidden by fermionic antisymmetry, this is essentially a non-interacting gas. A full description of such gases can be found elsewhere[75]. I present here a few basic results. The Fermi-Dirac distribution function is

$$f(\epsilon) = \frac{1}{e^{\beta(\epsilon-\mu)} + 1},$$

where $\beta = \frac{1}{k_B T}$. $f(\epsilon)$ is the occupation probability of a state with energy ϵ. The chemical potential μ is given by the normalization condition for the total number of atoms N in the trap:

$$N = \int d\epsilon f(\epsilon) g(\epsilon), \tag{3.1}$$

where $g(\epsilon)$ is the density of energy states. Only harmonic traps with cylindrical symmetry will be discussed (the usual experimental scenario). If the trapping frequencies are $(\omega_1, \omega_2, \omega_3) = (\omega_\perp, \omega_\perp, \omega_z)$, and defining the aspect ratio $\lambda = \omega_z/\omega_\perp$, the density of states $g(\epsilon) = \frac{\epsilon^2}{2\lambda(\hbar\omega_\perp)^3}$ has a quadratic dependence on energy. Integrating Eqn. 3.1 at $T = 0$ gives the Fermi energy $E_F(N) \equiv \mu(T = 0, N)$:

$$E_F = \hbar\omega_\perp (6N\lambda)^{1/3} \tag{3.2}$$

Since the exact wavefunctions in a harmonic trap are well-known, the properties of a harmonically trapped gas can in principle be directly computed by summing over these states. However it suffices (and is usually computationally necessary) to make the semi-classical "Thomas-Fermi" approximation which is valid in the large N limit [75] and consists of labelling the state of each atom by a position $\mathbf{x}$ and momentum $\mathbf{p}$. This is equivalent to the local density approximation where each position $\mathbf{x}$ is associated with local Fermi quantities - density, temperature, and the Fermi temperature. Essentially, the gas is considered locally homogeneous and all the formulas used to describe homogeneous Fermi gases can be applied. The local Fermi energy is given by:

$$E_F(\mathbf{x}) = \frac{\hbar^2 k_F^2(\mathbf{x})}{2m} = E_F - U_{\mathrm{h}}(\mathbf{x}),$$

where $k_F(\mathbf{x}) = p_F(\mathbf{x})/m$ is the local Fermi wavevector and $U_{\mathrm{h}}(\mathbf{x}) = \frac{1}{2}\sum_i \omega_i^2 x_i^2$. This now gives the local density as simply the volume of the momentum space Fermi sea:

$$n(\mathbf{x}, T) = -\frac{1}{\Lambda_T^3} g_{\frac{3}{2}}(-e^{-(U_{\mathrm{h}}(\mathbf{x})-\mu)/(k_B T)}), \tag{3.3}$$

where $\Lambda_T = \sqrt{\frac{2\pi\hbar^2}{mk_B T}}$ is the thermal de-Broglie wavelength and $g_\alpha(x) = \sum_{k=1}^\infty x^k/k^\alpha$ is the poly-logarithm function. The zero-temperature density reduces to:

$$n(\mathbf{x}; T=0) = \frac{k_F^3(\mathbf{x})}{6\pi^2} = \frac{4}{3}\pi \left(\frac{2mE_F}{h^2}\right)^{3/2} (1 - \frac{m}{2E_F}\Sigma_i \omega_i^2 x_i^2)^{3/2} \tag{3.4}$$

We now have an expression for a direct experimental observable. Eqn. 3.3 forms the basis of fitting functions for characterizing our experimentally produced degenerate Fermi gas (Chapter 4). Our standard detection method of absorption imaging measures a 2-D "column" density distribution. The fitting function is then a spatial integral of Eqn. 3.3 which is an expression in the poly-logarithm function g_2. The 1-D projection involves another spatial integral and results in $g_{5/2}$. We use both 2-D and 1-D fits to characterize our ultracold gases.

Absorption imaging can also be applied after turning off the trap suddenly and allowing the gas to expand ballistically for a variable time-of-flight (TOF). The spatial distribution in TOF from a harmonic trap is obtained by a substitution of coordinate x_i by $\frac{x_i}{\sqrt{1+\omega_i^2 t^2}}$, accompanied by the necessary volume rescaling $\frac{1}{\Pi_i \sqrt{1+\omega_i^2 t^2}}$ [76]. Thus, the density distribution for a non-interacting zero-temperature Fermi gas in time-of-flight out of a harmonic trap is (from Eqn. 3.4):

$$n(\mathbf{x}, t; T=0) = \frac{4}{3}\pi \left(\frac{2mE_F}{h^2}\right)^{3/2} \frac{(1 - \frac{m}{2E_F}\Sigma_i \frac{\omega_i^2 x_i^2}{1+\omega_i^2 t^2})^{3/2}}{\Pi_i (1+\omega_i^2 t^2)^{1/2}} \tag{3.5}$$

3.2 Interactions in Trapped Fermi Gases

At the heart of every interaction is a collision process. In this section I introduce the different collision processes that will be discussed in this thesis.

For the μK temperatures common in ultracold atom traps, interactions are dominated by two-body s-wave scattering. This is because, for typical collisions, $kR \ll 1$, where $\hbar k$ is the relative momentum (determined by the temperature) and R is the range of the potential. This is equivalent to the de-Broglie wavelength being much larger than the range of the interatomic potential. The de-Broglie wavelength of ^{6}Li at $1\,\mu K$ is $\sim 200\,\mathrm{nm}$, while the potential range $R \sim 50a_0 \sim 2.5\,\mathrm{nm}$. Since a spin-polarized Fermi gas is non-interacting, all the s-wave interactions between ^{6}Li atoms will occur in mixtures of different internal states. Most of the activity in the ultracold atom field takes place in the weakly interacting

$(k|a| \ll 1)$ and dilute $(n|a|^3 \ll 1)$ limit where a is the s-wave scattering length which parametrizes the strength of the interaction and n is the gas density. This allows the use of an effective contact interaction between particles [73, 77, 78]:

$$U(\mathbf{x} - \mathbf{x}') = \frac{4\pi\hbar^2 a}{m}\delta(\mathbf{x} - \mathbf{x}') = U_0\delta(\mathbf{x} - \mathbf{x}'), \qquad (3.6)$$

where m is the mass of an atom. In this description, particles only interact when they are "on top of" or "in contact with" each other. The determination of the scattering length a involves solving the Schrodinger equation for scattering from the molecular potentials. Although straightforward in principle, this scattering problem is fairly difficult to solve accurately, principally because of insufficient knowledge of the real molecular potentials.

The interaction potential of two ground state alkali atoms is relatively simple compared to multi-electron atoms since alkalis possess only one valence electron. The interaction potential is composed of two parts - one corresponding to the electric dipole-dipole interaction, often called the central part U^c and the other corresponding to the magnetic dipole-dipole interaction U_{md} [73]. The central part can be divided into two broad classes of interactions:

$$U^c = U_s\mathcal{P}_0 + U_t\mathcal{P}_1, \qquad (3.7)$$

the singlet U_s and the triplet U_t interactions. $\mathcal{P}_0$ and $\mathcal{P}_1$ are the projection operators for the two-electron singlet and triplet states respectively. The singlet interaction corresponds to the valence electrons approaching in an antisymmetric spin combination, whereas the triplet interaction involves them approaching in a symmetric spin combination. As may be expected, the singlet and the triplet potentials are identical at large distances, decaying with the usual attractive van der Waals $1/r^6$ behavior. The difference occurs only in the short range part where the spatial wavefunction is symmetric (singlet) or antisymmetric (triplet). At very short internuclear distances, the potential is essentially hardcore repulsive.

3.2.1 Collision Channels

A set of internal quantum numbers (like the spin projection, total spin and so on) which describes a two-particle state is referred to as a "channel". In this language, collisions which only couple the entrance channel to itself are single-channel processes whereas those which can couple the entrance channel to a different exit channel are called multi-channel processes.

The kinetic energy of s-wave collisions is usually too small to allow endothermic processes between different channels which have energy separations on the order of hyperfine energies. Thus, in ultracold atoms, the entrance channel is often called the "open" channel while higher lying channels are called "closed" channels (Fig. 3-1). Atoms cannot leave each other after a collision in any closed channel.
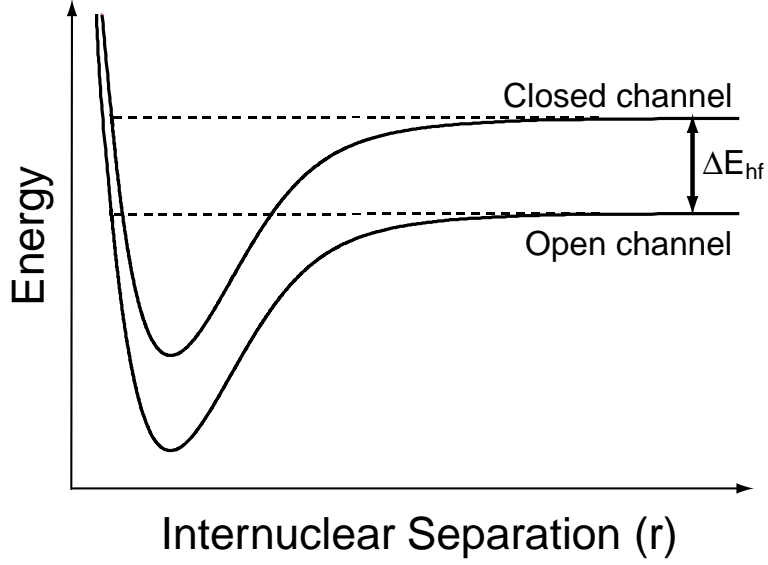
Figure 3-1: Intermolecular potentials for 2 body scattering. The free atoms approach along the open channel. The closed channel corresponds to a molecular state that can couple to the open channel via U^{c} or U_{md}. The difference in threshold (kinetic energy $K.E. \to 0$) energies ΔE_{hf} between the two channels is on the order of hyperfine energies and typically much larger than the kinetic energies available in ultracold atom clouds.

3.2.2 Inelastic Collisions

Inelastic collisions change the total kinetic energy of collision partners by changing concurrently some internal degree of freedom. Typically, these result in a decay of the system under study. I review very briefly the standard inelastic decay mechanisms that occur in atom trapping experiments.

Background gas

Collisions with the background gas in a vacuum chamber causes an exponential (single-body) loss: $\dot{N} = -N/\tau$. The effects of these collisions can be reduced by improving the pressure in the system. Pressures of $\sim 10^{-11}$ mbar, the ultra-high-vacuum (UHV) typical in ultracold atom experiments, results in lifetimes of several tens of seconds (or even hundreds). In our experiments, we take extra precautions to maintain these UHV conditions.

Spin Exchange Collisions

This process involves two-body collisions from the central potential U^{c} which change the internal states of the collision partners while preserving the total spin. The rate for this process is proportional to atomic density (since it is a 2-body process) and independent

of relative velocity. Therefore it becomes an increasing problem in an atom cooling experiment as the temperature is lowered and the density increases. The usual solution is to choose atomic states in which either spin-exchange collision channels do not exist or are endothermic (as shown in the example of Fig 3-1) and thus suppressed at low temperatures.

Dipolar Decay

This process involves two-body scattering from the interatomic magnetic dipole-dipole potential U_{md}. Total spin need not be preserved in such collisions. The potential can change the relative angular momentum of the spatial wavefunction by $2\hbar$[73]. The rate for this process is also proportional to atomic density, however, as mentioned earlier, it becomes significant only if spin-exchange collisions are suppressed. As usual, experimental states should be carefully chosen to eliminate or at least minimize this loss channel.

Three-Body Decay

Three-body recombination is a process in which two atoms form a bound state and a third atom carries away the energy (including molecular binding energy) and momentum to satisfy the usual conservation requirements. Since three particles need to collide, the rate scales with the square of the density. For dense BECs, this is usually the loss mechanism that limits the lifetime in an atom trap. Three-body decay can also be enhanced near scattering resonances (Section 3.3) and form a strong decay channel in such regimes. However, the symmetry/antisymmetry of the collision partners can suppress this rate since the process does require multiple particles to be in close proximity. As one might expect, at low temperatures, the rate for fermions is indeed suppressed. Threshold ($K.E. \to 0$) laws have been derived for 3-body recombination in [79]. These calculations show that for a spin-polarized Fermi gas, the rate is suppressed as T^2 (or T_F^2 for $T < T_F$) and for a 2-spin gas, as T (or T_F). Bosons as well as distinguishable particles approach a rate independent of energy at threshold.

3.2.3 Elastic Collisions

Elastic collisions refer to scattering from the central potential U^{c} in which the incoming and exiting channels are the same. They play an important role in the field of ultracold atoms because they preserve the internal state of the system and only change the external state towards thermal equilibrium. Elastic collisions have to always compete against the deleterious effects of inelastic collisions, to preserve the stability of the system.

S-wave elastic collisions at low temperature in weakly interacting and dilute gases lead to energy shifts in the form of mean field interactions. The connection between thermalizing collisions and interaction shifts will now be discussed. They are both important in the strongly interacting regime that we want to explore.

The s-wave scattering amplitude

Eqn. 3.6 describes the effective contact interaction that is used to describe elastic interactions in ultracold gases. It correctly predicts the mean field shift as $\frac{4\pi\hbar^2 a}{m}n$ for interaction of a particle with a gas of density n. However, it is only correct to lowest order in ka. This thesis will be concerned with behavior of ultracold gases for $ka \gg 1$. Therefore, I now introduce the more correct form for the contact interaction where the scattering length a is replaced by $-f_0(k)$, the s-wave scattering amplitude [77, 73]:

$$U(\mathbf{x} - \mathbf{x}') = -\frac{4\pi\hbar^2 f_0}{m}\delta(\mathbf{x} - \mathbf{x}'). \tag{3.8}$$

The scattering amplitude can be derived from the usual partial wave analysis for a spherically symmetric potential and is related to the s-wave scattering length as [80]:

$$f_0(k) = -\frac{a}{1 + ika} = -\frac{a(1 - ika)}{(1 + ika)(1 - ika)} = -\frac{a}{1 + k^2 a^2} + i\frac{ka^2}{1 + k^2 a^2}. \tag{3.9}$$

The real part corresponds to the usual mean field interaction, except now we have the behavior appropriate for $ka > 1$. The imaginary part corresponds to the decay of the (relative) momentum state and is responsible for the thermalization of the system. The optical theorem relates the imaginary part to the more common expression for the thermalization scattering cross-section:

$$\mathrm{Im}(f_0) = \frac{k\sigma}{4\pi} \qquad \Longrightarrow \qquad \sigma = \frac{4\pi a^2}{1 + k^2 a^2} \tag{3.10}$$

For small ka, this is recognizable as the s-wave cross-section for distinguishable particles $4\pi a^2$. For large ka, this approaches the unitarity limit $\frac{4\pi}{k^2}$, independent of a.

The real part corresponds to collisions that do not change the relative momentum of the scatterers. These collisions are experimentally detectable as energy shifts. The imaginary part contributes to what is usually meant by elastic collisions. Using Eqns. 3.8, 3.9, and 3.10, the scattering cross-section can be used to rewrite the imaginary part of the interaction (for a gas density n) as:

$$\frac{4\pi\hbar^2}{m}n\frac{ka^2}{1 + k^2 a^2} = \hbar n\sigma v = \hbar\Gamma_{\mathrm{scat}}$$

where $\Gamma_{\mathrm{scat}} = n\sigma v$ is the usual scattering rate for collisions at relative velocity v.

Eqn. 3.9 also suggests the analogy of an atom wave and a light wave propagating through an atomic medium of density n. The real part corresponds to the refractive index while the imaginary part to the absorption in the medium. Thus, the real part gives rise to "coherent" scattering while the imaginary part to "incoherent" scattering.

It is important to re-iterate that this form of the interaction is valid for any value of ka provided $kR \ll 1$. In particular, it may be used to understand (at least qualitatively) the

behavior near scattering resonances, where a diverges (Section 3.3).

Introducing the scattering amplitude thus draws the distinction between coherent and incoherent collisions and extends our interpretation of s-wave interactions into the $ka \gg 1$ regime near Feshbach resonances.

Low temperature, Pauli blocking

Fermions at temperatures satisfying $kR \ll 1$ are below the p-wave threshold and do not interact in the same state[1]. Another qualitative threshold occurs when the gas becomes deeply degenerate and a large fraction of states below T_F are occupied. As a rule of thumb, this is about $0.3-0.4\,T_F$, since this is where observed collision rates start to deviate strongly from the classical predictions [81]. The deviation arises due to the significant population of energetically accessible final states for an elastic collision. This effect, often called Pauli blocking, reduces the rate of incoherent collisions and decreases the efficiency of cooling fermions. The two energy scales corresponding to $kR \sim 1$ (mK) and T_F (μK) are separated by about three orders of magnitude in typical atom trapping experiments. As the system cools, the s-wave regime is reached first. Substantial further cooling must take place before the regime of Pauli blocking is reached.

Since coherent collisions do not involve an overall change in momentum of collision partners, they are not affected by Pauli blocking of final states. Thus, there are no incoherent elastic collisions in a trapped zero-temperature two-spin Fermi gas with finite interstate scattering length. However, mean field energy exists in such a gas. As we will see in Chapter 6, this zero-temperature Fermi gas may undergo elastic collisions when released from the atom trap.

3.2.4 Observations of Interactions

Typically, inelastic collisions in a trapped atom cloud result in a release of kinetic energy and/or the production of un-trapped states. Thus the experimentally observed gas (column) density will correspond to an increased temperature as well as a reduced density. The system will thus "decay" away. Generally, a stable system corresponds to a lifetime limited only by background losses. A study of the stability of a strongly-interacting system ^{6}Li system by monitoring inelastic losses is reported in Chapter 5 [4].

We have also experimentally observed effects from both the real and the imaginary parts of the scattering amplitude. The effect of incoherent elastic collisions was observed in the mutual thermalization of a two-spin state mixture (Section 4.5). Chapter 6 discusses effects that manifest due to a very large rate of incoherent collisions as well as the role of Pauli blocking.

---

[1]p-wave interactions do contribute, but only with a cross-section which goes to zero according to the Wigner threshold law[80]

The effect of coherent elastic collisions can be observed in shifts of transition frequencies between internal atomic states. Chapter 7 describes our use of radio-frequency techniques to measure such shifts and thus scattering lengths.

3.3   Feshbach Resonance

Scattering resonances correspond to a divergence of the scattering length. One instance of such a resonance occurs when a vibrational state in the open channel becomes just bound at threshold ($K.E. \to 0$). This is a phenomenon familiar from the treatment of scattering from a square well potential. The zero-energy scattering length diverges as a function of well depth, whenever the potential can just support a new bound state. Another example is a "shape" resonance. A shape resonance occurs if the potential characterizing a collision process can support a virtual bound state at the collision energy. This occurs for $kR \gtrsim 1$, higher partial wave scattering.
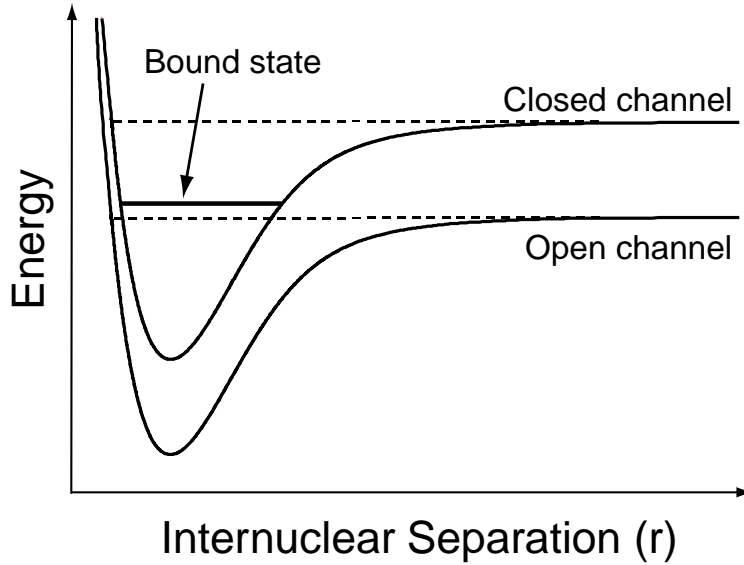
Figure 3-2: Schematic of a Feshbach resonance. The solid lines represent the potential energy as a function of internuclear separation. The free atoms interact via the open channel. The closed channel corresponds to the potential experienced by atoms in a different two-particle superposition of hyperfine states. The two channels are coupled by the hyperfine interaction. A resonance occurs if a bound state in the closed channel crosses the open channel asymptote. The effective scattering length corresponding to the figure is large and negative.

The above examples are single-channel effects and can occur in atoms which have no internal structure. However, the presence of internal structure allows multi-channel scatter-

ing to occur via the electrostatic potential U^c (Section 3.2). This allows the possibility of Feshbach resonances which occur when a bound state in one of the closed channels comes into resonance with the kinetic energy in the open channel (Figure 3-2). Far away from scattering resonances, a will have a small non-resonant value. Typically, this is on the order of the interatomic potential range ($\sim 50 a_0$). However, near a Feshbach resonance, one of the molecular bound states becomes important and dominates the scattering behavior. If a molecular bound state has a different magnetic moment than the total magnetic moment of the free atomic collision partners, then the position of the bound state can be adjusted relative to the open channel threshold by simply changing the external magnetic field. The scattering length undergoes a resonance when the bound state is tuned across this threshold. Such a resonance is known as a Feshbach resonance. Near a Feshbach resonance, the scattering length changes from $a \to \infty$ for bound state below threshold (real molecule) to $a \to -\infty$ bound state above threshold ("virtual" molecule). Fig. 3-2 corresponds to a large attractive interaction for atoms at zero kinetic energy.

The usual parametrization of a near a Feshbach resonance is[82]:

$$a(B) = a_{\mathrm{nr}}(1 + \frac{\Delta}{B - B_0}), \tag{3.11}$$

where a_{nr} is the non-resonant scattering length far away from the resonance (of the order of the range of the potential R). B_0 is the position and Δ is the width of the Feshbach resonance. The positions and widths of Feshbach resonances can be calculated by performing coupled-channel calculations using potentials derived from up-to-date experimental data.

3.3.1 Strongly Interacting Fermi Gases

Resonant Enhancement of the Scattering Length, Unitarity Limit

Strongly interacting gaseous systems can be "engineered" by utilizing Feshbach resonances. At a divergence of a, the behavior of the effective scattering length $a_{\mathrm{eff}} = -f_0$ can be obtained by taking the $a \to \infty$ limit of Eq.3.9:

$$a \to \infty \quad \Rightarrow \quad \mathrm{Re}(a_{\mathrm{eff}}) \to \frac{1}{k^2 a} \quad \text{and} \quad \mathrm{Im}(a_{\mathrm{eff}}) \to -\frac{1}{k}. \tag{3.12}$$

The real part approaches zero near a scattering resonance, which may seem astonishing at first. However, this is understandable on the basis of the analogy with the dispersive light-atom interaction. The real part of the index of refraction goes to zero on resonance. The imaginary part of a_{eff} reaches an a-independent plateau corresponding to the usual unitarity limit of collisions. The behavior of the effective scattering length a_{eff} is shown in Fig 3-3 as a function of the bare scattering length a.

In a gas, the momentum-dependent a_{eff} should be averaged over the different collision momenta. For a two-spin gas, each with Fermi momentum k_F, the momentum average at
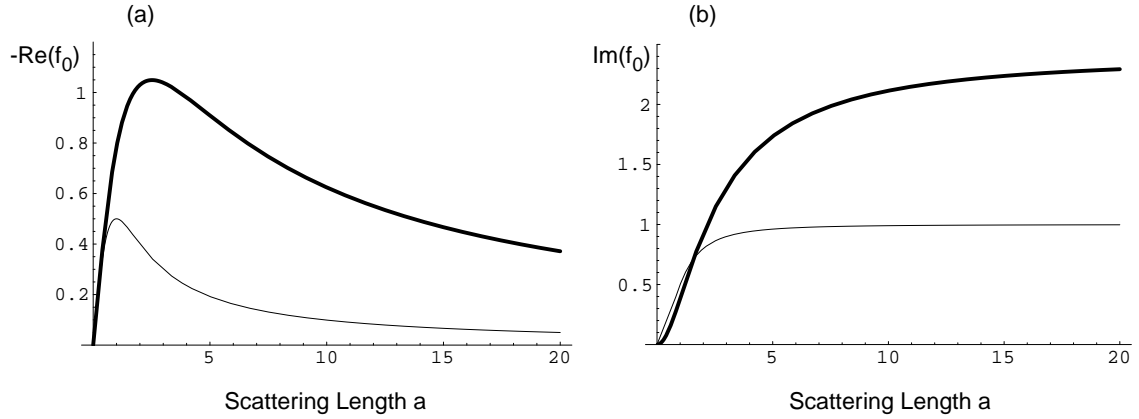
Figure 3-3: The thin lines show (a) -Re(f_0) and (b) Im(f_0) as a function of a (Eq. 3.9 with relative momentum $k = 1$). The thick lines show the averages over a zero temperature Fermi distribution with Fermi momentum $k_F = 1$ for each spin state. The thick line in (a) deviates from the thin line for $a \geq 1(1/k_F)$ and approaches zero much more gently. The thick line in (b) has a similar rise as the thin line with a but saturates at the higher value of 2.4.

$T = 0$ produces the thick lines shown in Fig. 3-3. Thus, the real part suppression at large a becomes slower, since the average contains contributions from $ka \ll 1$ as well. These $ka \ll 1$ contributions initially decrease (slightly) and eventually increase (factor > 2) the imaginary part, proportional to σ, the scattering cross-section[2]. However, the qualitative behavior of both real and imaginary parts remain the same in spite of the averaging.

Universality of the Unitarity Limit in two-spin Fermi gases

It has been shown theoretically [83, 84, 85] that the unitarity-limited mean field for interacting fermions is negative and proportional to the Fermi energy. Defining β as the relevant many-body parameter, we have:

$$U_{\mathrm{mf}} = -\beta E_F, \qquad k_F a \gg 1. \tag{3.13}$$

This is a surprising result because it implies that for very large and repulsive two-body interactions, the effective many-body interaction is attractive. In the context of achieving fermionic superfluidity, this is good news because it increases the parameter range of strong attractive interactions.

β has been calculated at zero temperature [83, 84] and measured at $< 0.1\,T_F$[86, 87] yielding consistent numbers of $0.4 - 0.6$. The fact that this attractive mean field is never stronger than the repulsive Fermi pressure, means that a two-spin interacting Fermi gas does not undergo phase separation or implosion and is mechanically stable even at a Feshbach

---

[2]Even though the scattering cross-section is finite, at $T = 0$, the scattering *rate* is zero because of Pauli blocking (see Section 3.2.3 and Chapter 6).

resonance. This is an important requirement towards producing a fermionic superfluid. The experimental observation of this effect[87] demonstrates another distinction from the behavior of Bose gases where phase separation between two spin components has been observed[88, 89][3].

The density distribution of the interacting gas deviates from that of the non-interacting gas (Eqn. 3.3), due to the attractive (repulsive) mean field shrinking (stretching) of the cloud. In the unitarity-limited regime, where Eqn. 3.13 is valid, the effect of the mean field is simply a rescaling of the trapping frequencies by $\frac{1}{\sqrt{1+\beta}}$. Fitting the spatial distribution in the trap by such a rescaling and using β as a fit parameter can then be used to determine β [86, 87].

Resonant Enhancement of three-body Decay

Near a Feshbach resonance, the three-body recombination rate is also enhanced. This was the signal used for the first observation of a Feshbach resonance in ultracold atoms [82]. As shown by [90] and [91], the three-body decay rate for bosons for $a \gg R$ (as near a Feshbach resonance) scales as a^4 in the ultracold limit where the collision energy goes to zero. For an ultracold two-spin fermion system, this rate gets an additional factor $\sim E/\epsilon_{\mathrm{bind}}$ [92] where E is the kinetic energy of the collision and $\epsilon_{\mathrm{bind}} \sim \hbar^2/ma^2$[93] is the binding energy of the molecular state. Thus the rate goes to zero at threshold ($E \to 0$). This can be understood as the requirement for at least two identical fermions to approach each other within the size of the bound molecular state. Thus, for an ultracold two-spin fermion system, the 3-body decay rate near a Feshbach resonance should scale as $\sim a^6 E_F$. Our observations of inelastic decay near a Feshbach resonance (Chapter 5) is probably due to this mechanism.

3.4   Ground State of ^{6}Li

In this section, I describe the hyperfine ground state of ^{6}Li, our fermion of choice. Fig. 3-4 shows the Breit-Rabi diagram for ^{6}Li ($I = 1$, $J = 1/2$). In Fig. 3-4(a), the six ground hyperfine states are labelled with the low magnetic field basis $|F, m_F\rangle$. In Fig. 3-4(b), the notation common to the field is adopted, where the six states are labelled $|1\rangle$ through $|6\rangle$ in order of increasing energy.

As will be discussed in Chapter 4, we cool ^{6}Li to degeneracy in state $|6\rangle$ by sympathetic collisions with ^{23}Na in a magnetic trap. We then transfer the ^{6}Li to an optical dipole trap (ODT) which can trap any of the states $|1\rangle$ through $|6\rangle$. The most stable pair of states in which to try to induce interactions is the $|1\rangle - |2\rangle$ combination. This has the least number of inelastic decay channels. Most of the symmetry-allowed processes are endothermic at ultralow temperatures and thus suppressed. The only possible two-body inelastic decay

---

[3]Note that a three state mixture of fermions may be mechanically unstable [84].
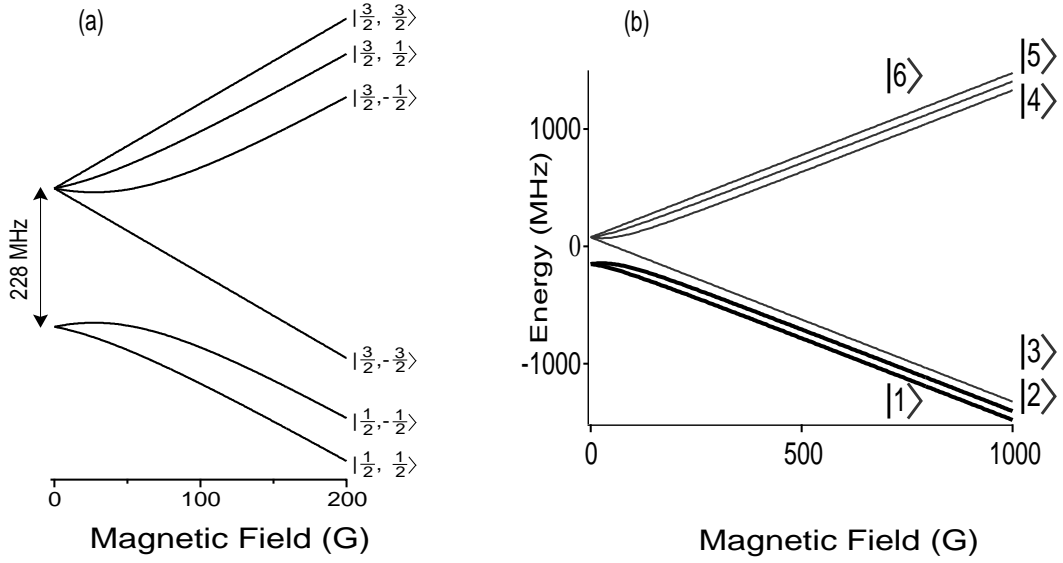
Figure 3-4: Ground state hyperfine levels of ^{6}Li.

channel is the dipolar process:

$$|1\rangle + |2\rangle \longrightarrow |1\rangle + |1\rangle. \tag{3.14}$$

If a $|1\rangle$ and a $|2\rangle$ atom collide s-wave, the symmetry of the dipolar operator (Section 3.2.2) can only allow the final products to leave d-wave. Since, the final states are identical, this is not allowed. Thus dipolar decay corresponding to Eqn. 3.14 is forbidden for the s-wave input channel. p-wave dipolar decay is allowed but highly suppressed at the typical ultralow temperatures of our experiment.

In addition to the promise of stability, the $|1\rangle - |2\rangle$ mixture also features s-wave Feshbach resonances at accessible magnetic fields (Fig. 3-5). Thus, the $|1\rangle - |2\rangle$ mixture is the ideal choice of states to try to induce strong interactions. Feshbach resonances also exist in other binary combinations of $|1\rangle$, $|2\rangle$ and $|3\rangle$ (Fig. 3-5). This rich resonance structure opens up a large parameter space to study interactions.

3.5 Fermionic Superfluidity

In this section, I briefly outline the ideas of fermionic superfluidity. The realization of these predictions is a major goal for the field.

Figure 3-5: Prediction of interstate s-wave Feshbach resonances in the ground state of ^{6}Li. Broad Feshbach resonances exist in a_{12} at $812\,\mathrm{G}$, in a_{13} at $680\,\mathrm{G}$ and in a_{23} at $843\,\mathrm{G}$. In addition, a narrow Feshbach resonance exists in a_{12} at $547\,\mathrm{G}$. 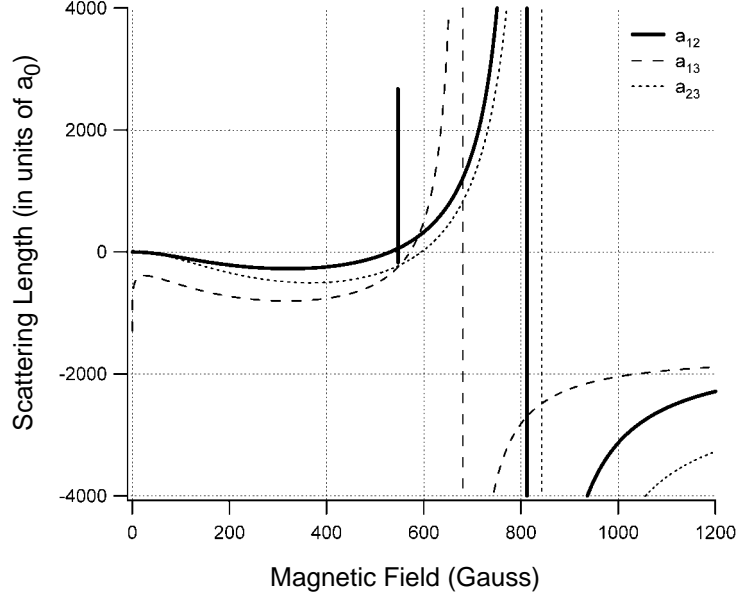This calculations by the group of B.J. Verhaar at Eindhoven, the Netherlands and includes all currently available experimental data to create the interaction potentials. Other (older) calculations will also be presented in this thesis at some points to preserve the story-line.

3.5.1 BCS Pairing

BCS pairing of fermions occurs via attractive interactions between particles. In the standard theory [31] which explains superconductivity in metals, electrons near the Fermi (momentum) surface of a metal can attract each other by phonon exchange. At a low enough temperature, this attraction can overcome Coulomb repulsion and electrons can undergo a pairing transition into a superfluid state. For metals, BCS pairing occurs at temperatures of $\sim 1\,\mathrm{K}$, which is about 10^5 times lower than the Fermi energy. The gap energy $\hbar\Delta$ characterizes the minimum excitation energy of the system. $\hbar\Delta = k_B T_c$ at zero temperature and decreases smoothly to zero as T goes to T_c.

The basic idea of BCS pairing has been applied to the case of trapped weakly-interacting atomic gases as well, with atomic mean-field interactions taking over the role of the phonon-mediated interaction[94, 95, 96, 97]. In this theory, s-wave pairing of a spin-mixture of fermions with inter-state scattering length $a(< 0)$ has been predicted to occur at a temperature of [94]:

$$T_c \simeq T_F \exp(-\frac{\pi}{2k_F|a|}), \qquad k_F a \ll 1 \qquad (3.15)$$

Although other pairing mechanisms have been investigated[95, 96], this one has the highest values of T_c/T_F for a given a. However, the weakly-interacting criterion $k|a| \ll 1$ immedi-

ately precludes an experimentally accessible T_c. Using some typical numbers of $a \sim 50a_0$ and $T_F \sim 1\,\mu\text{K}$, we get $T_c \sim T_F \exp(-100)$, far below current experimental accessibility.

In addition to this very low T_c, the relevant timescale for formation of the superfluid should be related to the gap as $1/\Delta \sim \exp(+100)\,\text{s}$. This is also far larger than typical system lifetimes, or any other experimental timescale for that matter. A more sophisticated calculation performed by [98] also gives similar pair formation time in the weakly interacting limit.

Achieving fermionic superfluidity will therefore require stronger interaction strengths. With their wide tunability, Feshbach resonances seem the ideal choice of mechanisms to enhance interactions. However, when $k_F|a|$ becomes comparable to 1, Eqn 3.15 starts to break down. A modified BCS theory is therefore needed to determine whether fermionic superfluidity is possible for large $k_F|a|$. A theory of "resonance superfluidity" has emerged over the last few years which aims to answer exactly this question.

3.5.2 Resonance Superfluidity

Near a Feshbach resonance, the scattering length a becomes very large, invalidating the $na^3 \ll 1$ assumption. Consequently, the appropriate interaction between atoms cannot be the usual mean-field, as assumed in Eqn. 3.15. However, an effective mean-field theory can still be derived in the s-wave ($kR \ll 1$) limit by explicitly including the bound state responsible for the Feshbach resonance in the interaction. Such a theory named resonance superfluidity has been developed by Murray Holland and others [99, 100, 101]. Their predictions of $T_c/T_F \sim 0.5$ for both ^{40}K and ^{6}Li is very encouraging for the prospect of a near-future experimental realization of dilute gas fermionic superfluidity.

Although the BCS transition is yet to be achieved in dilute gases, several interaction phenomena have been observed which are interesting in their own right. The results reported in Chapters 5, 6, and 7 describe some of these.

Chapter 4

Experimental Techniques

This chapter describes several aspects of the apparatus on which the experiments described in this thesis were performed. Although originally designed to Bose-condense ^{23}Na atoms [17], the apparatus has recently been upgraded into a two-species machine for ^{23}Na bosons and ^{6}Li fermions. Using forced evaporative cooling of the bosons and sympathetic cooling of the fermions by the bosons, we are now capable of producing degenerate bosons, fermions or Bose-Fermi mixtures. Features have also been added to produce fermion spin-state mixtures of tunable interaction strengths.

Descriptions of all the elements of the machine that are required for Bose condensation of ^{23}Na can be found in previous theses [9, 10]. The basic BEC setup was used to construct the atom interferometer described in Chapter 2. The major additions to allow two-species operation are a combined ^{23}Na-^{6}Li atomic beam and laser light (at 671 nm) to cool and trap ^{6}Li. Details of these additions can be found in the concurrently written thesis of Zoran Hadzibabic [12].

In this chapter, I will first briefly discuss the sympathetic cooling part of the experiment which produces a degenerate, spin-polarized Fermi gas that is essentially non-interacting. An attached paper reports on the technique and results:

- *Z. Hadzibabic, S. Gupta, C.A. Stan, C.H. Schunck, M.W. Zwierlein, K. Dieckmann, and W. Ketterle, "Fifty-fold improvement in the number of quantum degenerate fermionic atoms" [6]. e-print available at arXiv:cond-mat/0306050. Included in Appendix B.*

I will follow the sympathetic cooling discussion with a description of the additional technical elements which have allowed us to produce and study a system of strongly interacting fermions. These are: (1) an optical trap for ^{6}Li, (2) the creation of magnetic fields which bring the system near Feshbach resonances and (3) the manipulation and detection of spin compositions.

4.1 Production of a Degenerate Fermi Gas

As with the production of degenerate alkali bosons, the initial cooling phase for alkali fermions can also proceed via the well established techniques of laser cooling and magneto-optical trapping[40]. In the case of bosons, atoms from the magneto-optical trap (MOT) are transferred into a magnetic trap[1], after which forced evaporative cooling is applied to cool the gas into degeneracy. The key ingredient for this last step to work is the existence of a large collision rate which can thermalize the gas. The typical degeneracy temperature for dilute alkali gases of $\sim \mu$K implies that the gas only interacts via s-wave collisions ($kR \ll 1$). As mentioned earlier (Chapter 3), fermionic antisymmetry prohibits elastic collisions between identical fermions at ultralow temperatures, and makes evaporative cooling of spin-polarized fermionic samples impossible. The solution to this problem is to use some form of mutual or sympathetic cooling between two types of distinguishable particles, either two spin states of the same atom[26, 29], or two different atoms[27, 28, 3, 30]. Our solution involves the use of bosonic ^{23}Na as a sympathetic cooling agent for fermionic ^{6}Li.
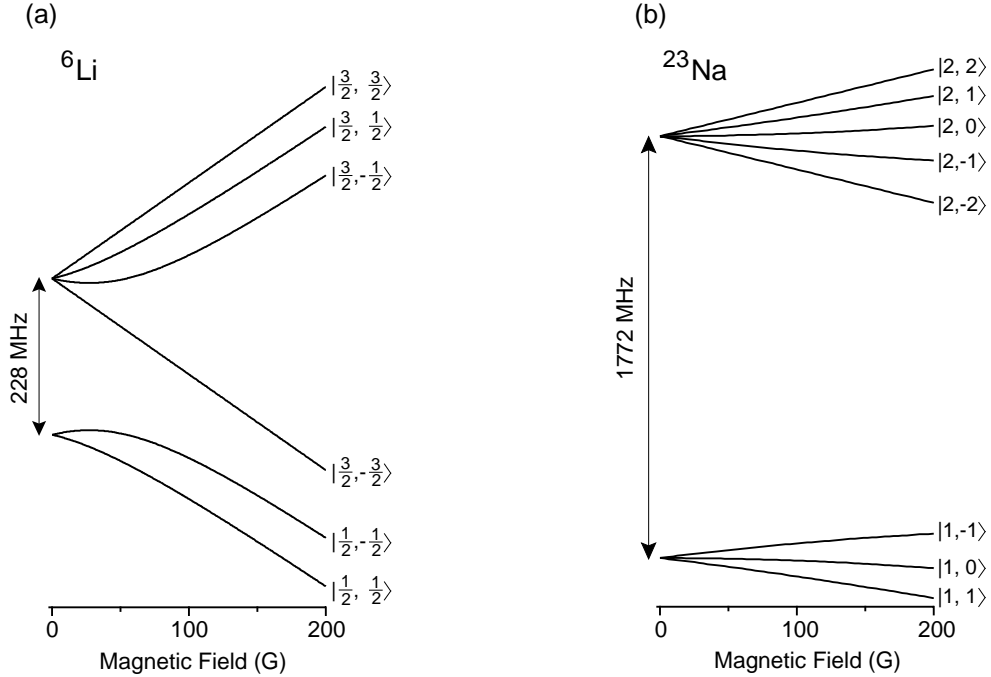
Figure 4-1: Ground state hyperfine structures of (a) ^{6}Li and (b) ^{23}Na. The states are labelled in the low field, $|F, m_F\rangle$ basis. Lithium (sodium) is loaded into the magnetic trap in the $|F = 3/2, +3/2\rangle$ ($|F = 2, +2\rangle$) state from the MOT. Sodium is evaporated on the $|F = 2, +2\rangle \rightarrow |F = 1, +1\rangle$ hyperfine transition near 1.7 GHz.

In our experiment, laser-cooled ^{23}Na and ^{6}Li atoms are transferred from a two-species MOT [3, 12] into a common magnetic trap (fig. 4-2). Forced evaporation cools ^{23}Na atoms,

---

[1]Optical traps based on the AC Stark effect are also used in a few laboratories such as [102].

which in turn thermalize and thus cool the ^{6}Li atoms "sympathetically". Using this procedure, we can efficiently cool both species into simultaneous degeneracy. A critical requirement for our strategy to work is the dominance of cross-species elastic collisions over inelastic decay mechanisms. We are fortunate that this is indeed the case.

Figure 4-2: Schematic of current-carrying coils for magnetic trapping and production of magnetic fields near ^{6}Li Feshbach resonances. Running current through the gradient, curvature and antibias coils in the directions shown create a conservative trapping potential about a field minimum for atoms that are weak-field seekers. The potential is harmonic near the minimum and has symmetry about the z-axis. T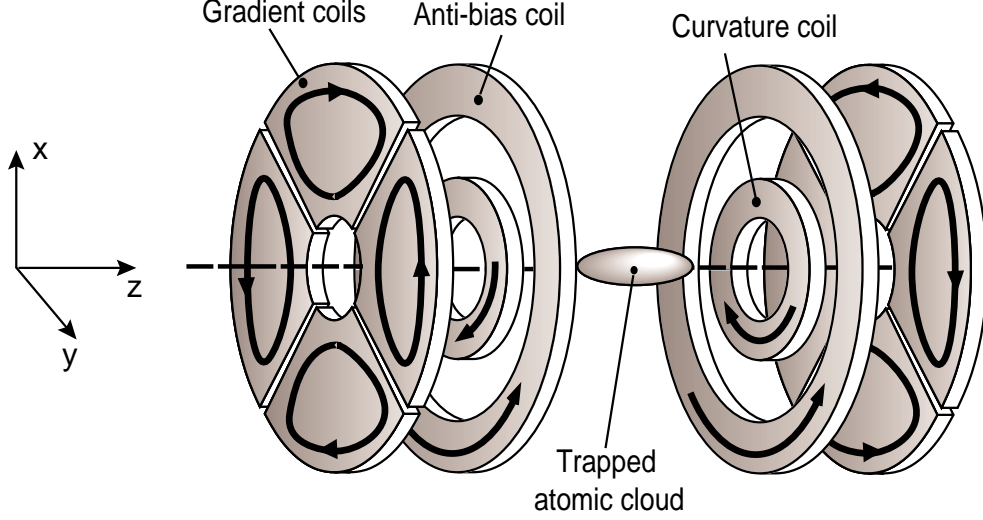he optical trap is aligned along the z-axis (Section 4.2). The Feshbach field is applied by running current only through the antibias coils (Section 4.3).

Lithium is sympathetically cooled in the stretched $|F = 3/2, +3/2\rangle$ state[2] by sodium in the $|F = 2, +2\rangle$ state (Fig. 4-1). Evaporation from the $|F = 2, +2\rangle$ to the untrapped $|F = 1, +1\rangle$ state is carried out by applying a microwave field at ~ 1.7 GHz. This frequency is far from any lithium resonance.

A schematic of the magnetic trap used for cooling is shown in Fig. 4-2. This design is based on the clover-leaf configuration first demonstrated by our group in 1996[63, 9]. The combination of gradient, curvature and antibias coils produce a magnetic field minimum. At the minimum, the field points along $+z$. For a weak field seeking state, there is confinement which is harmonic near the minimum with cylindrical symmetry about z. The confinement is stronger radially (x, y), making the atom cloud cigar-shaped. The real trap consists of current-carrying wires wound in the shapes shown and packed together tightly using epoxy. They are rigidly mounted outside the stainless steel vacuum chamber used for the experiment. The shapes of the coils are chosen to simultaneously optimize magnetic confinement, vacuum requirements and optical access. A full description of our magnetic

---

[2]this was identified as state $|6\rangle$ in the previous chapter.

trap can be found in the diploma thesis of Christian Schunck [103]. Our typical trapping currents give rise to a Fermi energy $E_F \sim k_B \times N^{1/3} 600\,\text{nK}$ where N is the atom number expressed in millions (Eqn 3.2).

The mixture of stretched states has an extremely favorable ratio of elastic to inelastic collisions. After about 30 s of cooling, we can produce up to 7×10^7 magnetically trapped ^{6}Li atoms at less than half the Fermi temperature (T_F). Further, in samples containing up to 3×10^7 atoms, we observed temperatures as low as $0.05\,T_F$. The final temperature of the fermions is ultimately limited by the finite heat capacity of the bosons. The numbers quoted above represent the current upper limits of the system capability. On a day-to-day basis, we can produce 30-50 million atoms at $\lesssim 0.5\,T_F$ or 10-30 million at $\lesssim 0.2\,T_F$.
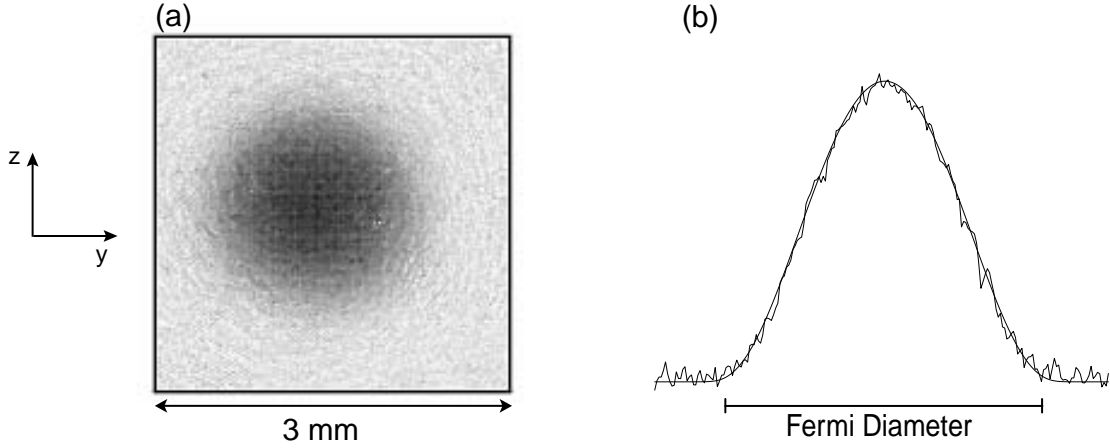
Figure 4-3: Large and ultra-degenerate Fermi sea. (a) Absorption image of 3×10^7 ^{6}Li atoms released from the magnetic trap and imaged after 12 ms of free expansion. (b) Axial (z-axis) line density profile of the cloud in (a). A semiclassical "Thomas-Fermi" fit (thin line) yields a temperature $T = 93\,\text{nK} = 0.05\,T_F$. At this temperature, the high energy wings of the cloud do not extend visibly beyond the Fermi energy, indicated in the figure by the momentum-space Fermi diameter (1D projection of the momentum space Fermi surface).

The atoms are probed along the (usually) x-direction with resonant absorption imaging onto a CCD (charge-coupled device) camera. An example image is shown in Fig. 4-3. The semi-classical fit to the line density profile (Section 3.1) yields a degeneracy parameter $T/T_F = 0.05$.

Although our (current) primary goal for sympathetic cooling is the production of large numbers of degenerate fermions, the system can be adjusted to produce pure ^{23}Na BECs with up to 10 million atoms[3], or simultaneously quantum degenerate Bose-Fermi mixtures, each containing several million atoms (Fig. 4-4).

---

[3]this also represents the first production of evaporatively cooled sodium BECs in the upper hyperfine state.

Figure 4-4: Two-species mixture of degenerate Bose and Fermi gases. Absorption images of ^{6}Li and ^{23}Na clouds on the same CCD camera using separate light pulses (see Section 4.4). The times of free expansion of the two gases can be varied independently. This dual-imaging techn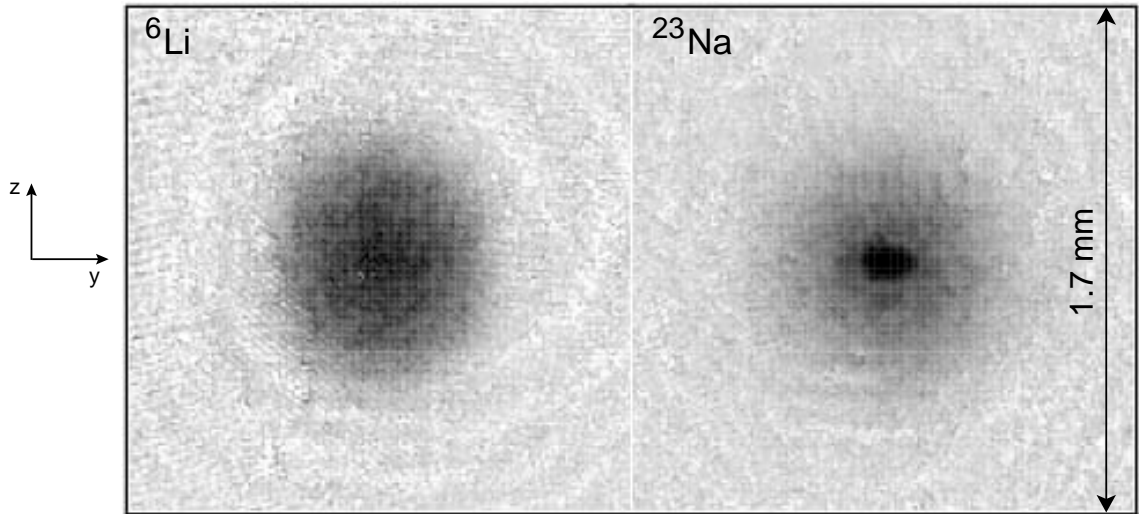ique allows for optimizing the cooling strategy for either single- or two-species experiments. For the displayed image, the expansion times were $\tau_{\mathrm{Li}} = 8\,\mathrm{ms}$ and $\tau_{\mathrm{Na}} = 25\,\mathrm{ms}$ and the atom numbers were $N_{\mathrm{Li}} \sim 10^7$ and $N_{\mathrm{Na}} \sim 6 \times 10^6$. Sodium was cooled below the condensation temperature, corresponding to $\sim 0.2\,T_F$ for the lithium cloud.

The sympathetic cooling discussed in this section has become standard in our laboratory since the end of 2002. An older strategy, based on keeping ^{23}Na in the $|F = 1, -1\rangle$ state, was used for about a year before that and is detailed in [3, 12]. The newer strategy increased the atom number by two orders of magnitude and reduced T/T_F by one order of magnitude. The experiment described in Chapter 5 was performed using the older sympathetic cooling, while the results of chapters 6,7 were obtained using the newer one.

4.2   Optical Trapping of Lithium

The most promising ^{6}Li spin mixture for inducing strong interactions is the $|1\rangle - |2\rangle$ combination (Section 3.4). In particular, the interstate s-wave scattering length a_{12} exhibits a very broad Feshbach resonance at $\sim 810\,\mathrm{G}$ and a narrow one at $545\,\mathrm{G}$ (Fig. 4-5(b)). At these high fields, both states are strong field seekers (Fig. 4-5(a)). Therefore neither can be magnetically trapped, necessitating the use of an optical dipole trap (ODT).

An atom exposed to a laser beam detuned to the red of an internal transition feels a force which is directed towards higher optical intensity. This optical dipole force can be used to confine atoms at a local intensity maximum such as the focus of a laser beam. Atoms then feel a conservative potential which is generally known as the AC Stark shift. This is the basis of the ODT.
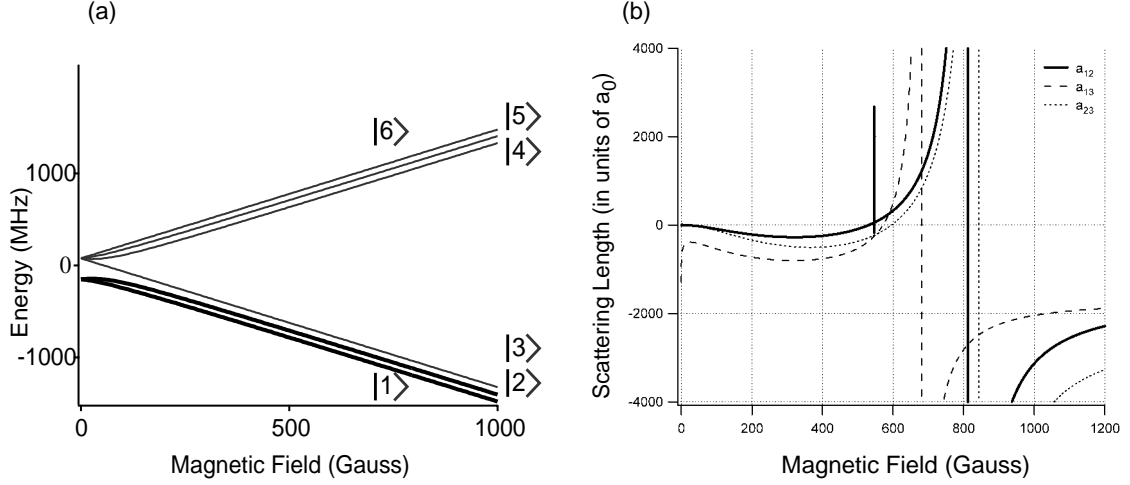
Figure 4-5: (a) Ground state hyperfine levels of ^{6}Li. (b) Prediction of interstate *s*-wave Feshbach resonances in the ground state of ^{6}Li. Calculations by the group of B.J. Verhaar at Eindhoven, the Netherlands. Broad Feshbach resonances exist in a_{12} at 810 G, in a_{13} at 680 G and in a_{23} at 845 G. In addition, a narrow Feshbach resonance exists in a_{12} at 545 G.

We use light at 1064 nm from a 20 W IPG Photonics fiber laser to trap lithium fermions (671 nm optical resonance). This large detuning from the optical resonance makes all 6 spin states of ^{6}Li (Fig. 4-5(a)) feel identical trapping potentials in our ODT. Although our group has been trapping Bose-Einstein Condensates in ODT's since 1998 [104], trapping of ultracold fermionic clouds is more challenging simply because of its larger size/energy (see Fig. 4-4). To get a crude estimate of this difference, we can compare the chemical potential μ of a BEC to the Fermi energy E_F of a zero temperature Fermi gas (assuming the same number of particles N and same mean trapping frequency $\bar{\omega} = (\omega_1 \omega_2 \omega_3)^{1/3}$[4]):

$$\frac{\mu}{E_F} \sim \frac{(\hbar^4 \bar{\omega}^6 N^2 m a^2)^{1/5}}{\hbar \bar{\omega} N^{1/3}} = \left(\frac{\hbar \bar{\omega} N^{1/3}}{(\hbar^2/ma^2)} \right)^{1/5} \sim \left(\frac{E_F}{(\hbar^2/mR^2)} \right)^{1/5} \tag{4.1}$$

for $a \sim R$, the range of the interatomic potential, which is usually the case far away from resonances. In the *s*-wave regime, $E_F \ll (\hbar^2/mR^2)$. This simple argument shows that the optical potential will need to be deeper to accommodate degenerate Fermi clouds. By assuming the same density for bosons and fermions, a relation similar to Eqn. 4.1 can be derived, except with a 1/3 power instead of 1/5 power on the right-hand side. Experimentally, we have found that we need considerably more optical power to trap degenerate fermions than to trap BECs.

The 20 W output of the laser is sent through an acousto-optic modulator (AOM), which acts as a switch and a variable attenuator for the 1064 nm radiation. In order to maximize

---

[4]note that neither of these assumptions are quantitatively valid, but they are made only to emphasize the role of quantum statistics in this technical problem.

the available intensity, we do not send the beam through an optical fiber (typically 50% efficiency). Instead, after passing through the AOM, the light goes directly through beam shaping optics and enters the vacuum chamber along the z-direction (Fig. 4-2). The focus of the beam is aligned with the position of the atoms in the magnetic trap. The ($< 100\%$) efficiency of the AOM together with losses in the shaping optics restrict the total available power at the atoms to about 5 W. The position and shape of the focus can be monitored on a CCD camera placed at an imaging plane of the atoms. The size of the focus w ($=1/e^2$ radius) varies from about $14\,\mu$m to $16\,\mu$m, depending on the exact alignment of all the optics. The Rayleigh range of the gaussian beam is then $\frac{\pi w^2}{\lambda} \sim 0.8$ mm for $w = 16\,\mu$m and $\lambda = 1064$ nm. Using the AC Stark shift potential for a gaussian laser beam [72][5], we can derive simple relations for the trap depth U_{trap}, radial(axial) trapping frequencies $\omega_\perp(\omega_z)$, Fermi temperature E_F, and the zero-temperature peak density n_0 in our system:

$$
\begin{aligned}
U_{\mathrm{trap}} &= 166\,\mu\mathrm{K} \times (\frac{16\,\mu\mathrm{m}}{w})^2 \times \frac{P}{1\,\mathrm{W}} \\
\omega_\perp &= 2\pi \times 9.3\,\mathrm{kHz} \times (\frac{16\,\mu\mathrm{m}}{w})^2 \times (\frac{P}{1\,\mathrm{W}})^{1/2} \\
\omega_z &= 2\pi \times 130\,\mathrm{Hz} \times (\frac{16\,\mu\mathrm{m}}{w})^3 \times (\frac{P}{1\,\mathrm{W}})^{1/2} \\
T_F &= 20.9\,\mu\mathrm{K} \times (\frac{16\,\mu\mathrm{m}}{w})^{7/3} \times (\frac{P}{1\,\mathrm{W}})^{1/2} \times (\frac{N}{1\,\mathrm{million}})^{1/3} \\
n_0 &= 1.9 \times 10^{14}\,\mathrm{cm}^{-3} \times (\frac{16\,\mu\mathrm{m}}{w})^{7/2} \times (\frac{P}{1\,\mathrm{W}})^{3/4} \times (\frac{N}{1\,\mathrm{million}})^{1/2}
\end{aligned}
\tag{4.2}
$$

Ultracold atoms confined in the magnetic trap are transferred into the optical trap by adiabatically (compared to trap frequencies) turning on the ODT. Typically, we remove all the ^{23}Na atoms by evaporation and are left only with the non-interacting fermions before turning on the ODT. After the optical power is ramped up to the desired value, the magnetic trap is switched off. This procedure allows up to 20 million atoms to be loaded into the ODT at about the Fermi temperature. Atoms in state $|3/2, +3/2\rangle = |6\rangle$ are then transferred to (now trappable) state $|1\rangle$ using a single photon transition at 228 MHz near zero field. This transfer is close to 100% efficient. Arbitrary spin states can then be prepared at arbitrary magnetic fields (Section 4.4). Additional cooling can also be performed in the optical trap (Section 4.5).

4.3 Magnetic Fields

A schematic of the magnet coils currently used in the experiment is shown in Fig. 4-2. An optically trapped ^{6}Li spin mixture can be brought near a Feshbach resonance by sending current only through the antibias coils (Fig. 4-2). To preserve the quantization axis of

---

[5]it is important to include the counter-rotating term as it contributes about 18% of the trap depth for ^{6}Li atoms trapped in 1064 nm light.

the atoms in the z-direction, this current is run in the opposite direction than during the magnetic trapping phase (Fig. 4-2).
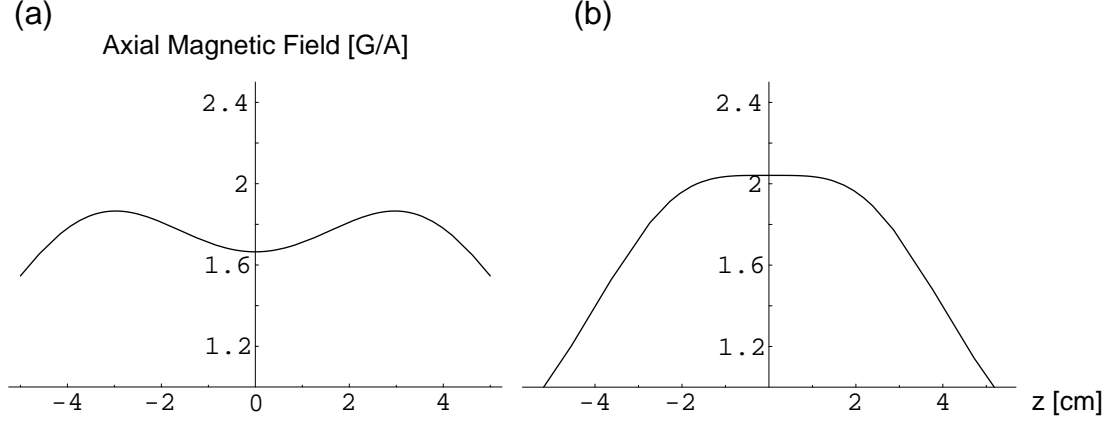
(a)

Axial Magnetic Field [G/A]

(b)

Figure 4-6: Homogeneity of the Feshbach field. Comparison of the (calculated) antibias fields from (a) old and (b) new magnetic traps. The new antibias coils are placed in a Helmholtz configuration and produces larger bias and far less curvature than the old antibias coils.

Full details of the design and construction of the magnetic trap can be found in [103]. This trap was built as a replacement to another one of similar design when the latter developed a short. The new magnetic trap improves on the old one in two important ways: (1) a high pressure water cooling system allows us to apply fields $\geq 1000\,\mathrm{G}$ continuously. Previously, we were restricted only to magnetic field pulses ($\leq 1\,\mathrm{s}$ at $1000\,\mathrm{G}$). (2) an optimized "Helmholtz" placement of the antibias coils has dramatically reduced the field curvature accompanying the application of large bias fields (Fig. 4-6). The curvature from the old trap was anti-trapping at the Feshbach resonance fields (Fig. 4-5) and reduced the effective trap depth. This caused substantial spilling of atoms from the ODT. Very careful optical alignment was required to match the centers of the ODT and the magnetic "anti"-trap, in order to minimize this spilling. With the new trap, this issue is non-existent.

The antibias coils produce a magnetic bias field of $2.06\,\mathrm{G/A}$ (Gauss/Amp) and a field curvature of $\sim 0.002\,(\mathrm{G/cm^2})/\mathrm{A}$. The bias was calibrated by locating optical resonances of $^6\mathrm{Li}$ at large magnetic fields ($500 - 1000\,\mathrm{G}$) and comparing the resonance positions with the Breit-Rabi predictions for the energy levels. The curvature was measured during the "bench"-test of the magnetic trap prior to installation, and is about 30 times lower than that of the older trap.

Magnetic fields of up to $1000\,\mathrm{G}$ can therefore be applied using a commercial $500\,\mathrm{A}$ power supply. This range encompasses all the Feshbach resonances of Fig. 4-5. As shown in Fig. 4-7(a), we can switch on these fields in a few milliseconds (limited by the power supply). The switch off time is a few hundred microseconds (Fig. 4-7(b)) and is fundamentally limited by the inductance of the coils.
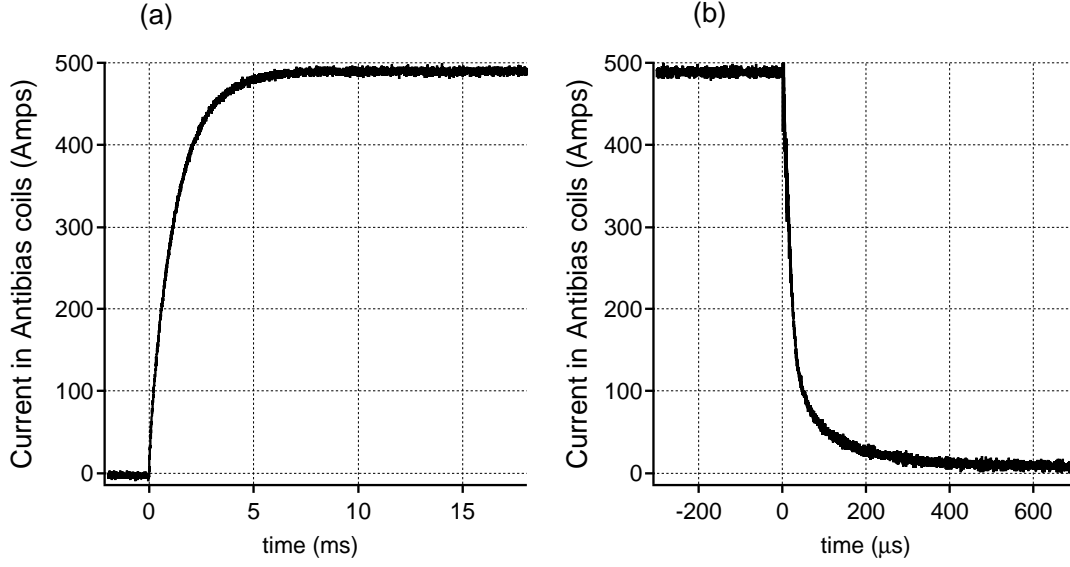
Figure 4-7: Current turn on and shut off in Feshbach (antibias) coils. Currents of 500 A (magnetic fields of 1000 G) can be (a) turned on in a few ms and (b) switched off in a few hundred µs.

4.4 Spin State Manipulation and Detection

We have spent substantial effort in developing flexible methods of spin state manipulation and detection in the optical trap at arbitrary magnetic fields. This can be useful for several reasons:

(1) Studies of interactions by imaging at near zero-field after turning off the Feshbach fields may be inadequate because (a) the timescale for turning off the field could compete with the timescales of dynamics that we wish to study or/and (b) the system could undergo inelastic decay while going through a loss resonance at a lower field during current turn-off. These inadequacies are remedied by imaging the atoms at the magnetic field of interest.

(2) As shown in Fig. 4-5, each binary mixture of states $|1\rangle$, $|2\rangle$ and $|3\rangle$ has at least one interstate Feshbach resonance. The ability to create and diagnose arbitrary spin compositions near these resonances opens up a large parameter space for studying strongly interacting fermions.

(3) Since fermionic superfluidity involves pairing of momentum states near the Fermi surface, the particle numbers (determining the Fermi surfaces, Eqn. 3.2) in the spin components need to be controlled. The degree to which this "Fermi surface matching" will be required for the superfluid transition is as yet unclear. However, tunability of the matching provides an experimental knob in the search for this transition.

(4) Mean field interactions can be directly measured as resonance shifts in transitions between spin states. These transitions can be monitored by detecting the spin state composition. Chapter 7 describes such experiments performed in our system.

Beginning with atoms in state $|1\rangle$ in the optical trap (Section 4.2), we can ramp up the field to any desired value (Section 4.3) and create an arbitrary composition of states $|1\rangle$, $|2\rangle$ and $|3\rangle$ using standard $\sim 80\,\mathrm{MHz}$ (Fig. 4-8) radio-frequency (RF) techniques. This involves an RF synthesizer, an amplifier and an RF coil - standard features of the experiment[105]. The new feature that was required was the implementation of simultaneous spin-selective imaging at arbitrary magnetic fields.
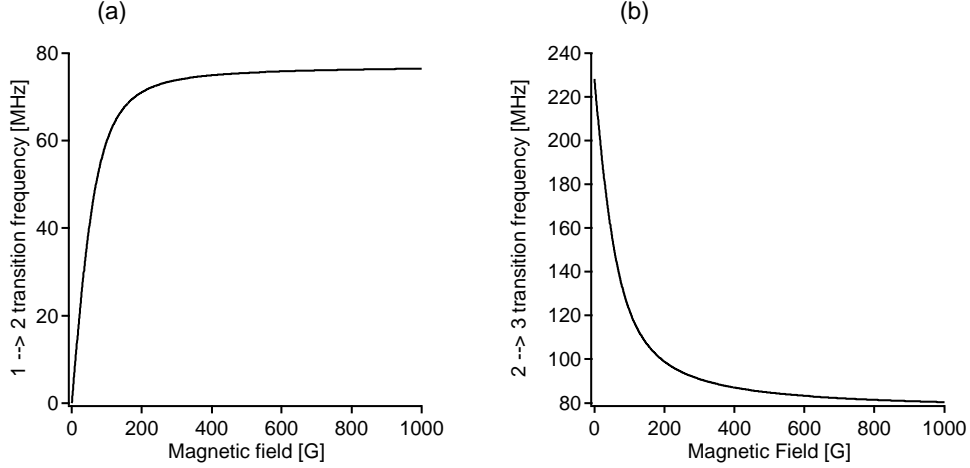

Figure 4-8: Energy difference between (a) states $|2\rangle$ and $|1\rangle$ and (b) states $|3\rangle$ and $|2\rangle$.

Imaging at arbitrary magnetic fields is accomplished by frequency shifting (with an AOM) the laser light used for cooling and trapping of ^{6}Li to the optical resonance at the desired field. The AOM has sufficient frequency tunability to encompass the Feshbach resonances shown in Fig. 4-5. More details can be found in [12].

Fig. 4-9 shows the ground $^2S_{1/2}$ state and excited $^2P_{3/2}$ state hyperfine structure of ^{6}Li. In the excited state, the m_I sub-levels are always unresolved within each m_J level (Fig. 4-9). Thus, optical transitions from states $|1\rangle$, $|2\rangle$ and $|3\rangle$ to any m_J level of the $^2P_{3/2}$ state are separated only by the ground state hyperfine splitting. At the Feshbach resonance fields (Fig. 4-5), these splittings are $\sim 80\,\mathrm{MHz}$ (Fig. 4-8), well above the natural linewidth of $6\,\mathrm{MHz}$. Thus, two beams separated in frequency by this splitting could each be selectively resonant with only one of the states. Both this frequency difference and the spatial separation required for independent imaging can be provided by an additional AOM.

An AOM which frequency downshifts light resonant with $|2\rangle$ at a particular magnetic field B, by the $|2\rangle - |3\rangle$ splitting at B, simultaneously produces spatially separated laser beams resonant with $|2\rangle$ (zeroeth order) and $|3\rangle$ (first order). These beams can then both be directed onto a $|2\rangle - |3\rangle$ binary mixture (either trapped or in free expansion). After passing through the atoms the two beams can be sent to two different parts of the CCD chip on the imaging camera. In this way, overlapping atom clouds can be simultaneously imaged onto different parts of the camera. An absorption image using such a geometry is
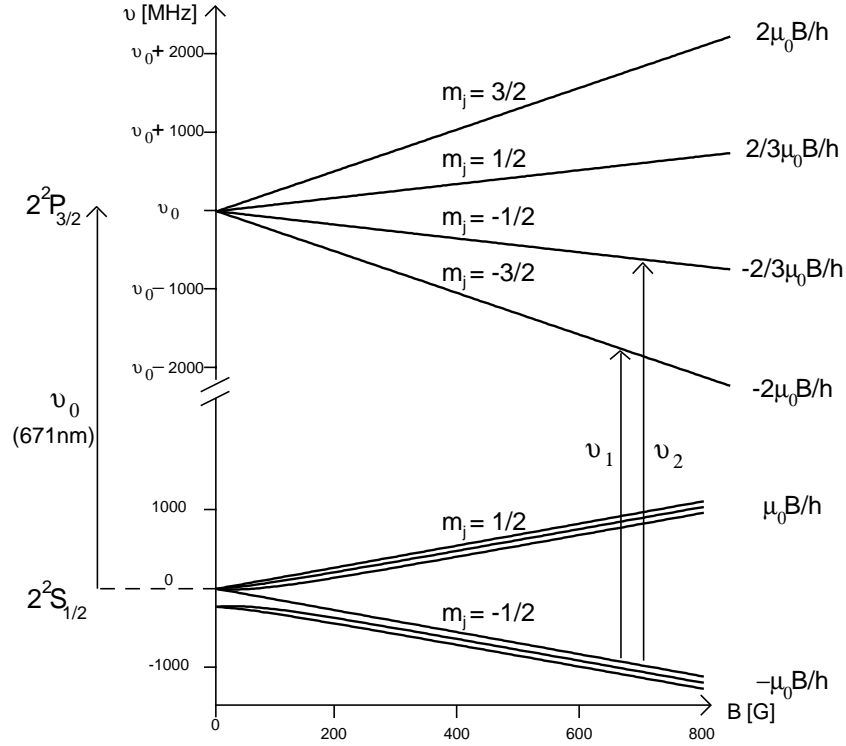
Figure 4-9: High field imaging of ^{6}Li. ν_1 and ν_2 are two optical transitions that we currently use for high field imaging. Each m_J level in the excited state has 3 unresolved m_I states. The optical frequencies from the ground $m_J = -1/2$ state are separated only by the ground state Zeeman separations of $\sim 80\,\text{MHz}$ at high fields. Within each of these optical lines, we select the state to be imaged ($|1\rangle$, $|2\rangle$ or $|3\rangle$) with AOMs as described in the text.

shown in 4-10(a).

Using a charge shifting feature of a CCD chip, we can extend the above simultaneous imaging capability to image all three states. It is possible to take multiple absorption images in quick succession by shifting (fast: $\sim$ millisecond) the charge corresponding to an image to a shielded part of the CCD chip before reading out the charge (slow: $\sim$ second). This is often called the "kinetics" mode of operation of a CCD camera. Two images can then be taken which are separated by a variable time. This time is only limited from below by the charge shifting time of $\sim 600\,\mu\text{s}$ for a typical $3\,\text{mm} \times 3\,\text{mm}$ exposure area. This separation time can be used to shift the light to the frequency appropriate to image the third state (state $|1\rangle$ in Fig. 4-10(b)) as well as provide a variable expansion time for a released atom cloud. Fig. 4-10(b) shows the image of a ternary mixture using this technique.

Using these imaging techniques, we have established a fairly flexible and robust system to prepare and study interacting fermions. Two consecutive images with an adjustable separation/expansion time using the kinetics mode also allows us to take images of ^{23}Na-^{6}Li mixtures as in Fig. 4-4. In this case, the yellow (sodium) and red (lithium) imaging
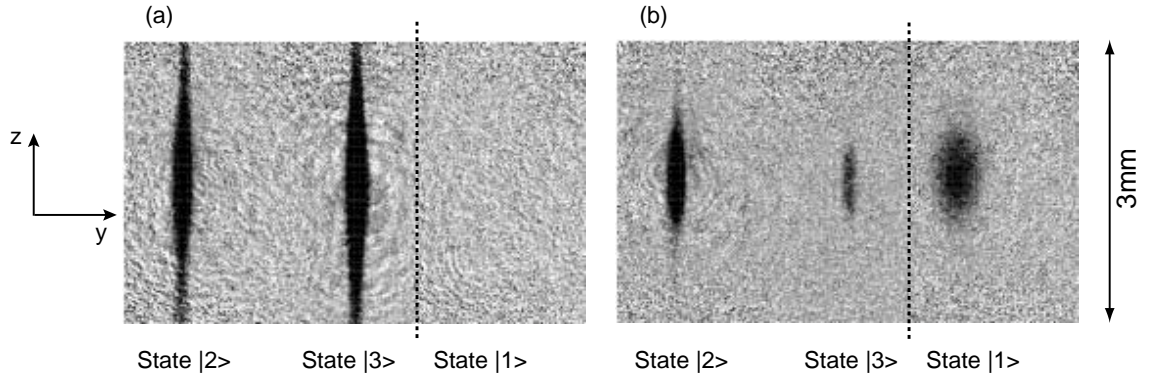
Figure 4-10: Simultaneous multiple state imaging in kinetics mode. The dashed line separates two different exposures in each image. Arbitrary spin compositions can be measured independently at high magnetic field. (a) shows a binary mixture of states $|2\rangle$ and $|3\rangle$. (b) shows a ternary mixture of states $|1\rangle, |2\rangle$ and $|3\rangle$.

beams are sent along identical imaging paths after being combined on a dichroic mirror.

4.5 Evaporative Cooling in the Optical Trap

A binary spin-mixture interacting with a finite interstate scattering cross-section will thermalize and evaporatively cool in a finite depth optical trap. Beginning with a 50-50 mixture, efficient cooling can be performed in this way [29]. The thermalization rate or alternatively atom loss can be used to measure the scattering cross-sections in interacting fermions [106, 107].

We have observed cooling and atom loss for the $|1\rangle - |2\rangle$ mixture in our ODT at various magnetic fields. Fig. 4-11 shows the behavior of $|1\rangle - |2\rangle$ mixtures at two different magnetic fields: 530 G and 900 G. At 530 G, the mixture shows no change on a 100 ms timescale while at 900 G, there is a visible atom loss and cloud size shrinkage, reflecting the cooling. This is consistent with the magnetic field dependence of a_{12} shown in Fig. 4-5.

A modestly degenerate $(T \lesssim T_F)$ cloud loaded into the ODT has an evaporation parameter η given using Eqns. 4.2 by:

$$\eta = \frac{U_{\text{trap}}}{T_F} = 8 \times (\frac{w}{16\,\mu\text{m}})^{1/3} \times (\frac{P}{1\,\text{W}})^{1/2} \times (\frac{1\,\text{million}}{N})^{1/3} \tag{4.3}$$

If we load 16 million atoms into a 4 W trap (near optimum conditions) and make a 50-50 mixture, $\eta = 8$, small enough for atom loss and cooling to take place even without lowering the trapping potential. This is consistent with our observations. Currently we can achieve temperatures of $\lesssim 0.5\,T_F$ in the ODT. Careful characterization and optimization of this cooling process [29, 86] should produce degeneracies comparable to those observed in the magnetic trap. Such conditions would doubtless bring us even closer to fermionic

530 G   900 G

3mm

z
y

10 ms wait

100 ms wait
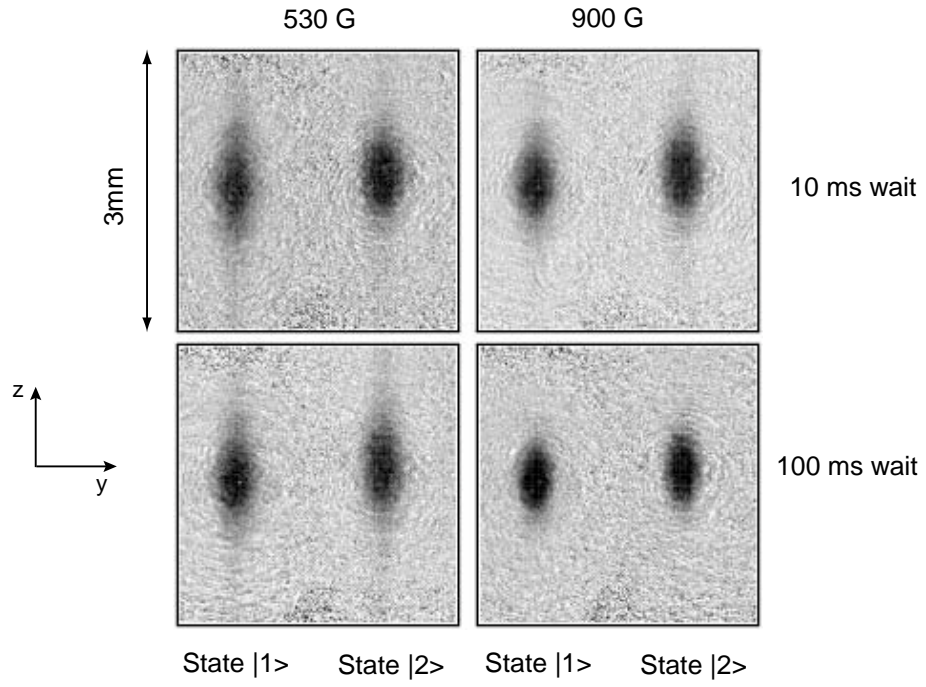
State |1>   State |2>   State |1>   State |2>

Figure 4-11: Mutual cooling of states $|1\rangle$ and $|2\rangle$ in the optical trap. The images are taken using the simultaneous imaging technique at an expansion time of $500\,\mu$s. The trap depth is kept constant at $\sim 330\,\mu$K.

superfluidity.

Chapter 5

Decay of an Ultracold Fermi Gas near a Feshbach Resonance

This chapter focuses on the experiment reported in the following publication:

- *K. Dieckmann, C.A. Stan, S. Gupta, Z. Hadzibabic, C.H. Schunck, and W. Ketterle, "Decay of an Ultracold Fermi Gas near a Feshbach Resonance" Phys. Rev. Lett., **89**, 203201 (2002) [4]. Included in Appendix C.*

This chapter describes our first experiments in an interacting regime with ultracold lithium atoms. We successfully located two Feshbach resonances between the two lowest Zeeman sub-levels of the ground state (states $|1\rangle$ and $|2\rangle$) by observing the magnetic field-dependent decay of a mixture of these two spin components. We also determined the lifetime of the $|1\rangle - |2\rangle$ mixture in the Feshbach resonance regime where fermionic superfluidity is predicted to occur[99, 108, 100]. The measured lifetimes are favorable compared to the estimated creation time of the predicted superfluid state.

As described in Section 3.4, for ^{6}Li, the natural choice of interacting states in an optical trap is the $|1\rangle - |2\rangle$ combination. This mixture has no energetically-accessible spin-exchange channels. In addition, the only energetically-accessible dipolar decay channel is forbidden s-wave, while p-wave contributions are suppressed by our ultralow temperatures.

The question arises as to what would be the most direct signature of a Feshbach resonance. Prior to our experiment, the JILA group had measured such a resonance in fermionic ^{40}K using a thermalization time measurement [109]. However, the first observation of Feshbach resonances in ultracold atoms was via the measurement of enhanced, field-dependent losses in a BEC in our group [82]. This is a straightforward measurement if the system does indeed have a resonantly-enhanced decay mechanism.

Guided by this previous experience in our group, we simply followed the steps of optical trapping, mixture preparation and magnetic field application and in true experimentalist fashion tried to "see what happens". We indeed saw atom loss as a function of magnetic field.

The losses that we observed were the first experimental signatures of scattering resonances in the ^{6}Li $|1\rangle - |2\rangle$ combination.

Since our publication [4], (Appendix C) details all the salient experimental aspects, I will restrict myself to a short summary of the experimental method and results. The interpretation of the nature of the observed decay will also be discussed.

5.1 Resonant Decay of an Ultracold Fermi Gas

5.1.1 Observation of Field-Dependent Losses
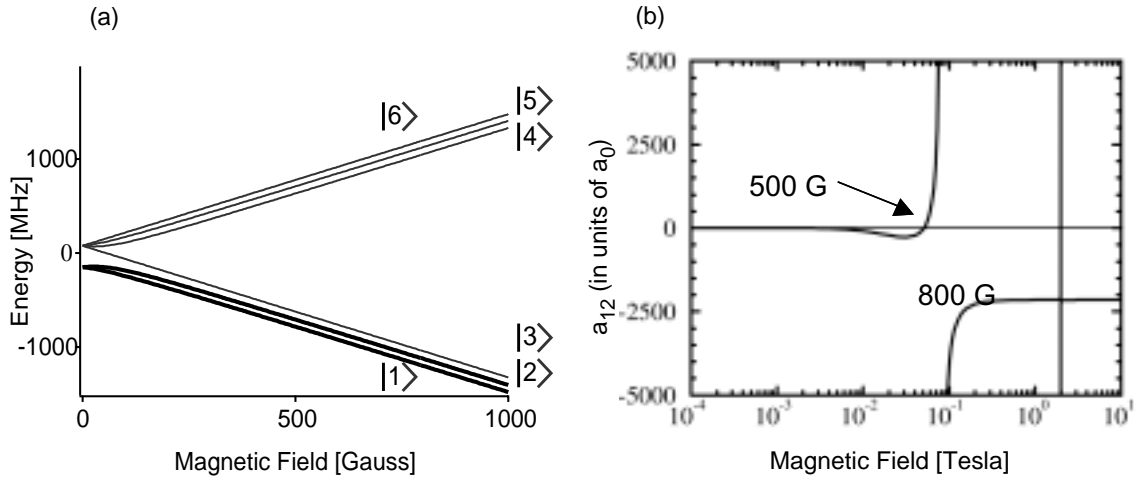
Figure 5-1: (a) Ground state hyperfine levels of ^{6}Li. (b) Predicted s-wave scattering length a_{12} between states $|1\rangle$ and $|2\rangle$ (thick lines in (a)). Feshbach resonances are predicted at $\sim 800\,\mathrm{G}$ and $\sim 20,000\,\mathrm{G}$. a_{12} goes through zero near $500\,\mathrm{G}$. At the experimentally accessible Feshbach resonance at $800\,\mathrm{G}$, states $|1\rangle$ and $|2\rangle$ are both high-field seeking, making optical trapping a necessity. Figure (b) is from reference [110].

As shown in Fig. 5-1, states $|1\rangle - |2\rangle$ of the ^{6}Li ground state were predicted to have an interstate s-wave Feshbach resonance at $\sim 800\,\mathrm{G}$. To achieve the corresponding experimental situation, we first created a degenerate gas in the $|2\rangle$ state in the magnetic trap using our first sympathetic cooling scheme (Chapter 4,[3]). After loading the gas from the magnetic trap into the optical trap, we created a mixture of states $|1\rangle$ and $|2\rangle$ by an RF-induced spin flip at a field of $\sim 1.5\,\mathrm{G}$. The magnetic field was then ramped up to a specific value where the atom number was monitored for two different wait times - $50\,\mathrm{ms}$ and $500\,\mathrm{ms}$. We repeated this procedure at many different magnetic field values in order to map out the field dependence of loss processes. The number was measured using absorption imaging after turning off the field. Taking the ratio of the two obtained numbers served as a normalization process guarding against systematics from loading losses. A second guard against systematics was carried out by doing the same experiments on the pure states $|1\rangle$ and $|2\rangle$. As a function of

magnetic field, the pure states were mostly featureless (not shown) while the 50-50 mixture showed pronounced loss features (Fig. 5-2).
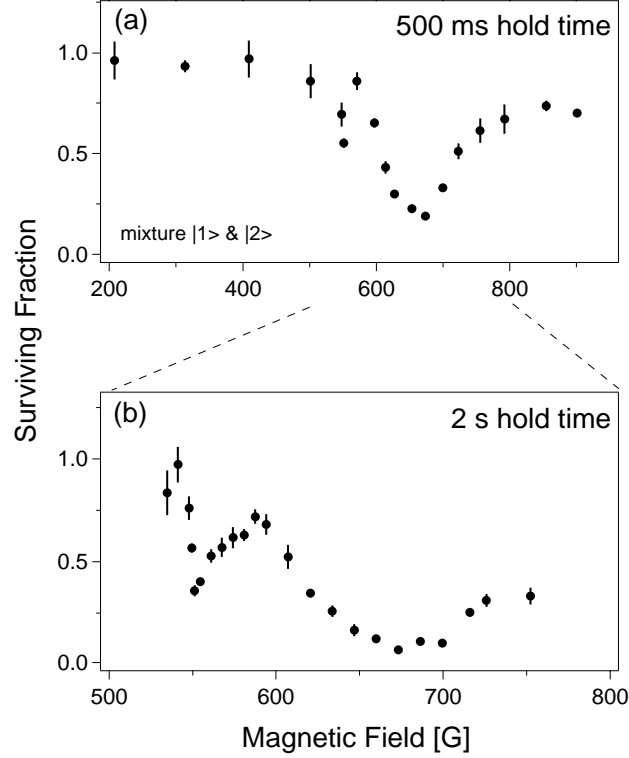
Figure 5-2: Feshbach resonances identified by losses. Beginning with a 50-50 mixture of states $|1\rangle$ and $|2\rangle$, the survival fraction is plotted as a function of the magnetic field. (a) is a scan over the range 200 G-850 G and shows the survival fraction calculated as the ratio of the atom number after wait times of 500 ms and 50 ms. The scan shows a pronounced loss feature peaked at $\sim$ 680 G. In addition, a narrow loss feature at $\sim$ 550 G can also be seen. The magnetic field scan in (b) covers a narrower range, has a higher density of measurements, and shows the survival fraction calculated from wait times of 2 s and 50 ms. The 550 G resonance is now obvious.

We saw a broad decay resonance at 680 G, near the predicted Feshbach resonance (800 G) and also *discovered* a narrow one at 550 G [4]. Although our decay peak for the broad feature occurred more than 100 G away from the predicted value [110], it was still within the predicted (unusually large) width (Fig. 5-1(b)). Our observation of a decay resonance at 550 G was followed soon after by the prediction of a narrow Feshbach resonance at this field value [106]. The older and the newer theoretical predictions are displayed in Fig.5-3. Our measurements therefore experimentally located two *s*-wave Feshbach resonances in the $|1\rangle - |2\rangle$ mixture.

The new theoretical prediction (Fig. 5-3(b)) benefitted from a careful measurement of the zero-crossing of a_{12} (at $\sim$ 530 G) by a group at Duke university[106]. The zero-crossing

was measured independently and with good agreement by a group at Innsbruck [107]. The field dependent losses for the wide resonance were also observed (almost simultaneously) in the Duke group [106] as well as (later) by the Paris group [111].
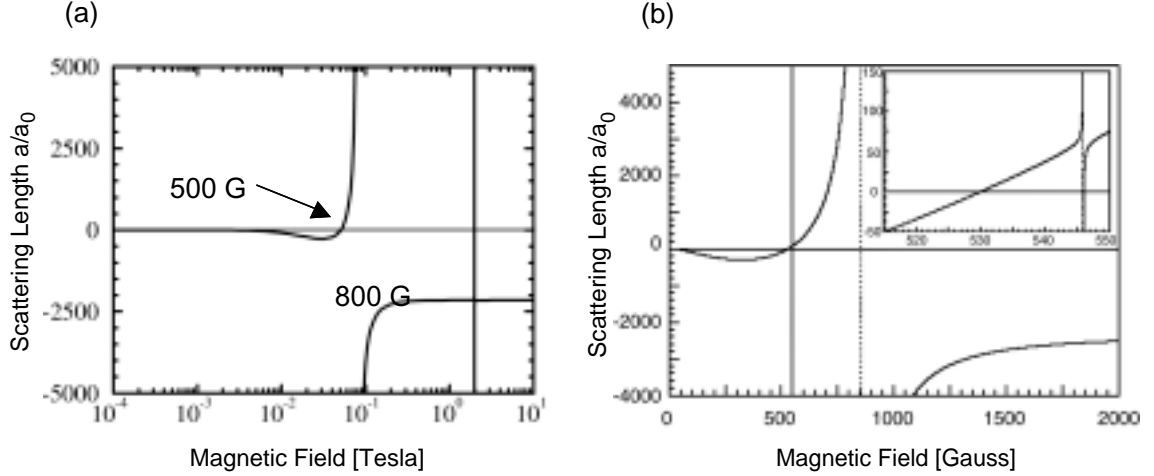
Figure 5-3: (a)Old prediction and (b)New prediction of s-wave Feshbach resonances between states $|1\rangle$ and $|2\rangle$. Figure (a) from reference [110] and Figure (b) from reference [106]. Note that (a) has a logarithmic x-scale, while (b) has a linear x-scale.

5.1.2 Decay Curves on resonance

The nature of the decay was studied by monitoring the system at various wait times for the same magnetic field. The decay curves obtained at $680\,\mathrm{G}$ is shown in Fig. 5-4. For a two-body (three-body) process, the loss rate of atoms $\dot{n}$ is proportional to n^2 (n^3), where n is the atomic density. For our modest degeneracies (in this experiment $T \sim T_F$), the density distribution is essentially classical and therefore should be *proportional* to atom number N, provided the temperature does not change. Thus $\dot{N}$ should be proportional to N^2 (N^3), for a two-body (three-body) process. This means that two-body processes should show a linear dependence of $1/N$ with time, while three-body processes should show a linear dependence of $1/N^2$ with time. The measurements shown in Fig. 5-4 are consistent with a two-body decay mechanism. Changes in temperature during decay which would invalidate our analysis were hard to characterize because of the low signal-to-noise as the cloud decayed[1].

---

[1]It can be shown that for a $T = 0$ Fermi gas, keeping track the changing volume due to atom loss actually results in $1/N$ changing linearly in time for a 3-body process. This was pointed out to us by Jean Dalibard.
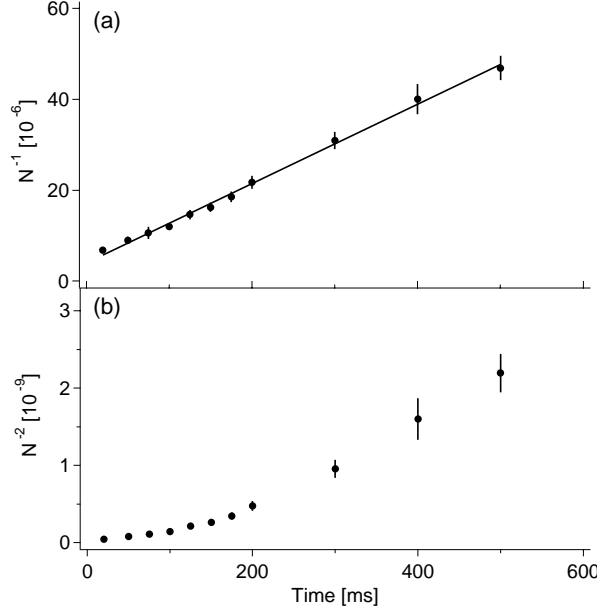
Figure 5-4: Decay of the atom number at $680\,\mathrm{G}$. (a) The data plotted as $1/N$ show a linear time dependency, consistent with two-body decay. (b) The same data plotted as $1/N^2$ clearly show non-linear dependency, inconsistent with three-body decay. For the resonance at $550\,\mathrm{G}$, the comparison of least square fits also revealed consistency with a two-body decay.

5.2 Loss Mechanism

Two questions naturally arise from our results:

(1) what is the collision process responsible for the observed decay?

(2) why is the loss peak shifted such a large amount in magnetic field ($> 100\,\mathrm{G}$) from the (predicted) divergence of the s-wave scattering length?

Let's examine question (1). The $|1\rangle - |2\rangle$ combination is immune to spin-exchange losses as well as dipolar losses in an incoming s-wave channel (Section 3.4). The leading inelastic 2-body collision which could contribute to the observed losses is then dipolar decay in an incoming p-wave channel. Our ultracold temperatures would highly suppress such a process. It is still possible that such a process contributes, for example in the presence of a p-wave Feshbach resonance [112]. However, theorists have concluded that there are no such resonances in the relevant magnetic field region[101]. The possibility of a non-resonant p-wave process being enhanced by the s-wave resonance as a collisional cascade is also unlikely because the shape of the loss curve deviates strongly from the predicted shape of the s-wave scattering cross-section (Fig. 5-3 and Eqn. 3.10).

Resonant enhancement of 3-body decay near a 2-body Feshbach resonance is another possibility. This mechanism may also answer question (2). As argued by Petrov [92], if the

binding energy released upon formation of the molecule does not exceed the trap depth, the 2 collision products (molecule + 3$^{\text{rd}}$ atom) can remain trapped. For large and positive a_{12}, the binding energy is positive and is given near resonance by the relation ([93]):

$$\epsilon_{\text{bind}} = \frac{\hbar^2}{ma_{12}^2} \tag{5.1}$$

This means that the energy released is smaller closer to the divergence of a_{12} (as the bound state tunes closer to threshold). The scattering length at which the loss should peak is then related to the trap depth U_{trap} as:

$$a_{\text{loss}} \sim \hbar/\sqrt{mU_{\text{trap}}}. \tag{5.2}$$

For our experimental trap depth, this corresponds to a field of $\sim 620\,\text{G}$, in the ballpark of the measured value. Currently, we believe that this 3-body loss mechanism is the most probable cause of the observed decay. The position of the same loss resonance observed by a group in Paris shows agreement with Eqn. 5.2[111]. This group has also observed a dependence of the position of the decay peak with trap depth [113].

The temporal behavior of the decay (Fig. 5-4) follows the characteristics of a two-body process rather than a three-body process. It is possible that near the resonance, long-lived $|1\rangle - |2\rangle$ quasi-bound states are formed (step 1) which can collide with either single spin state in a three-body process (step 2). Since the quasi-bound state is long-lived, it would take a long time to form. The timescale for this overall process would then be determined by step (1) and the subsequent decay rate would have the characteristics of a two-body process. Such a 2-step mechanism has been discussed in the context of recombination processes in spin-polarized atomic hydrogen [114].

5.3 Outlook

Our experiment proves that the $|1\rangle - |2\rangle$ mixture is stable on a timescale of $100\,\text{ms}$ for all magnetic fields of interest and for typical densities of a few times $10^{13}\,\text{cm}^{-3}$. If resonance high-T_{c} superfluidity (Section 3.5) were to occur, the gap energy $\hbar\Delta$ would be $\sim (0.5k_BT_F)$. This should give the relevant timescale for the formation of the superfluid as $1/\Delta < 1\mu\,\text{s}$, for our typical parameters. The magnitude of this timescale relative to our loss timescale bodes well for the realization of superfluidity in the ^{6}Li system.

The experiment reported in this chapter represents our first observations of interacting fermions. Since then, the apparatus has been upgraded in several ways. As of the end of 2002, we had implemented new magnetic coils, high-field and multiple-state imaging, as well as a new sympathetic cooling scheme which increased our atom number a hundred-fold (see Chapter 4). The experimental results reported in the rest of this thesis were performed using the improved apparatus.

Chapter 6

Collisions in zero temperature Fermi Gases

This chapter focuses on the theoretical results reported in the following paper:

- *S. Gupta, Z. Hadzibabic, J.R. Anglin and W. Ketterle, "Collisions in Zero Temperature Fermi Gases" [8]. Included in Appendix D. e-print available at arXiv:cond-mat/0307088.*

A simple and useful tool to diagnose the behavior of trapped atomic gases is to release them suddenly from their confines and observe the evolution of the spatial density. This merely involves switching off the magnetic or optical trap and subsequently imaging the atom cloud with near-resonant light - features which usually come for free during setup of an atom trapping experiment. This is a fundamentally new knob that atomic physicists possess over their traditional condensed matter counterparts. Hydrodynamic expansion from an anisotropic trap results in a reversal of anisotropy after a sufficiently long time (several radial trapping frequencies). This arises due to the different pressure gradients along different directions. The "smoking gun" demonstration of an interacting BEC is the observation of anisotropic hydrodynamic free expansion. This chapter deals with the behavior of interacting Fermi gases during free expansion.

Considerable excitement was generated in the ultracold atom field with the observation of anisotropic hydrodynamic expansion of an interacting Fermi gas [86]. This had followed rapidly in the wake of the theoretical prediction that a fully superfluid Fermi gas would expand hydrodynamically (just like its bosonic counterpart) [115]. This idea necessarily needs to be modified with the idea of classical hydrodynamics in a strongly interacting system [116]. Interacting Fermi gases realized near Feshbach resonances can be collisionally hydrodynamic because of the large cross-section for incoherent collisions (Section 3.2.3). This has been observed in various groups [86, 117, 111] as well as by us (unpublished, Section 6.2). The distinction (if any) between classically collisional and superfluid behavior hinges critically on the role of Pauli blocking for degenerate fermions.

A highly degenerate Fermi gas is of course almost collisionless in the trap, even in the vicinity of a Feshbach resonance. However this Pauli suppression of collisions breaks down when an interacting system is released from a spatially anisotropic atom trap. Even in a zero temperature Fermi gas, the expansion deforms the Fermi surface and allows collisions to take place. We have found theoretically that more than half the classically allowed collisions can take place for highly anisotropic traps [8].

In this chapter, I first introduce the standard theoretical treatment for analyzing the expansion behavior of atomic gases. I then present our data exhibiting hydrodynamic expansion of a strongly interacting Fermi gas. Finally, I discuss our theoretical results regarding the collisional behavior of degenerate Fermi gases which are detailed in the paper attached (Appendix D, [8]).

6.1 Free Expansion of Atomic Gases

6.1.1 Expansion of non-degenerate gases

The expansion of classical Boltzmann gases, Bose gases above T_c, as well as Fermi gases in the normal (non-superfluid) phase, can be described by means of a scaling formalism [116, 118]. This theory is valid in the semi-classical limit, where the thermal energy is large compared to the separation between the energy eigenvalues of the potential.

The Boltzmann-Vlasov equation can be used to describe the dynamics of the phase-space distribution $f(\mathbf{x}, \mathbf{p}, t)$:

$$\frac{\partial f}{\partial t} + \frac{\mathbf{p}}{m} \cdot \frac{\partial f}{\partial \mathbf{x}} - \frac{\partial (U_{\mathrm{h}} + U_{\mathrm{mf}})}{\partial \mathbf{x}} \cdot \frac{\partial f}{\partial \mathbf{p}} = \Gamma_{\mathrm{coll}}[f] \tag{6.1}$$

This is simply the standard Boltzmann equation [77] with the addition of the mean-field potential U_{mf}. U_{h} is the harmonic trapping potential. The right hand side is the usual Boltzmann collision integral. Free expansion distorts the local phase space distribution while collisions try to preserve the local equilibrium. The local equilibrium corresponds to an isotropic thermal distribution where all the local quantities of Chapter 3 can be defined. In the limit of no collisions, $\Gamma_{\mathrm{coll}}[f] = 0$, we obtain the equations of ballistic expansion. For cylindrically symmetric traps (frequencies $\omega_\perp, \omega_z$), the aspect ratio (radial size/axial size) is given by:

$$A_{\mathrm{ballistic}}(t) = \frac{\omega_z}{\omega_\perp} \sqrt{\frac{1 + \omega_\perp^2 t^2}{1 + \omega_z^2 t^2}} \tag{6.2}$$

This will be derived in Section 6.3. An initially anisotropic cloud approaches spatial isotropy as $t \to \infty$. The final spatial distribution mirrors the initial momentum space isotropy.

In the opposite limit, where the collision timescale is shorter than all the other timescales in the system, the local phase space distribution f is always in equilibrium and isotropic.

One then obtains the classical hydrodynamic scaling solutions [116, 118]:

$$\ddot{b}_i = \frac{\omega_i^2}{(b_x b_y b_z)^{2/3} b_i}$$

$$(6.3)$$

where b_i is the scaling parameter in the i direction. The spatial distributions retain their original form (Gaussian, Bose-Einstein, or Fermi-Dirac) but get scaled in size linearly by the b_i's. For cylindrically symmetric traps, the aspect ratio during expansion is:

$$A_{\text{hydro}}(t) = \frac{\omega_z}{\omega_\perp} \frac{b_\perp(t)}{b_z(t)}.$$

$$(6.4)$$

The collision rate competes with the inverse trap frequency to determine whether the gas expands ballistically or hydrodynamically. Comparing the collision rate with the inverse trap frequency is equivalent to comparing the collisional mean free path with the initial size of the cloud. Collisional hydrodynamics ensues when the mean free path is much smaller than the cloud size.

The expansion behavior of gases in the (experimentally relevant) regime between ballistic and hydrodynamic has only recently been examined using an extension of the scaling analysis [118]. However, the case of ultra-degenerate normal fermionic gases (where Pauli blocking becomes important) is not covered by this analysis. Our work (Section 6.3) provides some rudimentary results in this regime.

6.1.2 Expansion of Superfluid Gases

The hydrodynamic equations of superfluids are applicable if the healing length is much smaller than the size of the sample [115]. This implies that the whole system behaves similar to a superfluid. The hydrodynamic description is based on the equation of continuity:

$$\frac{\partial}{\partial t} n + \frac{1}{m} \frac{\partial}{\partial \mathbf{x}} (n\mathbf{p}) = 0,$$

and on the Euler equation:

$$\frac{\partial \mathbf{p}}{\partial t} + \frac{\partial}{\partial \mathbf{x}} [\mu(n) + U_{\text{h}} + \frac{p^2}{2m}] = 0$$

where $\mu(n)$ is the chemical potential of a uniform gas calculated at the density n. If the equation of state is a power law $\mu \sim n^\gamma$, then the above equations have scaling solutions during expansion. If the Thomas-Fermi radii evolve according to $R_i(t) = R_i(0) b_i(t)$, then the scaling parameters b_i obey [115]:

$$\ddot{b}_i = \frac{\omega_i^2}{(b_x b_y b_z)^\gamma b_i}$$

$$(6.5)$$

For a BEC,

$$\mu \sim n^1, \qquad \gamma = 1,$$

[73]. For a Fermi superfluid, the authors [115] use

$$\mu \sim n^{2/3}, \qquad \gamma = 2/3,$$

the relation in a normal gas at zero temperature[1]. The scaling prediction for a classical gas and a superfluid Fermi gas in the hydrodynamic limit are then identical (Eqn. 6.3). Note that the prediction for a BEC is different. However, this difference only becomes significant in pancake shaped traps and is negligible in cigar shaped traps [116].

For cylindrical geometries, defining $\tau = \omega_\perp t$, $\lambda = \frac{\omega_z}{\omega_\perp}$ (initial aspect ratio) and for $\gamma = 2/3$, we get the non-linear differential equations:

$$\frac{d^2 b_\perp}{d\tau^2} \;\; = \;\; \frac{1}{b_\perp^{7/3} b_z^{2/3}} \qquad\qquad (6.6)$$

$$\frac{d^2 b_z}{d\tau^2} \;\; = \;\; \frac{1}{b_\perp^{4/3} b_z^{5/3}}. \qquad\qquad (6.7)$$

These equations can be solved numerically quite easily in Mathematica.

6.2 Observation of hydrodynamic expansion in a strongly-interacting Fermi gas mixture

Anisotropic expansion of interacting Fermi gases out of a cylindrically symmetric trap have been observed recently by several groups [86, 117, 111]. We have also observed this phenomenon. Fig. 6-1 shows simultaneous absorption images of states $|1\rangle$ and $|2\rangle$ at different times-of-flight after release from our cylindrically symmetric optical trap in a regime of strong interactions (900 G). The reversal of anisotropy during expansion is obvious.

The expansion data were fitted with 2-D gaussians. The resulting aspect ratio is plotted in Fig. 6-2. Also shown are the expectations from ballistic and hydrodynamic scaling (Eqns. 6.2, 6.4 and 6.6 solved for $\gamma = 2/3$ using Mathematica). Clearly, we are deep in the hydrodynamic regime.

The classical collision rate is given by $\Gamma_{\rm Cl} = n\sigma v$ where n is the density, σ is the scattering cross-section and v is the relative velocity. During the expansion, the density drops and the expansion of strongly interacting systems falls out of the hydrodynamic regime very quickly. However in the unitarity limit, the scattering cross-section also changes with the density. Eqn. 3.12 gives $\sigma \sim 1/k_F^2 \sim 1/n^{2/3}$, where k_F is the local Fermi momentum.

---

[1]The difference essentially stems from the fact that a BEC has essentially 0 kinetic energy and μ is dominated by the mean field interaction energy proportional to n and the fermion kinetic energy is set by the Fermi energy proportional to $n^{2/3}$.
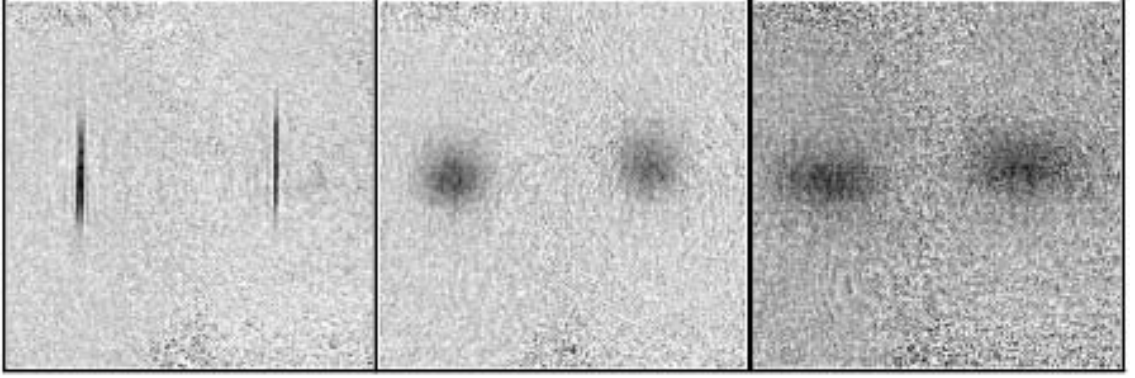
Figure 6-1: Anisotropic expansion of ^{6}Li from the optical trap at $900\,\text{G}$ (about 1.5 million atoms in each state). The atoms were cooled for $500\,\text{ms}$ at $900\,\text{G}$. This lowered the temperature from $\sim T_F$ to $\sim 0.5\,T_F$. (a) in trap, (b) $900\,\mu s$ TOF, (c) $1500\,\mu s$ TOF. The reversal of the anisotropy is obvious. States $|1\rangle$ and $|2\rangle$ are imaged simultaneously as explained in Section 4.4.

The relative velocity scales as $v \sim k_F \sim n^{1/3}$. This gives $\Gamma_{\text{Cl}} = n\sigma v \sim n^{2/3}$. When the system is unitarity limited, the scattering rate actually drops slower during expansion and hydrodynamic conditions can be maintained for longer expansion times. This $n^{2/3}$ drop is maintained until the local Fermi momentum no longer satisfies $ak_F \gtrsim 1$. Thereafter, the usual scaling with n is restored.

6.3   Expansion of a zero temperature Fermi gas

I now discuss collisions in zero temperature Fermi gases. The manuscript attached as Appendix D [8] presents our results in great detail. This section is meant to be a supplement to that presentation. I only summarize the major aspects of the paper and detail some subtleties.

6.3.1   Momentum Space Fermi Surface

The momentum space Fermi surface can be constructed by using the simplification allowed by zero temperature Heaviside distribution functions and harmonic traps. The local Fermi surface is then a sphere in the trap:

$$\Sigma_i p_i^2/2m = E_F - \Sigma_i m\omega_i^2 x_i^2/2, \tag{6.8}$$

which deforms into an ellipsoid during time-of-flight:

$$\Sigma_i \frac{(1+\omega_i^2 t^2)}{2m}\left(p_i - \frac{mx_i}{t}\frac{\omega_i^2 t^2}{1+\omega_i^2 t^2}\right)^2 = E_F - \Sigma_i \frac{m\omega_i^2 x_i^2}{2(1+\omega_i^2 t^2)}, \tag{6.9}$$
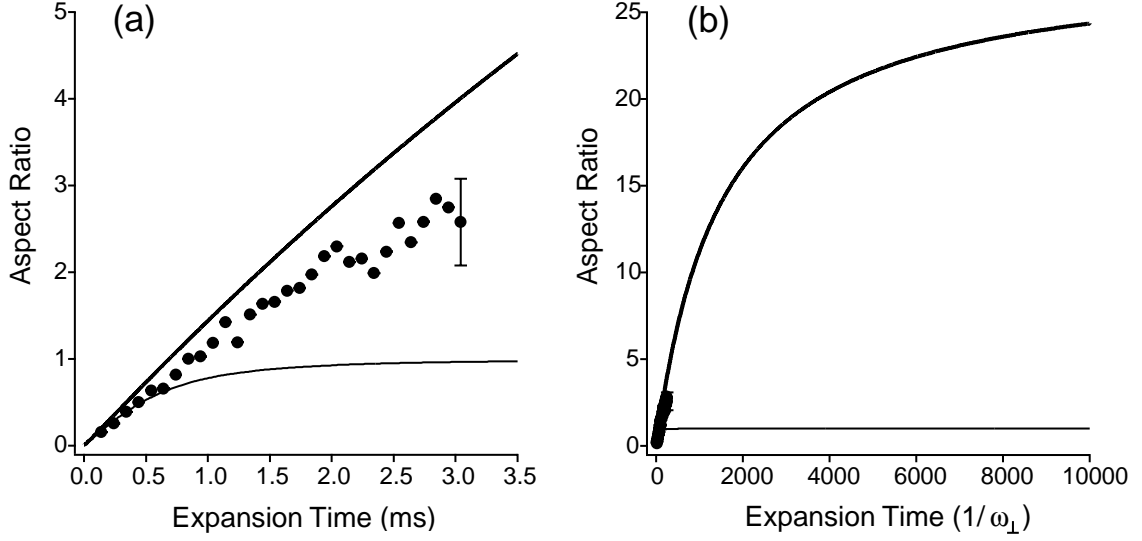
Figure 6-2: Aspect ratio vs time for the conditions of Fig.6-1. (a) shows the measured aspect ratio as a function of time of flight up to $\sim 3\,\mathrm{ms}$ for an initial aspect ratio $\lambda = 0.015$ (our trap). For the longest expansion times, the aspect ratio climbs up to > 2.5. The lines are theoretical predictions for 2W power, and $16\,\mu\mathrm{m}$ waist giving trapping frequencies of $13.2\,\mathrm{kHz}$ and $197.6\,\mathrm{Hz}$. $1\,\mathrm{ms}$ then corresponds to $\omega_\perp t \sim 83$ inverse radial trapping frequencies. (b) shows the asymptotic behavior expected from hydrodynamics. The calculated aspect ratio grows strongly even after several thousand inverse trapping times! The asymptotic aspect ratio expected from full hydrodynamic scaling is $\sim 0.38/\lambda \sim 25$ [119].

via the ballistic property $\mathbf{x}(0) = \mathbf{x}(t) - \mathbf{p}t/m$. For a cylindrically symmetric trap, the momentum space aspect ratio is:

$$\sqrt{\frac{1 + \omega_z^2 t^2}{1 + \omega_\perp^2 t^2}}. \tag{6.10}$$

Fig. 6-3(a,b) shows an example of this variable aspect ratio (or deformation).

This momentum space picture allows a direct calculation of the spatial density. Using $\int dx\,dp = h$, the phase-space volume for a quantum state in 1-D, the volume for N fermions is $\int d^3x\,d^3p\,f(\mathbf{x}, \mathbf{p}, t) = h^3 N$. The spatial density is simply the integral of the phase space distribution over momentum space with the appropriate $1/h^3$ factor. Thus:

$$
\begin{aligned}
n(\mathbf{x}, t) &= \frac{1}{h^3} \int d^3p\ f(\mathbf{x}, \mathbf{p}, \mathbf{t}) \\
&= \text{volume of momentum ellipsoid} \\
&= \frac{4}{3}\pi\ \text{product of semi} - \text{axes} \\
&= \frac{4}{3}\pi \left(\frac{2mE_F}{h^2} \right)^{3/2} \frac{(1 - \frac{m}{2E_F}\Sigma_i \frac{\omega_i^2 x_i^2}{1+\omega_i^2 t^2})^{3/2}}{\Pi_i(1 + \omega_i^2 t^2)^{1/2}},
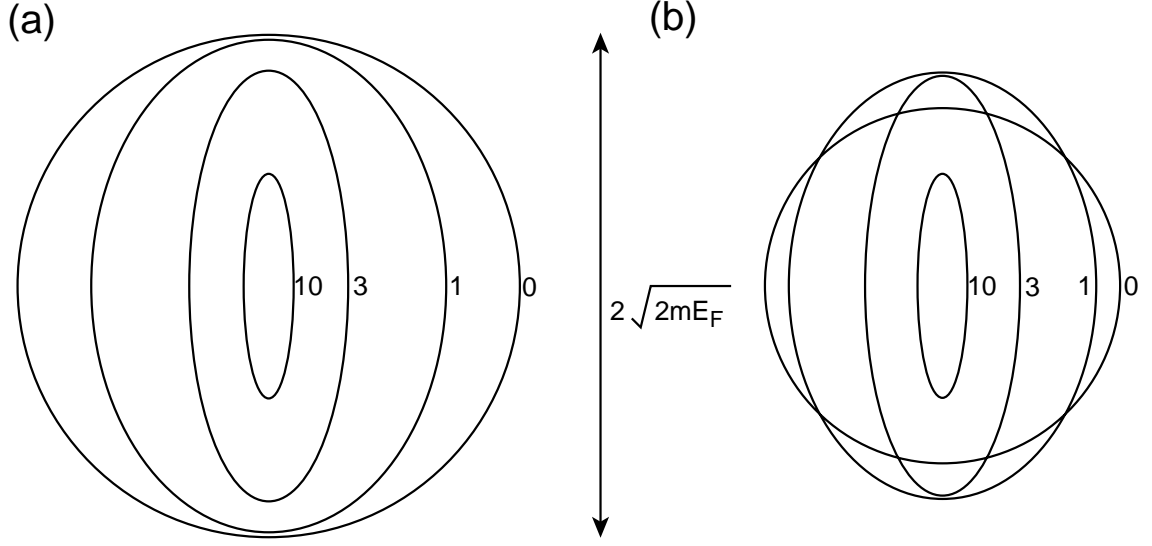\end{aligned}
\tag{6.11}
$$

Figure 6-3: (a) Deformation of the momentum space Fermi surface at $\mathbf{x} = \mathbf{0}$, from a sphere to an ellipsoid during expansion from an anisotropic harmonic trap. The case of cylindrical symmetry is shown, where the three-dimensional distribution is symmetric about the vertical axis. The parameters chosen are an aspect ratio $\lambda = 0.2$ and expansion times $\omega_\perp t = 0,1,3$ and 10. (b) The deformation at a position radially displaced by $\sqrt{E_F/m\omega_\perp^2}$. Note that the central momentum also changes with time for $\mathbf{x} \neq \mathbf{0}$ (Eqn. 6.9), an effect which is not shown in the figure. However, this has no effect on the collision rate.

as in Eqn 3.5. Notice that for long times, the spatial aspect ratio goes to 1 as expected for ballistic expansion and with the scaling given by Eqn. 6.2.

6.3.2 Collisions in the Perturbative Limit

For a two-spin system interacting with a finite s-wave scattering cross-section σ, the collision integral of Eqn. 6.1 can be written as:

$$\Gamma(\mathbf{x}, \mathbf{p_1}, t) = -\frac{\sigma}{4\pi h^3} \int_{(\mathbf{x},t)} d^3 q_1 d^2\Omega \frac{|\mathbf{p_1} - \mathbf{q_1}|}{m} \times \tag{6.12}$$
$$[f(\mathbf{p_1})f(\mathbf{q_1})(1 - f(\mathbf{p_2}))(1 - f(\mathbf{q_2})) - f(\mathbf{p_2})f(\mathbf{q_2})(1 - f(\mathbf{p_1}))(1 - f(\mathbf{q_1}))]$$

Eq. 6.12 has a σ in front, integrates over the momentum ellipsoid and has the relative velocity in the integrand. It thus has the general form $n\sigma v$, a collision rate. The collision integral takes into account the availability of final states (the $(1 - f)$ terms), the basis of Pauli blocking. Fig. 6-4(a) shows the geometrical representation of elastic collisions in the local phase space picture. Collisions have the tendency to restore the deformed Fermi surface into a spherical shape corresponding to an equilibrium Fermi-Dirac distribution[2].

---

[2]The concept of Pauli blocking removal by ballistic expansion can be applied also to other situations such as p-wave collisions in a single-spin system.
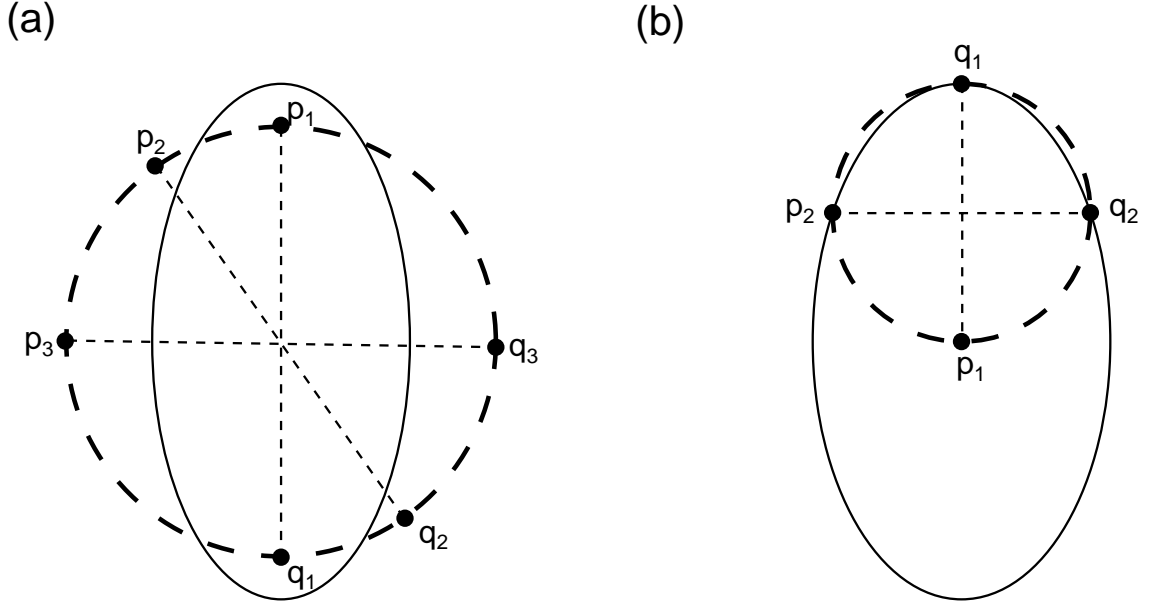
(a)

(b)

Figure 6-4: Geometrical representation of collisions in momentum space. (a) The two spin states have identical distributions and are labelled with $\mathbf{p}$ and $\mathbf{q}$. The deformation of the Fermi surface into an ellipsoid opens up final states for scattering. The processes $\mathbf{p_1} + \mathbf{q_1} \to \mathbf{p_2} + \mathbf{q_2}$ and $\mathbf{p_1} + \mathbf{q_1} \to \mathbf{p_3} + \mathbf{q_3}$ are examples of allowed collisions in a zero-temperature gas. (b) For collisions involving $\mathbf{p_1}$ at the center of the ellipsoid (calculation done in the paper), a minimum deformation of $1 : \sqrt{3}$ is needed before energetically accessible final states become available. The process $\mathbf{p_1} + \mathbf{q_1} \to \mathbf{p_2} + \mathbf{q_2}$ is among the first contributing collisions as a function of increasing deformation (all final states on the horizontal ring formed by rotating $\mathbf{p_2} - \mathbf{q_2}$ about $\mathbf{p_1} - \mathbf{q_1}$ as well as the symmetric ring in the lower hemisphere start contributing simultaneously).

One can work out the collision integral of Eqn. 6.12 corresponding to ellipsoids for different ballistic expansion times (Eqn. 6.9) using numerical integration in Mathematica. This forms a perturbative result for the collision rate and the effects of Pauli blocking. The result for $\Gamma(\mathbf{0}, \mathbf{0})$ is shown in Fig. 6-5. This is compared to the result neglecting Pauli blocking (setting all the $(1 - f)$ terms to zero, $\Gamma_{\mathrm{Cl,p}}$ in the figure). Fig. 6-5(b) shows that as the initial aspect ratio λ approaches 0 (high anisotropy), the total number of collisions allowed by Fermi statistics approaches ~ 0.55 of the number neglecting Pauli blocking. This of course shatters the assumption of high Fermi degeneracy suppressing collisions during expansion. Zero temperature Fermi gases can collide strongly during expansion.

Two aspects of the calculation are now explained. The fact that the collision rate abruptly rises from zero at a finite expansion time in Fig. 6-5(a) is because a minimum deformation is needed before the center of the ellipsoid $(\mathbf{0}, \mathbf{0})$ can collide with any other point in the momentum ellipsoid (Fig. 6-4(b)). From the figure, one easily sees that this point corresponds to an aspect ratio $\sqrt{3}$ (simple coordinate geometry). Using this relation
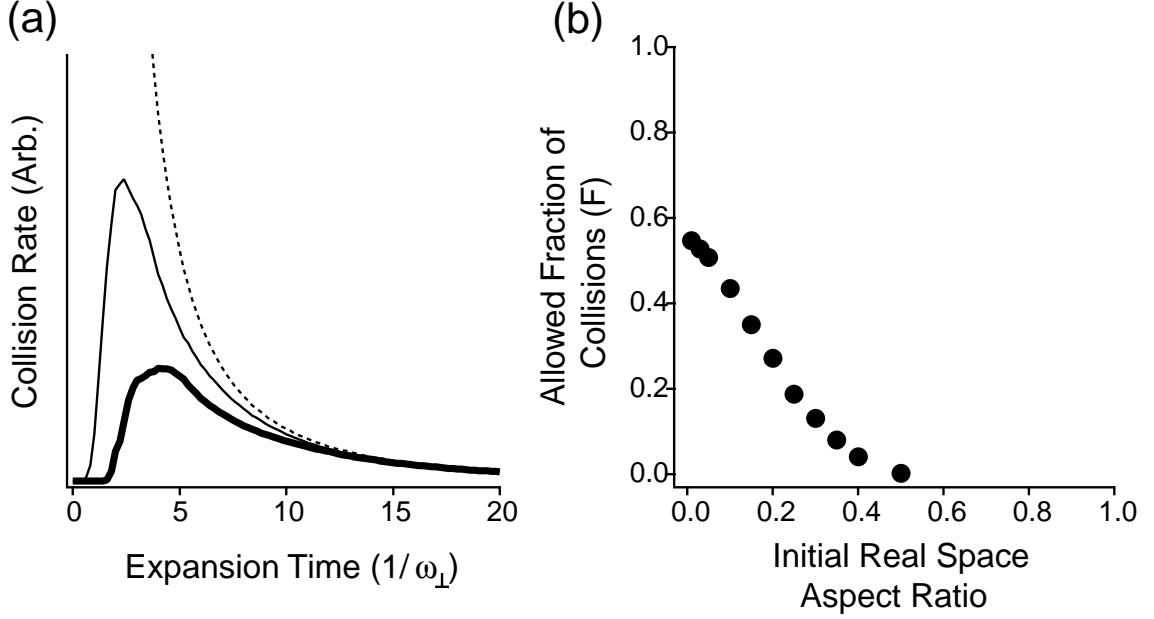
Figure 6-5: (a) Collision rate as a function of expansion time in the perturbative approximation for the initial aspect ratio $\lambda = 0.03$. Dashed line - total classical collision rate Γ_{cl}, thin line - $\Gamma_{\mathrm{cl,p}}$, thick line - Γ. Γ and $\Gamma_{\mathrm{cl,p}}$ are defined in the text. Γ_{cl} is defined as the first term on the right-hand-side of Eqn. 6.12 with the $1 - f$ factors artificially set to 1 and corresponds to what is usually called the classical collision rate. The displayed rates were evaluated at $\mathbf{x} = \mathbf{0}$ and $\mathbf{p} = \mathbf{0}$ and give an effective upper bound on the Fermi suppression. (See Appendix D for details). (b) Allowed fraction of collisions $F(\lambda)$ for a zero-temperature two-spin Fermi gas. For an initial aspect ratio $\lambda = 0.05$, F is 0.5. For large anisotropy ($\lambda \to 0$), F approaches ~ 0.55.

in Eqn. 6.10, one can solve to get $\omega_\perp t = \tau = \sqrt{\frac{2}{1-3\lambda^2}}$. For $\lambda = 0.03$, this dimensionless time is $\sim \sqrt{2} \sim 1.4$, in agreement with the calculation (Fig. 6-5(a)). A similar reasoning explains why the collision rate in Fig. 6-5(b) rises above zero only below a finite λ. The critical time of $\omega_\perp t = \tau = \sqrt{\frac{2}{1-3\lambda^2}}$ is never reached when the denominator is imaginary i.e., for $\lambda \gtrsim 0.58$ (in agreement with the figure). A calculation summing the contribution over all $\mathbf{p_1}$ would smoothen the rise of both these curves from $t = 0$ (Fig. 6-5(a)) and $\lambda = 1$ (Fig. 6-5(b)).

6.3.3 Perturbation from Hydrodynamic Behavior

For a strongly-interacting system, one can look at the effect of expansion deformation as a perturbation on the isotropy required by local equilibrium. The expansion-driven anisotropy is damped (strongly) by collisions. James Anglin, our local theorist, found to lowest order in the momentum space anisotropy, the zero temperature collisional response of the Fermi-Dirac distribution to the deformations of time-of-flight. His result is included in the manuscript attached in Appendix D [8]. A more quantitative calculation with enough

detail to differentiate between superfluid and collisional hydrodynamics in expansion may warrant a re-examination of the current expansion data available in different laboratories. This remains a theoretical goal in the field.

6.4 Concluding Thoughts

The easy to use diagnosis of time-of-flight expansion and absorption imaging turns out not to be a qualitative tool for distinction between superfluid and normal gases in the strongly-interacting regime. However, if the collisional hydrodynamics contribution could be discarded by working away from Feshbach resonances and thus lowering the collisional cross-section, then hydrodynamic behavior could be unambiguously interpreted as a signature of superfluidity. However, as Section 3.5 discusses, the low temperatures that would then be required are way beyond current experimental possibilities.

The last section alluded to the theoretical goal of obtaining a full description of the collisional expansion of a normal gas in order to find quantitative differences from the behavior of a superfluid. This approach also requires a full understanding of the expansion of a superfluid. If for example, the pairing only takes place near the Fermi surface, then the whole system may not behave hydrodynamically, thus negating the approach of [115] and modifying the hydrodynamic predictions for superfluids. These are hard questions for the theoretical community to resolve. The experimentalists have moved on to explore other possible signatures for fermionic superfluidity, such as those involving radio-frequency techniques (next chapter).

Hydrodynamic behavior also manifests itself in the shift of collective oscillation frequencies [120, 116, 118]. This can also be used to measure the transition from collisionless to hydrodynamic behavior [121]. This is of course a more difficult measurement than free expansion. However, Pauli blocking *is* important in the trap. Evidence of in-trap hydrodynamic behavior at ultra-low degeneracy may therefore indeed be proof of superfluidity. At least one experimental group is currently pursuing such experiments [122].

Chapter 7

RF Spectroscopy of Ultracold Fermions

This chapter focuses on the experiments reported in the following publication:

- *S. Gupta, Z. Hadzibabic, M.W. Zwierlein, C.A. Stan, K. Dieckmann, C.H. Schunck, E.G.M. van Kempen, B.J. Verhaar and W. Ketterle, "RF Spectroscopy of Ultracold Fermions" Science* **300**, *1723 (2003) [5]. Included in Appendix E.*

Radio-frequency(RF) spectroscopy has been a valuable tool for atomic physicists for several decades since Fermi and Rasetti introduced it in 1925 [123]. The technology to produce and manipulate these frequencies is now standard (Chapter 4).

The extension of RF spectroscopy to ultracold fermions (Boulder - ^{40}K [117], MIT - ^{6}Li [5]) was motivated by the possibility of studying the strong interactions near Feshbach resonances with the sensitivity and ease of RF methods. In addition to being sensitive to interactions in normal Fermi gases, RF probes may also be able to detect the superfluid phase [124, 125, 126].

Using RF methods, we observed a number of effects in ultracold Fermi gases which are described in this chapter:

(1) In the s-wave regime, an RF transition in spin-polarized fermions is unshifted in frequency from the single particle resonance. Our observation of this effect verifies this simple yet startling hypothesis and also opens the door for future atomic clocks based on fermions. The current standard based on bosons is limited by interaction "clock" shifts. We have also demonstrated the absence of interaction shifts in a two-spin mixture of fermions [7, 12].

(2) Interactions between fermions can be measured by forming a statistical mixture of two spin states and then driving transitions to a third state. Using a mixture of the two lowest hyperfine states and driving transitions from the second to the third hyperfine state, we were able to map out interactions in ^{6}Li as a function of magnetic field.

(3) At ultracold temperatures ($kR \ll 1$), these interactions are proportional to the s-wave scattering length a, for small a. At an s-wave Feshbach resonance, where a diverges, we leave the dilute gas approximation. Using RF methods we observed saturating of the interaction energy at a large *negative* value regardless of the sign of the two-particle scattering length a. Although this result is not yet fully understood, it is consistent with some many-body theory predictions in the $ka \gg 1, kR \ll 1$ regime (section 3.3) [83, 84, 85]).

7.1 Clock Shifts

Atomic clocks are based on the notion that the energy difference between eigenstates of isolated atoms are a constant of nature. The unit of time is then defined from the energy (frequency) difference between any two atomic eigenstates. In practice, two states are chosen whose energy difference is amenable to easy measurement with the least amount of perturbation from external sources. Perturbations can change the atomic resonance frequency resulting in a "clock shift". Researchers have now studied the systematics of such measurements to levels which allow probing of changes of fundamental constants, such as the fine structure constant α, which determines the separations between energy eigenstates [71].

Since 1967, the SI unit of time, the second, has been based on defining the ground-state hyperfine transition in ^{133}Cs to be $9\,192\,631\,770$ Hz. Currently, the best realization of the second is via Ramsey spectroscopy of this transition in laser cooled atomic fountains [71]. Laser cooled atoms are launched upwards and interact with a microwave field twice - once on its way up and once on its way down. This microwave field (~ 9 GHz) is generated by an external oscillator, like a quartz crystal[1]. This setup is analogous to the separated oscillatory fields of the Ramsey method [127, 128, 129]. The atoms are detected after the two interactions and the fractional populations in each state exhibit the usual Ramsey fringes as a function of microwave detuning. An error signal generated from these fringes is then fed back to the quartz crystal. The macroscopic oscillator (crystal) is thus locked to the microscopic oscillators (atoms). The crystal can now provide a standard of time based on an atomic transition.

Laser cooled clouds are of course composed of a large number of particles, rendering the isolated atom assumption flawed. Current experiments are sensitive to the mean field interaction arising from coherent collisions between atoms in the cloud. In fact, the mean field clock shift is the limiting systematic in current atomic clocks [130, 71]. Consider a bosonic atom with the hyperfine ground states $|1\rangle$ and $|2\rangle$. At ultracold temperatures, only s-wave interactions are allowed. Let the s-wave scattering lengths be a_{11}, a_{12} and a_{22}. Adopting the usual convention that positive scattering length a corresponds to a repulsive two-particle interaction, for a gas of $|1\rangle$ atoms at density n, the mean field shift of the

---

[1]more recently sapphire cryogenic oscillators are the external oscillators of choice.

transition is given by

$$\Delta\nu_B = \frac{2\hbar}{m}n(a_{12} - a_{11}).$$ (7.1)

S-wave interactions between atoms are in effect during the coherent drive to transfer state $|1\rangle$ to state $|2\rangle$. For a perturbative drive, we can neglect the density in state $|2\rangle$. Every atom transferred therefore needs an additional energy given by the difference in mean field energy of a state $|2\rangle$ atom in a bath of state $|1\rangle$ and a state $|1\rangle$ atom in a bath of state $|1\rangle$, as described by Eqn.7.1.
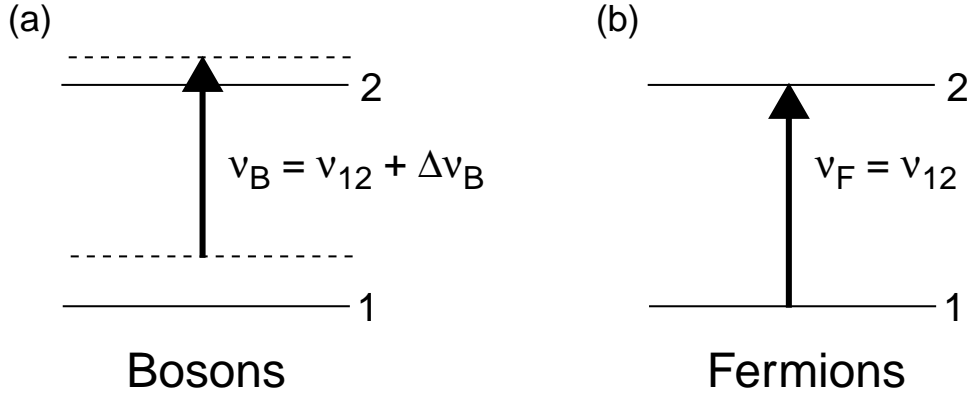

(a) $\nu_B = \nu_{12} + \Delta\nu_B$ Bosons

(b) $\nu_F = \nu_{12}$ Fermions

Figure 7-1: The difference in the clock shift for Bose and Fermi atoms. (a) In bosons, the s-wave interaction between identical particles shifts the initial and final states connected by the RF unequally. (b) In fermions, s-wave interactions cannot take place between identical particles and an RF drive then connects two states which have the same energy difference as in an isolated atom.

S-wave interactions are absent in spin-polarized fermions. A spin-polarized fermionic gas remains spin-polarized during a coherent drive and therefore no interactions take place between atoms. This results in an absence of the clock shift for ultracold fermions, $\Delta\nu_F = 0$. A schematic of this difference between the two types of fundamental particles is shown in Fig.7-1.

The error from the clock shift for bosons is at the level of 10^{-16} in current cesium clocks [71, 130], constituting the dominant systematic. Experiments with rubidium have a much lower contribution - ~ 50 times less [130, 71]. Efforts are underway to determine the overall feasibility of rubidium atomic clocks.

Gibble and Verhaar have pointed out the use of fermion clocks to suppress the mean-field shift problem [131]. The experiment described in the following subsection constitutes the first observation of this feature of fermions - the absence of the clock shift in a spin-polarized gas.

7.1.1 Absence of the Clock Shift in Fermions

For ease of applying RF methods, a transition must be chosen that is relatively insensitive to fluctuations of the magnetic field. For alkali bosons, the popular choice is the (appropriately named) "clock" transition $|I-1/2, 0\rangle \rightarrow |I+1/2, 0\rangle$, in the ground state hyperfine manifold, at near zero bias fields. The clock transition is first order magnetic field insensitive and therefore less prone to systematics from magnetic field fluctuations both in space and in time[2].

For alkali fermions, since I is always an integer, the state $|F, 0\rangle$ does not exist. However, one can find first order field independent transitions. For example, in ^{6}Li, the transition $|1/2, -1/2\rangle \rightarrow |3/2, +1/2\rangle$ is first order field independent at low fields (Fig. 4-8). However, for this particular case, the two states are not stable against spin-exchange, and would not be a practical system at high density. At large enough magnetic fields (above **I.J** decoupling), the electron spin dominates the splitting and the sublevels due to the nuclear spin are essentially parallel to each other within each electron spin level [3] (fig.4-8). We used the $|1\rangle \rightarrow |2\rangle$ transition at high field (see Chapter 4 for the magnetic field sensitivity of this transition). As argued in chapter 5, this is also a stable combination of states.

(a) (b)
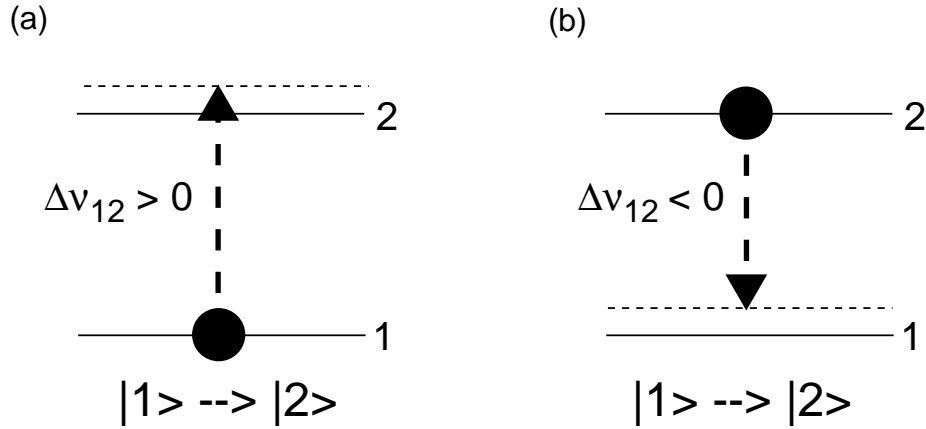
Figure 7-2: Shift in equilibrium energy in a 2-level Fermi system for (a) all the atoms in state $|1\rangle$ (b) all the atoms in state $|2\rangle$.

For bosons, the clock shift is usually determined by extracting the microwave frequency from the Ramsey fringes as a function of density [71]. Since this is linear in the density

---

[2]other options include the $|I-1/2, I-1/2\rangle \rightarrow |I+1/2, I-1/2\rangle$ transition in ground state alkalis. Though this is first order field insensitive, it is formally unstable against spin-exchange, the notable exception being ^{87}Rb [132, 133, 134].

[3]The Zeeman energy levels deviate from their simple linear form due to **I.J** decoupling which gives rise to the "Back-Goudsmit" linear levels at moderately high fields. These persist upto **L.S** decoupling, which in turn gives rise to the linear "Paschen-Back" levels at even higher fields.

(Eq. 7.1), the intercept of a straight line fit gives the unshifted value. The error bar on the slope then includes the error contribution from cold collisions.

Our approach to demonstrate the absence of the clock shift was based on measuring the resonance frequency of the $|1\rangle - |2\rangle$ system using a single oscillatory field (Rabi technique [135]). This technique is in general less sensitive than the two-pulse Ramsey method [127] but is quite adequate for our purpose. Varying the density of one of the states and measuring the (lack of) change in the transition frequency to the other state is a rather cumbersome task. We instead compared the transition frequency of the $|1\rangle \rightarrow |2\rangle$ transition and the $|2\rangle \rightarrow |1\rangle$ transition on identical pure state samples of $|1\rangle$ and $|2\rangle$ respectively. The expectation from assuming that the frequency is shifted by the equilibrium energies (for a perturbative transfer) is shown in Fig.7-2. For any finite scattering length a_{12}, equilibrium energies of the transferred atoms shift in the same direction (higher for positive scattering length). The spectra thus might be expected to shift in opposite directions. Our measurement then determines a suppression of this effect from the (small) difference in the two Rabi spectra.

Fig. 7-3(a) shows the Rabi spectra taken for the $|1\rangle \rightarrow |2\rangle$ and $|2\rangle \rightarrow |1\rangle$ transitions at 570 G. The pulse length used was $140\,\mu$s and dominates the broadening of the spectra. The scattering length a_{12} at this field is $\sim 150\,a_0$. The measurements were performed at a density of $3 \times 10^{13}\,\text{cm}^{-3}$. The equilibrium energy shifts are $\pm 5\,$kHz in this case. The Gaussian fits are separated by $0.04 \pm 0.35\,$kHz. The deduced suppression is then ≈ 30.
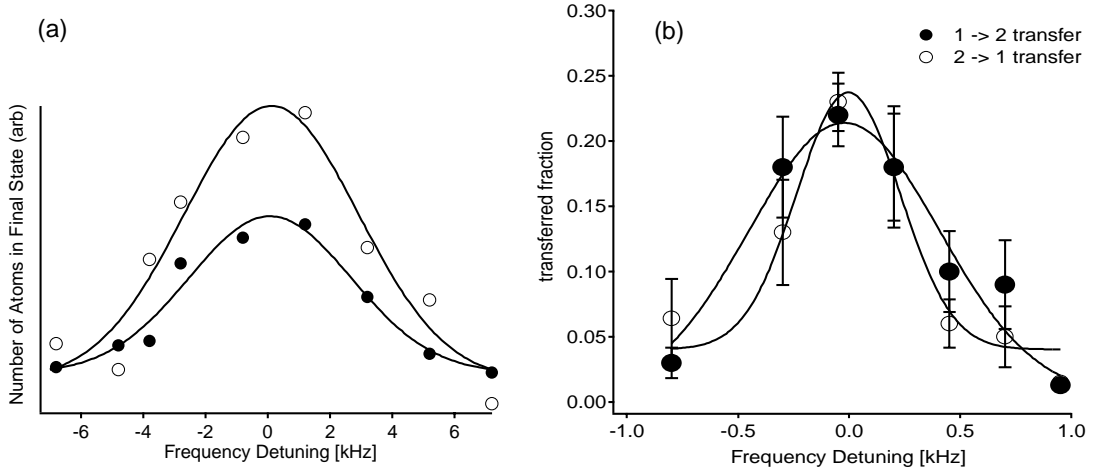
Figure 7-3: Absence of the clock shift in fermions. RF transitions were driven between states $|1\rangle$ and $|2\rangle$ on a system prepared purely in state $|1\rangle$ (filled circles), and purely in state $|2\rangle$ (open circles). (a) Experiment at 570 G. Mean-field interactions would result in 5 kHz shifts for the two curves in opposite directions. Gaussian fits (solid lines) to the data are separated by $0.04 \pm 0.35\,$kHz. This gives a clock shift suppression factor of 30. (b) Absence of clock shift at 860 G with three orders of magnitude suppression. The pulse length used is 1 msec which is responsible for the much narrower width than in (a). The magnetic field sensitivity $\partial\nu/\partial B$ is 0.5 kHz/G about 10 times lower than at 500 G, allowing the application of longer pulses and the correspondingly smaller widths.

Fig. 7-3(b) shows the suppression of the clock shift in a regime of unitary-limited interactions - 860 G, near the divergence of the bare scattering length [106]. In this unitarity limited interaction regime, one cannot use the bare scattering length a_{12} to estimate the interaction energy, as will be shown later. However, we can estimate the equilibrium energy from expansion measurements. Using the measurements of [111], and scaling to our parameters, we arrive at a suppression factor of more than three orders of magnitude.

For bosons, the intercept of the shift vs density line provides the clock transition frequency. Additionally, the slope of this line gives a relation for the scattering lengths in the system (Eq. 7.1). Such a measurement is of course impossible for fermions with coherent drives on a pure state. Since, our initial reason to pursue RF spectroscopy of fermions was the measurement of interactions (scattering lengths), we had to come up with a different system.

Our solution was to use a 3-level system (Fig. 7-4). After forming a superposition state and waiting for it to decohere (next section), the equilibrium energy levels are as shown in Fig. 7-4. Transitions to a third level are then independent of the $|2\rangle - |3\rangle$ scattering length a_{23} (absence of clock shift out of a pure state) and are only by the interactions of state $|1\rangle$ with states $|2\rangle$ and $|3\rangle$ (a_{12} and a_{13}):

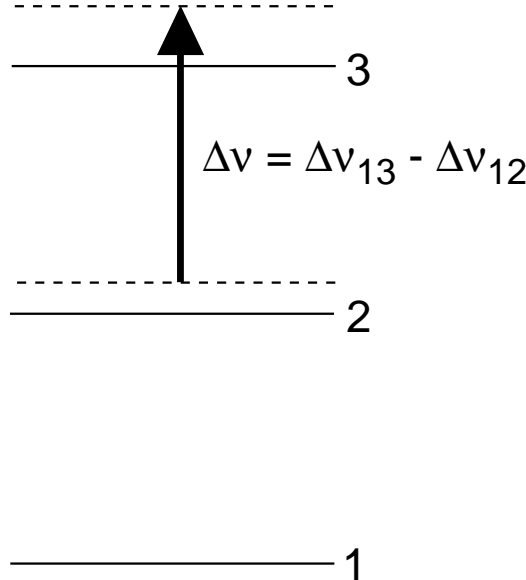$$\Delta\nu = \frac{2\hbar}{m} n_1 (a_{13} - a_{12}) \tag{7.2}$$

Figure 7-4: The RF resonance is sensitive to mean field shifts in a 3-level system. The diagram shows the case for positive a_{12} and a_{13} with $a_{13} > a_{12}$.

Since the shift in this resonance takes place over a finite time, the decoherence time, probing the $|2\rangle \rightarrow |3\rangle$ transition at varying times also provides a way to measure the decoherence time of our system.

7.2   Emergence of Mean Field Shifts in a Fermi System

The evolution of a superposition state into a statistical mixture has been the subject of numerous discussions involving topics ranging from NMR to error correction in quantum computation. The understanding of the mechanisms of decoherence presents another avenue of research with degenerate fermions. In this section, I will first discuss the decohering mechanisms in our system. Next, I will present an experiment which measured this decoherence time using RF methods.
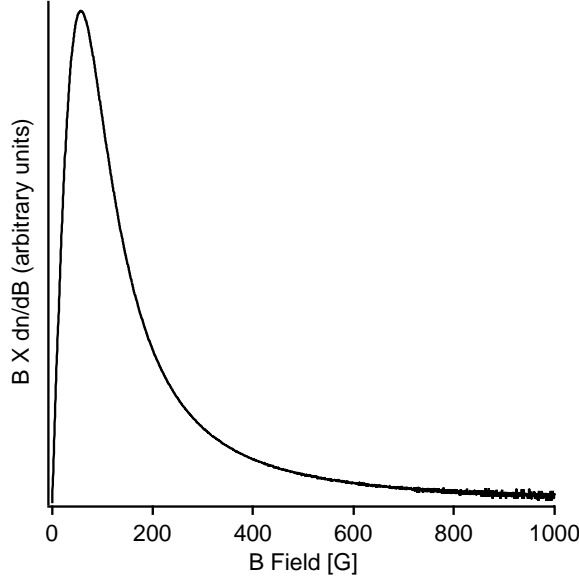
Figure 7-5: Decoherence rate due to inhomogeneous magnetic fields. Plot of $B \times \partial\nu_{12}/\partial B$. The maximum of $B \times \partial\nu_{12}/\partial B$ is at $\sim 57.46\,\mathrm{G}$.

7.2.1   Decoherence in our system

Since spin-polarized ultracold fermions are very near the epitome of a non-interacting system, all decohering mechanisms must be related to single atom effects. These would then include any spatial variations of the energy difference of the two spin components across the phase space experienced by the particles. Other effects might be collisions with background gas particles or interactions with ambient photons. Without going into detailed study of all these effects, we can with some confidence say that the most relevant mechanism is magnetic field inhomogeneity. The finite sensitivity of the transition to magnetic field quantified by

$\frac{\partial \nu}{\partial B}$ acts together with the imperfections of the magnetic field (which scales with B, for standard power supplies energizing the magnetic field coils). The product $\frac{\partial \nu}{\partial B} \times B$ is then the quantity which determines the decoherence time. A plot of this quantity for the $|1\rangle \rightarrow |2\rangle$ transition is shown in fig.7-5.

This has to be contrasted with the case of ultracold bosons where s-wave interactions do take place at all temperatures. This means that mean field is an additional contribution to decoherence. A remarkable experiment in Eric Cornell's group at JILA actually uses these two effects to cancel each other and increase the coherence time in a bosonic system [134].

There may be additional effects coming in once partial decoherence has already occurred. For example, elastic collisions do start to occur once any degree of non-orthogonality exists in a system. The level of decoherence from these elastic collisions is still not fully understood.
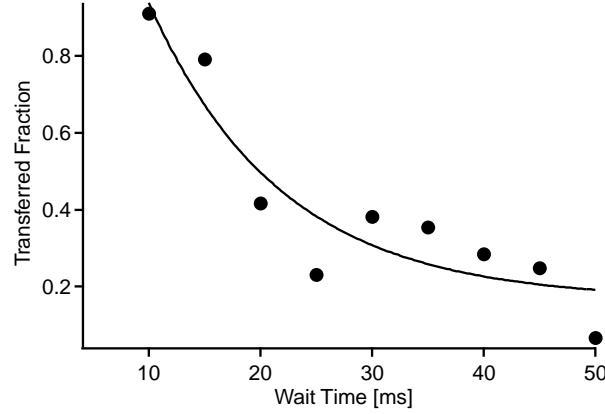

Figure 7-6: Emergence of mean field shifts due to decoherence at $500\,\mathrm{G}$. Decoherence leads to a reduction of the $|2\rangle \rightarrow |3\rangle$ transfer at the unperturbed resonance ν_{23}. An exponential fit to the data (solid line) gives the time constant of $12\,\mathrm{ms}$.

We measured the decoherence time of our $|1\rangle - |2\rangle$ system by driving the transition $|2\rangle \rightarrow |3\rangle$ (see fig.7-4) at varying times after creating a superposition state of $|1\rangle$ and $|2\rangle$. For a pure superposition state, the resonance occurs at the unperturbed frequency $\nu_{coh} = \nu_{23}$. For a fully decohered state, the resonance is shifted by $\Delta\nu$ (Eq. 7.2), i.e., $\nu_{decoh} = \nu_{23} + \Delta\nu = \nu_{23} + \frac{2\hbar}{m}n_1(a_{13} - a_{12})$. For a finite $\Delta\nu$ and a broadening dominated by trap inhomogeneity, the transfer at ν_{23} decays in time. We measured the transfer fraction as a function of time at $500\,G$ and fit an exponential curve (Fig.7-6). We did not study the evolution dynamics from the pure superposition to the statistical mixture. [4]. Therefore our choice of the exponential curve may not be accurate.

We also measured longer decoherence times at higher fields ($\sim 800\,\mathrm{G}$), in agreement with the expectation from fig. 7-5. In principle, the decoherence times can be arbitrarily extended by tuning the field variation across the sample. A perfectly flat bias field would

---

[4]this could form the subject of a future project!

give rise to extremely long decoherence times. Our field curvature produces $\sim 2\,\mathrm{Hz}$ trapping frequency at $500\,\mathrm{G}$.

7.3 RF Spectroscopy of a 3-level system

Our experimental scheme to measure the interactions given by Eq.7.2 is shown in Fig.7-7. The main idea is to measure $\Delta\nu$. This can be obtained from the difference in the $|2\rangle \to |3\rangle$ spectrum of the pure $|2\rangle$ state and a statistical mixture of $|1\rangle$ and $|2\rangle$ and the knowledge of the $|1\rangle$ density n_1.
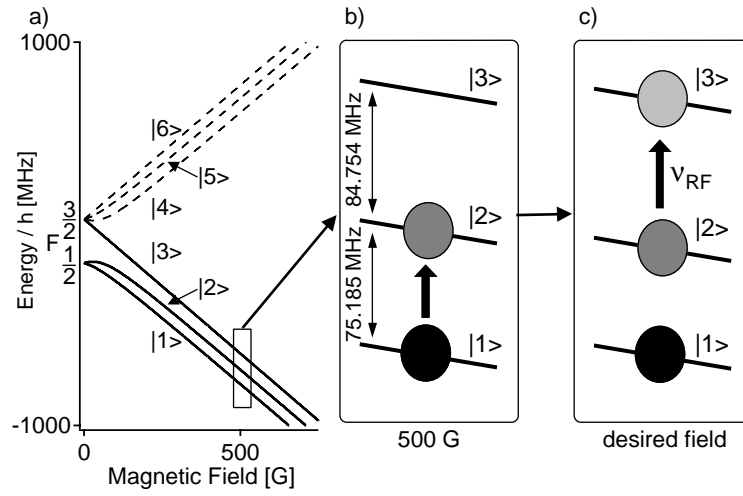

Figure 7-7: (a) Hyperfine structure of the ground state of ^{6}Li. (b and c) Experimental scheme: (b) preparation of a mixture of atoms in states $|1\rangle$ and $|2\rangle$, and (c) RF spectroscopy of the $|2\rangle \to |3\rangle$ transition.

Starting from the pure state $|1\rangle$ at low field in the ODT, we first ramped up the field to $500\,\mathrm{G}$ in a few ms. Here, the choice of state was made. By applying a slow, adiabatic Landau-Zener frequency sweep, a pure state $|2\rangle$ sample was created. By applying a fast, non-adiabatic sweep and letting the superposition decohere in $200\,\mathrm{ms}$ ($\gg 12\,\mathrm{ms}$), the statistical mixture was prepared. The Rabi technique was used with pulses of $140\,\mu\mathrm{s}$ duration. Typical parameters for the decohered $|1\rangle - |2\rangle$ mixture were mean-density $n_1 \sim 2.4 \times 10^{13}\,\mathrm{cm}^{-3}$ and temperature $T \sim 0.7\,T_F$. Here the mean density is lower than the peak density by $2\sqrt{2}$ for our modest degeneracy, where the Gaussian approximation can be used.

Using the triple imaging technique described in Chapter 4, we monitored the appearance of atoms in state $|3\rangle$ and the disappearance of atoms in state $|2\rangle$. Recording state $|1\rangle$ provided the required density n_1. Using the separation $\Delta\nu$ of the two spectra for the transferred fraction $\frac{N_3}{N_2+N_3}$ and n_1 for normalization, $(a_{13} - a_{12})$ can be determined from Eq. 7.2. A typical spectrum (at $480\,\mathrm{G}$) is shown in Fig.,7-8. In addition to the easily resolved separation of the two peaks ($\sim 16\,\mathrm{kHz}$), the spectra also show considerable difference in
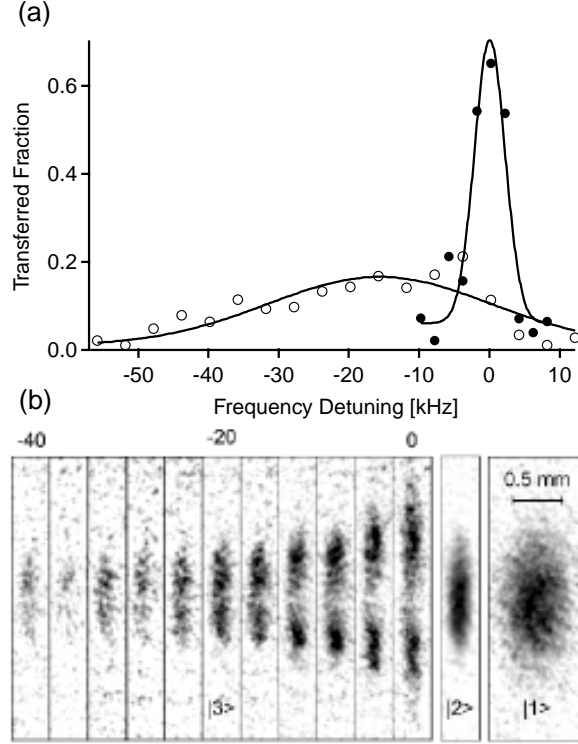
Figure 7-8: (a) Fraction of atoms transferred from $|2\rangle$ to $|3\rangle$, with $|1\rangle$ atoms absent (filled circles), and present (open circles). The mean-field shift is computed from gaussian fits to the data (solid lines). (b) Spatial images of state $|3\rangle$ for the perturbed resonance. The optical trap was turned off immediately after the RF pulse and absorption images of the atoms were taken after $120\,\mu s$ expansion time. The central section of $\sim 150\,\mu m$ vertical extent was used to extract the transferred fractions in (a). (b) also shows images of states $|2\rangle$ and $|1\rangle$ for zero RF detuning. States $|3\rangle$ and $|2\rangle$ were imaged simultaneously to observe their complementary spatial structure. State $|1\rangle$ was imaged after $760\,\mu s$ expansion time to record its density for normalization purposes.

their widths. For the pure state transfer (filled circles), the broadening is dominated by the pulse width. For the incoherent mixture (open circles), the width is dominated by the inhomogeneous density distribution according to Eq. 7.2. The measured $\Delta\nu$ for a wide range of magnetic fields $300 - 750\,\mathrm{G}$, are shown in Fig. 7-9(a).

We compared our measurements with calculations from the Eindhoven group (Fig. 7-9)(b). The calculated scattering lengths and the measured density were used to compute the theoretical curve for $\Delta\nu$ as a function of magnetic field. We see that there is good agreement at low fields. The RF method is sensitive to the narrow Feshbach resonance at $545\,\mathrm{G}$ and the sign change in Eq. 7.2 at $\sim 600\,\mathrm{G}$. Although the data tracks this theory quite well for fields below $630\,\mathrm{G}$, substantial deviations occur near the wide Feshbach resonances at $680\,\mathrm{G}$ (a_{13}) and $810\,\mathrm{G}$ (a_{12}).
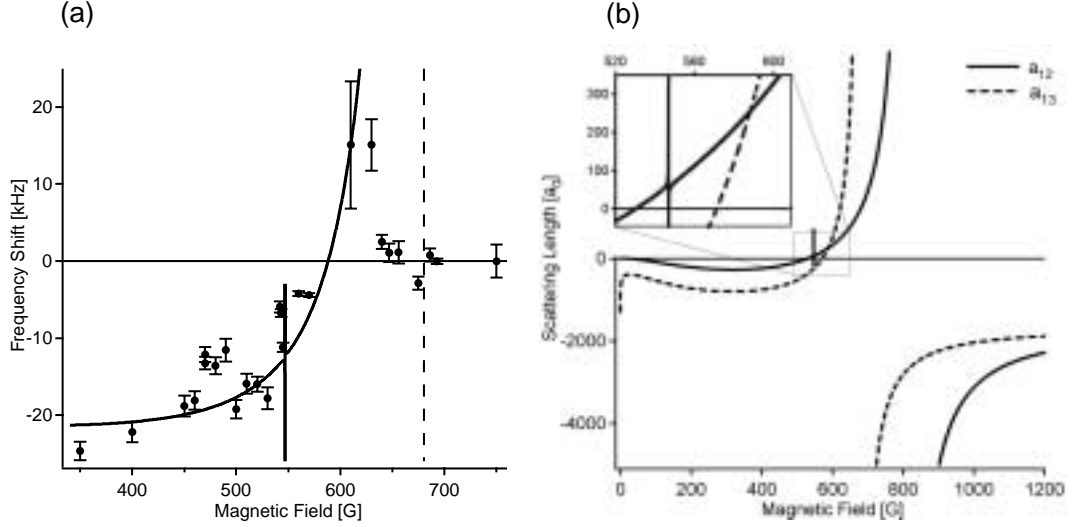
Figure 7-9: Spectroscopic measurement of interaction energy. (a) Frequency shift vs. magnetic field of the $|2\rangle \to |3\rangle$ resonance due to atoms in state $|1\rangle$. The shifts are computed by monitoring the arrival fraction in state $|3\rangle$ for $140\,\mu$s RF pulses, except at $750\,$G. Here, because of strong inelastic losses between $|3\rangle$ and $|1\rangle$ atoms, we monitored the loss of atoms in state $|2\rangle$ after applying RF sweeps of $3\,$ms duration and $2\,$kHz width. All the data points are normalized to the same atom number in state $|1\rangle$. The fit at low fields (solid line) uses Eq. 7.2 with $n_1 = 2.2 \times 10^{13}\,\mathrm{cm}^{-3}$ and the theoretical calculations of the scattering lengths. The error bars reflect uncertainty in the state $|1\rangle$ atom number, and the uncertainty in the gaussian fits to the spectra. The dashed line indicates the position of the predicted a_{13} resonance. (b) s-wave Feshbach resonances in a_{12} and a_{13}. s-wave scattering lengths a_{12} and a_{13} as a function of magnetic field, obtained from a highly model-independent quantum scattering calculation. The calculation makes use of the presently available ^{6}Li experimental data [136] in a coupled channel approach to deduce accumulated phases that characterize the less well-known short range parts of the ^{6}Li $+$ ^{6}Li scattering potential [137]. a_{12} has a narrow Feshbach resonance at $550\,$G and a wide one at $810\,$G. a_{13} has a wide Feshbach resonance at $680\,$G.

7.4 Observations of Unitary and Universal Behavior

The Feshbach resonances in a_{12} and a_{13} are wide and overlap substantially. This distinguishes it from the ^{40}K system where the Feshbach resonances are narrow and well separated [109, 117]. Even though the width is in some sense forgiving - one does not need to have great magnetic field stability to be in the vicinity of the resonance, the overlap of different resonances makes understanding the 3-level RF spectra more complicated.

As can be seen in Fig.7-9(a), the shifts for fields up to $\sim 630\,$G lie in agreement with the expectation from Eq.7.2. Above this field, there is a noticeable deviation from this simple prediction. This is because the two assumptions of dilute gas mean field theory: $ka \ll 1$, $na^3 \ll 1$ start to break down. The broad structure of the Feshbach resonances allows us to see the unitary behavior over large magnetic field ranges.

The description of quantum mechanical unitarity in Chapter 6 helps us see some of this deviation. The mean field, proportional to $Re(f)$ reaches a maximum near $1/k_F$ and then starts to decrease gently. This means, that the shifts can never diverge like the scattering length does. Once both interactions a_{12} and a_{13} are unitarity limited, they have the same magnitude. This implies that they should cancel each other giving near zero spectroscopic shifts when they are of the same sign. This explanation works below 680 G where a_{13} diverges. However between 680 G and 810 G, a_{13} and a_{12} are large and of opposite sign and should then produce a large negative shift. However, we observe close to zero shifts in this region as well.

The explanation of this puzzle may lie in our having left the low density limit and entered a regime where higher order many-body effects can become important. Some recent many-body calculations [83, 84, 85] do indeed suggest a universality of interaction energy in the unitarity limit, making the "mean field" independent of the sign of the bare two-particle interaction. This is a possible explanation of what we see and is consistent with other measurements in highly interacting Fermi systems - both by expansion energy measurements [138, 106, 111] and by RF spectroscopy methods [117]. The fact that these theories predict a universal *negative* (attractive) sign of the interaction is of course good news from the point of view of achieving superfluidity in these strongly interacting systems.

7.5 Outlook

The use of RF methods to study ultracold fermions has generated considerable excitement in the field. In addition to RF spectroscopy [117, 5], RF photodissociation has also been used to detect molecules formed out of a mixture of ultracold fermions [139]. The RF tool remains the best way to tailor the spin composition, an important component en route to superfluidity. Finally, the proposals of Zoller et. al. [125, 126] to use Raman methods to couple the superfluid and normal states can be modified to RF methods and remains a possible method to detect the superfluid fraction.

Chapter 8

Conclusions and Outlook

Two sets of experimental studies were reported in this thesis. The first involved the development of a new atom interferometer scheme which shows promise for high accuracy metrology using Bose-Einstein condensed gases. The second involved the production and exploration of a strongly interacting Fermi gas mixture which is predicted to undergo a superfluid phase transition under current experimental conditions.

We have demonstrated an atom interferometer using optical standing wave diffraction gratings which has several desirable features for a high precision measurement of the photon recoil frequency ω_{rec} [1]. ω_{rec} can be used in conjunction with other measurements to determine the fine structure constant α, a fundamental constant of physics. Our preliminary result for $\omega_{\text{rec,Na}}$ at 7×10^{-6} precision obtained using a ^{23}Na BEC and horizontal standing waves deviates from the currently accepted value at the 2×10^{-4} level. We believe that this deviation arises from the mean-field interaction between atoms. A future measurement would involve converting to an atomic fountain setup with vertical standing waves to increase the interaction times in the interferometer. The precision in such a geometry should approach ppb values. The mean-field systematic should be suppressible to this level using very low density BECs[74]. We hope to obtain a $\lesssim 1$ ppb value for ω_{rec} in a second generation experiment in which BECs are created elsewhere and transported into the interferometer[140].

We have upgraded our ^{23}Na BEC machine with the capability to cool and trap ^{6}Li fermions. By cooling ^{6}Li sympathetically with ^{23}Na in a magnetic trap, we can produce quantum degenerate Bose-Fermi mixtures as well as very large and deeply degenerate Fermi gases. Optimization of our sympathetic cooling strategy has established a (currently) unmatched system performance in terms of atom number (both in the mixture and pure fermion operation) as well as degeneracy of pure fermions $(0.05\,T_F)$ [6]. Degenerate Bose-Fermi mixtures promise to be fertile research ground [141, 142]. We have however concentrated on studying the degenerate Fermi gas in a strongly interacting regime.

Using the variation of interaction strength offered by magnetically-tunable Feshbach scattering resonances, we have explored physical regimes in which a new type of BCS su-

perfluid is predicted to form [99, 100, 108] at modest degeneracies (high T_c) of $\sim 0.5\,T_F$. The creation of this fermionic superfluid would establish a model system for studying superfluid phenomena at densities which are a billion times lower than in previous realizations in ^{3}He and superconductors.

Since suitable Feshbach resonances in ^{6}Li only exist in spin states that cannot be magnetically trapped, we transfer our degenerate gas into an optical trap. By monitoring the magnetic field dependent stability of a two-spin mixture of ^{6}Li fermions, we have located two s-wave Feshbach resonances [4]. The measured stability in the strongly interacting regime is encouraging for the prospects of creating the superfluid state in ^{6}Li.

In the vicinity of Feshbach resonances, several groups [86, 117, 111] including us (unpublished) have observed strong hydrodynamic behavior in a fermion spin mixture during expansion out of an asymmetric trap. The possible interpretation of this behavior as a signature of superfluidity (as in the case of BEC) has been considered [115, 86]. However, classical collision processes can also give rise to such behavior, mitigated only by the Pauli suppression of collisions at low temperatures. By examining the deformation of the Fermi surface during expansion out of anisotropic traps, we theoretically analyzed the collisional behavior of an expanding, zero-temperature gas[8]. Our calculations indicate that unlike in the case of a BEC, hydrodynamic expansion of Fermi gases near Feshbach resonances cannot be a dramatic, qualitative signal for the existence of the superfluid state, regardless of the temperature of the gas.

Another proposed method to detect the BCS state is to monitor shifts of resonances between atomic internal states due to the presence of the superfluid [125, 126] (corresponding to a pair-breaking energy). Our efforts in this direction (and those at JILA[117]) using radio-frequency (RF) transitions betweens ^{6}Li (^{40}K) spin states have not (yet) observed such a shift. However, we have measured shifts in RF transitions due to interactions between different spin states in a three-state system. Our measurements indicate a saturation of the interaction energy near Feshbach resonances which has a negative sign regardless of the sign of the bare (two-particle) interaction. Although this is consistent with other measurements [111], there is no clear agreement on the mechanism which would cause such behavior. While some many-body theorists predict a universally negative interaction parameter in the strongly interacting s-wave regime ($n|a|^3 \gg 1, nR^3 \ll 1$) of current experiments, others propose an explanation based on molecule formation [111, 143]. Using RF techniques we also observed the absence of interaction shifts in two-state fermion systems [5, 7]. This is encouraging for the prospects of using fermions in future atomic clocks. The use of the RF tool to observe a fermionic superfluid remains on our experimental agenda.

The experimental observation of fermionic superfluidity is currently the foremost goal in our research group. For a robust observation and characterization of the superfluid state, a relatively direct and easy-to-implement experimental diagnostic would be ideal. For BEC's time-of-flight expansion serves such a purpose. As indicated above, in the current regime

of experiments, such a diagnostic cannot be a qualitative tool. On the other hand, RF diagnostics still appears promising.

A new direction currently being followed by some groups involves the creation of molecules from a two-spin Fermi gas by adiabatically varying the magnetic field across a Feshbach resonance [139, 143, 144]. Trapped, long-lived (upto 10 s [144]) molecules have been created in this way [143, 144]. These molecules could undergo Bose-Einstein condensation if they are cooled to below the critical temperature. The production of such a molecular BEC would alone be an achievement of considerable scientific significance. Additionally, the molecular BEC could cross-over into a BCS state [145] by a further tuning of the interaction with the magnetic field.

It seems quite safe to predict that the observation of fermionic superfluidity in dilute gases will cause an explosion of interest and activity in the field as in the case of bosonic superfluidity (1995 onwards). The range of new and exciting physics that the creation of such a system will produce is difficult to overestimate. An important theme will be the understanding of the behavior of other Fermi systems such as high T_c superconductors. Probably the most interesting studies will be the ones that we cannot predict at this point.

Appendix A

Contrast Interferometry using Bose-Einstein Condensates to Measure h/m and α

This appendix includes the following paper [1]: S. Gupta, K. Dieckmann, Z. Hadzibabic, and D.E. Pritchard, "Contrast Interferometry using Bose-Einstein Condensates to Measure h/m and α", *Phys. Rev. Lett.* **89**, 140401 (2002).

Contrast Interferometry using Bose-Einstein Condensates to Measure h/m and α

S. Gupta, K. Dieckmann, Z. Hadzibabic, and D. E. Pritchard

Department of Physics, MIT-Harvard Center for Ultracold Atoms, and Research Laboratory of Electronics, MIT, Cambridge, Massachusetts 02139

The kinetic energy of an atom recoiling due to absorption of a photon was measured as a frequency, using an interferometric technique called "contrast interferometry." Optical standing wave pulses were used to create a symmetric three-path interferometer with a Bose-Einstein condensate. Its recoil phase, measurable with a single shot, varies quadratically with additional recoils and is insensitive to errors from vibrations and ac Stark shifts. We have measured the photon recoil frequency of sodium to 7 ppm precision, using a simple realization of this scheme. Plausible extensions should yield sufficient precision to attain a ppb-level determination of h/m and the fine structure constant α.

Comparison of accurate measurements of the fine structure constant α in different subfields of physics offers one of the few checks for global errors across these different subfields. The $(g-2)$ measurement for the electron and positron, together with QED calculations, provides a 4 ppb measurement of α [1,2]. This has stood as the best measurement of the fine structure constant since 1987. The second most accurate published value of α, at 24 ppb, comes from condensed matter experiments [3]. This is worse by a factor of 6, limiting the scientific value of cross-field comparisons. A new and more robust route based on atomic physics measurements has emerged in the past decade [4]:

$$\alpha^2 = \left(\frac{e^2}{\hbar c}\right)^2 = \frac{2R_\infty}{c}\frac{h}{m_e} = \frac{2R_\infty}{c}\frac{M}{M_e}\frac{h}{m}. \tag{1}$$

The Rydberg constant R_∞ is known to 0.008 ppb [5,6] and the electron mass M_e to 0.7 ppb [7]. M and m are the mass of some test particle in atomic and SI units, respectively. Equation (1) offers the possibility of a ppb-level measurement of α if M and h/m can be determined accurately.

h/m can be measured by comparing the de Broglie wavelength and velocity of a particle, as demonstrated by Krüger, whose measurement using neutrons has yielded a 73 ppb value for h/m_n [8]. For an atom, h/m can be extracted from a measurement of the photon recoil frequency,

$$\omega_{\text{rec}} = \frac{1}{2}\frac{\hbar}{m}k^2, \tag{2}$$

where k is the wave vector of the photon absorbed by the atom. Recent experiments allow Eqs. (1) and (2) to be applied to cesium. M_{Cs} is known to 0.17 ppb[9] and k_{Cs} to 0.12 ppb [10]. $\omega_{\text{rec,Cs}}$ has been measured at Stanford using an atom interferometer based on laser-cooled atoms to 6 ppb [11–13]. Similar experiments are also possible with alkali atoms such as sodium and rubidium, where M has been measured [9] and k is accurately accessible [10].

In this Letter, we demonstrate a new atom interferometer scheme which shows promise for a high precision measurement of ω_{rec}. Our symmetric three-path configuration encodes the photon recoil phase in the *contrast* of the interference fringes, rather than in their *phase*. Because it is insensitive to the fringe phase, the method is not sensitive to vibrations, accelerations, or rotations. The symmetry also suppresses errors from magnetic field gradients, and our use of only one internal state suppresses errors arising from differences in the ac Stark shifts between different internal states. A crucial aspect of this new interferometer is the use of atomic samples with subrecoil momentum distribution. We use a Bose-Einstein condensate (BEC) as a bright subrecoil atom source. This allows the contrast oscillations to persist for many cycles, permitting precise determination of the recoil phase in a single "shot." This also allows for extra photon recoils to be added within the interferometer, increasing the recoil phase shift and, hence, the measurement precision quadratically.

The Stanford scheme to measure ω_{rec} uses different internal states to separately address different interferometer paths, allowing a linear increase of measurement precision by additional photon recoils. However, vibrations and ac Stark shifts have been of great concern in this scheme [12]. An alternative interferometer to measure the photon recoil using laser-cooled atoms in a single internal state was demonstrated using rubidium atoms [14]. Like ours, this scheme also incorporates a symmetric arrangement and operates by measuring contrast. This interferometer should also suppress vibration noise and systematics arising from ac Stark shifts between different internal states. However, different paths cannot be individually addressed in this scheme, making it difficult to extend to competitive precision. Our interferometer extends these previous schemes and combines their advantages. The precision of the Stanford scheme increases linearly with additional recoils. Quadratic scaling schemes have been proposed [15] and demonstrated in a

multipath interferometer based on dark states [16]. However, the number of additional recoils in this scheme is limited by the internal atomic structure.

Our scheme is based on the asymmetric interferometer of Fig. 1(a). At time $t = 0$ a BEC is split coherently into two momentum components, $|2\hbar k\rangle$ and $|0\hbar k\rangle$, by a first order Bragg $\pi/2$ pulse [17]. These are shown as paths 1 and 2 in the figure. At time $t = T$, a second order Bragg π pulse reverses the direction of path 1, while leaving path 2 unaffected. Around $t = 2T$, a moving matter wave grating, with spatial periodicity $\lambda/2$ (wave vector $2k = \frac{2\pi}{\lambda/2}$), is formed due to the overlap and interference of the two paths. The phase of this grating at $2T$ is determined by the relative phase $\Phi_1 - \Phi_2 = 8\,\omega_{rec}T$, accumulated between paths 1 and 2 due to the difference in their kinetic energies. A measurement of this phase for different values of T will then determine ω_{rec}. If the momentum of path 1 is increased N times by additional photon recoils, the corresponding grating phase will be $\Phi_1 - \Phi_2 = N^2 8\,\omega_{rec}T$, leading to an N^2-fold improvement in the measurement precision. The fringes of all atoms will be in phase at $2T$, forming a high-contrast matter wave grating. This dephases in a time $\frac{1}{k\Delta v}$, the coherence time, where Δv is the atomic velocity spread.

Extension of this interferometer to a symmetric three-path arrangement is shown in Fig. 1(b). Three momentum states (paths 1, 2, and 3) are generated by replacing the first Bragg pulse with a short Kapitza-Dirac pulse [17]. At $t = 2T$, there are now two matter wave gratings with period $\lambda/2$, one from paths 1 and 2, and one from paths 2 and 3. These move in opposite directions at a relative speed $4\hbar k/m$. If the maxima of the two gratings line up to produce large contrast at time t, the maxima of one will line up with the minima of the other at $t + \pi/4\,\omega_{rec}$, to produce zero contrast. This results in an oscillatory growth and decay of the contrast of the overall pattern

FIG. 1.   Space-time representation of the contrast interferometer. (a) A simple two-path interferometer sensitive to the photon recoil phase. The $2k$ matter wave grating is shown at $2T$ and at $2T + \pi/4\,\omega_{rec}$. The extension to the three-path geometry is shown in (b). The overall $2k$ grating has large contrast at $2T$ and zero contrast at $2T + \pi/4\,\omega_{rec}$.

with time. The recoil induced phase can be determined from this temporally oscillating contrast.

The time evolution of this contrast can be monitored by continuously reflecting a weak probe beam from the grating (the additional grating formed by paths 1 and 3 has period $\lambda/4$, which does not reflect the probe beam). The reflected signal can be written as

$$S(T, t) = C(T, t)\,\sin^2\!\left(\frac{\Phi_1(t) + \Phi_3(t)}{2} - \Phi_2(t)\right)$$
$$= C(T, t)\,\sin^2[8\,\omega_{rec}T + 4\,\omega_{rec}(t - 2T)], \quad (3)$$

where $C(T, t)$ is an envelope function whose width is the grating coherence time, $\frac{1}{k\Delta v}$. This motivated our use of a BEC atom source. This allowed many contrast oscillations in a single shot. Using the phase of the reflection at $t = 2T$, $\Phi(T) = 8\,\omega_{rec}T$, ω_{rec} can be determined by varying T. Vibrational phase shifts and the effect of magnetic bias fields and gradients cancel in the evaluation of $\frac{\Phi_1(t) + \Phi_3(t)}{2} - \Phi_2(t)$, due to the symmetry of our scheme.

In this experiment, we realized the scheme of Fig. 1(b) and measured $\omega_{rec,Na}$ to 7 ppm precision. We also demonstrated the insensitivity of the contrast signal to vibrations and the N^2 scaling of the recoil phase.

We used sodium BECs containing a few million atoms in the $|F = 1, m_F = -1\rangle$ state as our atom source. The light pulses were applied ≈ 15 ms after releasing the BEC from a weak magnetic trap. This lowered the peak density to about 10^{13} cm^{-3}, thus preventing superradiance effects [18] and reducing frequency shifts from mean field interactions. Two horizontal counterpropagating (to ≤ 1 mrad) laser beams were used for the diffraction gratings. The light for the gratings was red-detuned by 1.8 GHz from the sodium D_2 line. Rapid switching ($<$ 100 ns) and intensity control of the light pulses was done by an acousto-optic modulator (AOM) common to the two beams. The phase and frequency of each beam were controlled by two additional AOMs, driven by two phase-locked frequency synthesizers.

The interferometer pulse sequence was started with a 1 μs, square Kapitza-Dirac pulse, centered at $t = 0$. We adjusted the beam intensity, to put $\approx 25\%$ of the condensate in each of the $|\pm 2\hbar k\rangle$ diffracted orders. This choice yielded the best final contrast signal. The second order Bragg pulse was centered at $t = T$ and was close to Gaussian shaped, with a width of 7.6 μs. The intensity was chosen to effect a π pulse between the $|\pm 2\hbar k\rangle$ states. The smooth pulse shape reduced the off-resonant population of undesired momentum states, yielding a transfer efficiency of $> 90\%$. The third pulse, used for reading out the contrast signal, was centered at $t = 2T$ and was typically 50 μs long. One of the Bragg beams was used as the readout beam while the other was blocked.

The light reflected from the atoms was separated from the readout beam path using a beam splitter and directed by an imaging lens onto a photomultiplier. A typical
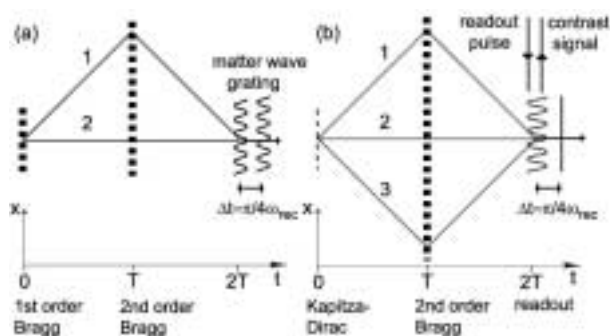
interferometer signal is shown in Fig. 2. We observed the expected contrast oscillations at frequency $8\,\omega_{rec}$, corresponding to a 5 μs period for sodium. We obtained the recoil phase $\Phi(T)$ from the contrast signal by fitting to a sinusoidal function as in Eq. (3).

The signal also contained a small pedestal of similar width as the envelope. This consists of a constant offset from residual background light and a smoothly varying contribution from a small asymmetry between the $|\pm 2\hbar k\rangle$ amplitudes of <5%. This asymmetry creates a non-oscillating component of the $2k$ matter wave grating which decays with the same coherence time. The uncertainty of the fitted phase is about 10 mrad, even if we neglect the envelope function, and assume a constant amplitude extended over a few central fringes. Similar uncertainty was obtained for large times $T \approx 3$ ms. We observe a shot-to-shot variation in the fitted value of the phase of about 200 mrad. We attribute this to pulse intensity fluctuations which randomly populated undesired momentum states at the <10% level. This resulted in spurious matter wave gratings which shifted the observed recoil phase.

The recoil frequency was determined by measuring the recoil phase around $T = 0.5$ ms and around $T = 3$ ms (Fig. 3). An upper bound on T was set by the atoms falling out of the 2 mm diameter beams. A straight line fit to these data produced a value for the sodium photon recoil frequency $\omega_{rec,Na} = 2\pi \times 24.9973$ kHz $(1 \pm 6.7 \times 10^{-6})$. This is 2×10^{-4} lower than the sub-ppm value calculated using the published measurements of α_{g-2}, R_∞, M_{Na} [9], M_e, and λ_{Na} [19] in Eqs. (1) and (2). The systematic mean field shift due to larger population in the middle path than the extreme paths probably explains this deviation. Estimated errors from beam misalignment and wave front curvature have the same sign as the observed deviation but several times lower magnitude.
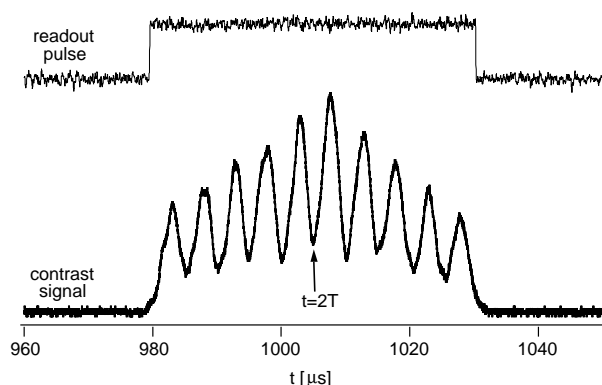
To demonstrate the insensitivity of the measurement to phase noise of the light due to mirror vibrations, we intentionally varied the phase θ of the second grating relative to the first one [20]. The contrast signal is not visibly affected by such phase variations [Fig. 4(a)]. We compared this to a phase-sensitive readout method [Fig. 4(b), inset]. This was realized by replacing the readout pulse with a third pulsed 1 μs light grating in the Kapitza-Dirac regime, phase-locked to the first two pulses. This projected the phase of the $2k$ pattern at $t=2T$ onto the fractional populations of the states $|0\,\hbar k\rangle$, $|2\,\hbar k\rangle$, and $|-2\,\hbar k\rangle$ which leave this interferometer. The populations were measured by time-of-flight absorption imaging. The $|0\,\hbar k\rangle$ fraction is shown for the same variation of θ, in Fig. 4(b). The oscillation [21] demonstrates the phase sensitivity of any position-sensitive readout.

These two interferometers respond differently to mirror vibrations. For large T, we have observed the effect of the mirror vibrations directly. At $T \approx 3$ ms, the shot-to-shot fluctuations of the phase-sensitive interferometer was of the order of the expected fringe contrast. This agrees with observations with a standard Mach-Zehnder interferometer constructed both by us and in [22]. In comparison, the stability of the contrast interferometer signal is independent of T within our measurements. This can be seen from the comparable statistical error bars for short and long times in Fig. 3(b). In fact, the residuals and the corresponding error bars are smaller at the longer times. We attribute this to the decreased amplitude of some of the spurious gratings at longer times, due to reduced overlap of the contributing wave packets.

The quadratic scaling of the accumulated recoil phase, with the number of transferred recoils N, was demonstrated by comparing $N=1$ and $N=2$ interferometers. An $N=2$ geometry, shown in Fig. 5(a), was realized using two additional first order Bragg π pulses spaced T_1 apart and affecting only the extreme paths. The acceleration pulse at $t=60$ μs drove transfers from $|\pm2\hbar k\rangle$ to

FIG. 2. Typical single-shot signal from the contrast interferometer. $T = 502.5$ μs, for this example. Ten oscillations with $\approx$ 60% contrast and ≈ 30 μs width are observed during the 50 μs readout. A low-pass filter at 300 kHz (12 dB per octave) was applied to the signal.
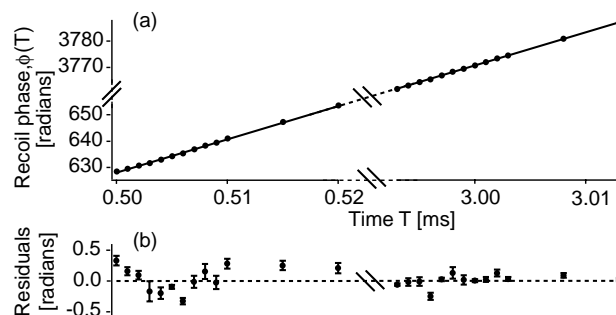

FIG. 3. Measurement of ω_{rec} in sodium. Two sets of recoil phase scans, around $T = 0.5$ ms and $T = 3$ ms, are shown in (a). Each point is the average of five measurements. The slope of the linear fit gave ω_{rec} to 7 ppm. The error bars ($\approx 0.05 - 0.1$ rad) are shown with the fit residuals in (b).
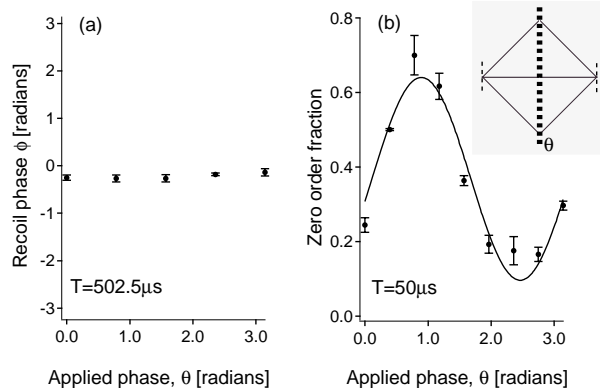
FIG. 4. Vibration insensitivity of the contrast interferometer. (a) The measured recoil phase at $T = 502.5$ μs from the contrast interferometer as a function of the applied phase θ. The recoil phase is constant and demonstrates our insensitivity to phase noise from the gratings. (b) The fractional population of the $|0\,\hbar k\rangle$ state from the phase-sensitive interferometer (inset) for a similar scan of θ at $T = 50$ μs. Also shown is the best-fit sinusoid of the expected period.
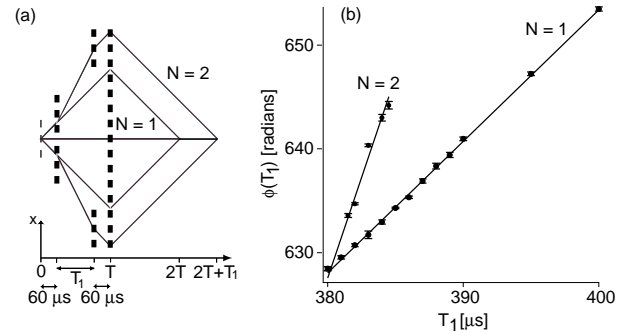

FIG. 5. Demonstration of the quadratic scaling of the recoil phase with additional photon recoils. (a) The $N = 1$ (inner) and $N = 2$ (outer) interferometers used. (b) The recoil phase at the recombination time under variation of T_1.

$|\pm 4\hbar k\rangle$. The deceleration pulse at $t = T_1 + 60$ $\mu s = T - 60$ μs drove transfers from $|\pm 4\hbar k\rangle$ back to $|\pm 2\hbar k\rangle$. During the period T_1, paths 1 and 3 accumulate phase $2^2 = 4$ times faster in the $N = 2$ scheme than in the $N = 1$ scheme. Additional time T_1 is required for the three paths to overlap in the $N = 2$ scheme. For this geometry, the $N = 2$ recoil phase should therefore evolve 3 times faster as a function of T_1 than the $N = 1$ recoil phase [Fig. 5(b)]. The corresponding linear fits give a slope ratio of 3.06 ± 0.1. At present, we do not have sufficient control over the timing and phase of the intermediate pulses to improve our $N = 1$ measurement precision by using $N > 1$.

In conclusion, we have demonstrated a contrast interferometer which has several desirable features for a high precision measurement of the photon recoil frequency. Such a measurement would involve converting to an atomic fountain setup with vertical Bragg beams. In this geometry, T can be extended by nearly 2 orders of magnitude. Our insensitivity to phase noise from mirror vibrations should greatly alleviate vibration isolation requirements of the system for long T [12]. The order N of the interferometer must also be increased, requiring improved timing and phase control of laser pulses. Direct scaling of our current precision of ≈ 0.01 rad/shot results in an estimated precision of <1 ppb/shot for $T = 100$ ms and $N = 20$. A rigorous study of systematics will have to be undertaken to increase the accuracy of our measurement. Estimates show that mean field effects can be suppressed to the ppb-level by reduction of atomic density to $\approx 10^{11}$ cm^{-3}, together with pulse control for $<5\%$ imbalance between populations in the middle and extreme

paths. In addition, our methods may provide a way to study mean field effects with interferometric precision. We hope to obtain a <1 ppb value for ω_{rec} in a second generation experiment in which BECs are created elsewhere and transported into the interferometer [23].

We thank W. Ketterle for valuable discussions. This work was supported by the NSF, ONR, ARO, NASA, and the David and Lucile Packard Foundation.

[1] R. S. Van Dyck, Jr. et al., Phys. Rev. Lett. 59, 26 (1987).
[2] T. Kinoshita, Phys. Rev. Lett. 75, 4728 (1995).
[3] M. E. Cage et al., IEEE Trans. Instrum. Meas. 38, 284 (1989).
[4] B. Taylor, Metrologia 31, 181 (1994).
[5] C. Schwob et al., Phys. Rev. Lett. 82, 4960 (1999).
[6] Th. Udem et al., Phys. Rev. Lett. 79, 2646 (1997).
[7] T. Beier et al., Phys. Rev. Lett. 88, 011603 (2002).
[8] E. Krüger et al., Metrologia 35, 203 (1998).
[9] M. P. Bradley et al., Phys. Rev. Lett. 83, 4510 (1999).
[10] Th. Udem et al., Phys. Rev. Lett. 82, 3568 (1999).
[11] D. S. Weiss et al., Phys. Rev. Lett. 70, 2706 (1993).
[12] B. C. Young, Ph.D. thesis, Stanford, 1997.
[13] J. M. Hensley, Ph.D. thesis, Stanford, 2001.
[14] S. B. Cahn et al., Phys. Rev. Lett. 79, 784 (1997).
[15] Atom Interferomtery, edited by P. Berman (Academic, New York, 1997), see pp. 281–282 and 379–381.
[16] M. Weitz et al., Appl. Phys. B 65, 713 (1997).
[17] S. Gupta et al., C.R. Acad. Sci. IV-Phys. 2, 479 (2001).
[18] S. Inouye et al., Science 285, 571 (1999).
[19] P. Juncar et al., Metrologia 17, 77 (1981).
[20] We scanned θ by electronically shifting the phase of the rf signal used to drive one of the two Bragg AOMs.
[21] The division of population into three output ports caused 74% ($<100\%$) contrast. We have seen $\approx 100\%$ contrast in a standard Mach-Zehnder interferometer.
[22] Y. Torii et al., Phys. Rev. A 61, 041602 (2000).
[23] T. L. Gustavson et al., Phys. Rev. Lett. 88, 020401 (2002).

Appendix B

Fifty-fold improvement in the number of quantum degenerate fermionic atoms

This appendix includes the following paper [6]: Z. Hadzibabic, S. Gupta, C.A. Stan, C.H. Schunck, M.W. Zwierlein, K. Dieckmann and W. Keterle, "Fifty-fold improvement in the number of quantum degenerate fermionic atoms", arXiV:cond-mat/ 0306050(2003), accepted in Phys. Rev. Lett.

Fifty-fold improvement in the number of quantum degenerate fermionic atoms

Z. Hadzibabic, S. Gupta, C.A. Stan, C.H. Schunck, M.W. Zwierlein, K. Dieckmann, and W. Ketterle

Department of Physics, MIT-Harvard Center for Ultracold Atoms, and Research Laboratory of Electronics,
MIT, Cambridge, MA 02139

(June 3, 2003)

We have produced a quantum degenerate ^{6}Li Fermi gas with up to 7×10^7 atoms, an improvement by a factor of fifty over all previous experiments with degenerate Fermi gases. This was achieved by sympathetic cooling with bosonic ^{23}Na in the $F = 2$, upper hyperfine ground state. We have also achieved Bose-Einstein condensation of $F = 2$ sodium atoms by direct evaporation.

PACS numbers: 05.30.Fk, 32.80.Pj, 39.25.+k, 67.60.-g

Over the last few years, there has been significant progress in the production of quantum degenerate atomic Fermi gases (^{40}K [1,2] and ^{6}Li [3–6]) and degenerate Bose-Fermi mixtures (^{7}Li-^{6}Li [3,4], ^{23}Na-^{6}Li [6], and ^{87}Rb-^{40}K [2]). These systems offer great promise for studies of new, interaction-driven quantum phenomena. The ultimate goal is the attainment of novel regimes of BCS-like superfluidity in a gaseous system [7–10]. The current efforts to induce and study strong interactions in a Fermi gas [11–20] are complemented with the ongoing efforts to improve fermion cooling methods, which would lead to lower temperatures and larger samples.

The main reason why studies of degenerate Fermi gases are still lagging behind the studies of atomic Bose-Einstein condensates (BECs), is the complexity of cooling methods. The Pauli exclusion principle prohibits elastic collisions between identical fermions at ultra-low temperatures, and makes evaporative cooling of spin-polarized fermionic samples impossible. For this reason, cooling of fermions must rely on some form of mutual or sympathetic cooling between two types of distinguishable particles, either two spin states of the same atom [1,5], or two different atoms [2–4,6]. A key element in fermion cooling is the design of better "refrigerators" for sympathetic cooling.

In this Letter, we report the first production of degenerate Fermi samples comparable in size with the largest alkali BECs [21]. We successfully cooled up to 7×10^7 magnetically trapped ^{6}Li atoms to below half the Fermi temperature (T_F). This is an improvement in atom number by a factor of 50 over the largest previously reported Fermi sea [20]. Further, in samples containing up to 3×10^7 atoms, we observed temperatures as low as $0.05\,T_F$, the lowest ever achieved. At these temperatures, the fractional occupation of the lowest energy state differs from unity by less than 10^{-8}.

As in our previous work [6], ^{6}Li atoms were magnetically trapped in the $F = 3/2$, upper hyperfine ground state, and sympathetically cooled by bosonic ^{23}Na. The crucial improvement was our achievement of forced evaporation of sodium in the $|F, m_F\rangle = |2, +2\rangle$, upper hyperfine ground state, producing large and stable BECs with up to 10^7 atoms. This allowed us to create a magneti-

cally trapped ^{23}Na-^{6}Li, Bose-Fermi mixture which is stable against spin-exchange collisions at all densities, and dramatically boosted our fermion atom number.
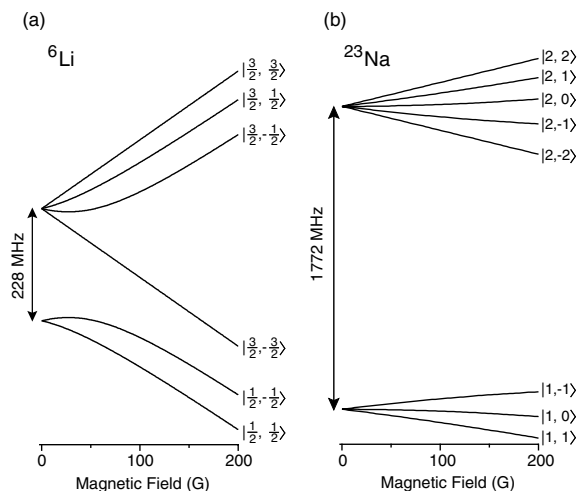

FIG. 1. Hyperfine structures of ^{6}Li and ^{23}Na. The states are labelled in the low field, $|F, m_F\rangle$ basis. (a) Due to finite trap depth of $\sim k_B \times 300\,\mu$K in the $|1/2, -1/2\rangle$ state, lithium can be efficiently loaded into the magnetic trap only in the upper, $F = 3/2$ hyperfine state. (b) Sodium is magnetically trappable in the $|1, -1\rangle$, and in the $|F = 2, m_F \geq 0\rangle$ states. Previously, sodium has been evaporatively cooled to BEC only in the $|1, -1\rangle$, lower hyperfine state.

The criteria for designing sympathetic cooling experiments include the heat capacity of the refrigerator, and the inter-species collisional properties, both elastic and inelastic. Large and stable ^{23}Na condensates are an appealing choice for sympathetic cooling of fermions. Further, a favorable mass ratio allows for simultaneous Zeeman slowing of ^{23}Na and ^{6}Li [6], and for simultaneous magnetic trapping without large differences in the gravitational sag. The inter-species collisional properties are generally not predictable, and have to be tested experimentally. In order to minimize all possible inelastic processes, the natural choice is to magnetically trap both species in their lower hyperfine ground states. However, at temperatures reachable by laser cooling ($\geq 300\,\mu$K), ^{6}Li can be efficiently magnetically trapped only in the

upper hyperfine state, $F = 3/2$ [4,6] (Fig. 1(a)). On the other hand, until now sodium has been successfully evaporated only in the lower, $F = 1$ hyperfine state. This was a limiting factor for sympathetic cooling of ^{6}Li, since the mixture of sodium in the lower, and lithium in the upper hyperfine state is not stable against spin-exchange collisions. The inelastic loss rate increases as the temperature is lowered and the density grows. In our previous work [6], we partially overcame this problem by transferring lithium atoms into the lower hyperfine state after an initial sympathetic cooling stage to $\sim 50 \,\mu$K. By achieving forced evaporative cooling and Bose-Einstein condensation of sodium in the $F = 2$ state, we have now realized a more robust sympathetic cooling strategy, and dramatically improved the size and temperature of a degenerate Fermi system.

We loaded $\sim 3 \times 10^9$ sodium and up to 10^8 lithium atoms in their upper hyperfine states from a two-species magneto-optical trap (MOT) into the magnetic trap. The adverse effect of light assisted collisions in a two-species MOT [6,22] was minimized by slightly displacing the two MOTs with respect to each other. During the typical 30 s of evaporative/sympathetic cooling, we observed no significant inelastic loss of lithium atoms (by three-body collisions or dipolar relaxation), the final number of degenerate atoms being at least half of the number initially loaded into the trap. On the other hand, we observed a favorable rate of elastic collisions between the two species, with the inter-species thermalization time being shorter than 1 s. Therefore, sodium atoms in the upper hyperfine state have ideal properties as a refrigerant for ^{6}Li.

Since our primary interest was cooling of fermions, we evaporated all sodium atoms in order to get lithium to the lowest possible temperatures. Even in our largest ^{6}Li samples, of $\sim 7 \times 10^7$ atoms, we achieved temperatures below $0.5 \, T_F$. Temperatures in the range $0.05 - 0.2 \, T_F$ could be achieved by reducing the ^{6}Li atom numbers only slightly, to $\sim 3 \times 10^7$. Such big clouds had a high enough optical density for crisp absorption imaging even after ballistic expansion to a size larger than one millimeter (Fig. 2(a)).

Temperatures were extracted from absorption images of expanding clouds released from the trap, using a semiclassical (Thomas-Fermi) fit to the Fermi-Dirac momentum distribution [6,23] (Fig. 2(b)). The quoted temperature range reflects both the shot-to-shot and day-to-day reproducibility, and the fact that the Fermi distribution is very insensitive to the temperature in this ultra-degenerate limit.

In these experiments, the ^{6}Li atom number was adjusted during the loading phase. Somewhat lower temperatures could possibly be achieved if the maximum lithium atom number was loaded into the magnetic trap, and then the hottest part of the cloud was selectively removed by direct evaporation once the sodium atom number dropped to the point where the heat capacities of the two species become comparable. However, at this point it appears unlikely that temperatures below $0.05 \, T_F$ could be conclusively extracted in order to differentiate the two strategies.
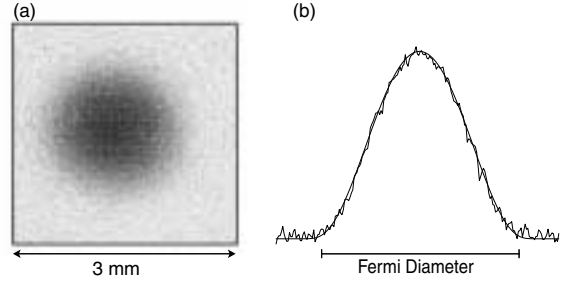

FIG. 2. Large and ultra-degenerate Fermi sea. (a) Absorption image of 3×10^7 ^{6}Li atoms released from the trap and imaged after 12 ms of free expansion. (b) Axial (vertical) line density profile of the cloud in (a). A semiclassical fit (thin line) yields a temperature $T = 93 \,\text{nK} = 0.05 \, T_F$. At this temperature, the high energy wings of the cloud do not extend visibly beyond the Fermi energy, indicated in the figure by the momentum-space Fermi diameter.

We also produced two-species degenerate Bose-Fermi mixtures with several million atoms in each species (Fig. 3). The mixture was stable, with a lifetime of several seconds, limited only by the three-body decay of the sodium cloud.
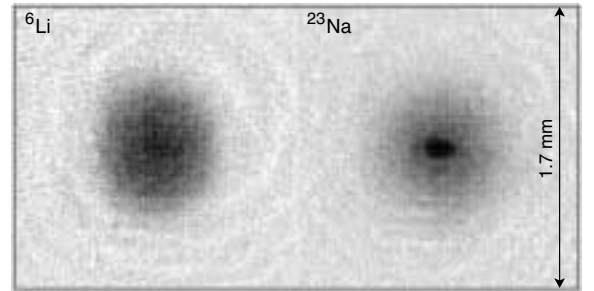
FIG. 3. Two-species mixture of degenerate Bose and Fermi gases. After release from the magnetic trap, both ^{6}Li and ^{23}Na clouds were imaged onto the same CCD camera using separate light pulses. The times of free expansion of the two gases could be varied independently. This dual-imaging technique allowed for optimizing the cooling strategy for either single- or two-species experiments. For the displayed image, the expansion times were $\tau_{Li} = 8 \,\text{ms}$ and $\tau_{Na} = 25 \,\text{ms}$, and the atom numbers were $N_{Li} \sim 10^7$ and $N_{Na} \sim 6 \times 10^6$. Sodium was cooled below the condensation temperature, corresponding to $\sim 0.2 \, T_F$ for the lithium cloud.

In the rest of the paper, we summarize the numerous steps which were introduced to prepare sodium in the $F = 2$ state as a refrigerant.

In contrast to ^{87}Rb, condensation of sodium by evaporative cooling was previously achieved only in the lower, $|1,-1\rangle$ hyperfine state. $F = 2$ sodium condensates could thus be studied only by transferring optically trapped $F = 1$ BECs into this state [24,25]. Condensation in the upper hyperfine state of sodium is more difficult than in the lower state for two reasons: (1) The requirement for efficient optical pumping in dense laser-cooled samples, and (2) an order of magnitude higher three-body loss rate coefficient [24].

The basic setup of our experiment is described in [6]. In 10 s, we collected typically $\sim 10^{10}$ ^{23}Na atoms, and $\sim 10^8$ ^{6}Li atoms in a magneto-optical trap (MOT). Typical MOT temperatures were 0.7-1 mK. Sodium was collected in a dark-SPOT variant of the MOT [26], and therefore most of the atoms were in the $F = 1$ hyperfine state. Lithium was collected in a "bright" MOT, with about 2/3 of the atoms in the $F = 3/2$ state.

Before the transfer into the magnetic trap, the atoms were optically pumped into the stretched hyperfine ground states, $|2,+2\rangle$ for ^{23}Na, and $|3/2,+3/2\rangle$ for ^{6}Li. A magnetic guide field of 3 G was applied, and the atoms were optically pumped for 2 ms, using σ^+ polarized light. To achieve both F (hyperfine) and m_F (Zeeman) pumping, two light beams where used for each species, resonant with the $|F = I \pm 1/2\rangle \rightarrow |F' = I \pm 1/2\rangle$ transitions. Here, I is the nuclear spin ($I = 3/2$ for ^{23}Na, and $I = 1$ for ^{6}Li), and F' is the total spin in the excited electronic state. In this way, almost all the lithium atoms could be pumped into the $|3/2,+3/2\rangle$ state. On the other hand, the density of sodium atoms in the dark-SPOT is $\geq 10^{11}$ cm^{-3}, and Zeeman pumping is notoriously difficult at such high densities. In our experiments, the fraction of atoms pumped into the $|2,+2\rangle$ state was limited to about 30 %, with most of the remaining atoms distributed among the other m_F sub-levels of the $F = 2$ manifold.

After the optical pumping stage, the atoms were loaded into a Ioffe-Pritchard magnetic trap with a radial gradient of 164 G/cm, and axial curvature of 185 G/cm^2. Sodium atoms in all three $|F = 2, m_F \geq 0\rangle$ states are (at least weakly) magnetically trappable (Fig. 1(b)). However, only pure $|2,+2\rangle$ samples are stable against inelastic spin-exchange collisions. A crucial step in preparing the samples for efficient forced evaporation was to actively remove $|F = 2, m_F = 0, +1\rangle$ atoms from the trap, before they engaged in inelastic collisions with the $|2,+2\rangle$ atoms. The atoms were loaded into a weak magnetic trap, with a high bias field of 80 G. This field splits the $F = 2$ Zeeman sub-levels by $\sim k_B \times 2.8$ mK. Since this splitting was larger than the temperature of the cloud, the different states could be resolved in microwave or rf spectroscopy, and the $|F = 2, m_F = 0, +1\rangle$ atoms could be selectively transferred to the untrapped $|F = 1, m_F = 0, +1\rangle$ lower hyperfine states. This transfer was done with a microwave sweep near the ^{23}Na hyperfine

splitting of 1.77 GHz. In this way, all the $|2,+2\rangle$ atoms initially loaded into trap could be preserved. We were even able to "recycle" some of the untrapped atoms by optically pumping them out of the $F = 1$ ground states, thus giving them a "second chance" to fall into the $|2,+2\rangle$ state. The final setup consisted of two microwave sweeps, the first of 0.8 s duration with the optical pumping light on, and the second of 2.4 s duration without the light. In this way, the overall transfer efficiency from the MOT to the magnetic trap was improved to about 35 %, comparable to our standard $F = 1$ BEC experiments [27].

After this purification of the $|2,+2\rangle$ sample, the magnetic trap was tightened by reducing the bias field to 3.8 G in 2.4 s. Resulting trapping frequencies were 204 Hz (400 Hz) radially, and 34 Hz (67 Hz) axially for the sodium (lithium) stretched state. This provided good conditions for forced runaway evaporation of sodium. Evaporation was done on the $|2,+2\rangle \rightarrow |1,+1\rangle$ microwave transition near 1.77 GHz. In contrast to radio-frequency evaporation, this insured that ^{6}Li was far off resonance. Further, microwave evaporation avoided any undesirable aspects of "incomplete evaporation" into the $|F = 2, m_F = 0, +1\rangle$ states, which could lead to inelastic losses [28].

After 15 s of evaporation, the sodium atoms reached a temperature of $T \sim 10 \,\mu$K. At this point, to avoid three-body losses in the $|2,+2\rangle$ state [24], the trap was weakened to frequencies of 49 Hz (96 Hz) radially, and 18 Hz (35 Hz) axially for sodium (lithium). The final evaporation to BEC took another 15 s. In this way, in the absence of lithium atoms, we could produce almost pure $|2,+2\rangle$ BECs containing up to 10 million atoms. The lifetime of the BEC in the weak trap was longer than 3 s. In contrast to our previous work [24,25], studies of $F = 2$ condensates are now possible without the added complexity of an optical trap.

In conclusion, by creating a superior refrigerant for sympathetic cooling of ^{6}Li, we have produced the coldest and by far the largest quantum degenerate Fermi gas so far. With the number of atoms comparable with the largest alkali BECs, and the temperatures reaching the practical detection limit, we have fully exploited the potential of laser and evaporative cooling to engineer samples of ultracold fermions. In analogy with Bose-Einstein condensates, we expect these large samples to insure sufficient signal-to-noise ratio for all the standard techniques of BEC research, such as velocimetry using long expansion times, rf spectroscopy with Stern-Gerlach separation during ballistic expansion, direct non-destructive imaging of the trapped clouds, and Bragg spectroscopy. The next challenge is to maintain a similar combination of number and temperature for an interacting two-component Fermi gas [19].

[1] B. DeMarco and D. S. Jin, Science **285**, 1703 (1999).

[2] G. Roati, F. Riboli, G. Modugno, and M. Inguscio, Phys. Rev. Lett. **89**, 150403 (2002).

[3] A. G. Truscott, K. E. Strecker, W. I. McAlexander, G. B. Partridge, and R. G. Hulet, Science **291**, 2570 (2001).

[4] F. Schreck, L. Khaykovich, K. L. Corwin, G. Ferrari, T. Bourdel, J. Cubizolles, and C. Salomon, Phys. Rev. Lett. **87**, 080403 (2001).

[5] S. R. Granade, M. E. Gehm, K. M. O'Hara, and J. E. Thomas, Phys. Rev. Lett. **88**, 120405 (2002).

[6] Z. Hadzibabic, C. A. Stan, K. Dieckmann, S. Gupta, M. W. Zwierlein, A. Görlitz, and W. Ketterle, Phys. Rev. Lett. **88**, 160401 (2002).

[7] M. Houbiers and H. T. C. Stoof, Phys. Rev. A **59**, 1556 (1999).

[8] M. Holland, S. J. J. M. F. Kokkelmans, M. L. Chiofalo, and R. Walser, Phys. Rev. Lett. **87**, 120406 (2001).

[9] Y. Ohashi and A. Griffin, Phys. Rev. Lett. **89**, 130402 (2002).

[10] W. Hofstetter, J. I. Cirac, P. Zoller, E. Demler, and M. D. Lukin, Phys. Rev. Lett. **89**, 220407 (2002).

[11] T. Loftus, C. A. Regal, C. Ticknor, J. L. Bohn, and D. S. Jin, Phys. Rev. Lett. **88**, 173201 (2002).

[12] K. Dieckmann, C. A. Stan, S. Gupta, Z. Hadzibabic, C. H. Schunck, and W. Ketterle, Phys. Rev. Lett. **89**, 203201 (2002).

[13] K. M. O'Hara, S. L. Hemmer, S. R. Granade, M. E. Gehm, J. E. Thomas, V. Venturi, E. Tiesinga, and C. J. Williams, Phys. Rev. A **66**, 041401 (2002).

[14] C. A. Regal, C. Ticknor, J. L. Bohn, and D. S. Jin, Phys. Rev. Lett. **90**, 053201 (2003).

[15] K. M. O'Hara, S. L. Hemmer, M. E. Gehm, S. R. Granade, and J. E. Thomas, Science **298**, 2179 (2002).

[16] M. E. Gehm, S. L. Hemmer, S. R. Granade, K. M. O'Hara, and J. E. Thomas, arXiv:cond-mat/0212499 (2002).

[17] C. A. Regal and D. S. Jin, arXiv:cond-mat/0302461 (2003).

[18] T. Bourdel, J. Cubizolles, L. Khaykovich, K. M. F. Magalhães, S. J. J. M. F. Kokkelmans, G. V. Shlyapnikov, and C. Salomon, arXiv:cond-mat/0303079 (2003).

[19] S. Gupta, Z. Hadzibabic, M. W. Zwierlein, C. A. Stan, K. Dieckmann, C. H. Schunck, E. G. M. van Kempen, B. J. Verhaar, and W. Ketterle, Science (2003).

[20] C. A. Regal, C. Ticknor, J. L. Bohn, and D. S. Jin, arXiv:cond-mat/0305028 (2003).

[21] J. R. Abo-Shaeer, C. Raman, J. M. Vogels, and W. Ketterle, Science **292**, 476 (2001).

[22] V. Wippel, C. Binder, and L. Windholz, Eur. Phys. J. D **21**, 101 (2002).

[23] D. A. Butts and D. S. Rokhsar, Phys. Rev. A **55**, 4346 (1997).

[24] A. Görlitz, T. L. Gustavson, A. E. Leanhardt, R. Löw, A. P. Chikkatur, S. Gupta, S. Inouye, D. E. Pritchard, and W. Ketterle, Phys. Rev. Lett. **90**, 090401 (2003).

[25] A. E. Leanhardt, A. Görlitz, A. P. Chikkatur, D. Kielpinski, Y. Shin, D. E. Pritchard, and W. Ketterle, Phys. Rev. Lett. **89**, 190403 (2002).

[26] W. Ketterle, K. B. Davis, M. A. Joffe, A. Martin, and D. E. Pritchard, Phys. Rev. Lett. **70**, 2253 (1993).

[27] M.-O. Mewes, M. R. Andrews, N. J. van Druten, D. M. Kurn, D. S. Durfee, and W. Ketterle, Phys. Rev. Lett. **77**, 416 (1996).

[28] B. Desruelle, V. Boyer, S. G. Murdoch, G. Delannoy, P. Bouyer, and A. Aspect and M. Lécrivain, Phys. Rev. A **60**, R1759 (1999).

Appendix C

Decay of an Ultracold Fermionic Lithium Gas near a Feshbach Resonance

This appendix includes the following paper [4]: K. Dieckmann, C.A. Stan, S. Gupta, Z. Hadzibabic, C.H. Schunck and W. Ketterle, "Decay of an Ultracold Fermionic Lithium Gas near a Feshbach Resonance", *Phys. Rev. Lett.* **89**, 203201 (2002).

Decay of an Ultracold Fermionic Lithium Gas near a Feshbach Resonance

K. Dieckmann, C. A. Stan, S. Gupta, Z. Hadzibabic, C. H. Schunck, and W. Ketterle

Department of Physics, MIT-Harvard Center for Ultracold Atoms,
and Research Laboratory of Electronics, MIT, Cambridge, Massachusetts 02139

We studied the magnetic field dependence of the inelastic decay of an ultracold, optically trapped fermionic ^{6}Li gas of different spin compositions. The spin mixture of the two lowest hyperfine states showed two decay resonances at 550 and 680 G, consistent with the predicted Feshbach resonances for elastic s-wave collisions. The observed lifetimes of several hundred ms are much longer than the expected time for Cooper pair formation and the phase transition to superfluidity in the vicinity of the Feshbach resonance.

Interactions between atoms can be strongly modified by tuning magnetic fields to Feshbach resonances where a molecular state has the same energy as the colliding atoms. This mechanism has been used to dramatically alter the properties of ultracold bosonic gases [1–4]. For degenerate Fermi gases, such control over the interaction strength is crucial in the search for a superfluid phase transition. For dilute Fermi gases, the predicted phase transition occurs at temperatures that are experimentally not accessible [5], unless the scattering length is resonantly enhanced. In this case, as was pointed out by [6–10], the transition temperature can be comparable to the temperatures achieved in current experiments [11–16].

Promising candidates for an experimental observation of fermionic superfluidity are ^{6}Li and ^{40}K. For an optically trapped mixture of two spin states of ^{40}K, a Feshbach resonance has been observed by measuring the thermalization time of the gas [17]. For an optically trapped spin mixture of the two lowest Zeeman states of ^{6}Li, a wide s-wave Feshbach resonance has been predicted first by [18]. Experiments with ^{6}Li have so far observed only a magnetic field dependence of the elastic cross section far away from the predicted resonance [14]. Near Feshbach resonances, the enhancement of the scattering length is usually accompanied by enhanced inelastic collisions which lead to rapid trap loss. This signature was used to identify Feshbach resonances in bosonic gases [20–22]. However, inelastic losses have also posed a severe limitation for experiments near Feshbach resonances, in particular, at high atomic densities. The superfluid phase transition for fermions will be observable only if the time for the formation of Cooper pairs is shorter than the decay time of the gas. For fermions, inelastic decay in the s-wave channel can be suppressed due to the Pauli exclusion principle. However, even in the zero-temperature limit the kinetic energy of the cloud is of the order of the Fermi energy. Therefore, inelastic collisions for higher partial waves are expected to limit the lifetime of the gas.

This Letter is the first report on the study of inelastic collisions in a fermionic system near Feshbach resonances. We have observed resonant magnetic field dependent inelastic decay of an ultracold, optically trapped spin mixture of ^{6}Li.

The ultracold lithium samples were prepared by sympathetic cooling of ^{6}Li by ^{23}Na as described previously [15]. The remaining ^{23}Na atoms were removed from the magnetic trap by rf induced spin flips to untrapped states. This typically produced 3×10^5 lithium atoms in the $|1/2, -1/2\rangle$ state at a temperature of 400 nK, equal to half the Fermi temperature. The atoms were transferred into an optical trap formed by a single far detuned beam with up to 1 W of power at 1064 nm. The beam had a 14 μm waist and was aligned horizontally along the symmetry axis of the magnetic trap. This generated a 175 μK deep trapping potential, with 12 Hz radial and 200 Hz axial trapping frequencies. Prior to the transfer, the cloud was adiabatically decompressed in the radial direction during 1 s to improve the spatial overlap with the optical trap. After this stage, the trap frequencies in the magnetic trap were 149 Hz radially and 26 Hz axially. We then adiabatically ramped up the power of the optical trap over 500 ms. Subsequently, the magnetic trapping fields were ramped down in 100 ms, leaving a 1.5 G guiding field along the trap axis. After the transfer, the cloud contained 3×10^5 atoms at 3×10^{13} cm^{-3} peak density and 22 μK temperature, close to the 21 μK Fermi temperature. We attribute the rise in temperature relative to the Fermi temperature to residual excitations during the transfer into the optical trap. (We often observed axial oscillations of the cloud after the transfer.)

We studied inelastic decay for three different spin compositions of the cloud. The lithium atoms were either trapped purely in the lowest ($|1\rangle$), or the second to lowest ($|2\rangle$) energy state, or in a 50%-50% mixture of these two Zeeman states. At low magnetic fields, the states $|1\rangle$ and $|2\rangle$ correspond to the $|F, m_F\rangle = |1/2, +1/2\rangle$ and $|1/2, -1/2\rangle$ states, respectively. A full transfer $|1/2, -1/2\rangle \rightarrow |1/2, +1/2\rangle$ was done at low magnetic

field by applying a 1 s rf-driven adiabatic passage between the two states, which was > 95% complete. The spin mixture was produced by a faster, nonadiabatic rf sweep of 200 ms duration. The population of the states was analyzed by applying a 7 G/cm magnetic field gradient along the trap axis with a 6.5 G offset field in the center, and reducing the strength of the optical confinement. This resulted in full spatial separation of the two spin states in the optical trap. Resonant absorption imaging was used to determine the atom number in each of the spin states. Using a full transfer we compared the absorption cross sections for circularly polarized light for the two spin states and found a ratio of 1:1.2. Taking this into consideration, we were able to control the relative population of the spin states by rf sweeps with an accuracy of ±4%.

In order to study the decay of the cloud near the Feshbach resonance, predicted to occur at about 800 G [18], we applied magnetic fields up to 900 G using the antibias coils of the cloverleaf magnetic trap [23]. The magnetic field strength was calibrated in two independent ways to 2% accuracy. For calibration of magnetic fields up to 100 G, we loaded ^{23}Na into the optical trap and drove rf transitions to magnetically untrapped states. Resonances were observed by measuring the remaining atom number after recapture into the magnetic trap. As a second method at about 700 G, we used direct absorption imaging of ^{6}Li in the optical trap in the presence of higher magnetic fields. The magnetic field values were then derived from the frequency shifts of the observed resonances from the lithium D2 line. We also verified that drifts of the magnetic field during the pulses, occurring from thermal expansion of the coils due to the high current load, were negligible.

We measured the magnetic field dependence of the decay by measuring the atom number at two different times, 50 and 500 ms, after switching on the magnetic field within about 4 ms. For measuring the remaining atom number, the magnetic field was rapidly switched off within 100 μs, and the cloud was probed by absorption imaging at low magnetic field. Normalizing the number at long time to the number at short time made the measurement less sensitive to atom number drifts and initial losses from the optical trap. These losses can occur due to the sloshing motion of the cloud and due to initial evaporation.

For the cloud purely in state $|2\rangle$, we observed no significant decay over the entire range of magnetic fields, as can be seen in Fig. 1(a). This also confirmed that during the measurement interval, one-body decay (e.g., due to collisions with particles from the background gas) was negligible.

The surviving fraction of the mixture is shown in Fig. 1(c). No significant decay was observed at low magnetic fields. At higher magnetic field, we found two decay resonances. A strong resonance occurred at 680 G with considerable losses over a range of approximately 100 G.

At even higher magnetic fields, the decay persisted at a weaker but constant level. In a more detailed scan, shown in Fig. 1(d), a second, much weaker and narrower resonance was found at 550 G, with an approximate width of
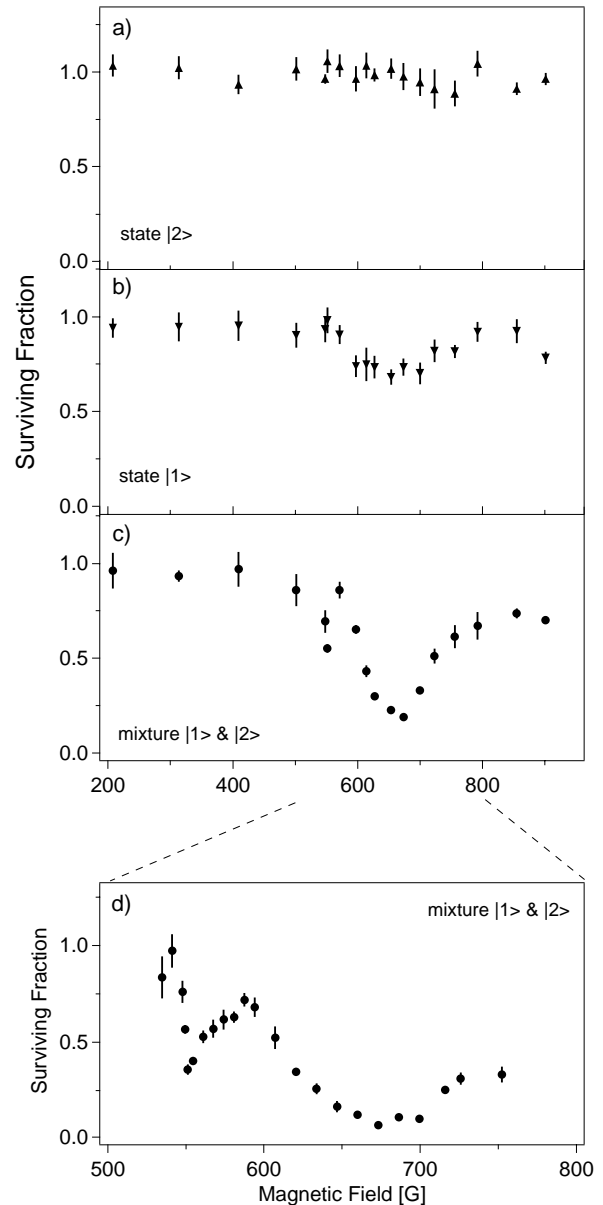
FIG. 1. Magnetic field dependence of inelastic decay in clouds of fermionic ^{6}Li. The fraction of atoms remaining after the 500 ms magnetic field pulse is shown for different spin compositions of the cloud. (a) For the state $|2\rangle$, no significant loss was observed. (b) The energetically lowest state $|1\rangle$ exhibits a weak decay resonance at ≈ 680 G. (c) The 50%-50% mixture of two spin states shows two decay resonances, at 550 and 680 G. (d) The two resonances are shown with higher density of data points and for 2 s magnetic field pulses. Each data point represents an average of three measurements.

20 G. The weaker resonance became more pronounced after 2 s of dwell time in the magnetic field, whereas the stronger resonance showed "saturation" broadening.

We also measured the time evolution of the atom number at the two resonances. For a two-body (three-body) process the loss rate of atoms $\dot{N}$ is proportional to N^2 (N^3), where N is the number of trapped atoms. The decay curves at 680 G are shown in Fig. 2. At both resonances we found that the values for $1/N$ showed a linear dependence on time, characteristic for a two-body process. In order to test for three-body decay we plotted the same data as $1/N^2$. The nonlinear behavior is not compatible with a simple three-body decay process.

Another experimental observation is the almost complete disappearance of the mixed cloud in Fig. 1(d). A resonantly enhanced three-body process would involve two atoms of opposite spin colliding, and a third in either of the spin states. Starting with a 50%-50% mixture, the decay would stop when all atoms in state $|1\rangle$ (or in state $|2\rangle$) are used up. Therefore, three-body decay can be consistent with the observation of complete disappearance only if the decay rate does not depend on the spin state of the third particle. In case of strongly different rates for the two spin orientations, the surviving fraction could not drop below 25%.

With the observation of two resonances and the position of the strongest decay of the main resonance deviat-

FIG. 2. Decay of the atom number at 680 G. (a) The data plotted as $1/N$ show a linear time dependency, consistent with two-body decay. (b) The same data plotted as $1/N^2$ clearly show nonlinear dependency. For the resonance at 550 G, the comparison of least square fits also revealed consistency with a two-body decay.

ing from the theoretical prediction [18], the question arises whether the observed decay of the spin mixture can be interpreted as a signature of the Feshbach resonance for elastic s-wave collisions. After the submission of this paper new improved theoretical calculations exhibited a second narrow Feshbach resonance for elastic collisions in the s-wave channel at 550 G [19], in good agreement with the position of the narrow decay resonance. The predicted magnetic field for the main resonance is 860 G. However, due to the huge width of the resonance it seems possible that the decay observed at 680 G is related to this s-wave resonance.

The measured decay curves suggest a two-body type of decay. Because of the Pauli exclusion principle dipolar relaxation is not possible in the s-wave channel [24]. Dipolar relaxation in the p-wave channel is possible, as even in the zero-temperature limit the kinetic energy of the cloud is of the order of the Fermi energy, and collisions in the p-wave channel do not completely freeze out. However, no occurrences of resonances in the dipolar decay are theoretically predicted [25].

Therefore, it is most likely that the observed decay is a signature of the Feshbach resonances for the elastic collisions, resulting in enhanced three-body decay. At present no exact theoretical description for the three-body decay mechanism of fermions near a Feshbach resonance is available. Three-body decay is not supported by the measured decay curves. However, one possibility is that the decay curve is affected by a change in temperature. An accurate measurement of the temperature was difficult due to technical reasons and a low signal-to-noise ratio, as the absorption signal drops significantly during the decay. If the sample had cooled down during the decay (e.g., due to an energy dependence of the loss rate) it could speed up the decay in a way that three-body loss results in a decay curve similar to a curve for two-body losses at constant temperature. Another possibility for the deviation from a three-body decay curve would be heating due to three-body recombination followed by trap loss due to evaporation, or other processes involving secondary collisions [26]. It should be noted that the observed resonances do not resemble the predicted magnetic field dependence for elastic collisions [18]. Therefore, our decay data cannot be explained by elastic collisions leading to evaporation.

We also observed resonant decay at 680 G of a cloud purely in state $|1\rangle$, as shown in Fig. 1(b). The fact that this resonance is at the same magnetic field as for the mixture suggests that the observed loss is due to a contamination of the cloud with atoms in state $|2\rangle$. For three-body of decay, our measured $> 95\%$ purity of the preparation of state $|1\rangle$ allows for a maximum of 15% decay of the cloud, compared to the measured 21%. Further measurements are needed to investigate whether there is an enhancement of losses by secondary collisions, or whether there is a decay mechanism for atoms purely in state $|1\rangle$.
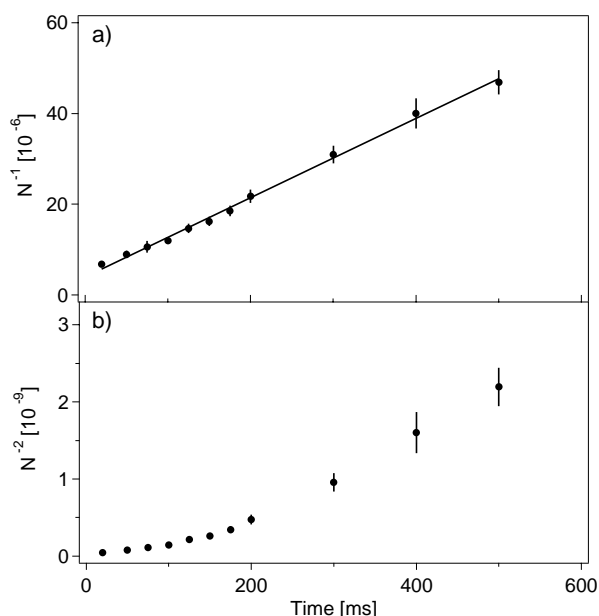
In conclusion, we observed two decay resonances for the ^{6}Li spin mixture and one resonance in the lowest spin state. Comparing our observations with recent theoretical calculations which exhibit two s-wave Feshbach resonances suggests that the observed decay is a signature of those resonances. Even on resonance, the observed decay happened on a time scale longer than the trap oscillation time, the time for elastic collisions, and the expected submillisecond time needed for the formation of Cooper pairs [27,28]. Therefore, the ^{6}Li system is well suited for the study of an interacting Fermi gas in the vicinity of an elastic Feshbach resonance, in particular, for the search for the phase transition to a superfluid state.

Note added.—After the submission of this paper several groups reported related results. Measurements of the elastic cross section near the zero crossing associated with the Feshbach resonance have recently been performed by [19,29]. Inelastic decay of ^{6}Li fermionic clouds near the Feshbach resonance was recently also observed in the groups of Thomas [19], and C. Salomon, and for ^{40}K in the group of D. S. Jin.

[1] S. Inouye, M. R. Andrews, J. Stenger, H.-J. Miesner, D. M. Stamper-Kurn, and W. Ketterle, Nature (London) **392**, 151 (1998).

[2] P. Courteille, R. S. Freeland, D. J. Heinzen, F. A. van Abeelen, and B. J. Verhaar, Phys. Rev. Lett. **81**, 69 (1998).

[3] A. J. Kerman, V. Vuletić, C. Chin, and S. Chu, Phys. Rev. Lett. **82**, 1406 (1999).

[4] S. L. Cornish, N. R. Claussen, J. L. Roberts, E. A. Cornell, and C. E. Wieman, Phys. Rev. Lett. **85**, 1795 (2000).

[5] A. J. Leggett, J. Phys. (Paris) **41**, C7 (1980).

[6] M. Houbiers, R. Ferwerda, H. T. C. Stoof, W. I. McAlexander, C. A. Sackett, and R. G. Hulet, Phys. Rev. A **56**, 4864 (1997).

[7] E. Timmermans, K. Furuya, P. W. Milonni, and A. K. Kerman, Phys. Lett. A **285**, 228 (2001).

[8] M. J. Holland, S. J. J. M. F. Kokkelmans, M. L. Chiofalo, and R. Walser, Phys. Rev. Lett. **87**, 120406 (2001).

[9] Y. Ohashi and A. Griffin, Phys. Rev. Lett. **89**, 130402 (2002).

[10] J. N. Milstein, S. J. J. M. F. Kokkelmans, and M. J. Holland, Phys. Rev. A **66**, 043604 (2002).

[11] B. DeMarco, S. B. Papp, and D. S. Jin, Phys. Rev. Lett. **86**, 5409 (2001).

[12] A. G. Truscott, K. E. Strecker, W. I. McAlexander, G. B. Partridge, and R. G. Hulet, Science **291**, 2570 (2001).

[13] F. Schreck, L. Khaykovich, K. L. Corwin, G. Ferrari, T. Bourdel, J. Cubizolles, and C. Salomon, Phys. Rev. Lett. **87**, 080403 (2001).

[14] S. R. Granade, M. E. Gehm, K. M. O'Hara, and J. E. Thomas, Phys. Rev. Lett. **88**, 120405 (2002).

[15] Z. Hadzibabic, C. A. Stan, K. Dieckmann, S. Gupta, M. W. Zwierlein, A. Görlitz, and W. Ketterle, Phys. Rev. Lett. **88**, 160401 (2002).

[16] G. Roati, F. Riboli, G. Modungo, and M. Inguscio, Phys. Rev. Lett. **89**, 150403 (2002).

[17] T. Loftus, C. A. Regal, C. Ticknor, J. L. Bohn, and D. S. Jin, Phys. Rev. Lett. **88**, 173201 (2002).

[18] M. Houbiers, H. T. C. Stoof, W. I. McAlexander, and R. G. Hulet, Phys. Rev. A **57**, R1497 (1998); see also Ref. [19].

[19] K. M. O'Hara, S. L. Hemmer, S. R. Granade, M. E. Gehm, J. E. Thomas, V. Venturi, E. Tiesinga, and C. J. Williams, cond-mat/0207717.

[20] J. Stenger, S. Inouye, M. R. Andrews, H.-J. Miesner, D. M. Stamper-Kurn, and W. Ketterle, Phys. Rev. Lett. **82**, 2422 (1999).

[21] J. L. Roberts, N. R. Claussen, S. L. Cornish, and C. E. Wieman, Phys. Rev. Lett. **85**, 728 (2000).

[22] C. Chin, V. Vuletić, A. J. Kerman, and S. Chu, Phys. Rev. Lett. **85**, 2717 (2000).

[23] M.-O. Mewes, M. R. Andrews, N. J. van Druten, D. M. Kurn, D. S. Durfee, and W. Ketterle, Phys. Rev. Lett. **77**, 416 (1996).

[24] H. T. C. Stoof, J. M. V. A. Koelman, and B. J. Verhaar, Phys. Rev. B **38**, 4688 (1988).

[25] S. J. J. M. F. Kokkelmans and E. Tiesinga (private communication).

[26] D. Petrov (private communication).

[27] M. Houbiers and H. T. C. Stoof, Phys. Rev. A **59**, 1556 (1999).

[28] E. Timmermans, Phys. Rev. Lett. **87**, 240403 (2001).

[29] M. B. S. Jochim, G. Hendl, J. H. Denschlag, R. Grimm, A. Mosk, and M. Weidemüller, cond-mat/0207098.

Appendix D

Collisions in Zero Temperature Fermi Gases

This appendix includes the following paper [8]: S. Gupta, Z. Hadzibabic, J.R. Anglin and W. Keterle, "Collisions in Zero Temperature Fermi Gases", arXiV:cond-mat/ 0307088(2003).

Collisions in zero temperature Fermi gases

Subhadeep Gupta, Zoran Hadzibabic, James R. Anglin, and Wolfgang Ketterle

Department of Physics, MIT-Harvard Center for Ultracold Atoms, and Research Laboratory of Electronics,
MIT, Cambridge, MA 02139
(July 3, 2003)

We examine the collisional behavior of two-component Fermi gases released at zero temperature from a harmonic trap. Using a phase-space formalism to calculate the collision rate during expansion, we find that Pauli blocking plays only a minor role for momentum changing collisions. As a result, for a large scattering cross-section, Pauli blocking will not prevent the gas from entering the collisionally hydrodynamic regime. In contrast to the bosonic case, hydrodynamic expansion at very low temperatures is therefore not evidence for fermionic superfluidity.

The last few years have seen rapid progress in the field of ultracold atomic Fermi gases [1–6]. Most recently, regimes of strong interactions have been observed in these gases near Feshbach resonances [7–10]. Studies of these systems are of particular importance because of the possibility of creating BCS-like superfluids [11,12]. Such a realization would establish highly controllable model systems for studying novel regimes of fermionic superfluidity.

A unique feature of atomic systems is the ability to analyze the gas by turning off the trapping potential and observing the expansion. The expansion behavior can reveal the momentum distribution and the effects of mean-field interactions and collisions. Hydrodynamic behavior can be easily detected when the gas is released from an anisotropic atom trap. In that case, the spatial anisotropy of the cloud reverses during free expansion. This is caused by the larger pressure gradient along the tightly confining direction, which leads to a faster expansion, and subsequent reversal of the spatial anisotropy. This anisotropic expansion was used to identify the formation of the Bose-Einstein condensate [13,14].

A BEC obeys the hydrodynamic equations of a superfluid [15]. However collisional hydrodynamics arising from a high elastic collision rate also results in anisotropic expansion [16,17]. Thus, the normal component can also expand anisotropically [18]. For the bosonic case, two key points make the distinction between the two fractions obvious: (i) At the typical transition temperature, the BEC has much less energy than the normal cloud, so the two components are clearly separated in size. (ii) The scattering rate needed to achieve condensation is usually not large enough that the normal gas is in the hydrodynamic regime. For these two reasons, the appearance of a dense anisotropic cloud during expansion is considered to be the "smoking-gun" for the formation of a Bose-Einstein condensate.

A superfluid Fermi gas is predicted to obey the superfluid hydrodynamic equations of motion [19–22] and therefore should show strong anisotropic expansion when released from an anisotropic harmonic trap [22]. The recent observation of anisotropic expansion of an ultracold, interacting, two-spin fermionic mixture [7–9] has created considerable excitement and raised the question under what conditions is this expansion a signature of fermionic superfluidity and not of collisional hydrodynamics. There are two major differences from the bosonic case: (i) Since the energy of ultracold fermions always remains on the order of the Fermi energy, the size in expansion for both normal and superfluid components will be similar. (ii) Current efforts towards inducing BCS pairing all take place in strongly interacting systems. This results in a large scattering rate modified only by the effects of Pauli blocking at low temperatures.

The interpretation of the observed anisotropic expansion in strongly interacting Fermi gases is therefore critically dependent on the role of Pauli blocking of collisions during the expansion. The tentative interpretation of anisotropic expansion as superfluid hydrodynamics [7] was based on the assessment that collisions are strongly suppressed at sufficiently low temperatures [7,23–28].

Here we show generally that the collision rate becomes independent of temperature and prevails even at zero temperature, if the Fermi surface is strongly deformed. This happens in an extreme way during ballistic expansion. In the small cross-section limit, we find that less than half of the total number of momentum changing collisions is suppressed. For a large scattering cross-section, the absence of suppression results in strong collisional behavior of normal Fermi gases during expansion for all initial temperatures. This result has the important consequence of rendering expansion measurements of Fermi gases near Feshbach resonances ambiguous for differentiating between superfluid and normal components.

We first consider the expansion of a single component Fermi gas. At ultralow temperatures, fermionic antisymmetry prevents s-wave scattering in a single component and renders the gas completely collisionless. The phase space occupation $f(x_1, x_2, x_3, p_1, p_2, p_3) = f(\mathbf{x}, \mathbf{p})$ at zero temperature in a harmonic trap with frequencies $(\omega_1, \omega_2, \omega_3)$ can be written as

$$f(\mathbf{x}, \mathbf{p}) = \Theta(E_F - \Sigma_i m\omega_i^2 x_i^2/2 - \Sigma_i p_i^2/2m)$$

where m is the particle mass, Θ is the Heaviside step

function defined as $\Theta(x) = 0(1)$ for $x \le 0(x > 0)$ and $E_F = \hbar(6N\Pi_i\omega_i)^{1/3}$ is the Fermi energy for N particles. At time $t = 0$, the trapping potential is turned off suddenly, allowing the gas to expand freely. At $t = 0$, the momentum space Fermi surface at $\mathbf{x} = (x_1, x_2, x_3)$ is

$$\Sigma_i p_i^2/2m = E_F - \Sigma_i m\omega_i^2 x_i^2/2, \tag{1}$$

a sphere of radius $\sqrt{2m(E_F - \Sigma_i m\omega_i^2 x_i^2/2)}$. In this non-interacting system, the evolution of the Fermi surface can be derived from the simple evolution law for ballistic expansion $\mathbf{x}(0) = \mathbf{x}(t) - \mathbf{p}t/m$. Substituting this in Eq. 1, we obtain:

$$\Sigma_i \frac{(1+\omega_i^2 t^2)}{2m}\left(p_i - \frac{mx_i}{t}\frac{\omega_i^2 t^2}{1+\omega_i^2 t^2}\right)^2 = E_F - \Sigma_i \frac{m\omega_i^2 x_i^2}{2(1+\omega_i^2 t^2)}, \tag{2}$$

which is an ellipsoid with generally unequal axes $\sqrt{2m(E_F - \Sigma_i \frac{m\omega_i^2 x_i^2}{2(1+\omega_i^2 t^2)})}(\frac{1}{\sqrt{1+\omega_1^2 t^2}}, \frac{1}{\sqrt{1+\omega_2^2 t^2}}, \frac{1}{\sqrt{1+\omega_3^2 t^2}})$. The anisotropy of the Fermi surface during expansion can be understood generally by noting that for long times t, at any position $\mathbf{x}$, the spread in momentum $\Delta p_i(t)$ can only arise from the initial spread in position $\Delta x_i(0)$. For anisotropic traps this gives rise to an anisotropic momentum distribution during ballistic expansion. For a mixture of two spin states, this deformation of the Fermi surface from a sphere into an anisotropic ellipsoid removes Pauli blocking of final states and allows collisions, as will be shown.

The momentum distribution at position $\mathbf{x}$ given by Eq. 2, also allows us to simply calculate the spatial density distribution as the volume of the momentum-space ellipsoid,

$$n(\mathbf{x}, t) = \frac{4}{3}\pi\left(\frac{2mE_F}{h^2}\right)^{3/2}\frac{(1 - \frac{m}{2E_F}\Sigma_i \frac{\omega_i^2 x_i^2}{1+\omega_i^2 t^2})^{3/2}}{\Pi_i(1+\omega_i^2 t^2)^{1/2}}, \quad (3)$$

in agreement with other derivations [29]. For long expansion times t, the spatial distribution becomes isotropic, mirroring the isotropic momentum distribution in the trap.

Specializing to the experimentally relevant case of a cylindrically symmetric trap, ballistic expansion deforms the local Fermi surface into a momentum ellipsoid of cylindrical symmetry with aspect ratio $\sqrt{\frac{1+\omega_z^2 t^2}{1+\omega_\perp^2 t^2}}$ (Fig. 1(a,b)). Here $\omega_\perp (\omega_z)$ is the radial (axial) trapping frequency. For long times t, this deformation reaches the asymptotic aspect ratio $\omega_z/\omega_\perp = \lambda$, the initial spatial aspect ratio in the trap.

Now consider an equal mixture of two spin states which interact via a finite s-wave scattering length. We assume that the trapping frequencies are identical for the two states (standard experimental conditions) and specialize to the usual case of two-body elastic collisions in the

local-density approximation. These collisions have an appealing geometrical picture in the local phase-space description (Fig. 1(c)). Each elastic collision involves one particle from each spin state. We label with $\mathbf{p}$'s and $\mathbf{q}$'s the momenta of the two different spin states. Consider the collision $\mathbf{p_1} + \mathbf{q_1} \to \mathbf{p_2} + \mathbf{q_2}$. Conservation of momentum and kinetic energy mandates $\mathbf{p_2} + \mathbf{q_2} = \mathbf{p_1} + \mathbf{q_1}$ and $|\mathbf{p_2} - \mathbf{q_2}| = |\mathbf{p_1} - \mathbf{q_1}|$. These relations restrict $\mathbf{p_2}$ and $\mathbf{q_2}$ to lie on diametrically opposite ends of the sphere with $\mathbf{p_1} - \mathbf{q_1}$ as a diameter. The deformation of the Fermi surface during expansion opens up unoccupied final states $\mathbf{p_2}, \mathbf{q_2}$ and therefore allows collisions to take place even in a zero temperature Fermi gas (Fig. 1(c)).
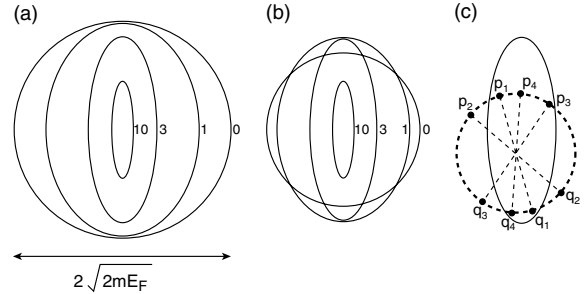

FIG. 1. (a) Deformation of the momentum space Fermi surface at $\mathbf{x} = \mathbf{0}$, from a sphere to an ellipsoid during expansion from an anisotropic harmonic trap. The case of cylindrical symmetry is shown, where the three-dimensional distribution is symmetric about the vertical axis. The parameters chosen are an aspect ratio $\lambda = 0.2$ and expansion times $\omega_\perp t = 0,1,3$ and 10. (b) The deformation at a position radially displaced by $\sqrt{E_F/m\omega_\perp^2}$. (c) Geometrical representation of collisions in momentum space. The two spin states have identical distributions. Three different types of collisions are shown for particles with initial momenta $\mathbf{p_1}$ and $\mathbf{q_1}$ - none, one or both of the final states are occupied.

The effect of collisions can be formally calculated from the Boltzmann transport equation for the evolution of the phase space distribution $f(\mathbf{x}, \mathbf{p}, t)$. In the absence of external potentials and neglecting mean field we have [30]:

$$\frac{\partial f}{\partial t} + \mathbf{v}.\frac{\partial f}{\partial \mathbf{x}} = \Gamma_{\text{coll}}[f] \tag{4}$$

where $\mathbf{v} = \mathbf{p}/m$ and $\Gamma_{\text{coll}}[f]$ describes the effect of collisions. Collisions attempt to restore local equilibrium by countering the deformation of the momentum space Fermi surface during free expansion (Eq. 2).

$\Gamma_{\text{coll}}[f]$ can be written as the collision integral:

$$\Gamma(\mathbf{x}, \mathbf{p_1}, t) = -\frac{\sigma}{4\pi h^3}\int_{(\mathbf{x},t)} d^3q_1 d^2\Omega \frac{|\mathbf{p_1} - \mathbf{q_1}|}{m} \times$$
$$[f(\mathbf{p_1})f(\mathbf{q_1})(1 - f(\mathbf{p_2}))(1 - f(\mathbf{q_2}))$$
$$- f(\mathbf{p_2})f(\mathbf{q_2})(1 - f(\mathbf{p_1}))(1 - f(\mathbf{q_1}))] \tag{5}$$

where σ is the momentum-independent scattering cross-section, $f(\mathbf{p_i}) = f(\mathbf{x}, \mathbf{p_i}, t)$, $f(\mathbf{q_i}) = f(\mathbf{x}, \mathbf{q_i}, t)$ and Ω points along $\mathbf{p_2} - \mathbf{q_2}$. The integral over $\mathbf{q_1}$ is over the momentum ellipsoid at position $\mathbf{x}$ and time t for one of the spin states. The first term in the integrand is the collision rate for the process $\mathbf{p_1} + \mathbf{q_1} \rightarrow \mathbf{p_2} + \mathbf{q_2}$. The second term corresponds to the reverse process $\mathbf{p_2} + \mathbf{q_2} \rightarrow \mathbf{p_1} + \mathbf{q_1}$, and ensures that only distribution changing collisions contribute.

Pauli blocking is expressed in the suppression factors for the final states $(1 - f)$ in Γ. The collision integral neglecting Pauli blocking, $\Gamma_{\text{Cl,p}}$, is furnished by setting the suppression factors all equal to 1 in Eq. 5. This is the rate for classical collisions which change the momentum distribution. The total classical collision rate Γ_{Cl} is the first term on the right hand side of Eq. 5 without any suppression factors. In addition to $\Gamma_{\text{Cl,p}}$, this also contains the rate for collisions which do not change the momentum distribution: if both final states are occupied, then the reverse process has the same rate. These additional collisions do not affect observables of the system. Fig. 1(c) shows examples of these different types of collisions. $\mathbf{p_1} + \mathbf{q_1} \rightarrow \mathbf{p_2} + \mathbf{q_2}$ contributes to Γ_{Cl}, $\Gamma_{\text{Cl,p}}$ and Γ. $\mathbf{p_1} + \mathbf{q_1} \rightarrow \mathbf{p_3} + \mathbf{q_3}$ contributes to Γ_{Cl} and $\Gamma_{\text{Cl,p}}$. $\mathbf{p_1} + \mathbf{q_1} \rightarrow \mathbf{p_4} + \mathbf{q_4}$ contributes only to Γ_{Cl}. To determine the effect of Pauli blocking, we compare Γ and $\Gamma_{\text{Cl,p}}$ for a small cross-section σ. The collision rate at a particular time t can then be calculated perturbatively, by propagating the system ballistically for the time t and then evaluating Eq. 5 with and without the suppression factors.

Fig. 2(a) displays the numerically calculated collision rates Γ, $\Gamma_{\text{Cl,p}}$ and Γ_{Cl}, evaluated at $\mathbf{x} = \mathbf{p} = \mathbf{0}$, as a representative case, for an initial aspect ratio $\lambda = 0.03$. Both Γ and $\Gamma_{\text{Cl,p}}$ increase initially as the deformation of the Fermi surface becomes more pronounced. For long times ($\omega_\perp t \gg 1$), they are both suppressed because both the density ($\int d^3 q_1$) and the relative velocity ($\frac{|\mathbf{p_1} - \mathbf{q_1}|}{m}$) drop. The two curves approach each other with time since Pauli blocking becomes less effective with stronger deformation. The fraction of momentum changing collisions which are not affected by Pauli blocking, $F(\lambda) = \int dt \Gamma(\mathbf{0}, \mathbf{0}, t) / \int dt \Gamma_{\text{Cl,p}}(\mathbf{0}, \mathbf{0}, t)$, is shown in Fig. 2(b). The main result of our paper is the inefficiency of Pauli blocking during expansion from anisotropic traps. For $\lambda < 0.05$, $F > 0.5$, and approaches ~ 0.55 as λ approaches 0. Most experiments work in this regime of trap aspect ratio.

The above results form an upper bound on the Fermi suppression even if we consider all the possible collisions occurring in the system, for arbitrary $\mathbf{x}$ and $\mathbf{p}$. First, we observe that for all $\mathbf{x}$, at any time t, the Fermi surface is identically deformed and different only in size according to the local density (Eqs. 2,3, Fig. 1(a,b)). We have checked numerically that to within 5%, the central mo-

mentum provides a lower bound on Γ within a momentum ellipsoid, at all $\mathbf{x}$ and for all times t. Next, we note that for $\mathbf{x} \neq \mathbf{0}$, the density $n(\mathbf{x}, t)$ puts more weight at longer times than $n(\mathbf{0}, t)$ (Eq. 3). Since Fermi suppression becomes less effective with time, Pauli blocking is most effective at $\mathbf{x} = \mathbf{0}$. The calculation for $\mathbf{x} = \mathbf{p} = \mathbf{0}$ thus provides an effective upper bound for the overall collisional suppression in the system. We conclude that more than half of all the possible collisions are not Pauli blocked for typical experimental values of λ.
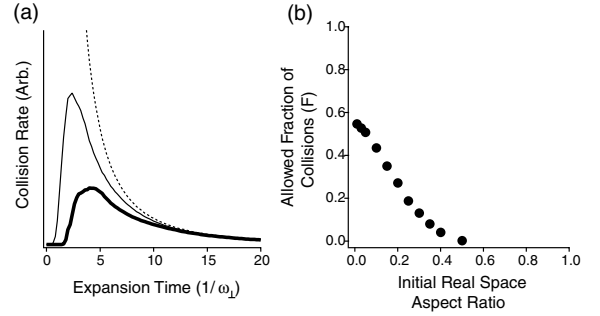

FIG. 2. (a) Collision rate as a function of expansion time in the perturbative approximation for the initial aspect ratio $\lambda = 0.03$. Dashed line - total classical collision rate Γ_{cl}, thin line - classical rate for momentum changing collisions $\Gamma_{\text{cl,p}}$, thick line - collision rate for fermions Γ. The displayed rates were evaluated at $\mathbf{x} = \mathbf{0}$ and $\mathbf{p} = \mathbf{0}$ and give an effective upper bound on the Fermi suppression. (b) Allowed fraction of collisions $F(\lambda)$ for a zero-temperature two-spin Fermi gas. For an initial aspect ratio $\lambda = 0.05$, F is 0.5. For large anisotropy ($\lambda \rightarrow 0$), F approaches ~ 0.55.

So far, we have not considered the effect of the collisions themselves on the momentum distribution. Collisions drive the system towards equilibrium, which corresponds to an isotropic Fermi-Dirac distribution. If this collisional relaxation (Eq. 5) is much faster than the non-equilibrium perturbation due to ballistic expansion (Eq. 2), the momentum distribution maintains local equilibrium at all times. If local equilibrium is maintained, the Boltzmann equation leads to the hydrodynamic equations [30]. For free expansion from anisotropic atom traps, these equations lead to the reversal of anisotropy [16,17]. Even if equilibrium is not fully maintained, collisions always have the effect of transferring momentum from the weakly confining axis to the strongly confining axis resulting in an eventual spatial aspect ratio > 1 [17].

We now want to reconcile our new result that Pauli blocking is inefficient during free expansion, with previous results [26] which show that at low temperatures, collisional damping of collective excitations is suppressed. For this, we derive an equation of motion for the momentum space anisotropy α to leading order in α and T/T_F [31]:

$$\dot{\alpha} = \frac{1}{3}(\partial_x v_x + \partial_y v_y - 2\partial_z v_z) - \frac{n \sigma p_F}{m} C\left(\alpha, \frac{T}{T_F}\right) \quad (6)$$

3

where C describes the collisional relaxation and has the asymptotic forms:

$$C\left(\alpha, \frac{T}{T_F}\right) = \frac{3\pi^2}{5}\left(\frac{T}{T_F}\right)^2 \alpha, \quad \alpha \ll \left(\frac{T}{T_F}\right)$$
$$\frac{96}{49}\alpha^3, \qquad \alpha \gg \left(\frac{T}{T_F}\right). \qquad (7)$$

In terms of α, the aspect ratio of the momentum space ellipsoid is $\sqrt{\frac{1-\alpha}{1+2\alpha}}$. p_F, T, T_F are the local Fermi momentum, temperature and Fermi temperature respectively. This equation was derived from the second momentum moment of the Boltzmann equation (Eqs. 4,5), using a Fermi-Dirac distribution with an anisotropic Fermi surface as ansatz [32]. The numerical coefficients in Eq. 7 were obtained by analytic integrations over momentum space.

At zero temperature, there is no linear term in α in Eq. 7. This shows that Pauli blocking is efficient as long as the anisotropy is small. This is the case for small amplitude excitations in a *trapped* degenerate gas [26]. However, for the large anisotropies of ballistic expansion, the α^3 term, which is independent of temperature and not affected by Pauli blocking, is responsible for collisional relaxation.

Eqs. 6,7 allow us to distinguish collisionless from hydrodynamic behavior in different regimes. The driving term involving $\mathbf{v}$ is on the order of the trap frequency $\omega_\perp$ and the damping term has a prefactor $n\sigma v_F$. Therefore, the dimensionless parameter characterizing the attainment of the hydrodynamic limit is $\Phi_0 = n\sigma v_F/\omega_\perp$. If $\Phi_0 \ll 1$, then one can neglect collisions entirely, and the gas will expand ballistically. For small anisotropies, hydrodynamic behavior requires $\Phi_0(T/T_F)^2 \gg 1$. For large anisotropies, hydrodynamic behavior requires $\Phi_0^{1/3} \gg 1$. At ultralow temperatures, the expansion after release from a highly anisotropic trap may be collisionless initially, but as α grows, the α^3 term in Eq. 7 will become important, and induce hydrodynamic behavior.

Our calculations clearly predict that for parameters of current experiments, $\Phi_0 > 1$, free expansion will not be collisionless, but show behavior which is at least intermediate between collisionless and hydrodynamic [17]. Full hydrodynamic behavior may not be achieved, since for small values of α, Pauli suppression becomes effective again. More quantitative studies are necessary in order to assess how much this behavior would differ from superfluid expansion. This could be realized by extending analytical studies [17] to high degeneracies or by Monte-Carlo techniques [33]. Our main conclusion is clear, however, that the breakdown of Pauli blocking under free expansion means that hydrodynamic expansion will not be the dramatic, qualitative signal for superfluidity in strongly interacting fermions, the way it was for BEC.

[1] B. DeMarco and D.S. Jin, Science **285**, 1703 (1999).
[2] A.G. Truscott et. al., Science **291**, 2570 (2001).
[3] F. Schreck et. al., Phys. Rev. Lett. **87**, 080403 (2001).
[4] S.R. Granade, M.E. Gehm, K.M. O'Hara, and J.E. Thomas, Phys. Rev. Lett. **88**, 120405 (2002).
[5] Z. Hadzibabic et. al., Phys. Rev. Lett. **88**, 160401 (2002).
[6] G. Roati, F. Riboli, G. Modungo, and M. Inguscio, Phys. Rev. Lett. **89**, 150403 (2002).
[7] K.M. O'Hara et. al., Science **298**, 2179 (2002).
[8] C.A. Regal and D.S. Jin, Phys. Rev. Lett. **90**, 230404 (2003).
[9] T. Bourdel et. al., arXiv:cond-mat/0303079 (2003).
[10] S. Gupta et. al., Science **300**, 1723 (2003).
[11] M. Houbiers and H.T.C. Stoof, Phys. Rev. A. **59**, 1556 (1999).
[12] M. Holland, S.J.J.M.F. Kokkelmans, M.L. Chiofalo, and R. Walser, Phys. Rev. Lett. **87**, 120406 (2001).
[13] M.H. Anderson et. al., Science **269**, 198 (1995).
[14] K.B. Davis et. al., Phys. Rev. Lett. **75**, 3969 (1995).
[15] S. Stringari, Phys. Rev. Lett. **77**, 2360 (1996).
[16] Y. Kagan, E.L. Surkov, and G.V. Shlyapnikov, Phys. Rev. A **55**, R18 (1997).
[17] P. Pedri, D. Guéry-Odelin, and S. Stringari, arXiv:cond-mat/0305624 (2003).
[18] I. Shvarchuck et. al., Phys. Rev. Lett. **89**, 270404 (2002).
[19] M.A. Baranov and D.S. Petrov, Phys. Rev. A **58**, R801 (1998).
[20] A. Minguzzi and M.P. Tosi, Phys. Rev. A **63**, 023609 (2001).
[21] F. Zambelli and S. Stringari, Phys. Rev. A **63**, 033602 (2001).
[22] C. Menotti, P. Pedri, and S. Stringari, Phys. Rev. Lett. **89**, 250402 (2002).
[23] G. Ferrari, Phys. Rev. A. **59**, R4125 (1999).
[24] W. Geist et. al., Phys. Rev. A. **61**, 013406 (1999).
[25] M. Holland, B. DeMarco, and D.S. Jin, Phys. Rev. A. **61**, 053610 (2000).
[26] L. Vichi, J. Low Temp. Phys. **121**, 177 (2000).
[27] W. Geist and T.A.B. Kennedy, Phys. Rev. A **65**, 063617 (2002).
[28] M.E. Gehm, S.L. Hemmer, K.M. O'Hara, and J.E. Thomas, arXiv:cond-mat/0304633(2003). The authors point out that the suppression of in-trap collisions is not sufficient to guarantee collisionless expansion.
[29] G.M. Bruun and C.W. Clark, Phys. Rev. A **61**,061601 (2000).
[30] K. Huang, *Statistical Mechanics*, (J. Wiley, New York 1987), 2nd. ed.
[31] J.R. Anglin et. al., in preparation (2003).
[32] The use of the Fermi-Dirac form neglects possible effects of strong interatomic correlations. Although such effects are not well understood, they are likely to shift a normal degenerate Fermi gas even further away from the colli-

sionless limit.

[33] H. Wu and E. Arimondo, Europhys. Lett. **43**, 141 (1998).

Appendix E

RF Spectroscopy of Ultracold Fermions

This appendix includes the following paper [5]: S. Gupta, Z. Hadzibabic, M.W. Zwierlein, C.A. Stan, K. Dieckmann, C.H. Schunck, E.G.M. van Kempen, B.J. Verhaar and W. Ketterle, "Radio-Frequency Spectroscopy of Ultracold Fermions",*Science* **300**, 1723 (2003).

Radio-Frequency Spectroscopy of Ultracold Fermions

**S. Gupta,[1]* Z. Hadzibabic,[1] M. W. Zwierlein,[1] C. A. Stan,[1]
K. Dieckmann,[1] C. H. Schunck,[1] E. G. M. van Kempen,[2]
B. J. Verhaar,[2] W. Ketterle[1]**

Radio-frequency techniques were used to study ultracold fermions. We observed the absence of mean-field "clock" shifts, the dominant source of systematic error in current atomic clocks based on bosonic atoms. This absence is a direct consequence of fermionic antisymmetry. Resonance shifts proportional to interaction strengths were observed in a three-level system. However, in the strongly interacting regime, these shifts became very small, reflecting the quantum unitarity limit and many-body effects. This insight into an interacting Fermi gas is relevant for the quest to observe superfluidity in this system.

Radio-frequency (RF) spectroscopy of ultracold atoms provides the standard of time. However, the resonance frequencies of ultracold atoms are sensitive to interactions between atoms, leading to the so-called clock shifts of the unperturbed resonances (1). These shifts limit the accuracy of current atomic clocks (2, 3), but can also be used to characterize atomic interactions.

RF spectroscopy has previously been applied to cold atoms to determine the size and temperature of atom clouds (4, 5). RF methods have also been used for evaporative cooling, for preparing spinor Bose-Einstein condensates (BECs) (6, 7), and as an output coupler for atom lasers (5, 8). In all these experiments, shifts and broadenings due to atomic interactions were negligible. Recently, density-dependent frequency shifts of RF transitions were observed in rubidium (9) and sodium (10) BECs. These frequency shifts are proportional to the difference in mean-field energies of two internal atomic states and allow scattering lengths to be extracted. Mean-field shifts in BECs have also been observed by optical spectroscopy (11, 12).

Here, we apply RF spectroscopy to ultracold clouds of fermions and demonstrate several phenomena: (i) the absence of a clock shift in a two-level system because of fermionic antisymmetry, (ii) the emergence of mean-field shifts in a three-level system after the relaxation of pair correlations, (iii) the limitation of mean-field shifts because of the unitarity limit, and (iv) the universality of the

[1]Department of Physics, Massachusetts Institute of Technology (MIT)–Harvard Center for Ultracold Atoms, and Research Laboratory of Electronics, MIT, Cambridge, MA 02139, USA. [2]Eindhoven University of Technology, Post Office Box 513, 5600 MB Eindhoven, Netherlands.

*To whom correspondence should be addressed. E-mail: deep@mit.edu

interaction energy in a dense cloud, independent of the attractive or repulsive nature of the two-particle interactions.

Research in ultracold fermions has advanced rapidly, with six groups now having cooled fermions into quantum degeneracy (13–18). A major goal of this research is to induce strong interactions by tuning magnetic fields to scattering resonances (called Feshbach resonances). Under these conditions, Cooper pairs of fermions may form, leading to superfluidity. This would establish a model system for studying Bardeen-Cooper-Schrieffer (BCS) pairing at densities nine orders of magnitude lower than in previous realizations in ^{3}He and superconductors. We show that RF spectroscopy can be used to characterize interactions between fermions in the regime where superfluidity has been predicted (19, 20).

Our experimental technique for preparing ultracold fermions has been considerably improved since our earlier work (17, 21). Because the Pauli exclusion principle suppresses elastic collisions between identical fermions at low temperatures and prevents evaporative cooling, we cooled fermionic ^{6}Li sympathetically with bosonic ^{23}Na loaded into the same magnetic trap. In contrast to previous work, we cooled both species in their upper hyperfine states (^{23}Na: $|F,m_F\rangle = |2,+2\rangle$, ^{6}Li: $|F,m_F\rangle = |3/2,+3/2\rangle$), where F and m_F are the quantum numbers for the total spin and its z component, respectively. This led to a reduction of inelastic loss processes and boosted our final fermion atom numbers by two orders of magnitude. We could produce BECs that contained up to 10 million sodium atoms in the $|2,+2\rangle$ state by evaporatively cooling pure bosonic samples in the magnetic trap. For a Bose-Fermi mixture, the finite heat capacity of the bosons limited the final lithium temperature after the 30-s evaporation cycle to $\sim 0.3\ T_F$ for 10 million fermi-

ons and $\sim T_F$ for 50 million fermions (22), where T_F is the Fermi temperature.

The spin states of ^{6}Li of most interest for superfluid pairing are the two lowest states $|1\rangle$ and $|2\rangle$ ($|1/2,+1/2\rangle$ and $|1/2,-1/2\rangle$ at low field), which are predicted to have an interstate s-wave (23) Feshbach resonance at ~ 800 G (24, 25). However, both states are high-field–seeking at these fields, which makes them unsuitable for magnetic trapping. We therefore transferred the atoms into an optical trap. For these experiments, 6 to 8 million $|3/2,+3/2\rangle$ lithium atoms were loaded into the optical trap at temperature $T \sim T_F \sim 35\ \mu$K (26). The atoms were then transferred to the lowest energy state $|1\rangle$, with an adiabatic frequency sweep around the lithium hyperfine splitting of 228 MHz. Magnetic fields of up to ~ 900 G were applied, a range that encompasses the $|1\rangle - |2\rangle$ Feshbach resonance. Using RF-induced transitions near 80 MHz, we could create mixtures of states $|1\rangle$, $|2\rangle$, and $|3\rangle$ ($|3/2, -3/2\rangle$ at low field) and explore interactions between fermions in these states.

Collisions between atoms cause a shift of their energy, which is usually described by the mean-field effect of all the other atoms on the atom of interest. For example, atoms in state $|2\rangle$ experience an energy shift, $[(4\pi\hbar^2)/(m)]n_1a_{12}$, that is due to the presence of atoms in state $|1\rangle$. Here $\hbar$ is Planck's constant h divided by 2π, m is the mass of the atom, n_1 is the density of $|1\rangle$ atoms, and a_{12} is the interstate scattering length between states $|1\rangle$ and $|2\rangle$. We use the convention that positive scattering length corresponds to a repulsive interaction. Density-dependent shifts of the resonance frequency for the transition that connects two states have been observed in laser-cooled (1) and Bose-condensed (9, 10) clouds.

In the case of ultracold fermions, only interactions between different internal states are allowed. For a system of density n, let us compare the energy of a gas prepared purely in state $|1\rangle$ to a gas in which one atom is transferred into state $|2\rangle$. The energy difference is $h\nu_{12} + [(4\pi\hbar^2)/(m)]na_{12}$, where ν_{12} is the resonance frequency of the noninteracting system. Similarly, the energy difference between a gas prepared purely in state $|2\rangle$ and a gas in which one atom is transferred into state $|1\rangle$ is $h\nu_{12} - [(4\pi\hbar^2)/(m)]na_{12}$.

However, these energy shifts should not affect the resonance for a coherent transfer out of a pure state. For fermions in the initial pure state, the pair-correlation function vanishes at zero distance because of the antisymmetry of the wave function. During any coherent transfer process, the state vectors of all the atoms rotate "in parallel" in Hilbert space; i.e., the superposition of the two spin states

has the same relative phase for all atoms. Thus, the atoms remain identical and cannot interact in the s-wave regime. The mean-field energy is thus established only after the coherence of the superposition state is lost and the pair correlations have relaxed, forming a purely statistical mixture of the two states.

It is a consequence of Fermi statistics that spectroscopic methods do not measure the equilibrium energy difference between the initial and final state of the system, but rather measure the unperturbed resonance frequency. The expected absence of the clock shift has led to suggestions for the use of fermions in future atomic clocks (27). Our work presents an experimental demonstration of this phenomenon.

We determined the transition frequency between states |1⟩ and |2⟩, first starting with a pure state |1⟩ and then with a pure state |2⟩ sample. The absence of a splitting between these two lines proves the suppression of the clock shift. Fig. 1 shows an example of such measurements. The magnetic field was ramped up to 570 G with the cloud in state |1⟩. At this field, $a_{12} \sim 150a_0$. Therefore, the expected equilibrium mean-field shifts were $\Delta\nu = \pm 5$ kHz for our mean density of 3×10^{13} cm^{-3} (28). The interaction between states |1⟩ and |2⟩ at this magnetic field was also observed in the mutual evaporative cooling of the two states in the optical trap. RF pulses 140 μs in duration were applied at frequencies near the unperturbed resonance $\nu_{12} \sim 76$ MHz. Atoms in states |1⟩ and |2⟩ could be monitored separately by absorption imaging, because they are optically resolved at this field. We observed a suppression of the clock shift by a factor of 30 (Fig. 1). Using the same method, we observed the absence of a clock shift at several other magnetic fields. In particular, we observed a suppression of more than three orders of magnitude at ~860 G (29).
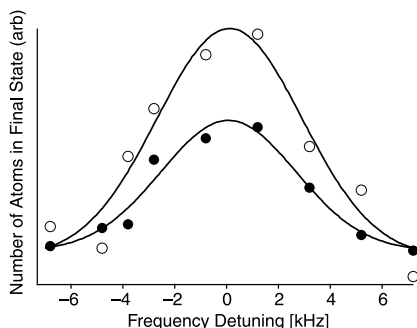
P-wave interactions (23) could lead to a nonvanishing clock shift. However, at these low temperatures, they are proportional to T or T_F, whichever is higher, and are therefore strongly suppressed.

We can observe mean-field shifts and scattering lengths spectroscopically by driving transitions from a statistical mixture of two states to a third energy level. [While this work was in progress, use of a similar method to measure scattering lengths in fermionic ^{40}K was reported (30).] Specifically, we recorded the difference between the RF spectra for the |2⟩ → |3⟩ transition in the presence and in the absence of state |1⟩ atoms. The presence of atoms in state |1⟩ is then expected to shift the resonance by (31).

$$\Delta\nu = \frac{2\hbar}{m} n_1(a_{13} - a_{12}) \quad (1)$$

In our experimental scheme to determine the interaction energy at different magnetic fields (Fig. 2), the system was prepared by ramping up the magnetic field to 500 G with the atoms

in state |1⟩. Either partial or complete RF transfer to state |2⟩ was then performed. The number of atoms in state |1⟩ was controlled by adjusting the speed of a frequency sweep around the |1⟩ → |2⟩ resonance. A fast, nonadiabatic sweep created a superposition of the two states, whereas a slow, adiabatic sweep prepared the sample purely in state |2⟩. A wait time of 200 ms was allowed for the coherence between states |1⟩ and |2⟩ to decay and the system to equilibrate.

Typical parameters for the decohered |1⟩ – |2⟩ mixture were mean-density $n_1 \sim 2.4 \times 10^{13}$ cm^{-3} and $T \sim 0.7\ T_F$. The magnetic field was then changed to the desired value, and the transition from state |2⟩ to state |3⟩ was driven with 140-μs RF pulses (Fig. 2C). We monitored the appearance of atoms in state |3⟩ and the disappearance of atoms from state |2⟩, using simultaneous absorption imaging. Fig. 2D shows the unperturbed and perturbed resonances at the magnetic field $B = 480$ G. The position of the unperturbed resonance
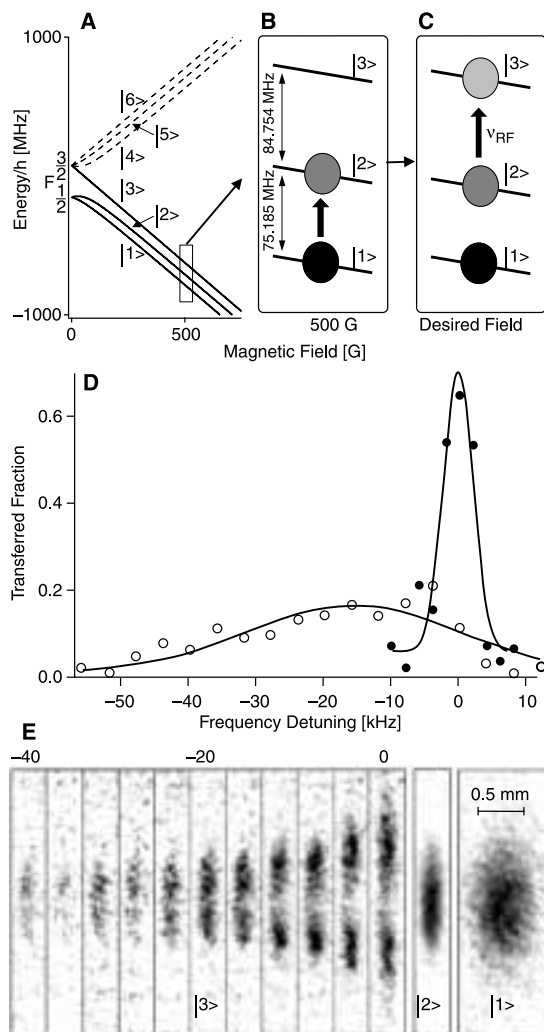

Fig. 2. Schematic of the mean-field measurement and representative spectra at 480 G. (A) Hyperfine structure of the ground state of ^{6}Li. (B and C) Experimental scheme: (B) Preparation of a mixture of atoms in states |1⟩ and |2⟩, and (C) RF spectroscopy of the |2⟩ → |3⟩ transition using a variable radio frequency (ν_{RF}). (D) The fraction of atoms transferred from |2⟩ to |3⟩, with |1⟩ atoms absent (solid circles) and present (open circles). The mean-field shift is computed from Gaussian fits to the data (solid lines). (E) Spatial images of state |3⟩ for the perturbed resonance. The optical trap was turned off immediately after the RF pulse and absorption images of the atoms were taken after 120 μs of expansion time. The central section of ~150-μm vertical extent was used to extract the transferred fractions in (D). (E) also shows images of states |2⟩ and |1⟩ for zero RF detuning. States |3⟩ and |2⟩ were imaged simultaneously to observe their complementary spatial structure. State |1⟩ was imaged after 760 μs of expansion time to record its density for normalization purposes.

Fig. 1. Absence of the clock shift. RF transitions were driven between states |1⟩ and |2⟩ on a system prepared purely in state |1⟩ (solid circles) and purely in state |2⟩ (open circles). Mean-field interactions would have resulted in 5-kHz shifts for the two curves in opposite directions. Gaussian fits (solid lines) to the data are separated by 0.04 ± 0.35 kHz. This gives a clock-shift suppression factor of 30. Arb., arbitrary units.

ν_{23} also determines the magnetic field to an accuracy of <0.1 G. Fig. 2E shows absorption images of atoms in state $|3\rangle$, obtained for different values of the applied radio frequency. One can clearly see the spatial dependence and thus the density dependence of the mean-field shift: Close to the unperturbed resonance, the low-density wings of the cloud are predominantly transferred, whereas the high-density central part of the cloud is transferred only at sufficient detuning. To suppress spurious effects from this spatial dependence, only a small central part of the images was used to extract the transferred atomic fraction.

To ensure that our mean-field measurements were performed on a statistical mixture, we measured the time scale for decoherence in our system. The decay of the $|1\rangle - |2\rangle$ coherence at 500 G was observed by monitoring the $|2\rangle \rightarrow |3\rangle$ transfer at the measured unperturbed resonance ν_{23}, as a function of wait time (Fig. 3). For wait times that are small compared to the decoherence time of the $|1\rangle - |2\rangle$ superposition, the $|2\rangle \rightarrow |3\rangle$ RF drive places each atom in an identical three-state superposition. All mean-field shifts are then absent and the resulting transfer is unchanged from the unperturbed case. For longer wait times, the $|1\rangle - |2\rangle$ superposition decoheres and mean-field interactions set in. This shifts the resonance frequency of the $|2\rangle \rightarrow |3\rangle$ transition, reducing the transferred fraction at ν_{23}. The measured decoherence time of ~ 12 ms was attributed mainly to the sensitivity of ν_{12} to magnetic field variations across the cloud. These inhomogeneities cause the relative phase of the $|1\rangle - |2\rangle$ superposition in different parts of the trap to evolve at different rates, given by the local ν_{12}. Atoms that travel along different paths within the trap therefore acquire different phases between their $|1\rangle$ and $|2\rangle$ components. Being no longer in identical states, s-wave interactions between them are allowed. The inhomogeneities scale with B, whereas the sensitivity of the transition scales with $\partial\nu_{12}/$

∂B. We would thus expect the decoherence time to vary inversely with the product of these two quantities. Our hypothesis is supported by our observation of longer decoherence times at higher fields, where $B \times \partial\nu_{12}/\partial B$ is lower.

Fig. 4A summarizes the results of our mean-field measurements for a wide range of magnetic fields up to 750 G. For magnetic fields up to 630 G, our data can be explained fairly well by using Eq. 1 with the theoretical calculations of the scattering lengths shown in Fig. 4B and an effective density of $n_1 = 2.2 \times 10^{13}$ cm^{-3}, which is consistent with the initial preparation of the system at 500 G. A narrow resonance of a_{12} at ~ 550 G (21, 25, 32) is indicated by the data but was not fully resolved. We also see additional structure near 470 G, which is not predicted by theory and deserves further study.

For fields above 630 G, the measured shifts strongly deviated from the predictions of Eq. 1, indicating a different regime of interactions. In the region between 630 G and 680 G, the two scattering lengths are expected to be large and positive, with $a_{13} \gg a_{12}$ (Fig. 4B). Eq. 1 would thus predict large positive mean-field shifts. In contrast, we observe very small shifts, indicating almost perfect cancellation of the two contributions. We also observe essentially no mean-field shifts between 680 G and 750 G, where the two scattering lengths are predicted to be very large in magnitude and of opposite signs, and in a simple picture should add up to a huge negative shift. These results are evidence for phenomena in a strongly interacting system, where

the scattering length becomes comparable to either the inverse wave vector of interacting particles or the interatomic separation.

Eq. 1 is valid only for low energies and weak interactions, where the relative wave vector of the two particles, k, satisfies $k \ll 1/|a|$. For arbitrary values of ka, the s-wave interaction between two atoms is described by replacing the scattering length a with the complex scattering amplitude f.

$$f = \frac{-a}{1+k^2 a^2}(1-ika) \qquad (2)$$

The real part of f, Re(f) determines energy shifts, and hence the ground state properties of an interacting many-body system. The imaginary part, Im(f) determines the (inverse) lifetime for elastic scattering out of a momentum state, and hence the dynamic properties of the system such as thermalization rates. For $k|a| \rightarrow \infty$, the elastic cross-section $\sigma = 4\pi\mathrm{Im}(f)/k$ monotonically approaches the well known "unitarity-limited" value of $4\pi/k^2$. On the other hand, the two-particle contribution to the mean-field energy, proportional to $-\mathrm{Re}(f) = a/(1 + k^2 a^2)$ peaks at $|a| = 1/k$ and then, counterintuitively, decreases as $1/|a|$ for increasing $|a|$. Averaging Re(f) over a zero-temperature Fermi distribution with Fermi momentum $\hbar k_F$ limits its absolute value to $1.05/k_F$ and markedly weakens its dependence on the exact value of a in the $k_F|a| > 1$ regime (33). This results in a prediction for the mean-field energy that is sensitive to the sign of the scattering length, remains finite for $k_F|a| \gg 1$, and never exceeds $0.45\ E_F$, where E_F is the Fermi energy. Hence,
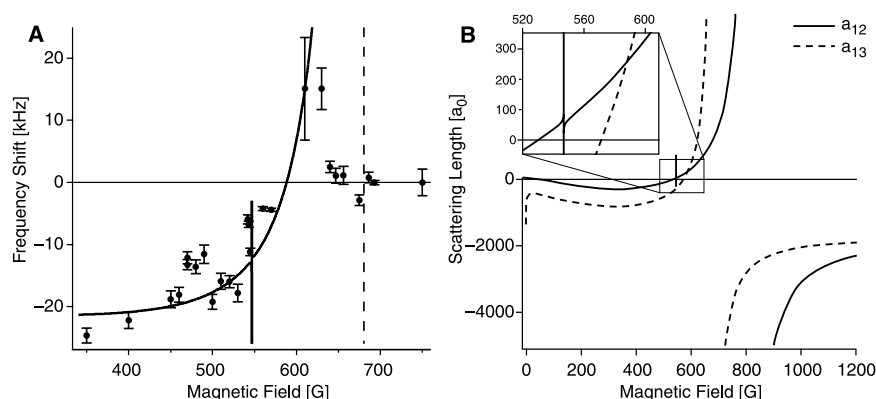
Fig. 4. Spectroscopic measurement of interaction energy. (**A**) Frequency shift versus magnetic field for the $|2\rangle \rightarrow |3\rangle$ resonance due to atoms in state $|1\rangle$. The shifts are computed by monitoring the arrival fraction in state $|3\rangle$ for 140-μs RF pulses, except at 750 G. At 750 G, because of strong inelastic losses between $|3\rangle$ and $|1\rangle$ atoms, we monitored the loss of atoms in state $|2\rangle$ after applying RF sweeps 3 ms in duration and 2 kHz in width. All the data points are normalized to the same atom number in state $|1\rangle$. The fit at low fields (solid line) uses Eq. 1 with $n_1 = 2.2 \times 10^{13}$ cm^{-3} and the theoretical calculations of the scattering lengths. The error bars reflect uncertainty in the state $|1\rangle$ atom number and the uncertainty in the Gaussian fits to the spectra. The dashed line indicates the position of the predicted a_{13} resonance. (**B**) S-wave scattering lengths a_{12} and a_{13} as a function of magnetic field, obtained from a highly model-independent quantum-scattering calculation. The calculation makes use of the presently available ^{6}Li experimental data (40) in a coupled channel approach to deduce accumulated phases that characterize the less well-known, short-range parts of the ^{6}Li + ^{6}Li scattering potential (32). a_{12} has a narrow Feshbach resonance at 550 G and a wide one at 810 G. a_{13} has a wide Feshbach resonance at 680 G.
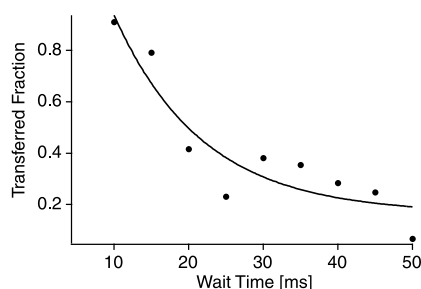

Fig. 3. Emergence of mean-field shifts due to decoherence at 500 G. Decoherence leads to a reduction of the $|2\rangle \rightarrow |3\rangle$ transfer at the unperturbed resonance ν_{23}. An exponential fit to the data (solid line) gives a time constant of 12 ms.

this approach could qualitatively explain our results in the 630 to 680 G region, but it is in clear contradiction with negligible resonance shifts in the 680 to 750 G region (*34*).

We suggest that these discrepancies might be due to the fact that we are in the high-density regime, where $n|a|^3$ approaches unity. In a degenerate Fermi gas, the interparticle spacing is comparable to the inverse Fermi wave vector, $k_F^3 = 6\pi^2 n$. Hence, the unitarity limit coincides with the breakdown of the low-density approximation ($n|a|^3 \ll 1$) and higher order many-body effects can become important. Some recent many-body calculations (*35–37*) suggest that in the regime $k_F|a| \gg 1$ (or $n|a|^3 \gg 1$), the interaction energy is always negative and independent of both sign and magnitude of a. This suggests that whenever the scattering length is large, either positive or negative, the interaction energy is a universal fraction of the Fermi energy (*33*). This is a possible explanation for the small line shifts that we observed for fields higher than 630 G, where the interactions are strong in both states.

This picture is consistent with other recent experimental observations (*30, 33, 38, 39*). Expansion energy measurements in a mixture of states $|1\rangle$ and $|2\rangle$ of ^{6}Li (*39*) showed a negative interaction energy at 720 G, which is on the repulsive side of the predicted Feshbach resonance. RF spectroscopy in ^{40}K (*30*) has also shown some saturation of the mean field in the vicinity of a Feshbach resonance, which may reflect the unitarity limit.

In characterizing an interacting Fermi gas by RF spectroscopy, we have demonstrated absence of clock shifts in a two-level system and introduced a three-level method for measuring mean-field shifts. For strong interactions, we have found only small line shifts that may reflect both the unitarity limit of binary collisions and many-body effects. It would be very important to distinguish between two-body and many-body effects by studying the gas over a broad range of temperatures and densities. In a very dilute and very cold gas, the weakly interacting limit could be extended to very large values of $|a|$, thus allowing for direct verification of molecular calculations. This presents experimental challenges, because cooling changes the density and the temperature together. It would also be interesting to study similar phenomena in bosonic gases, in order to distinguish to what extent the high density many-body effects depend on quantum statistics. This insight into the physics of strongly interacting Fermi gases must be taken into account in the search for superfluidity in these systems.

References and Notes

1. K. Gibble, S. Chu, *Phys. Rev. Lett.* **70**, 1771 (1993).
2. C. Fertig, K. Gibble, *Phys. Rev. Lett.* **85**, 1622 (2000).
3. Y. Sortais *et al.*, *Phys. Scr.* **T95**, 50 (2001).
4. A. G. Martin, K. Helmerson, V. S. Bagnato, G. P. Lafyatis, D. E. Pritchard, *Phys. Rev. Lett.* **61**, 2431 (1988).
5. I. Bloch, T. W. Hänsch, T. Esslinger, *Phys. Rev. Lett.* **82**, 3008 (1999).
6. M. R. Matthews *et al.*, *Phys. Rev. Lett.* **81**, 243 (1998).
7. J. Stenger *et al.*, *Nature* **396**, 345 (1998).
8. M.-O. Mewes *et al.*, *Phys. Rev. Lett.* **78**, 582 (1997).
9. D. M. Harber, H. J. Lewandowski, J. M. McGuirk, E. A. Cornell, *Phys. Rev. A.* **66**, 053616 (2002).
10. A. Görlitz *et al.*, *Phys. Rev. Lett.* **90**, 090401 (2003).
11. T. C. Killian *et al.*, *Phys. Rev. Lett.* **81**, 3807 (1998).
12. B. DeMarco, D. S. Jin, *Science* **285**, 1703 (1999).
13. A. G. Truscott, K. E. Strecker, W. I. McAlexander, G. B. Partridge, R. G. Hulet, *Science* **291**, 2570 (2001).
14. F. Schreck *et al.*, *Phys. Rev. Lett.* **87**, 080403 (2001).
15. S. R. Granade, M. E. Gehm, K. M. O'Hara, J. E. Thomas, *Phys. Rev. Lett.* **88**, 120405 (2002).
16. Z. Hadzibabic *et al.*, *Phys. Rev. Lett.* **88**, 160401 (2002).
17. G. Roati, F. Riboli, G. Modungo, M. Inguscio, *Phys. Rev. Lett.* **89**, 150403 (2002).
18. M. Houbiers, H. T. C. Stoof, *Phys. Rev. A.* **59**, 1556 (1999).
19. M. Holland, S. J. J. M. F. Kokkelmans, M. L. Chiofalo, R. Walser, *Phys. Rev. Lett.* **87**, 120406 (2001).
20. K. Dieckmann *et al.*, *Phys. Rev. Lett.* **89**, 203201 (2002).
21. Z. Hadzibabic *et al.*, preprint available at http://arXiv.org/abs/cond-mat/0306050 (2003).
22. *S*-wave and *p*-wave interactions refer to two-body interactions with relative angular momentum 0 and $\hbar$, respectively.
23. M. Houbiers, H. T. C. Stoof, W. I. McAlexander, R. G. Hulet, *Phys. Rev. A.* **57**, R1497 (1998).
24. K. M. O'Hara *et al.*, *Phys. Rev. A.* **66**, 041401 (2002).
25. The transfer efficiency is limited by finite optical-trap depth and residual heating during the transfer.
26. K. Gibble, B. J. Verhaar, *Phys. Rev. A.* **52**, 3370 (1995).
27. For our modest degeneracy, we can use a Gaussian approximation for the density distribution. The mean density is then lower than the peak density by a factor of $2\sqrt{2}$.
28. Our estimate uses the direct mean field measurement of Bourdel *et al.* (*39*), scaled to our parameters.
29. C. Regal, D. S. Jin, preprint available at http://arXiv.org/abs/cond-mat/0302461 (2003).

30. C. Regal, D. S. Jin, preprint available at http://arXiv.org/abs/cond-mat/0302461 (2003).
31. Because of fermionic antisymmetry, there is no clock shift from interactions between atoms in states $|2\rangle$ and $|3\rangle$. Mean-field shifts arise only during a decoherence time (see later in the text) but are negligible if the population of atoms in state $|3\rangle$ is small.
32. E. G. M. van Kempen *et al.*, in preparation.
33. M. E. Gehm, S. L. Hemmer, S. R. Granade, K. M. O'Hara, J. E. Thomas, preprint available at http://arXiv.org/abs/cond-mat/0212499 (2002).
34. For fields higher than 630 G, number losses generally reduced n_1, and all the shifts in this region were scaled up by a factor of 1.1 to 2.7 but still remained negligible.
35. J. V. Steele, preprint available at http://arXiv.org/abs/nucl-th/0010066 (2000).
36. H. Heiselberg, *Phys. Rev. A.* **63**, 043606 (2001).
37. R. Combescot, preprint available at http://arXiv.org/abs/cond-mat/0302209 (2003).
38. K. M. O'Hara, S. L. Hemmer, M. E. Gehm, S. R. Granade, J. E. Thomas, *Science* **298**, 2179 (2002).
39. T. Bourdel *et al.*, preprint available at http://arXiv.org/abs/cond-mat/0303079 (2003).
40. This includes the recent measurement of 800 ± 40 G for the resonance in a_{12} (*39*).
41. The work at MIT was supported by NSF, the Office of Naval Research, the Army Research Office, and NASA. The work at Eindhoven is part of the research program of the Stichting voor Fundamenteel Onderzoek der Materie, which is financially supported by the Nederlandse Organisatie voor Wetenschappelijk Onderzoek.

The Interface Phase and the Schottky Barrier for a Crystalline Dielectric on Silicon

R. A. McKee,[1]* F. J. Walker,[1,2] M. Buongiorno Nardelli,[1,3] W. A. Shelton,[1] G. M. Stocks[1]

The barrier height for electron exchange at a dielectric-semiconductor interface has long been interpreted in terms of Schottky's theory with modifications from gap states induced in the semiconductor by the bulk termination. Rather, we show with the structure specifics of heteroepitaxy that the electrostatic boundary conditions can be set in a distinct interface phase that acts as a "Coulomb buffer." This Coulomb buffer is tunable and will functionalize the barrier-height concept itself.

When Schottky (*1*) and Mott (*2*) formulated the barrier-height theory for a metal-semiconductor junction and later when Anderson (*3*) formulated the band-edge offset problem for semiconductor-semiconductor junctions, there was no consideration given to interface states as contributions to the electrostatic boundary conditions. The charge distribution at the interface was treated simply as a superposition of the bulk-terminated junction. Certainly these theories have been insightful, but they consistently misrepresent the barrier height or band-edge offsets because real interfaces, apparently from interfacial structure variations, modify the intrinsic band alignment (*4–6*).

Although the bulk-termination view of the problem has been enhanced over the years with an ever-increasing formalization of theoretical techniques (*7–15*), recent bond polarization ar-

[1]Oak Ridge National Laboratory, Oak Ridge, TN 37831, USA. [2]University of Tennessee (UT), Knoxville, TN 37996, USA. [3]North Carolina State University, Raleigh, NC 27695, USA.

*To whom correspondence should be addressed. E-mail: mckeera@ornl.gov

Bibliography

[1] S. Gupta, K. Dieckmann, Z. Hadzibabic, and D. E. Pritchard, "Contrast Interferometry using Bose-Einstein Condensates to Measure h/m and α," Phys. Rev. Lett. **89**, 140401 (2002).

[2] S. Gupta, A. E. Leanhardt, A. D. Cronin, and D. E. Pritchard, "Coherent Manipulation of Atoms with Standing Light Waves," Cr. Acad. Sci. IV-Phys **2**, 479 (2001).

[3] Z. Hadzibabic, C. A. Stan, K. Dieckmann, S. Gupta, M. W. Zwierlein, A. Görlitz, and W. Ketterle, "Two-species mixture of quantum degenerate Bose and Fermi gases," Phys. Rev. Lett. **88**, 160401 (2002).

[4] K. Dieckmann, C. A. Stan, S. Gupta, Z. Hadzibabic, C. H. Schunck, and W. Ketterle, "Decay of an Ultracold Fermionic Lithium Gas near a Feshbach Resonance," Phys. Rev. Lett. **89**, 203201 (2002).

[5] S. Gupta, Z. Hadzibabic, M. W. Zwierlein, C. A. Stan, K. Dieckmann, C. H. Schunck, E. G. M. van Kempen, B. J. Verhaar, and W. Ketterle, "RF Spectroscopy of Ultracold Fermions," Science **300**, 1723 (2003).

[6] Z. Hadzibabic, S. Gupta, C. A. Stan, C. H. Schunck, M. W. Zwierlein, K. Dieckmann, and W. Ketterle, "Fifty-fold inprovement in the number of quantum degenerate fermionic atoms," arXiv:cond-mat/0306050, Phys. Rev. Lett., in press (2003).

[7] M. W. Zwierlein, Z. Hadzibabic, S. Gupta, and W. Ketterle, "Spectroscopic insensitivity to cold collisions in a two-state mixture of fermions," arXiv:cond-mat/0306627 (2003).

[8] S. Gupta, Z. Hadzibabic, J. R. Anglin, and W. Ketterle, "Collisions in Zero Temperature Fermi Gases," arXiv:cond-mat/0307088 (2003).

[9] D. M. Stamper-Kurn, "Peeking and Poking at a New Quantum Fluid: Studies of Bose-Einstein Condensates in Magnetic and Optical Traps," PhD Thesis (unpublished). (2000).

[10] S. Inouye, "Manipulating Bose-Einstein Condensates with Laser Light," PhD Thesis (unpublished). (2001).

[11] A. P. Chikkatur, "Colliding and Moving Bose-Einstein Condensates: Studies of superfluidity and optical tweezers for condensate transport," PhD Thesis (unpublished). (2002).

[12] Z. Hadzibabic, "Studies of a Quantum Degenerate Fermionic Lithium Gas," PhD Thesis (unpublished). (2003).

[13] T. H. Maiman, "Stimulated Optical Radiation in Ruby," Nature **187**, 493 (1960).

[14] A. Javan, W. R. Bennett, and D. Herriott, "Population Inversion and Continuous Optical Maser Oscillation in a Gas Discharge Containing a He-Ne Mixture," Phys. Rev. Lett. **6**, 106 (1961).

[15] M. H. Anderson, J. R. Ensher, M. R. Matthews, C. E. Wieman, and E. A. Cornell, "Observation of Bose-Einstein Condensation in a Dilute Atomic Vapor," Science **269**, 198 (1995).

[16] C. C. Bradley, C. A. Sackett, J. J. Tollet, and R. G. Hulet, "Evidence of Bose-Einstein Condensation in an Atomic Gas with Attractive Interactions," Phys. Rev. Lett. **75**, 1687 (1995).

[17] K. B. Davis, M.-O. Mewes, M. R. Andrews, N. J. van Druten, D. S. Durfee, D. M. Kurn, and W. Ketterle, "Bose-Einstein Condensation in a Gas of Sodium Atoms," Phys. Rev. Lett. **75**, 3969 (1995).

[18] P. Nozires and D. Pines, *The Theory of Quantum Liquids* (Addison-Wesley, Redwood City, CA, 1990).

[19] D. G. Fried, T. C. Killian, L. Willmann, D. Landhuis, S. C. Moss, D. Kleppner, and T. J. Greytak, "Bose-Einstein Condensation of Atomic Hydrogen," Phys. Rev. Lett. **81**, 3811 (1998).

[20] S. L. Cornish, N. R. Claussen, J. L. Roberts, E. A. Cornell, and C. E. Wieman, "Stable ^{85}Rb Bose-Einstein Condensates with Widely Tunable Interactions," Phys. Rev. Lett. **85**, 1795 (2000).

[21] A. Robert, O. Sirjean, A. Browaeys, J. Poupard, S. Nowak, D. Boiron, C. I. Westbrook, and A. Aspect, "A Bose-Einstein Condensate of Metastable Atoms," Science **292**, 461 (2001).

[22] F. P. D. Santos, J. Leonard, J. M. Wang, C. J. Barrelet, F. Perales, E. Rasel, C. S. Unnikrishnan, M. Leduc, and C. Cohen-Tannoudji, "Bose-Einstein condensation of metastable helium," Phys. Rev. Lett. **86**, 3459 (2001).

[23] G. Modugno, G. Ferrari, G. Roati, R. J. Brecha, A. Simoni, and M. Inguscio, "Bose-Einstein Condensation of Potassium Atoms by Sympathetic Cooling," Science **294**, 1320 (2001).

[24] T. Weber, J. Herbig, M. Mark, H.-C. Nägerl, and R. Grimm, "Bose-Einstein condensation of cesium," Science **299**, 232 (2003).

[25] Y. Takasu, K. Maki, K. Komori, T. Takano, K. Honda, M. Kumakura, T. Yabuzaki, and Y. Takahashi, "Spin-Singlet Bose-Einstein Condensation of Two-Electron Atoms," Phys. Rev. Lett. **90**, 040404 (2003).

[26] B. DeMarco and D. S. Jin, "Onset of Fermi Degeneracy in a Trapped Atomic Gas," Science **285**, 1703 (1999).

[27] A. G. Truscott, K. E. Strecker, W. I. McAlexander, G. B. Partridge, and R. G. Hulet, "Observation of Fermi Pressure in a Gas of Trapped Atoms," Science **291**, 2570 (2001).

[28] F. Schreck, L. Khaykovich, K. L. Corwin, G. Ferrari, T. Bourdel, J. Cubizolles, and C. Salomon, "Quasipure Bose-Einstein Condensate Immersed in a Fermi Sea," Phys. Rev. Lett. **87**, 080403 (2001).

[29] S. R. Granade, M. E. Gehm, K. M. O'Hara, and J. E. Thomas, "Preparation of a degenerate, two-component fermi gas by evaporation in a single beam optical trap," Phys. Rev. Lett. **88**, 120405 (2002).

[30] G. Roati, F. Riboli, G. Modungo, and M. Inguscio, "Fermi-Bose Quantum Degenerate ^{40}K - ^{87} Mixture with Attractive Interaction," Phys. Rev. Lett. **88**, 160401 (2002).

[31] J. Bardeen, L. N. Cooper, and J. R. Schreiffer, "Theory of Superconductivity," Phys. Rev. **108**, 1175 (1957).

[32] *Atom Interferometry*, edited by P. Berman (Academic Press, New York, 1997).

[33] P. Bouyer and M. A. Kasevich, "Heisenberg-limited spectroscopy with degenerate Bose-Einstein gases," Phys. Rev. A **56**, R1083 (1997).

[34] Y. Torii, Y. Suzuki, M. Kozuma, T. Sugiura, T. Kuga, L. Deng, and E. W. Hagley, "Mach-Zehnder Bragg interferometer for a Bose-Einstein condensate," Phys. Rev. A. **61**, 041602 (2000).

[35] J. E. Simsarian, J. Denschlag, M. Edwards, C. W. Clark, L. Deng, E. W. Hagley, K. Helmerson, S. L. Rolston, and W. D. Phillips, "Imaging the Phase of an Evolving Bose-Einstein Condensate Wave Function," Phys. Rev. Lett. **85**, 2040 (2000).

[36] Y. I. Shin, A. E. Leanhardt, M. Saba, T. Pasquini, W. Ketterle, and D. E. Pritchard, "Atom interferometry with Bose-Einstein condensates in a double-well potential," arXiv:cond-mat/0306305 (2003).

[37] C. R. Ekstrom, J. Schmiedmayer, M. S. Chapman, T. D. Hammond, and D. E. Pritchard, "Measurement of the electric polarizability of sodium with an atom interferometer," Phys. Rev. A **51**, 3883 (1995).

[38] M. Kasevich and S. Chu, "Atomic Interferometry Using Stimulated Raman Transitions," Phys. Rev. Lett. **67**, 181 (1991).

[39] S. B. Cahn, A. Kumarkrishnan, U. Shim, T. Sleator, P. R. Berman, and B. Dubetsky, "Time-Domain de Broglie Wave Interferometry," Phys. Rev. Lett. **79**, 784 (1997).

[40] H. J. Metcalf and P. van der Straten, *Laser Cooling and Trapping* (Springer-Verlag New York, Inc., 1999).

[41] A. Aspect, E. Arimondo, R. Kaiser, N. Vansteenkiste, and C. Cohen-Tannoudji, Phys. Rev. Lett. **61**, 826 (1988).

[42] A. Aspect, E. Arimondo, R. Kaiser, N. Vansteenkiste, and C. Cohen-Tannoudji, J. Opt. Soc. Am. B **6**, 2112 (1989).

[43] M. Marte and S. Stenholm, "Multiphoton resonances in atomic Bragg scattering," App. Phys. B **54**, 443 (1992).

[44] P. J. Martin, B. G. Oldaker, A. H. Miklich, and D. E. Pritchard, "Bragg Scattering of Atoms from a Standing Light-Wave," Phys. Rev. Lett. **60**, 515 (1988).

[45] C. G. Shull, "Obeservation of Pendellösung Fringe Structure in Neutron Diffraction," Phys. Rev. Lett. **21**, 1585 (1968).

[46] P. Ewald, "Zur Begründung der Kristalloptik," Ann. d. Phys. **54**, 519 (1917).

[47] D. M. Giltner, R. W. McGowan, and S. A. Lee, "Theoretical and Experimental-Study of the Bragg Scattering of Atoms from a Standing Light-Wave," Phys. Rev. A **52**, 3966 (1995).

[48] M. Kozuma, L. Deng, E. W. Hagley, J. Wen, R. Lutwak, K. Helmerson, S. L. Rolston, and W. D. Phillips, "Coherent splitting of Bose-Einstein condensed atoms with optically induced Bragg diffraction," Phys. Rev. Lett. **82**, 871 (1999).

[49] J. Stenger, S. Inouye, A. P. Chikkatur, D. M. Stamper-Kurn, D. E. Pritchard, and W. Ketterle, "Bragg spectroscopy of a Bose-Einstein condensate," Phys. Rev. Lett. **82**, 4569 (1999).

[50] P. L. Kapitza and P. A. M. Dirac, "The reflection of electrons from standing light waves," Proc. of the Camb. Philos. Soc. **29**, 297 (1933).

[51] P. L. Gould, G. A. Ruff, and D. E. Pritchard, "Diffraction of Atoms by Light - the near-Resonant Kapitza-Dirac Effect," Phys. Rev. Lett. **56**, 827 (1986).

[52] Y. B. Ovchinnikov, J. H. Muller, M. R. Doery, E. J. D. Vredenbregt, K. Helmerson, S. L. Rolston, and W. D. Phillips, "Diffraction of a released Bose-Einstein condensate by a pulsed standing light wave," Phys. Rev. Lett. **83**, 284 (1999).

[53] D. W. Keith, C. R. Ekstrom, Q. A. Turchette, and D. E. Pritchard, "An Interferometer for atoms," Phys. Rev. Lett. **66**, 2693 (1991).

[54] B. C. Young, M. A. Kasevich, and S. Chu, "Precision Atom Interferometry with Light Pulses," *Atom Interferometry*, edited by P. Berman (Academic Press, New York, 1997).

[55] J. M. Hensley, "A Precision Measurement of the Fine Structure Constant," Ph.D. thesis, Stanford (2001).

[56] T. Kinoshita, "The fine structure constant," Rep. Prog. Phys. **59**, 1459 (1996).

[57] B. Taylor, "Determining the Avogadro Constant from Electrical Measurements," Metrologia **31**, 181 (1994).

[58] A. Wicht, J. M. Hensley, E. Sarajlic, and S. Chu, "A Preliminary Measurement of the Fine Structure Constant based on Atom Interferometry," Physica Scripta **T102**, 82 (2002).

[59] P. J. Mohr and B. N. Taylor, "Codata recommended values of the fundamental constants: 1998," Rev. Mod. Phys. **72**, 351 (2000).

[60] M. Büchner, R. Delhuille, A. Mifre, C. Robilliard, J. Vigué, and C. Champenois, "Diffraction phases in atom interferometers," Phys. Rev. A. **68**, 013607 (2003).

[61] P. R. Bevington and D. K. Robinson, *Data Reduction and Error Analysis for the Physical Sciences* (McGraw-Hill, 1992).

[62] M. P. Bradley, J. V. Porto, S. Rainville, J. K. Thompson, and D. E. Pritchard, "Penning Trap Measurements of the Masses of ^{133}Cs, ^{87,85}Rb, and ^{23}Na with Uncertainties $\leq$ 0.2 ppb," Phys. Rev. Lett. **83**, 4510 (1999).

[63] M.-O. Mewes, M. R. Andrews, N. J. van Druten, D. M. Kurn, D. S. Durfee, and W. Ketterle, "Bose-Einstein Condensaion in a Tighly Confining cd Magnetic Trap," Phys. Rev. Lett. **77**, 416 (1996).

[64] S. Inouye, A. P. Chikkatur, D. M. Stamper-Kurn, J. Stenger, D. E. Pritchard, and W. Ketterle, "Superradiant Rayleigh Scattering from a Bose-Einstein Condensate," Science **285**, 571 (1999).

[65] J. R. S. Van Dyck, P. B. Schwinberg, and H. G. Dehmelt, "New High-precision Comparison of Electron and Positron g factors," Phys. Rev. Lett. **59**, 26 (1987).

[66] T. Kinoshita, "New Value of the alpha 3 Electron Anomalous Magnetic Moment," Phys. Rev. Lett. **75**, 4728 (1995).

[67] C. Schwob, L. Jozefowski, B. de Beauvoir, L. Hilico, F. Nez, L. Julien, F. Biraben, O. Acef, and A. Clairon, "Optical Frequency measurement of the $2S - 12D$ Transitions in Hydrogen and Deuterium: Rydberg Constant and Lamb Shift Determinations," Phys. Rev. Lett. **82**, 4960 (1999).

[68] T. Udem, A. Huber, B. Gross, J. Reichert, M. Prevedelli, M. Weitz, and T. W. Hnsch, "Phase-Coherent MEasurement of the Hydrogen $1S - 2S$ Transition Frequency with an Optical Frequency Interval Divider Chain," Phys. Rev. Lett. **79**, 2646 (1997).

[69] T. Beier, H. Hffner, N. Hermanspahn, S. G. Karshenboim, H.-J. Kluge, W. Quint, S. Stahl, J. Verd, and G. Werth, "New Determination of the Electron's Mass," Phys. Rev. Lett. **88**, 011603 (2002).

[70] P. Juncar, J. Pinard, J. Hamond, and A. Chartier, "Absolute Determination of the Wavelengths of the Sodium D_1 and D_2 Lines by Using a CW Tunable Dye Laser Stabilized on Iodine," Metrologia **17**, 77 (1981).

[71] Y. Sortais, S. Bize, M. Abgrall, S. Zhang, C. Nicolas, C. Mandache, P. Lemonde, P. Laurent, G. Santarelli, N. Dimarcq, P. Petit, A. Clairon, A. Mann, A. Luiten, S. Chang, and C. Salomon, "Cold atom clocks," Physica Scripta **T95**, 50 (2001).

[72] W. Ketterle, D. S. Durfee, and D. M. Stamper-Kurn, in *Bose-Einstein condensation in atomic gases, Proceedings of the International School of Physics Enrico Fermi, Course CXL*, edited by M. Inguscio, S. Stringari, and C. Wieman (IOS Press, Amsterdam, 1999), pp. 67–176.

[73] C. J. Pethick and H. Smith, *Bose-Einstein Condensation in Dilute Gases* (Cambridge University Press, Cambridge, U.K., 2002).

[74] A. E. Leanhardt, T. A. Pasquini, M. Saba, A. Schirotzek, Y. Shin, D. Kielpinski, D. E. Pritchard, and W. Ketterle, "Adiabtic and Evaporative Cooling of Bose-Einstein Condensates Below 500 Picokelvin," Science, in press (2003).

[75] D. A. Butts and D. S. Rokhsar, "Trapped Fermi gases," Phys. Rev. A **55**, 4346 (1997).

[76] G. M. Bruun and C. W. Clark, "Ideal gases in time-dependent traps," Phys. Rev. A **61**, 061601 (2000).

[77] K. Huang, *Statistical Mechanics* (Wiley, New York, 1987).

[78] J. Dalibard, in *Bose-Einstein condensation in atomic gases, Proceedings of the International School of Physics Enrico Fermi, Course CXL*, edited by M. Inguscio, S. Stringari, and C. Wieman (IOS Press, Amsterdam, 1999), pp. 321–349.

[79] B. D. Esry, C. H. Greene, and H. Suno, "Threshold laws for three-body recombination," Phys. Rev. A **65**, 010705(R) (2001).

[80] J. J. Sakurai, *Modern Quantum Mechanics* (Addison-Wesley, Reading, Massachusetts, 1994).

[81] B. DeMarco, S. B. Papp, and D. S. Jin, "Pauli Blocking of Collisions in a Quantum Degenerate Atomic Fermi Gas," Phys. Rev. Lett. **86**, 5409 (2001).

[82] S. Inouye, M. R. Andrews, J. Stenger, H.-J. Miesner, D. M. Stamper-Kurn, and W. Ketterle, "Observation of Feshbach resonances in a Bose-Einstein condensate," Nature **392**, 151 (1998).

[83] J. V. Steele, "Effective Field Theory Power Counting at Finite Density," arXiv:nucl-th/0010066 (2000).

[84] H. Heiselberg, "Fermi Systems with long scattering lengths," Phys. Rev. A. **63**, 043606 (2001).

[85] R. Combescot, "Feshbach resonance in dense ultracold Fermi gases," arXiv:cond-mat/0302209 (2003).

[86] K. M. O'Hara, S. L. Hemmer, M. E. Gehm, S. R. Granade, and J. E. Thomas, "Observation of a Strongly Interacting Degenerate Fermi Gas of Atoms," Science **298**, 2179 (2002).

[87] M. E. Gehm, S. L. Hemmer, K. M. O'Hara, and J. E. Thomas, "Unitarity-limited Elastic Collision Rate in a Harmonically-Trapped Fermi Gas," Phys. Rev. A. **68**, 011603(R) (2003).

[88] H.-J. Miesner, D. M. Stamper-Kurn, J. Stenger, S. Inouye, A. P. Chikkatur, and W. Ketterle, "Observation of metastable states in spinor Bose-Einstein condensates," Phys. Rev. Lett. **82**, 2228 (1999).

[89] D. S. Hall, M. R. Matthews, J. R. Ensher, C. E. Wieman, and E. A. Cornell, "The Dynamics of Component Separation in a Binary Mixture of Bose-Einstein Condensates," Phys. Rev. Lett. **81**, 4531 (1998).

[90] P. O. Fedichev, Y. Kagan, G. V. Shlyapnikov, and J. T. M. Walraven, "Influence of nearly resonant light on the scattering length in low-temperature atomic gases," Phys. Rev. Lett. **77**, 2913 (1996).

[91] E. Nielsen and J. H. Macek, "Low-Energy Recombination of Identical Bosons by Three-Body Collisions," Phys. Rev. Lett. **83**, 1566 (1999).

[92] D. S. Petrov, "Three-body problem in Fermi gases with short-range interparticle interaction," Phys. Rev. A **67**, 010703(R) (2003).

[93] L. D. Landau and E. M. Lifshitz, *Quantum Mechanics, Non-relativistic Theory* (Pergamon Press, Oxford, 1977).

[94] L. P. Gor'kov and T. K. Melik-Barkhudarov, JETP Lett. **13**, 1018 (1961).

[95] A. J. Leggett, "Cooper Pairing in Spin-Polarized Fermi Systems," Journal de Physique **41**, C7 (1980).

[96] M. A. Baranov, Y. Kagan, and M. Y. Kagan, "On the possibility of a superfluid transition in a Fermi gas of neutral particles at ultralow temperatures," JETP Lett. **64**, 301 (1996).

[97] M. Houbiers, H. T. C. Stoof, and E. A. Cornell, "Critical Temperature of a Trapped Bose Gas: Mean-Field Theory and Fluctuations," Phys. Rev. A **56**, 2041 (1997).

[98] M. Houbiers and H. T. C. Stoof, "Cooper-pair Formation in Trapped Atomic Fermi Gases," Phys. Rev. A **59**, 1556 (1999).

[99] M. J. Holland, S. J. J. M. F. Kokkelmans, M. L. Chiofalo, and R. Walser, "Resonance superfluidity in a quantum degenerate fermi gas," Phys. Rev. Lett. **87**, 120406 (2001).

[100] M. L. Chiofalo, S. J. J. M. F. Kokkelmans, J. N. Milstein, and M. J. Holland, "Signatures of Resonance Superfluidity in a Quantum Fermi Gas," Phys. Rev. Lett. **88**, 090402 (2002).

[101] Private communication with S. J. J. M. F. Kokkelmans and E. Tiesinga.

[102] M. D. Barrett, J. A. Sauer, and M. S. Chapman, "All-Optical Formation of an atomic Bose-Einstein Condensate," Phys. Rev. Lett. **87**, 010404 (2001).

[103] C. H. Schunck, "Study of an ultracold cloud of fermionic ^{6}Li atoms near a Feshbach resonance," Diploma Thesis (unpublished). (2002).

[104] D. M. Stamper-Kurn, M. R. Andrews, A. P. Chikkatur, S. Inouye, H.-J. Miesner, J. Stenger, and W. Ketterle, "Optical confinement of a Bose-Einstein condensate," Phys. Rev. Lett. **80**, 2027 (1998).

[105] M.-O. Mewes, M. R. Andrews, D. M. Kurn, D. S. Durfee, C. G. Townsend, and W. Ketterle, "Output coupler for Bose-Einstein condensed atoms," Phys. Rev. Lett. **78**, 582 (1997).

[106] K. M. O'Hara, S. L. Hemmer, S. R. Granade, M. E. Gehm, J. E. Thomas, V. Venturi, E. Tiesinga, and C. J. Williams, "Measurement of the zero crossing in a Feshbach resonance of fermionic ^{6}Li," Phys. Rev. A **66**, 041401 (2002).

[107] M. B. S. Jochim, G. Hendl, J. H. Denschlag, R. Grimm, A. Mosk, and M. Weidemüller, "Magnetic Field Control of Elastic Scattering in a Cold Gas of Fermionic Lithium Atoms," Phys. Rev. Lett. **89**, 273202 (2002).

[108] S. J. J. M. F. Kokkelmans, J. N. Milstein, M. L. Chiofalo, R. Walser, and M. J. Holland, "Resonance Superfluidity: Renormalization of resonance scattering theory," Phys. Rev. A **65**, 053617 (2002).

[109] T. Loftus, C. A. Regal, C. Ticknor, J. L. Bohn, and D. S. Jin, "Resonant control of elastic collisions in a optically trapped fermi gas of atoms," Phys. Rev. Lett. **88**, 173201 (2002).

[110] M. Houbiers, H. T. C. Stoof, W. I. McAlexander, and R. G. Hulet, "Elastic and inelastic collisions of ^{6}Li atoms in magnetic and optical traps," Phys. Rev. A **57**, R1497 (1998).

[111] T. Bourdel, J. Cubizolles, L. Khaykovich, K. M. F. Magalhães, S. J. J. M. F. Kokkelmans, G. V. Shlyapnikov, and C. Salomon, "Measurement of the Interaction Energy near a Feshbach Resonance in a ^{6}Li Fermi Gas," Phys. Rev. Lett. **91**, 020402 (2003).

[112] C. A. Regal, C. Ticknor, J. L. Bohn, and D. S. Jin, "Tuning p-wave interactions in an ultracold Fermi gas of atoms," Phys. Rev. Lett. **90**, 053201 (2003).

[113] Christophe Salomon, personal communication.

[114] See pp. 239 in *Progress in Low Temperature Physics*, Volume 10, edited by D. F. Brewer (North-Holland Physics Publishing, a division of Elsevier Science Publishers B.V., Amsterdam, The Netherlands, 1986).

[115] C. Menotti, P. Pedri, and S. Stringari, "Expansion of an Interacting Fermi Gas," Phys. Rev. Lett. **89**, 250402 (2002).

[116] Y. Kagan and B. V. Svistunov, "Evolution of Correlation Properties and Appearance of Broken Symmetry in the Process of Bose-Einstein Condensation," Phys. Rev. Lett. **79**, 3331 (1997).

[117] C. A. Regal and D. S. Jin, "Measurement of Positive and Negative Scattering Lengths in a Fermi Gas of Atoms," Phys. Rev. Lett. **90**, 230404 (2003).

[118] P. Pedri, D. Guéry-Odelin, and S. Stringari, "Dynamics of a classical gas including dissipative and mean field effects," arXiv:cond-mat/0305624 (2003).

[119] For higly elongated traps ($\lambda \ll 1$), the asymptotic value of the aspect ratio is given by $0.38/\lambda$ [G.V. Shlyapnikov, private communication] - ref. 14 within [115].

[120] S. Stringari, "Collective Excitations of a Trapped Bose-Condensed Gas," Phys. Rev. Lett. **77**, 2360 (1996).

[121] S. D. Gensemer and D. S. Jin, "Transition from collisionless to hydrodynamic behavior in an ultracold Fermi gas," Phys. Rev. Lett. **87**, 173201 (2001).

[122] Duke group - John Thomas, talk at Gordon conference 2003.

[123] E. Fermi and S. Rasetti, "Effect of an Alternating Magnetic Field on the Polarisation of the Resonance Radiation of Mercury Vapour," Nature **115**, 764 (1925).

[124] K. G. Petrosyan, "Fermionic atom laser," JETP Lett. **70**, 11 (1999).

[125] P. Torma and P. Zoller, "Laser Probing of Atomic Cooper Pairs," Phys. Rev. Lett. **85**, 487 (2000).

[126] G. Bruun, P. Torma, M. Rodriguez, and P. Zoller, "Laser probing of Cooper-paired trapped atoms," Phys. Rev. A. **64**, 033609 (2001).

[127] N. Ramsey, "A Molecular Beam Resonance Method with Separated Oscillating Fields," Phys. Rev. **78**, 695 (1950).

[128] M. Kasevich, E. Riis, S. Chu, and R. deVoe, "rf Spectroscopy in an Atomic Fountain," Phys. Rev. Lett. **63**, 612 (1989).

[129] A. Clairon, C. Salomon, S. Guellati, and W. D. Phillips, "Ramsey Resonance in a Zacharias Fountain," Europhys. Lett. **16**, 165 (1991).

[130] C. Fertig and K. Gibble, "Measurement and Cancellation of the Cold Collision Frequency Shift in an ^{87}Rb Fountain Clock," Phys. Rev. Lett. **85**, 1622 (2000).

[131] K. Gibble, S. Chang, and R. Legere, "Direct observation of s-wave atomic collisions," Phys. Rev. Lett. **75**, 2666 (1995).

[132] H. J. Lewandowski, D. M. Harber, D. L. Whitaker, and E. A. Cornell, "Observation of Anomalous Spin-State Segregation in a Trapped Ultracold Vapor," Phys. Rev. Lett. **88**, 070403 (2002).

[133] J. M. McGuirk, H. J. Lewandowski, D. M. Harber, T. Nikuni, J. E. Willeams, and E. A. Cornell, "Spatial Resolution of Spin Waves in an Ultracold Gas," Phys. Rev. Lett. **89**, 090402 (2002).

[134] D. M. Harber, H. J. Lewandowski, J. M. McGuirk, and E. A. Cornell, "Effect of cold collisions on spin coherence and resonance shifts in a magnetically trapped ultracold gas," Phys. Rev. A. **66**, 053616 (2002).

[135] I. Rabi, S. Millman, P. Kusch, and J. Zacharias, "The Molecular Beam Resonance Method for Measuring Nuclear Magnetic Moments," Phys. Rev. **55**, 526 (1939).

[136] Our estimate uses the direct mean field measurement of Bourdel *et. al.*[111] scaled to our parameters .

[137] E. G. M. van Kempen and et. al., in preparation (2003).

[138] M. E. Gehm, S. L. Hemmer, S. R. Granade, K. M. O'Hara, and J. E. Thomas, "Mechanical stability of a strongly interacting Fermi gas of atoms," Phys. Rev. A **68**, 011401(R) (2003).

[139] C. A. Regal, C. Ticknor, J. L. Bohn, and D. S. Jin, "Creation of ultracold molecules from a Fermi Gas of Atoms," Nature **424**, 47 (2003).

[140] T. L. Gustavson, A. P. Chikkatur, A. E. Leanhardt, A. Görlitz, S. Gupta, D. E. Pritchard, and W. Ketterle, "Transport of Bose-Einstein Condensates with Optical Tweezers," Phys. Rev. Lett. **88**, 020401 (2002).

[141] K. Mlmer, "Phase collapse and excitations in Bose-Einstein condensates," Phys. Rev. A **58**, 566 (1998).

[142] G. Modugno, G. Roati, F. Riboli, F. Ferlaino, R. J. Brecha, and M. Inguscio, "Collapse of a degenerate Fermi gas," Science **68**, 011601 (2002).

[143] J. Cubizolles, T. Bourdel, S. J. J. M. F. Kokkelmans, G. V. Shlyapnikov, and C. Salomon, "Production of Long-Lived Ultracold Li_2 Molecules from a Fermi Gas," cond-mat/0308018 (2003).

[144] S. Jochim, M. Bartenstein, A. Altmeyer, G. Hendl, C. Chin, J. H. Denschlag, and R. Grimm, "Pure gas of Optically Trapped Molecules Created from Fermionic Atoms," arXiv:cond-mat/0308095 (2003).

[145] Y. Ohashi and A. Griffin, "BCS-BEC crossover in a gas of Fermi atoms with a Feshbach resonance," Phys. Rev. Lett. **89**, 130402 (2002).